Nonlinear Control of Rotating Stall and Surge with Axisymmetric Bleed and Air Injection on Axial Flow Compressors

Thesis by
Chung-hei (Simon) Yeung

In Partial Fulfillment of the Requirements
for the Degree of
Doctor of Philosophy

California Institute of Technology
Pasadena, California

1999

(Defended 28th August, 1998)

Acknowledgment

During the past five years of my life, I have not only learned a great deal about science and engineering but also the process of learning itself. This experience would not have existed without contributions from a number of people.

First and foremost I wish to thank my advisor, Professor Richard M. Murray for everything he has done for me. His devotion and energetic approach to solving problems, persistence in technical excellence, and adventurous spirit in performing research for a wide range of topics, has inspired my own dedication. I am especially thankful for his enthusiasm when there is a discovery, understanding when there is little progress, and the vision of the bigger picture. In research, it is extremely easy for one to allow oneself to get trapped and lost in the process of pursuing details. The guidance he provided and questions he asked have rescued me from falling into this trap numerous times. Aside from the technical contribution, Richard's plentiful resources also helped a great deal in allowing research without hassle and worries. I wish to also thank Professors G. R. Gavalas, R. C. Flagan, T. K. Caughey, and F. E. C. Culick for taking their time to be my Ph.D. committee and offering their valuable comments.

There are also a number of fellow students, some now former students, who have contributed to my work directly or indirectly. Raffaello D'Andrea and Robert Behnken helped me understand the principles and tricks in experimentation and the art of problem solving. They have taught me a great deal in making things work. It is especially gratifying when experimental results correlate well with the theory! I would also like to thank Asif Khalak who built the facility as his SURF project.

Sudipto Sur, Robert Behnken, and Michiel van Nieuwstadt have contributed

much to my knowledge of computers. In transitioning the local computer network system administration job, they have taught and demonstrated to me procedures and issues in system administration, along with knowledge in computer hardware and software. The experience has strengthened my background and added to my diversity.

Some of the work presented in this thesis is a result of collaboration with other people. In particular I wish to thank Yong Wang for the collaboration on the bleed valve part of the work. I would also like to thank Sean Humbert, Adrienne Bourque, and Evan Tsang for their help in obtaining data from experiments.

There are also people whom some of us take for granted sometimes. The two people whom I wish to thank sincerely are Charmaine Boyd in Control and Dynamical Systems and Maria Koeper in Mechanical Engineering. They have helped in countless occasions to complete the administrative (and sometimes even personal!) requests. I would also like to thank Kathy Bubash in Chemical Engineering and Jackie Beard in Mechanical Engineering for their help.

Outside of Caltech, I wish to thank Professor Jim Paduano, John Protz, and John Chi from M.I.T., Professor Art Krener from UC Davis, Gonzalo Rey, Scott Copeland, and Andrzej Banaszuk from United Technologies Research Center, Professors Petar Kokotović and Igor Mezic, Michael Larsen, and Dan Fontaine from UC Santa Barbara, Professor Miroslav Krstić from UC San Diego, and Hsin-hsiung Wang from University of Maryland, for the conservations and opportunities to work together. Useful insights and current and future directions have resulted from discussions with them.

And last but not least, I would like to thank members of my family. My wife Leon Lo, my father Kenneth Yeung, and my mother Molly Yeung for their patience and support during the years. They have cheered with me through the good times and encouraged me through the bad times.

Abstract

The study of compressor instabilities in gas turbine engines has received much attention in recent years. In particular, rotating stall and surge are major causes of problems ranging from component stress and lifespan reduction to engine explosion. In this thesis, modeling and control of rotating stall and surge using bleed valve and air injection is studied and validated on a low speed, single stage, axial compressor at Caltech.

Bleed valve control of stall is achieved only when the compressor characteristic is actuated, due to the fast growth rate of the stall cell compared to the rate limit of the valve. Furthermore, experimental results show that the actuator rate requirement for stall control is reduced by a factor of fourteen via compressor characteristic actuation. Analytical expressions based on low order models (2–3 states) and a high fidelity simulation (37 states) tool are developed to estimate the minimum rate requirement of a bleed valve for control of stall. A comparison of the tools to experiments show a good qualitative agreement, with increasing quantitative accuracy as the complexity of the underlying model increases.

Air injection control of stall and surge is also investigated. Simultaneous control of stall and surge is achieved using axisymmetric air injection. Three cases with different injector back pressure are studied. Surge control via binary air injection is achieved in all three cases. Simultaneous stall and surge control is achieved for two of the cases, but is not achieved for the lowest authority case. This is consistent with previous results for control of stall with axisymmetric air injection without a plenum attached.

Non–axisymmetric air injection control of stall and surge is also studied. Three existing control algorithms found in literature are modeled and analyzed. A three–state model is obtained for each algorithm. For two cases, conditions for linear stability and bifurcation criticality on control of rotating stall are derived and expressed in terms of implementation–oriented variables such as number of injectors. For the third case, bifurcation criticality conditions are not obtained due to complexity, though linear stability property is derived. A theoretical comparison between

the three algorithms is made, via the use of low–order models, to investigate pros and cons of the algorithms in the context of operability.

The effects of static distortion on the compressor facility at Caltech is characterized experimentally. Results consistent with literature are obtained. Simulations via a high fidelity model (34 states) are also performed and show good qualitative as well as quantitative agreement to experiments. A non–axisymmetric pulsed air injection controller for stall is shown to be robust to static distortion.

Contents

Nomenclature

Symbols:

A	amplitude of first Fourier mode
A_c	compressor duct area
A_i	amplitude of ith Fourier mode
a	area of deflected jet normal to ζ–axis
a_i	entrainment coefficients
a_s	speed of sound
B	Greitzer B parameter for surge, $B = \dfrac{U}{2a_s}\sqrt{\dfrac{V_p}{A_c L_c}}$
b	radius of deflected jet normal to ζ–axis
b_x	radius of jet in the direction normal to axial flow
C_j	magnitude of injected velocity
C_x	mean axial velocity
C_{xj}	magnitude of axial component of injected velocity
c	circumference of deflected jet normal to ζ–axis
d	diameter of circular jet
f/c	camber ratio = maximum camber height divided by chord
H	fitting coefficient for Moore–Greitzer type cubic compressor characteristic
J	squared amplitude of first Fourier mode, $J = A^2$
K_{RS}	gain for control of rotating stall in Liaw–Abed control law
K_{SU}	gain for control of surge in Eveker et al. [24] control law
K_X	gain estimation from method X
L_c	total aerodynamic length of system, $L_c = l_c R$
L_r	rotor losses
L_r^{ss}	steady–state rotor losses
L_s	stator losses
L_s^{ss}	steady–state stator losses
l_I	length of inlet duct, nondimensionalized by R
l_E	length of exit duct, nondimensionalized by R
l_a	radial distance of annulus
l_c	nondimensional effective length of compression system

m	throttle exit parameter
P	static pressure
P_{isen}	isentropic pressure rise
P_{qs}	quasi–static pressure rise, $P_{\text{qs}} = P_{\text{isen}} - \delta p$
p_i	static pressure at station i
p_{t_i}	total pressure at station i
R	mean rotor radius
R_{X}	rate estimation from method X
$\tilde{R}$	reaction ratio
r	time–dependent phase angle of stall cell
t	time
t/c	maximum thickness divided by chord
U	mean rotor speed
U_0	initial velocity of jet
U_1	free–stream velocity
u	cross–sectional mean velocity of jet along ζ–axis
u_x	mean axial velocity of jet
u_j	control effort via air injection
u_{mag}	magnitude saturation of the bleed actuator as percentage of Φ^*
u_{rate}	bleed valve rate limit in rotor revolutions for valve to open from fully closed
V_p	volume of plenum
v_e	entrainment velocity as found in Platten and Keffer [74]
$\hat{v}_e$	entrainment velocity as found in Hoult and Weil [43]
$\tilde{v}_e$	entrainment velocity as found in this thesis
W	fitting coefficient for Moore–Greitzer type cubic compressor characteristic
α	inlet flow angle
α_o	outlet flow angle
β set	angle between chord and plane of rotor disk
δC_{x_i}	axial velocity perturbation at station i
δl_j	distance of opening of injector in plane normal to axial direction
δp	losses across a cascade

δp_i static pressure perturbation at station i

δp_{t_i} total pressure perturbation at station i

$\delta \phi$ nondimensional axial velocity perturbation

$\delta \phi_i$ nondimensional axial velocity perturbation at station i, $\delta \phi_i = \delta C_{x_i}/U$

$\delta \Theta$ disturbance velocity potential

ϵ noise level of the system expressed as a percentage of J

γ throttle coefficient

λ rotor inertia parameter

μ fluid inertia parameter

ν fraction of cascade affected by air injection

Ω rotor angular velocity

ϕ nondimensional axial velocity, $\phi = \Phi + \delta \phi$

Φ^* Φ at peak of compressor characteristic

ϕ_i nondimensional axial velocity at station i

Φ_j nondimensional injected velocity, $\Phi_j = C_j/U$

Φ_{xj} nondimensional injected velocity in axial direction

Φ nondimensional mean axial velocity, $\Phi = C_x/U$

Ψ nondimensional mean pressure rise coefficient

Ψ^* Ψ at peak of compressor characteristic

$\Psi_c, \Psi_c^{\text{qs}}$ compressor characteristic, $\Psi_c = P_{\text{qs}}/(\rho U^2)$

Ψ_c^{isen} nondimensional isentropic compressor characteristic, $\Psi_c^{\text{isen}} = P_{\text{isen}}/(\rho U^2)$

Ψ_{c0} fitting coefficient for Moore–Greitzer type cubic compressor characteristic

ρ density of air

τ_r nondimensional unsteady rotor loss dynamics time constant

τ_s nondimensional unsteady stator loss dynamics time constant

θ circumferential angle

θ_0 initial angle of jet

θ_1 angle of jet at downstream location

ξ nondimensional time, $\xi = tU/R$

ζ jet–axis

Superscripts and subscripts:

qs   quasi–steady

ss   steady–state

Chapter 1

Introduction, Background, and Motivation

The development of gas turbine engines dates back to as far as the 18th and 19th centuries. A patent was issued to J. Barber [3, 75] in 1791 for the concept of a gas turbine. Stolz received a patent in 1872 for the concept of a gas turbine engine with multi–stage rotating components [84]. The concept was turned into a design, built, and tested in 1900 but suffered from low component efficiencies [83].

After more than two hundred years, gas turbine engines are widely used today in aircraft as well as stationary power plants. For aircraft flying at altitude over 20,000 feet and Mach 0.4, gas turbine engines have replaced reciprocating engines due to favorable attributes such as lower weight and vibration levels [31]. Engines used in aircrafts ranging from civilian transports to fighter planes to unmanned aerial vehicles (UAV) and drones typically have higher efficiency, while those used for power generation lower.

There are many different types of instabilities that occur in a gas turbine engine (see Figure 1.1). Some examples are inlet buzz at the front, rotating stall, surge, and flutter in compressors, pressure oscillations in combustors, tip clearance issues in turbine, and jet noise at the back. In particular, rotating stall refers to a non–axisymmetric flow perturbation that travels around the annulus of the compressor (sometimes referred to as a stall cell), while surge is a large axial oscillation of the flow. Typical effects associated with stall are high mechanical stress level in the blading, large drop in performance, and possible turbine overheating due to the

Inlet Separation

Flutter and Forced Response
High Cycle Fatigure

Compressor Stall & Surge

Combustion Instab.

Shear Layer Instab.
Turbulence

Inlet Buzz

Distortion
Noise

Bearing & Seal
Technology

Turbine Tip Clearance
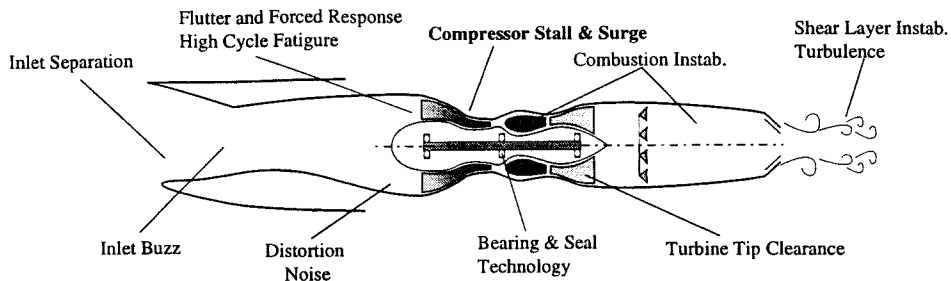
Figure 1.1 Simplified engine diagram. (Figure courtesy of Professor James D. Paduano at M.I.T.)

decreased flow. Furthermore, the stall condition is irrecoverable in some systems, in which case a shut–down of the entire setup is in order. Surge induces high blade and casing stress levels and possible reverse flow in the case of deep surge. Due to the presence of a combustion process downstream, surge is often detrimental to the flight process and can cause engine explosion.

These various instabilities associated with the components of an engine have been popular topics of research in recent years. For aircraft gas turbine engines, as part of an effort to make gas turbine engines more energy efficient, safer, and compliant with increasingly restrictive Federal Aviation Administration (FAA) emissions regulations, concepts of active controls and smart engine technologies have been at the center of attention and research in recent years. Stationary power plants can also make use of active control concepts to allow safer, more efficient power generation, and possibly increased life–time hours of the engines.

In this chapter, an overview of compressors is given. Some background of compressor operation, design, and instabilities is presented. The potential role, benefits, and issues of active controls are discussed. Previous work in the area of rotating stall and surge relevant to, as well as the contribution of this thesis are described. An outline of this thesis ends the chapter.

1.1   Concepts in Compression Systems

Roughly speaking, an aircraft engine is a machine that combines a compressor, a combustor, and a turbine into a thermal engine. The compressor compresses and passes air into the combustor. Fuel is added to and a chemical reaction initiated in the combustion chamber, and the expanded air is then used to drive the turbine which provides the power for the aircraft and the compressor. The power required to drive the compressor is lower than that extracted from the turbine, and the difference gives rise to thrust for the aircraft[1]. The ratio of the pressure at the compressor outlet to that at the inlet is defined to be the compression ratio (≥ 1). Compressors with low compression ratios (close to 1) are often referred to as "low speed" compressors in which the air speed is typically subsonic.

A simplified version of the aircraft engine design procedure is described in Mattingly et al. [60]. Requirements such as corrected mass flow, thrust, and specific fuel consumption of the engine/aircraft are specified. The design points (and the appropriate thermodynamic cycles) of the compressor, combustor, and turbine are then specified in order to fulfill requirements of the engine. Off–design performance analysis is carried out to provide updates for the detailed design stage. After detailed designs of the components are available, the prototype is then manufactured and tested. Further modifications are specified after the prototype is tested, and the design–test loop is iterated until the results are satisfactory. The final design schematics are then used in production, from which feedback is derived for the current or next generation of the engine (see Figure 1.2).

After the design operating point of a compressor is specified, a detailed design is needed. Aircraft engines are exposed to a wide variety of disturbances, both internal and external [68]. Traditionally, the disturbances are categorized and sized in terms of compressor performance variables such as corrected mass flow and pressure ratio. These elements are then combined additively to give the stall/surge margin requirements, from which the peak performance of the compressor is derived. A pictorial view of the categorization and sizing of these elements are summarized in Figure 1.3

---

[1]For instance, an ideal turbojet operates as a Brayton cycle [69].
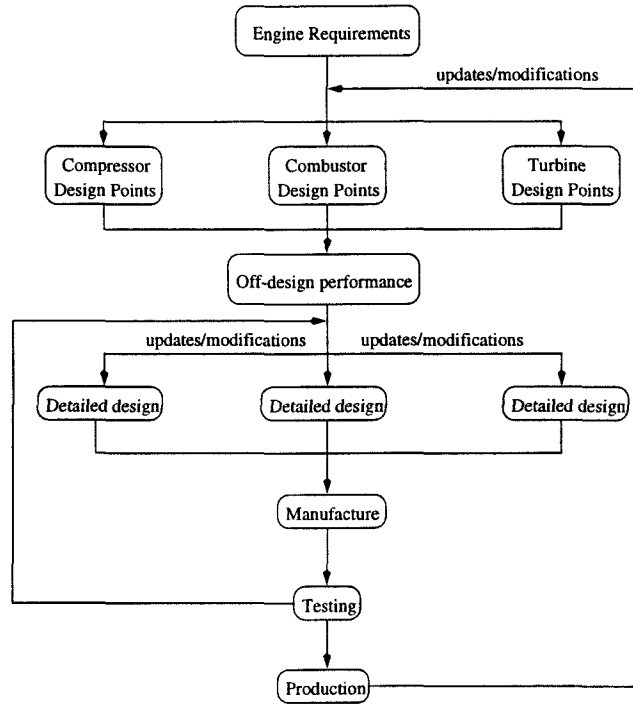
Figure 1.2 Simplified view of the design procedure of an aircraft engine.

which is sometimes referred to as a stability stack [68]. Detailed design guidelines such as number of stages, blades, and efficiency are then derived according to the requirements.

In research facilities, an approximation of an engine is often used (Figure 1.4). A throttle is typically used as the load of the system which controls the pressure rise across the system. A plenum inserted between the compressor outlet and the throttle simulates a combustion chamber volume and allows investigation of the effects of compliance. The pressure ratio is often replaced by simply the pressure rise across the compressor, and corrected mass flow by axial velocity at the rotor face. These quantities are nondimensionalized so that different compressors can be compared on the same basis. The flow coefficient $\Phi = C_x/U$ is defined as the axial velocity C_x at the compressor face nondimensionalized by the mean wheel speed U, and pressure rise coefficient $\Psi = \Delta P/\rho U^2$ the total–to–static pressure rise across the compressor ΔP nondimensionalized by the density of air ρ and the square of

1). comp. manufacturing tolerances
2). deterioriation
3). thermal transient
4). stator tracking error
5). distortion
6). distortion tolerance
7). remaining margin
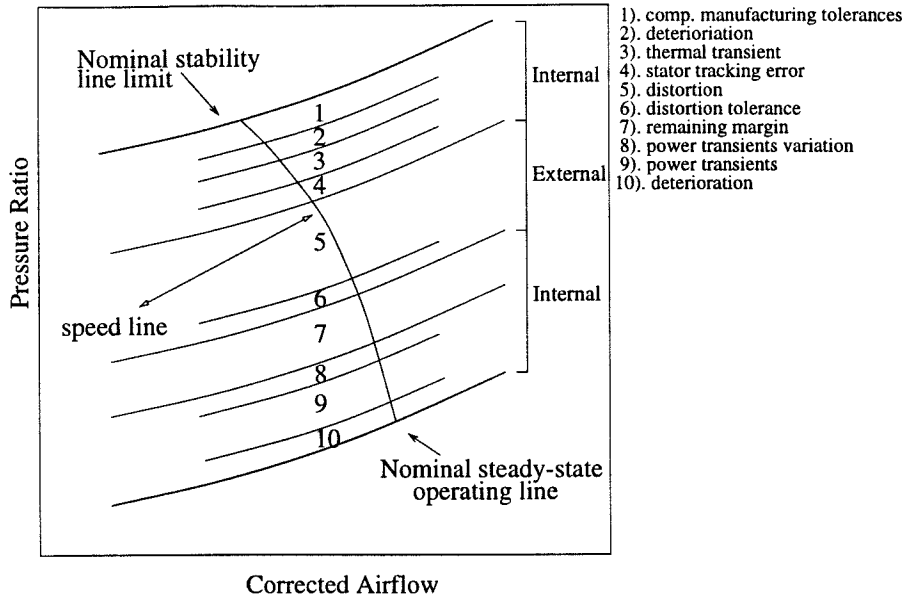8). power transients variation
9). power transients
10). deterioration

Figure 1.3 Stability stack diagram for compressors.
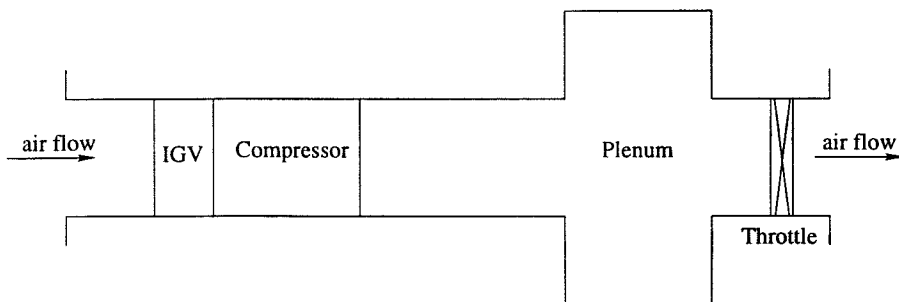
Figure 1.4 Typical research compression system facility.

Surge: large axisymmetric oscillation of flow
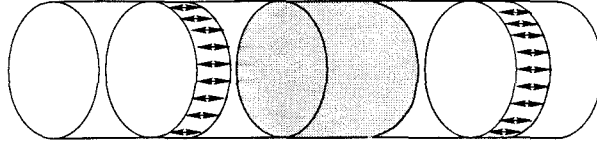
Stall: non-axisymmetric flow disturbance
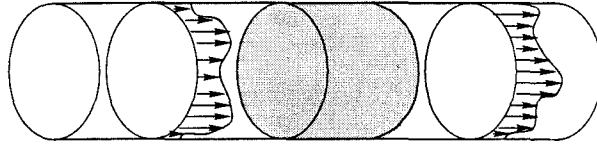
Figure 1.5 Pictorial representation of stall and surge.

the mean wheel speed.

1.2   Rotating Stall and Surge

A general description for rotating stall is a non-axisymmetric flow perturbation that travels around the annulus of a compressor, and surge represents a large axial flow oscillation. Figure 1.5 shows the instabilities pictorially.

Rotating stall in compressors is related to the aerofoil stall phenomenon. On aerofoils, stall occurs when a critical angle-of-attack is reached at which point separation occurs. The aerofoil suffers a performance loss in terms of a decrease in lift and an increase in drag. Figure 1.6 shows a picture, found in Küchemann [17], of leading and trailing edge stall on an aerofoil and the corresponding lift curve as a function of angle-of-attack.

For cascades of blades in compressors, a compressor characteristic curve (sometimes referred to as a speed line) is used to characterize the steady-state performance of a compression system. The presence of rotating stall in axial flow compressors often leads to a hysteresis effect (Figure 1.7). As the flow-rate is reduced, the flow disturbance in the system grows as the pressure rise is increased (path 1); when the system approaches the stall point (point A), the pressure rise drops abruptly, and the system goes into stall (point B); if the flow-rate is then increased, the system

1. Attached boundary layer

2. Rear separation

3. Leading-edge separation
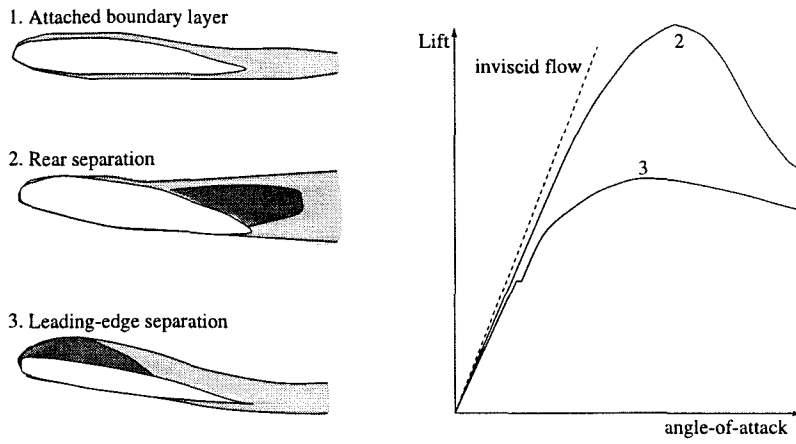
Figure 1.6 Pictorial representation of aerofoil stall and lift.
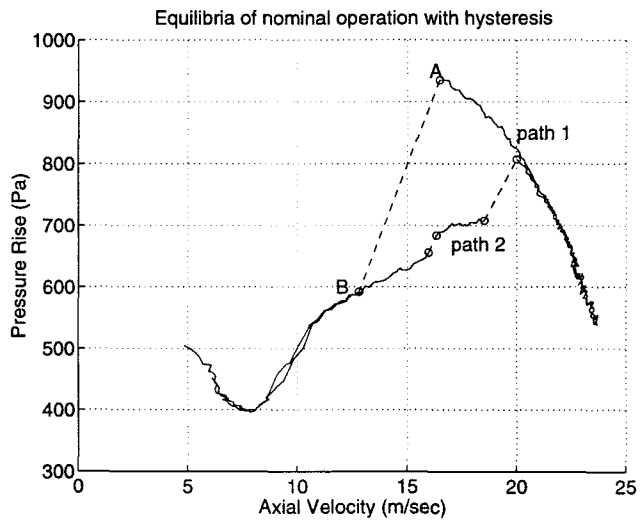
Figure 1.7 Sample of speed line and stalled operation.
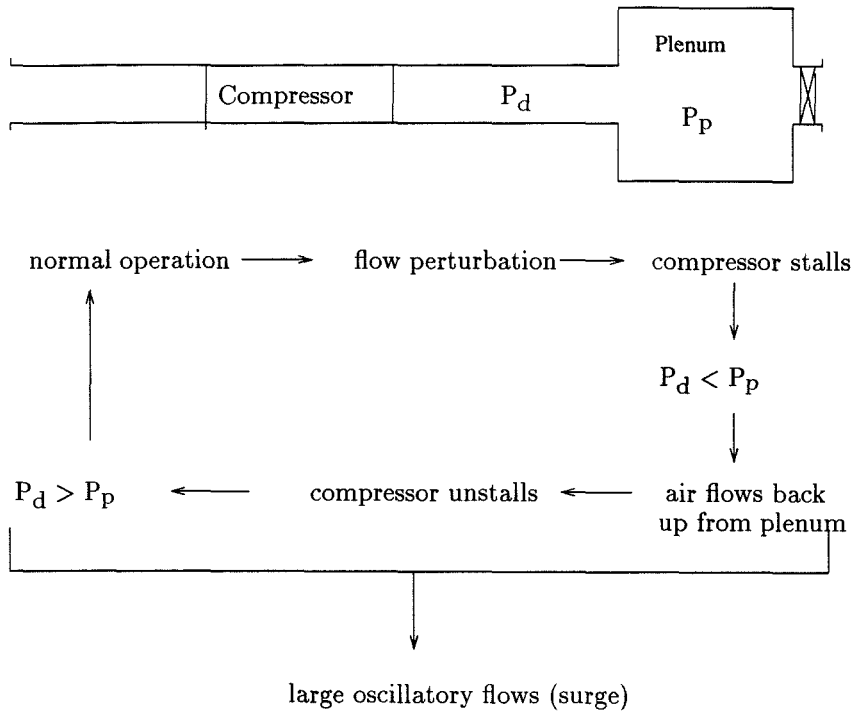
Figure 1.8 Cause of surge.

does not jump back to point A but follows path 2, and eventually goes out of stall and joins path 1.

Surge can occur in several ways. Researchers [15] speculate that one of such ways is through the presence of rotating stall. During steady operation, the pressure in the outlet duct is the same as that in the plenum. When the system is stalled, the pressure in the outlet duct suddenly decreases. The resulting difference in pressure causes the air to flow back from the plenum up into the outlet duct. As the air is traveling backwards, the system goes out of stall, and the pressure in the outlet duct is thus increased back to the original level, hence pushing the air back into the plenum. As the air travels into the plenum, the disturbance in the fluid grows to be large enough for stall to occur, and the process repeats itself, forming an oscillatory flow. Figure 1.8 displays the idea pictorially.

1.3 Motivation for and Issues with Active Controls

Due to the presence of compressor instabilities, engineers often design compressors used in jet engines with a safety margin to avoid possible stall and surge (Figure 1.3). This margin between the stall/surge inception point and the actual operating point is characterized by a stability stack. Although the actual operating point is normally designed to have a high efficiency, the stall/surge margin represents compression capability, and hence weight, that is not used.

Active control of rotating stall and surge can lead to an increase in the stability/operability of a compressor against various disturbances such as thermal transients, inlet distortions, and power transients. As a result, a compressor with active controls can operate closer to the current stall/surge line, implying a reduction of the stall/surge margin without compromising safety and/or performance during on-design operation. For applications on some aircrafts (e.g. civilian transports) where cost is important, a re-design of the compressor with active controls strategies can allow the reduction of the stall/surge margin to be realized in a number of ways such as fewer number of stages/blades per stage. The weight reduction can then be translated into benefits such as lower take-off gross weight and lower specific fuel consumption. For other aircraft (e.g. fighter aircraft) and stationary power plants where performance and safety are important, the increased stability/operability can provide the ability to run at higher capacity or speed, resulting in increased points of efficiency, higher performance, and/or stability/operability enhancement in maneuvers. Examples can be found in a set of reports prepared by Pratt and Whitney [46], General Electric Aircraft Engines [22], and Allison Gas Turbine [21] for the National Technical Information Service of the U.S. Department of Commerce on an evaluation of control concepts applied to gas turbine engine operations for both civilian and military aircrafts.

Modern gas turbine engines have certain control and scheduling capabilities via full authority digital engine controllers (FADECS). Active control of rotating stall and surge, however, is still in a proof-of-concept/evaluation stage. One of the most important issues is the choice and availability of sensors and actuators. Sensing

is often difficult given the highly vibratory and hostile environment found in gas turbines. Existing actuation mechanisms on compressors are typically low in bandwidth while proposed active control schemes are speculated to require high bandwidth actuators [76]. The issue of maintenance and weight of the actuators is also important from a practicality point of view [21, 22, 46]. Also, redesigning an engine is a long and expensive process. Hence, software changes are much more welcome than hardware ones. If a hardware change is imminent, retrofitting an engine with the least number of elements is by far the most preferable way to incorporate active control strategies. As a result, the issue of number and authority of actuators, or more generally, actuator limits, needs to be addressed. Valuable tools for control of compressor instabilities thus include items such as predictive tools for actuator requirement and methods to lower these requirements, in addition to sound models and control design.

The effects of the various elements in the stability stack are also important. Since the motivation for implementing active control strategies is to increase stability/operability of the engine in the presence of elements that induce instabilities, characterization of and robustness of control strategies with respect to these elements are important issues.

1.4 Previous Work

The current state–of–the–art actuators used for control of rotating stall and surge include actuated inlet guide vanes (IGV), bleed valves, air injection, and combinations of them. The work in these areas have been a combination of experiments, simulations, as well as theory. Most of the previous work focuses on demonstration of control.

Bleed valves is an existing technology on current gas turbine engines. They are primarily low bandwidth and used for control of boundary layers, cooling of combustor and turbine operations [60], and regulation of compressor behavior during engine start–up[2] [69].

---

[2]During start–up of an engine containing a multistage compressor, earlier stages of the com-

Modeling and active control of rotating stall and surge has been investigated by a number of researchers. A simplified model was derived by Moore and Greitzer [37, 65] for a compression system that exhibits rotating stall and surge. Based on this model, Liaw and Abed [54] and Krstić et al. [49] derived control laws using bleed valves for rotating stall. Eveker et al. [24] is the first group to report successful experimental implementation of a bleed valve controller. Their results indicate no subtleties or major difficulties.

Aside from bleed valves, various implementations of air injection for control of rotating stall have also been studied [4, 6, 12, 15, 30, 38, 92, 95, 96]. In particular, Behnken [4] and Freeman et al. [30] have implemented axisymmetric air injection with various injection configuration and obtained success for control of stall, and Weigl [95] presented some preliminary work on simultaneous control of stall and surge, though without success.

Aside from an axisymmetric implementation, air injection can also be used in a non–axisymmetric fashion. Behnken [4], Behnken et al. [6], D'Andrea et al. [12], Day [15], Gysling and Greitzer [38], Vo [92], Weigl [95], Weigl et al. [96] have implemented non–axisymmetric air injection in various different forms and obtained success for extending stability and/or operability of the underlying compression systems beyond their respective nominal stall inception points.

In particular, Vo [92], Weigl [95], and Weigl et al. [96] make use of high bandwidth, proportional, motor–driven valves to exert bi–directional harmonic control for rotating stall. The actuation essentially "cancels" the stall cell and extends linear stability. The analysis and synthesis methods found in Vo [92], Weigl [95], and Weigl et al. [96] associated with this approach are primarily linear. Some efforts in modeling have been carried out by Gysling and Greitzer [38], in which the mass and momentum effects of air injection are taken into account in a linear context.

In Behnken [4], Behnken et al. [6], and D'Andrea et al. [12], high bandwidth, binary, solenoid–driven valves are used to implement a discrete, nonlinear, pulsed algorithm for control of stall. In this case, the nominally hysteretic, abrupt stall

---

pressor tend to stall while later ones tend to windmill. Bleeding air at the appropriate stages can regulate the air velocity in the compressor and resolve the issue.

behavior is changed to progressive stall with no hysteresis, i.e. operability but *not* stability, is extended. The analysis approach as found in Behnken [4], Behnken et al. [6], and D'Andrea et al. [12] is bifurcation–theoretic via a low–order model. Similar to Gysling and Greitzer [38], the mass and momentum effects of air injection are taken into account in Behnken [4] but in a nonlinear context. An attempt to account for the compressor performance change due to air injection is also made.

The ultimate role of active control is to improve the operability of the compressor in the occasional presence of disturbances that may render the compressor, and thus the engine, inoperable. One such example is inlet disturbances.

External total pressure disturbances at the compressor inlet comprise of a major portion of the surge tolerance margin of aeroengines as depicted in Figure 1.3. There are three main sources of inlet disturbances: planar waves, static distortions, and rotating distortions. Since a significant portion of the surge margin is devoted to avoiding stall and surge of engines due to distortions, the subject of the effects of inlet disturbances and characterization thereof has naturally received a lot of attention over the years.

Various aspects of the effects of static and rotating total pressure distortions on axial compressors have been studied by research groups in the past, including but not limited to Lucas et al. [58], the SAE S–16 committee [81, 82], Chue et al. [9], Hynes et al. [45], Longley and Greitzer [56], Longley et al. [57], Greitzer et al. [36], Stenning [88], and Mazzawy [61]. Some results for control in the presence of static distortion have been achieved by Schalkwyk et al. [91] and Spakovszky et al. [87].

1.5 Contribution of Current Work

The work described in this thesis serves to provide a better understanding on the modeling, usage, and subtleties of bleed valve and air injection control of rotating stall and surge. Robustness of non–axisymmetric air injection to static distortion is also explored.

Eveker et al. [24] is the first group to report successful experimental implemen-

tation of a bleed valve controller. In particular, the bleed valve actuation method tested by Eveker et al. [24] employs a 25 Hz (full open/full close) bleed valve and reports results on a compressor at rotor frequencies between 22.5 and 26.7 Hz. For industrial applications where the compressors may be significantly more powerful (higher flow and pressure rise, higher rotor frequency, etc.) than research compressors, obstacles such as control actuator magnitude and rate saturation can become crucial in these active control methods. Tools that predict and reduce the rate requirements of actuators for purposes of control of rotating stall in compressors can be valuable in designing actuators and circumventing possible actuator magnitude and rate limitations that may prevent successful active control implementations.

The goals of the bleed valve study are to demonstrate control of stall and surge and investigate the effects of actuator limits. Theoretical and simulation tools are developed for assessing effects of actuator limits on bleed valve control of stall. An investigation of the trade-off between actuation of the compressor characteristic and the bleed valve rate requirement is carried out, with the following goals:

1. Identify possible functional dependence of the rate limit of a bleed valve in control of rotating stall on the shape of the compressor characteristic.

2. Validate proposed tools.

3. Provide a possible route to circumvent bleed valve rate limitation given the capability of actuation or modification of the compressor characteristic.

4. Provide insights for designing a compressor-bleed pair for purposes of stabilization of rotating stall.

Behnken [4], Freeman et al. [30], and Weigl [95] demonstrate control of stall using axisymmetric air injection via slightly different implementations. Some preliminary work on axisymmetric air injection control of stall and surge is reported in Appendix D in Weigl [95]. The results in [95] show that stall is stabilized but the system goes into classic surge.

A more thorough investigation into simultaneous stabilization of stall and surge with axisymmetric air injection is carried out in this thesis. If successful, new pos-

sibilities such as various combinations of actuation mechanisms for control of compressor instabilities will be created. Comparison and trade–off studies for various actuation mechanisms can then be performed. Also, with a multi–block representation of the compressor where actuation is possible for each block, the issue of actuator allocation can also be addressed and formulated.

The goals of the axisymmetric air injection study are to provide a simple model of axisymmetric air injection and a theoretical basis for control of stall and surge. The ideas are then validated against the experiments, and simultaneous stabilization of stall and surge via axisymmetric air injection is compared to other combinations of actuators.

For non–axisymmetric air injection, researchers including but not limited to Behnken [4], Behnken et al. [6], D'Andrea et al. [12], Day [15], Freeman et al. [30], Gysling and Greitzer [38], Vo [92], Weigl [95], and Weigl et al. [96] have implemented air injection in various different forms and obtained success for extending stability and/or operability of the underlying compression systems beyond their respective nominal stall inception points.

Despite all of the reported success, an understanding of the effects of air injection on compression systems and explanation of certain observed phenomena are still missing. For instance, the yaw effects of injection on compressor performance reported in Behnken [4], Behnken et al. [6], D'Andrea et al. [12], and Weigl [95] have not been explained. Furthermore, *closed–loop control results that differ quantitatively as well as qualitatively* have been reported in D'Andrea et al. [12] and Weigl [95], where different implementations of the *same* underlying actuation mechanism, namely, air injection, are used.

Some modeling efforts such as those by Gysling and Greitzer [38] and Behnken [4] can be found in the literature. Considerations of losses and incidence angle in cascade performance can also be found in the literature, such as that by Horlock [41] in the 50s, as well as that by Fréchette [29] in recent years. In particular, Fréchette addresses losses, deviation, time lags, etc. in the context of modeling the nominal compressor cascade stability and performance, and stall inception in high–speed

machines.

There has been no account, however, on the changes in losses and incidence angle in the compression system as a result of air injection. In the current work, a method of modeling air injection in axial flow compressors that is motivated by both unexplained observations as well as various control results is proposed. The effects of air injection on cascade performance is modeled as incidence angle and losses management. The losses from the nominal compressor is parameterized by the incidence angle. The resulting description is then used to compute the new losses for a given air injection configuration. A parallel compressor approach [45, 61] is adopted to sum and average the parts with and without air injection to give the "shifted" compressor characteristic. The shifted characteristic is then combined with the mass and momentum addition to give the resulting "aggregate" compressor characteristic.

The goal of the non–axisymmetric air injection study is to provide a simple, control–oriented model of air injection that is derived from fluid mechanic principles. The proposed model explains the yaw angle effects and exhibits the proper behavior when control laws reported in literature are substituted. Conditions (dependent on "implementation–oriented" variables such as number of injectors) of linear and bifurcation properties for existing control laws are obtained. A trade–off study is also carried out to investigate effects of parameters such as number/width of injectors and maximum injected velocity on linear and bifurcation properties of the system. In addition to the theoretical comparison, a simulation tool based on a high fidelity model proposed by Mansoux et al. [59], realistic dynamics proposed by Haynes et al. [39], and air injection effects developed in this thesis is built and validated.

Some modeling, characterization, as well as control results can be found for static distortion [9, 36, 45, 56, 61, 81, 82, 87, 88, 91]. The effects of various static distortion patterns on the Caltech facility are explored experimentally. An existing model found in literature [9, 45] is validated against the experiments. Robustness of control of stall via a non–axisymmetric air injection controller to static distortion is also evaluated experimentally.

1.6 Outline of Thesis

This thesis is outlined as follows. Chapter 2 describes a collection of modeling efforts that are used as bases of results presented in this thesis. A history of models for rotating stall and surge is given, followed by a review of a low order model proposed by Moore and Greitzer [37, 65] and a high fidelity model proposed by Mansoux et al. [59]. The chapter ends with a description of a model for air injection in the context of the Moore–Greitzer model.

Chapter 3 describes work associated with characterization and validation of the proposed models. The experimental apparatus at Caltech along with the behavior of nominal operation is described first. The theory and results for an identification algorithm using surge cycles proposed by Behnken [4] is described and discussed next. Validation of the air injection model is then presented.

Chapters 4, 5, and 6 describe work associated with controls. Chapter 4 presents control of rotating stall and surge using bleed valves. Demonstration of closed–loop control of rotating stall and surge is described first, followed by a comparison study between theory, simulation, and experiments aimed to investigate effects of actuator rate limits.

Air injection control of stall and surge is discussed in Chapters 5 and 6. Results with axisymmetric as well as non–axisymmetric implementations are given. For axisymmetric air injection, theoretical justification for control of rotating stall and surge is presented in Chapter 5. Experimental results are presented and a discussion of the observations given. Some preliminary work on accounting for the effects of actuator rate and magnitude limits for axisymmetric air injection is also presented.

Chapter 6 describes the results for non–axisymmetric air injection. Three existing control approaches found in literature are modeled in "implementation–oriented" variables, such as number and authority of the injectors, using the air injection model proposed in Chapter 2. Linear and bifurcation properties are explored for each approach. A theoretical comparison is then performed in the context of operability to investigate the pros and cons of the controllers. In addition to the theoretical comparison, a simulation tool for a non–axisymmetric pulsed air injection algorithm

is developed and validated against experiments.

In addition to work in undistorted flow, modeling and control in the presence of static distortion is also investigated in Chapter 7. Five static distortion patterns are tested in open– as well as closed–loop, with a non–axisymmetric pulsed air injection control active for the latter.

A set of conclusions are drawn from the effort and presented in Chapter 8. Possible future avenues of research are also discussed. Funding for the work presented in this thesis was provided in part by AFOSR grant F49620-95-1-0409.

Chapter 2

Modeling

In this chapter, a collection of modeling efforts is presented. A brief account of the history of models for stall is given in Section 2.1. A low order phenomenological model proposed by Moore and Greitzer [37, 65] and a higher fidelity counterpart by Mansoux et al. [59] are described in Sections 2.2 and 2.3 respectively. The former model is used as the basis for further modeling efforts, analysis, and controls and the latter for simulations. Air injection in the context of the Moore–Greitzer model is then described in Section 2.4, where the mass, momentum, and cascade performance effects due to air injection are modeled.

2.1 Introduction

Models are essential for analysis and control synthesis. While accurate models for the rotating stall and surge in axial flow compressors do exist, they tend to be high dimensional (e.g. computational fluid dynamical models [11, 13, 14, 23], typically having greater than 10^4 states). For models of such size, numerical simulations can be performed only at high expense, and physical insights are often difficult to obtain. In light of this, the use of simplified, low order models for obtaining qualitative trends and insights is often accepted as a reasonable approach.

Low order modeling of rotating stall and surge has been an on–going research topic. Models for rotating stall and surge range from ones based on correlations to ones based on physics. Detailed accounts can be found in Greitzer [34, 35] and
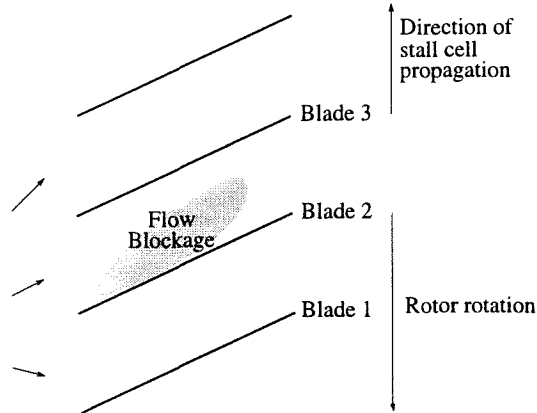
Figure 2.1 Emmons model of rotating stall.

Longley [55].

The use of empirical relations is a popular approach. Correlations of stall inception to parameters such as Reynolds number [50], tip clearance levels and aspect ratios [28, 62, 85, 86], a lumped parameter referred to as the diffusion factor (D-factor) [51, 52, 80], and a few others found in Horlock [42] have been reported.

The earliest physics–based linear model for rotating stall dates back to Emmons et al. [20] in 1955. Rotating stall is modeled as a flow separation phenomenon on the suction side of the blades governed by angle–of–attack. Figure 2.1 shows a picture of the idea. The rotor blades are approximated with flat plates in the picture. The annulus is "unwrapped" so rotation of the blades appears as vertical motion in the picture. With a reduction of the axial velocity, triggered by a static distortion for instance, the angle of attack on blade 2 is increased. Flow separation occurs on the suction side of blade 2 and a flow blockage is formed. The incoming flow is redirected by the flow blockage such that blade 1/3 has a lower/higher angle of attack, thus making blade 1/3 less/more likely to stall. The flow blockage then moves from blade 2 to 3, implying rotation when the annulus is "wrapped". This rotating blockage is sometimes referred to as a rotating stall cell. Readers should note that stall inception governed by other processes have been reported, such as one due to secondary flow near the tip region of the compressor by Goto [32]. Derivations similar to the one in Emmons et al. [20] can also be found in Dunham [18], Emmons
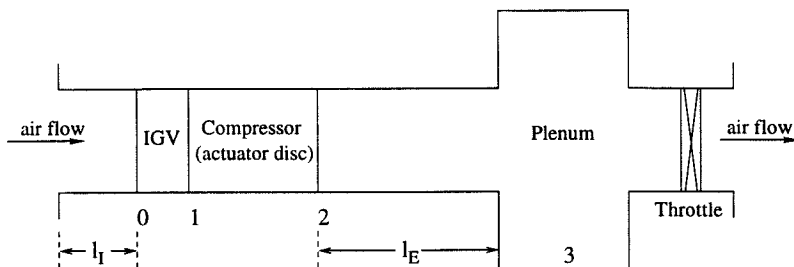
Figure 2.2 Simplified view of compression system in an aircraft engine.

et al. [19], Fabri [25, 26], and Nenni and Lugwig [67].

Aside from a linear approach, formulation of nonlinear models has also been reported in Adamczyk [1], Day et al. [16], Greitzer [33], Mongomery and Braun [63], Moore [64], Moore and Greitzer [37, 65], Orner [70], Pandolfi and Colasurdo [73], and Takata and Nagano [89]. In particular, one that receives perhaps the most attention in recent years is due to Moore and Greitzer [37, 65]. It is a phenomenological model, derived based on fluid mechanic principles applied on an approximation of a gas turbine engine, that exhibits the qualitative behavior of rotating stall and surge on axial flow compressors. A more detailed description of the Moore–Greitzer model and its high fidelity counterpart is given in Sections 2.2 and 2.3.

2.2 Basic Moore–Greitzer Model [37, 65]

In this section, a phenomenological model derived by Moore and Greitzer [37, 65] is reviewed. The model contains the essential physics of rotating stall and surge in axial flow compressors.

A simplified view of a compression system in an aircraft engine is shown in Figure 2.2. Assuming potential flow upstream of the inlet guide vanes (IGV) and applying Bernoulli's equation, the total–to–static pressure rise upstream of the compressor can be written as

$$\frac{p_1 - p_T}{\rho U^2} = -\frac{\phi^2}{2} - l_I \frac{d\Phi}{d\xi} - \frac{\partial \delta\phi}{\partial \xi},$$

where p_i denotes the static pressure at station i, p_T the total pressure at ambient condition, ρ the density of air, U the mean rotor speed, l_I the nondimensional length of inlet duct, $\Phi = C_x/U$ the nondimensional mean axial velocity where C_x is the mean axial velocity, $\delta\phi$ the nondimensional axial velocity perturbation, $\phi = \Phi + \delta\phi$ the nondimensional axial velocity, and $\xi = tU/R$ the nondimensional time where t is the time and R the mean rotor radius.

The compressor is modeled as a semi–actuator disc such that

$$\frac{p_2 - p_1}{\rho U^2} = F(\phi) - \lambda\frac{\partial\phi}{\partial\theta} - \mu\frac{\partial\phi}{\partial\xi},$$

where $F(\phi)$ denotes a nonlinear pressure rise map for the compressor as a function of the axial flow, λ the rotor inertia parameter, θ the circumferential angle, and μ the fluid inertia parameter.

Assuming that the pressure perturbation approximately satisfies Laplace's equation, the downstream dynamics evaluate to

$$\frac{p_3 - p_2}{\rho U^2} = -l_E\frac{d\Phi}{d\xi} - (m-1)\frac{\partial\delta\phi}{\partial\xi},$$

where l_E denotes the nondimensional length of exit duct and m the throttle exit parameter. By defining $\Psi = (p_3 - p_T)/(\rho U^2)$ and summing the upstream, compressor, and downstream dynamics, the following PDE is obtained.

$$\Psi = \Psi_c(\Phi + \delta\phi) - l_c\frac{d\Phi}{d\xi} - \lambda\frac{\partial\delta\phi}{\partial\theta} - \mu\frac{\partial\delta\phi}{\partial\xi} - m\frac{\partial\delta\phi}{\partial\xi}, \qquad (2.1)$$

where $\Psi_c(\phi) = F(\phi) + \phi^2/2$ denotes the compressor characteristic, and $l_c = l_E + l_I + \mu$ the effective length of the setup.

Equation (2.1) can be projected onto basis functions to produce ODEs. Choosing $\delta\phi = A_1(\xi)\sin(\theta - r(\xi))$ and computing the annulus–average, sine, and cosine moments of equation (2.1) gives rise to a set of equations describing **the time evolution**

of Φ, $J = A_1^2$, and r. These equations are given by the following.

$$\frac{d\Phi}{d\xi} = \frac{1}{l_c}(\Psi_c(\Phi) - \Psi + \frac{J}{4}\frac{\partial^2\Psi_c(\Phi)}{\partial\Phi^2}),$$
$$\frac{dJ}{d\xi} = \frac{2}{m+\mu}J(\frac{\partial\Psi_c(\Phi)}{\partial\Phi} + \frac{J}{8}\frac{\partial^3\Psi_c(\Phi)}{\partial\Phi^3}),$$

and $dr/d\xi = \lambda/(m+\mu)$. The equation for $dr/d\xi$ merely states that stall rotates at a constant speed.

The dynamics across the exit throttle can be modeled as a pressure drop across an orifice. Balancing the mass going into, leaving, and being stored in the plenum gives

$$l_c\frac{d\Psi}{d\xi} = \frac{1}{4B^2}(\Phi - \gamma\sqrt{\Psi}),$$

where $B = \dfrac{U}{2a_s}\sqrt{\dfrac{V_p}{A_cL_c}}$ denotes the Greitzer B parameter for surge with a_s as the speed of sound, V_p the volume of the plenum, A_c the compressor duct area, $L_c = l_cR$ the aerodynamic length of the system, and γ the throttle coefficient. For small and large values of B, the dominant instability of the system is rotating stall and surge respectively. Collecting the equations for Φ, Ψ, and J, the following 3–state system is used as a low order model for stall and surge:

$$\dot{\Phi} = \frac{1}{l_c}(\Psi_c(\Phi) - \Psi + \frac{J}{4}\frac{\partial^2\Psi_c(\Phi)}{\partial\Phi^2}),$$
$$\dot{\Psi} = \frac{1}{4l_cB^2}(\Phi - \gamma\sqrt{\Psi}),$$
$$\dot{J} = \frac{2}{m+\mu}J(\frac{\partial\Psi_c(\Phi)}{\partial\Phi} + \frac{J}{8}\frac{\partial^3\Psi_c(\Phi)}{\partial\Phi^3}). \qquad (2.2)$$

2.3 Collocated Model

While the simplicity of the 3–state Moore–Greitzer model in equation (2.2) is appealing, quantitatively reliable simulations cannot be obtained unless higher stall harmonics and other realistic effects are incorporated into the model.

By expressing the higher harmonics in terms of the local flow using discrete

Fourier transform, a high fidelity, collocated model proposed by Mansoux et al. [59] is used as the basis of the simulation tool. The model proposed by Mansoux et al. takes the form

$$
\begin{aligned}
\dot{\phi} &= -\tilde{E}^{-1} \cdot \tilde{A} \cdot \phi + \Psi_c(\phi) - T \cdot \Psi, \\
\dot{\Psi} &= \frac{1}{4B^2 l_c}(S \cdot \phi - \Phi_T(\Psi)),
\end{aligned}
\tag{2.3}
$$

where

$$
\tilde{E} = G^{-1} \cdot D_E \cdot G, \quad \tilde{A} = G^{-1} \cdot D_A \cdot G,
$$

$$
D_E = \begin{bmatrix}
l_c & 0 & 0 & 0 & \ldots & 0 \\
0 & (\frac{m}{1}+\mu) & 0 & 0 & \ldots & 0 \\
0 & 0 & (\frac{m}{1}+\mu) & 0 & \ldots & 0 \\
& & & \vdots & & \\
0 & 0 & 0 & \ldots & (\frac{m}{N}+\mu) & 0 \\
0 & 0 & 0 & \ldots & 0 & (\frac{m}{N}+\mu)
\end{bmatrix},
$$

$$
D_A = \begin{bmatrix}
0 & 0 & 0 & 0 & \ldots & 0 \\
0 & 0 & \lambda & 0 & \ldots & 0 \\
0 & -\lambda & 0 & 0 & \ldots & 0 \\
& & & \vdots & & \\
0 & 0 & 0 & \ldots & 0 & N\lambda \\
0 & 0 & 0 & \ldots & -N\lambda & 0
\end{bmatrix},
$$

$$
G = \sqrt{\frac{2}{M}} \begin{bmatrix}
\frac{1}{\sqrt{2}} & \frac{1}{\sqrt{2}} & \cdots & \frac{1}{\sqrt{2}} \\
\cos(\theta_1) & \cos(\theta_2) & \ldots & \cos(\theta_M) \\
\sin(\theta_1) & \sin(\theta_2) & \ldots & \sin(\theta_M) \\
\cos(2\theta_1) & \cos(2\theta_2) & \ldots & \cos(\theta_M) \\
\sin(2\theta_1) & \sin(2\theta_2) & \ldots & \sin(2\theta_M) \\
\vdots & \vdots & \vdots & \vdots \\
\cos(2\theta_1) & \cos(2\theta_2) & \ldots & \cos(\theta_M) \\
\sin(N\theta_1) & \sin(N\theta_2) & \ldots & \sin(N\theta_M)
\end{bmatrix},
$$

$$\theta_n \;=\; \frac{2\pi n}{M}, \quad S = \begin{bmatrix} \frac{1}{M} & \frac{1}{M} & \cdots & \frac{1}{M} \end{bmatrix}, \quad T = \begin{bmatrix} 1 & 1 & \cdots & 1 \end{bmatrix}^{\mathrm{T}},$$

and $M = 2N + 1$, where N is the number of Fourier modes. This formulation of the Moore–Greitzer model is suitable for control analysis and design, and allows accounting of higher modes.

Some realistic considerations can be included. One example of such effects is unsteady loss dynamics which is a model for the transient pressure losses across the rotor and the stator [39]. The unsteady loss dynamics have the following form:

$$
\begin{aligned}
\Psi_c = \Psi_c^{\mathrm{qs}} &= \Psi_c^{\mathrm{isen}} - L_r - L_s, \\
\dot{L}_r &= \frac{1}{\tau_r}(L_r^{\mathrm{ss}} - L_r), \\
L_r^{\mathrm{ss}} &= \tilde{R}(\Psi_c^{\mathrm{isen}} - \Psi_c^{\mathrm{qs}}), \\
\dot{L}_s &= \frac{1}{\tau_s}(L_s^{\mathrm{ss}} - L_s), \\
L_s^{\mathrm{ss}} &= (1 - \tilde{R})(\Psi_c^{\mathrm{isen}} - \Psi_c^{\mathrm{qs}}),
\end{aligned}
$$

where $\Psi_c^{\mathrm{qs}} = \Psi_c$ is the quasi–static compressor characteristic, Ψ_c^{isen} the isentropic compressor characteristic, L_r the losses associated with the rotor, L_s the losses associated with the stator, $\tilde{R}$ the reaction ratio, and τ_r and τ_s the nondimensional unsteady rotor and stator loss dynamics time constants respectively. The superscripts "ss" stands for steady–state and "qs" quasi–steady. Roughly speaking, the pressure response, resulting from a change in the axial flow condition for instance, takes time to propagate from the leading edge of the blade to the trailing edge. In the model proposed by Haynes et al. this response is modeled as a first order linear system.

Another example is the dynamics of an actuator such as magnitude, bandwidth, and rate limitations. Additional modeling efforts with respect to air injection and inlet disturbances can be incorporated into the collocated model also.
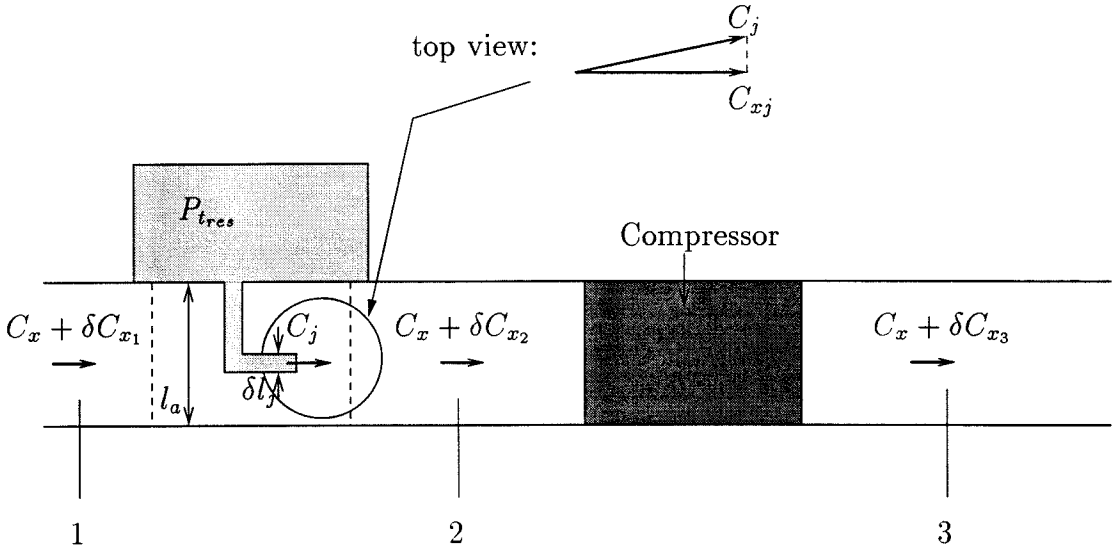
Figure 2.3 Mass and momentum addition by air injection.

2.4 Effects of Air Injection in Axial Flow Compressors

In this section, a model for accounting the effects of air injection on axial flow compressors in the context of the Moore–Greitzer model [37, 65] (equation (2.1)) is proposed. The approach takes into account the mass and momentum effects due to air injection, and also the change of cascade performance via an account of the changes in the incidence angle and losses.

2.4.1 Mass and Momentum Effects

The basic idea of modeling the mass and momentum addition by air injection has been given in Hendricks and Gysling [40] and Behnken [4]. The relevant picture is displayed in Figure 2.3. Similar to equation (2.1), the total–to–static pressure rise between stations 2 and 3 can be written as

$$\frac{p_3 - p_{t_2}}{\rho U^2} = \hat{\Psi}_c(\phi_2, \Phi_j) - \lambda \frac{\partial \phi_2}{\partial \theta} - \mu \frac{\partial \phi_2}{\partial \xi}, \qquad (2.4)$$

where p_{t_i} denotes the total pressure at station i and ϕ_i the nondimensional axial velocity at station i.

A word of clarification is in order. The addition of air injection can be thought of as changing the incidence angle of the air on the leading edge of the compressor blades and the corresponding losses associated with the region. As a result, the compressor characteristic is *not* the nominal open–loop compressor characteristic but a shifted one $\hat{\Psi}_c(\phi_2, \Phi_j)$. The amount and direction of the injected air thus needs to be taken into account in order to determine the shifted characteristic. This procedure is described in the next subsection.

With the assumption that the contribution of the injected air appears mainly in the perturbation, the macroscopic mass balance across stations 1 and 2 can be written as

$$\rho l_a (C_x + \delta C_{x_1}) + \rho \delta l_j C_j = \rho l_a (C_x + \delta C_{x_2}),$$

where δC_{x_i} denotes the axial velocity perturbation at station i, δl_j the distance of opening of the injector in the plane normal to the axial direction, C_j the injected velocity, and l_a the radial distance of annulus. Nondimensionalizing in the standard way results in the following.

$$\delta \phi_2 = \delta \phi_1 + \frac{\delta l_j}{l_a} \Phi_j, \qquad (2.5)$$

where $\Phi_j = C_j/U$ denotes nondimensional injected velocity and $\delta \phi_i = \delta C_{x_i}/U$ the nondimensional flow perturbation at station i.

The macroscopic axial momentum balance across stations 1 and 2 gives

$$l_a(P + \delta p_1) + \rho l_a (C_x + \delta C_{x_1})^2 + \rho \delta l_j C_{x_j}^2 = l_a(P + \delta p_2) + \rho l_a (C_x + \delta C_{x_2})^2,$$

where P denotes the static pressure, δp_i the static pressure perturbation at station i, and C_{x_j} the magnitude of axial component of injected velocity. This relation simplifies and nondimensionalizes to

$$\frac{\delta p_1}{\rho U^2} + 2\Phi \delta \phi_1 + \delta \phi_1{}^2 + \frac{\delta l_j}{l_a} \Phi_{xj}^2 = \frac{\delta p_2}{\rho U^2} + 2\Phi \delta \phi_2 + \delta \phi_2{}^2,$$

where $\Phi_{x_j} = C_{x_j}/U$ denotes the nondimensional injected velocity in the axial direction. For station i, the relation between total and static pressure perturbations can be written as

$$\frac{\delta p_{t_i}}{\rho U^2} = \frac{\delta p_i}{\rho U^2} + \Phi \delta \phi_i + \frac{1}{2}\delta \phi_i^2,$$

where δp_{t_i} denotes the total pressure perturbation. This relation can be substituted into the momentum balance to give

$$\frac{\delta p_{t_2} - \delta p_{t_1}}{\rho U^2} = \frac{\delta l_j}{l_a}(\Phi_{x_j}^2 - (\Phi + \delta \phi_1)\Phi_j) - \frac{1}{2}\left(\frac{\delta l_j}{l_a}\Phi_j\right)^2. \tag{2.6}$$

Together with equation (2.4), the total-to-static pressure between stations 1 and 3 can then be expressed as

$$\frac{p_3 - p_{t_1}}{\rho U^2} = \hat{\Psi}_c(\phi_2, \Phi_j) - \lambda\frac{\partial \phi_2}{\partial \theta} - \mu\frac{\partial \phi_2}{\partial \xi} + \frac{\delta l_j}{l_a}(\Phi_{x_j}^2 - (\Phi + \delta \phi_1)\Phi_j) - \frac{1}{2}\left(\frac{\delta l_j}{l_a}\Phi_j\right)^2. \tag{2.7}$$

The terms $\frac{\delta l_j}{l_a}(\Phi_{x_j}^2 - (\Phi + \delta \phi_1)\Phi_j) - \frac{1}{2}\left(\frac{\delta l_j}{l_a}\Phi_j\right)^2$ represent the momentum addition by the air injection. Using equation (2.7) in place of its analog in the Moore–Greitzer model [37, 65], the following PDE is obtained:

$$\begin{aligned}
\Psi = \ &\hat{\Psi}_c(\phi_2, \Phi_j) - l_c\frac{d\Phi}{d\xi} - \lambda\frac{\partial \delta \phi_2}{\partial \theta} - \mu\frac{\partial \delta \phi_2}{\partial \xi} - m\frac{\partial \delta \phi_2}{\partial \xi} + \frac{\delta l_j}{l_a}(\Phi_{x_j}^2 - (\Phi + \delta \phi_1)\Phi_j) \\
&-\frac{1}{2}\left(\frac{\delta l_j}{l_a}\Phi_j\right)^2.
\end{aligned} \tag{2.8}$$

A few remarks are in order. Firstly, the lags associated with the various terms need to be distinguished. For instance, if unsteady loss dynamics is to be included for purposes such as simulations (e.g. in [4]) or modal stability consideration, caution must be taken to ensure that the momentum terms are considered separately and *not* lagged by the unsteady loss dynamics time constant but by one associated with momentum transport lag for the actuation[1]. Secondly, for non–axisymmetric control

---

[1]A good example is when the injectors are positioned at the inlet versus the rotor face; the temporal and spatial distribution of the former is *significantly* different from that of the latter.

of stall, the local flow at the compressor inlet $\phi_2 = \Phi + \delta\phi_1 + \frac{\delta l_j}{l_a}\Phi_j$ contains the modal modification that is relevant for the implementation of interest.

Also, equation (2.8) is derived by considering air injection as an independent block from the compressor. For simplicity, one may wish to extend the semi–actuator disc approximation from only the compressor (i.e. station 2 to 3 in Figure 2.3) to the air injection with the compressor (i.e. station 1 to 3 in Figure 2.3). In other words, the mass and momentum effects can be lumped together with the cascade performance shifting effects and incorporated into the model as part of the "aggregate" compressor characteristic. While this approach is appealing from a complexity point of view, the various effects are not distinguished and hence the lags associated with the corresponding terms will not be taken into account properly.

2.4.2 Effects of Air Injection on Cascade Performance

Various approximations of the quasi–static pressure rise of a cascade of blades can be found in the literature. For instance, Horlock [41] derives the quasi–static pressure rise P_{qs} to depend on the inlet and outlet air flow angles on the blades. The expression is given by

$$\frac{P_{\mathrm{qs}}}{\frac{1}{2}\rho C_x^2} = \frac{P_{\mathrm{isen}} - \delta p_{\mathrm{loss}}}{\frac{1}{2}\rho C_x^2} = \left(1 - \frac{\cos^2\alpha}{\cos^2\alpha_o}\right) - \frac{\delta p_{\mathrm{loss}}}{\frac{1}{2}\rho C_x^2}, \qquad (2.9)$$

where P_{isen} denotes the isentropic pressure rise across the cascade, C_x the inlet air velocity, α the inlet air flow angle, α_o the outlet air flow angle, and δp_{loss} the pressure loss through the cascade. A similar approximation is found in Fréchette [29]. The common feature between the two approaches is an isentropic pressure rise P_{isen} and the losses δp_{loss}. Assuming that the change in α_o is small, the isentropic pressure rise P_{isen} is given by $P_{\mathrm{isen}}(C_x, \alpha)$. Given a quasi–static pressure rise $P_{\mathrm{qs}}(C_x, \alpha)$, the losses δp_{loss} can then be found as $\delta p_{\mathrm{loss}}(C_x, \alpha)$ (Figure 2.4).

Air injection can be modeled by velocity diagrams as shown in Figure 2.5. As the pictures show, air injection can alter the inlet flow angle α, the effective axial flow C_x, and the effective rotor angular velocity Ω. In the case of straight–on injection,
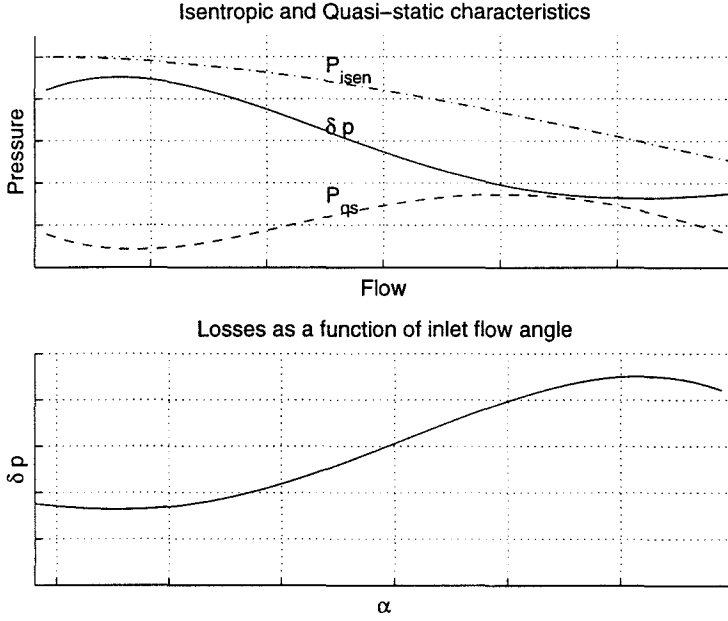
Figure 2.4 Sample characteristics and losses distribution.

the magnitude of the axial velocity is augmented to C_{x1}, and the inlet flow angle α is reduced to α_1. The new isentropic pressure rise is thus given by $P_{\text{isen}}(C_{x1}, \alpha_1)$, and the losses by $\delta p_{\text{loss}}(C_{x1}, \alpha_1)$, resulting in a new quasi–static pressure rise map $P_{\text{qs}}(C_{x1}, \alpha_1) = P_{\text{isen}}(C_{x1}, \alpha_1) - \delta p_{\text{loss}}(C_{x1}, \alpha_1)$. The argument can be applied to the angled injection cases analogously.

To accurately model the change in α due to straight–on or angled air injection, the evolution of an oblique jet in a free–stream as a function of the axial (x) and perpendicular (y) directions needs to be addressed. Figure 2.6 shows the setup pictorially, where U_0 and U_1 denote the initial velocity of the oblique jet and free stream velocity respectively, d the diameter of the circular jet, ζ the jet–axis, u the cross–sectional mean velocity of the jet along ζ–axis, u_x the mean axial velocity of jet, b the radius of deflected jet normal to ζ–axis, b_x the radius of the jet in the y–direction, and θ_0 and θ_1 the angle of the jet initially and at some downstream location respectively.

An account of a number of modeling approaches for oblique jets in a free stream and experimental results can be found in Rajaratnam [77]. The common feature
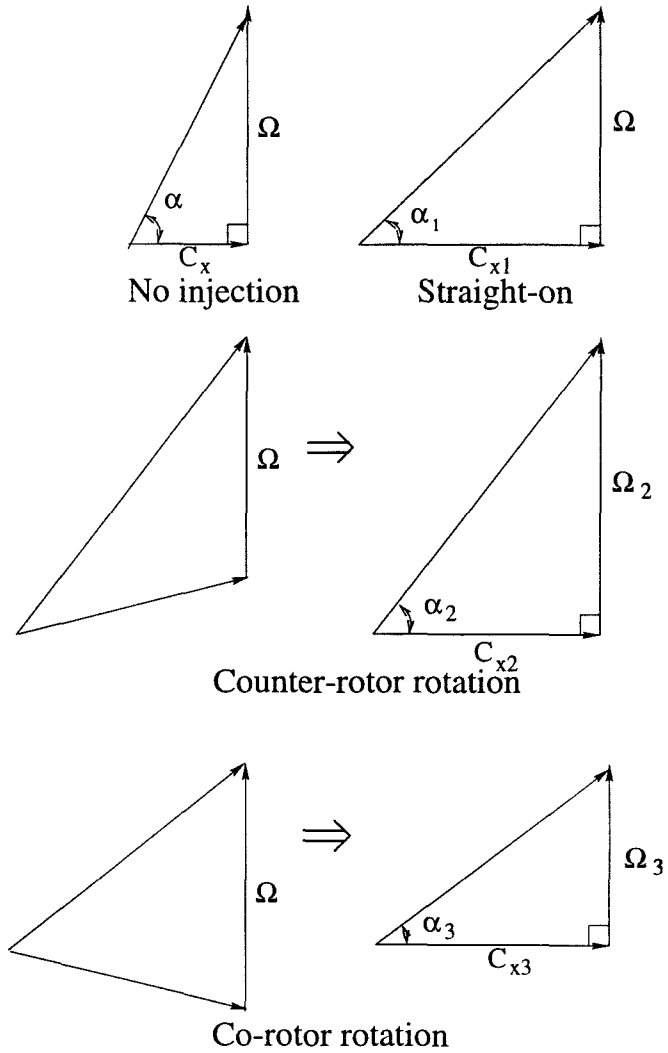
Figure 2.5 Velocity diagram representation of air injection.
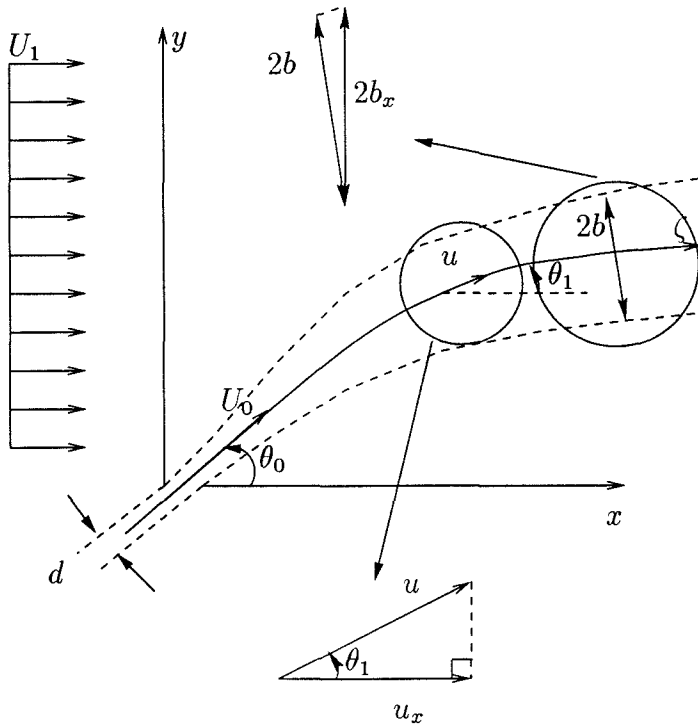
Figure 2.6 Pictorial representation of an oblique jet evolution in a free-stream.

among the approaches is to book–keep the mass and momentum effects during deflection of the jet flow. Examples of such models that take the effects of entrainment into account can be found in Platten and Keffer [74] and Hoult and Weil [43]. Consider the setup shown in Figure 2.6. In Platten and Keffer, the mass and momentum balances are written as

$$\frac{d}{d\zeta}(au) = \rho c v_e, \qquad \frac{d}{d\zeta}(au^2 \sin \theta_1) = 0,$$

$$\frac{d}{d\zeta}(au^2 \cos \theta_1) = c v_e U_1,$$

$$v_e = a_1(u - U_1 \cos \theta_1) + a_2 U_1(\cos \theta_1 - \cos \theta_0), \qquad (2.10)$$

where a, c, and u denote the cross–sectional area, circumference, and mean velocity of the jet normal to the ζ–axis, v_e the entrainment velocity, and a_i the entrainment coefficients for $i = 1, 2$. The first equation accounts for the mass as a result of entrainment. The second and third book–keep the momentum in the y– and x– direction respectively.

Equation (2.10) can be numerically integrated with the appropriate initial conditions to simulate oblique jet in a background flow. Platten and Keffer [74] fitted the entrainment coefficients a_i for $i = 1, 2$ to match experimental data obtained for various values of θ_0 and U_0/U_1. This particular approach does not take into account of the variation of a and c along the ζ–axis but assumes knowledge of them. There is also no account of entrainment in the y–direction.

A similar approach can be found in Hoult and Weil [43]. The mass and momentum balances are written as

$$\frac{d}{d\zeta}(b^2 u) = 2b\hat{v}_e,$$

$$b^2 u^2 \frac{d\theta_1}{d\zeta} = -U_1 \sin \theta_1 \frac{d}{d\zeta}(b^2 u),$$

$$\frac{d}{d\zeta}(b^2 u^2) = U_1 \cos \theta_1 \frac{d}{d\zeta}(b^2 u),$$

$$\hat{v}_e = a_1|u - U_1 \cos \theta_1| + a_3|U_1 \sin \theta_1|, \qquad (2.11)$$

where b is the radius of the deflected jet normal to the ζ–axis, $\hat{v}_e$ the entrainment velocity, and a_i entrainment coefficients for $i = 1, 3$.

Similar to Platten and Keffer [74], the entrainment coefficients are fitted to match the experiments in Hoult and Weil [43]. Although equation (2.11) tries to take the variation of the cross–sectional area and entrainment in the direction normal to the jet axis into account, no explanation was given for writing the second equation in the way shown in (2.11).

By combining the two approaches, the mass and momentum balances can be written as the following.

$$
\begin{aligned}
\frac{d}{d\zeta}(b^2 u) &= 2b\tilde{v}_e, \\
\frac{d}{d\zeta}(b^2 u^2 \sin \theta_1) &= 0, \\
\frac{d}{d\zeta}(b^2 u^2 \cos \theta_1) &= 2bU_1 \left(a_1(u - U_1 \cos \theta_1) + a_2 U_1(\cos \theta_1 - \cos \theta_0) \right), \\
\tilde{v}_e &= a_1(u - U_1 \cos \theta_1) + a_2 U_1(\cos \theta_1 - \cos \theta_0) + \\
&\quad a_3 U_1 \sin \theta_1,
\end{aligned}
\tag{2.12}
$$

where the explicit dependence of u, b, and θ_1 on ξ has been dropped for simplicity. The first equation accounts for the mass. The second and third equations account for the momentum in the y– and x–direction respectively. Assuming that a_i are given for $i = 1, 2, 3$, equation (2.12) can be numerically integrated to obtain the u, b, and θ_1 at any desired downstream location. The information can then be used to estimate the shifted compressor characteristic.

In practice, often only part of the compressor cascade is affected by air injection. In this case, a parallel compressor approach [45, 61] can be adopted to obtain the cascade performance. Denoting the fraction of cascade affected by air injection by ν, the nominal incidence angle and axial flow α and C_x respectively, and that with air injection $\hat{\alpha}$ and $\hat{C}_x$ respectively, the quasi–static pressure rise characteristic can

be expressed as

$$
\begin{aligned}
P_{\text{qs}}((1-\nu)C_x + \nu\hat{C}_x) &= (1-\nu)\left(P_{\text{isen}}(C_x, \alpha) - \delta p_{\text{loss}}(C_x, \alpha)\right) \\
&\quad + \nu\left(P_{\text{isen}}(\hat{C}_x, \hat{\alpha}) - \delta p_{\text{loss}}(\hat{C}_x, \hat{\alpha})\right).
\end{aligned}
$$

Validation of the proposed model is presented in Section 3.4.

Chapter 3

Experimental Apparatus and Characterization

In this chapter, the experimental facility at Caltech is described in Section 3.1. Data corresponding to stable, stalled, and surging operation is presented in Section 3.2. The results of the application of the identification algorithm using surge cycles proposed by Behnken [4], as well as those corresponding to the attempts of improvements, are presented in Section 3.3. The results of validating the air injection model are described in Section 3.4. The characterization of inlet disturbances on the Caltech facility presented in Section 3.5 ends the chapter.

3.1 Experimental Setup

The Caltech compressor rig is a single stage, low speed, axial flow compressor with sensing and actuation capabilities (Figure 3.1). Figure 3.2a shows a drawing of the rig and 3.2b a magnified view of the sensor and injection actuator ring.

The compressor is a low speed, single stage, axial compressor by Able Corporation, model 29680, with 14 blades, a tip radius of 8.5 cm, and a hub radius of 6 cm. The blade stagger angle varies from 30° at the tip to 51.6° at the hub, and the rotor to stator distance is approximately 12 cm (1.4 rotor radii). Experiments are run with a rotor frequency of 100 Hz, giving a tip Mach number of 0.17. In the configuration shown in Figure 3.2, rotating stall is observed to occur with a frequency of approximately 67 Hz. With a 1.81 m^3 plenum attached at the outlet (for compliance effects), surge occurs at approximately 1.8 Hz. Data taken for a
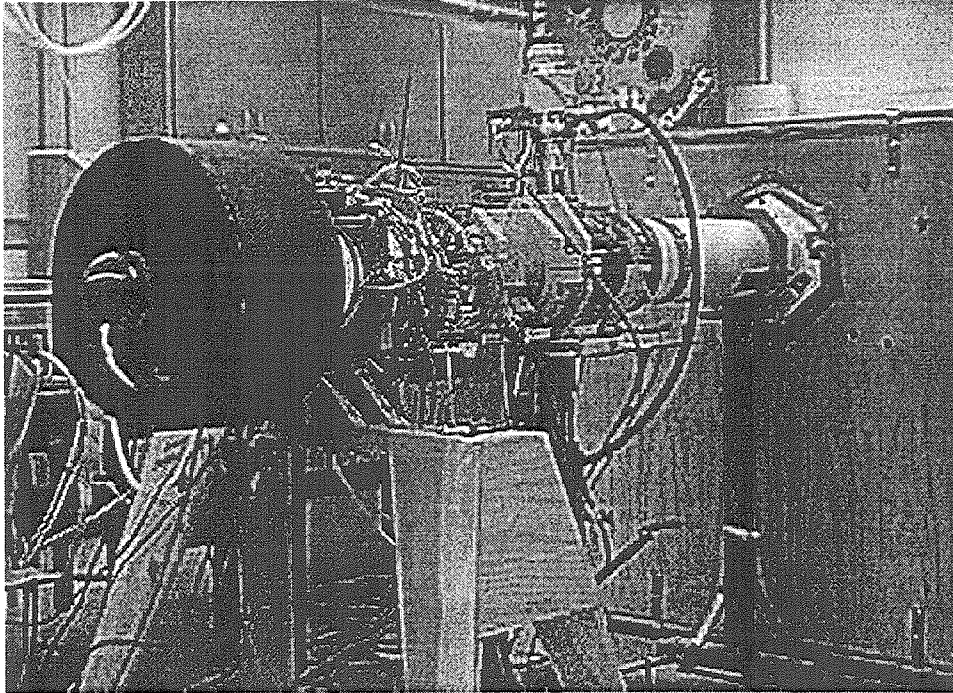
Figure 3.1 Picture of experimental apparatus.

stall transition event suggests that the stall cell grows from the noise level to its fully developed size in approximately 30 msec (3 rotor revolutions). At the stall inception point, the velocity of the flow through the compressor is approximately 16 m/sec.

Six static pressure transducers with 1000 Hz bandwidth are evenly distributed along the annulus of the compressor at approximately 5.7 cm (1.1 rotor radii) from the rotor face. By performing a discrete Fourier transform on the signals from the transducers, the amplitude and phase of the first and second Fourier modes of the pressure perturbation of a non–axisymmetric disturbance can be obtained. The difference between the pressure obtained from one static pressure transducer mounted at the piezostatic ring at the inlet and that from the piezostatic ring downstream near the outlet of the system is computed as the pressure rise across the compressor. For the velocity of the system, a hotwire anemometer is mounted approximately 13.4 cm (1.6 rotor radii) upstream of the rotor face. All of the sensor

Piezostatic Ring   Air injection +   High speed   Piezostatic Ring
                    Instrumentation   valve   Disturbance
Inlet   ring   valve
Nozzle   Throttle
           11.4 cm   Axial-   17.8 cm
                     flow fan

|← 28 cm →| |← 79 cm →|

(a)

sensor ring   rotor   stator

injector   pressure
           sensor

air
injector

6 cm

8.5 cm

pressure
sensor

4.7 cm   12 cm
    5.7 cm
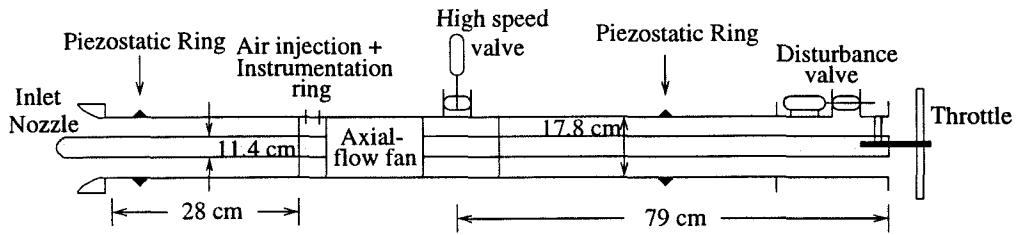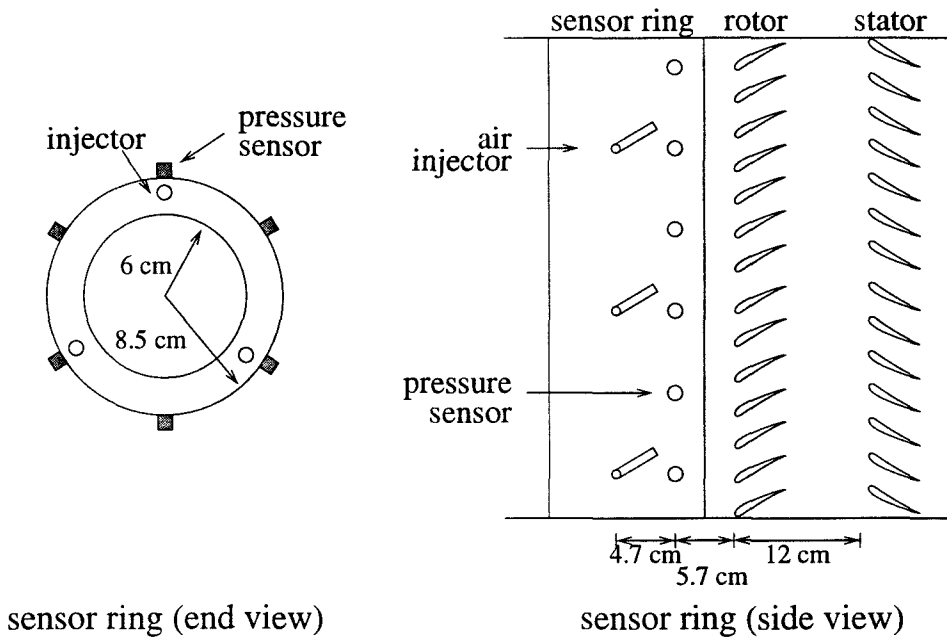
sensor ring (end view)   sensor ring (side view)

(b)

Figure 3.2 Experimental setup: (a). Experimental setup in stall configuration; (b). Sensor and injection actuator ring.

signals are filtered through a 4th order Bessel low pass filter with a cutoff frequency of 1000 Hz before the signal processing phase in the software.

A high speed and a low speed bleed valve are available on the Caltech rig. The high speed bleed valve, used primarily for stall control, has a magnitude saturation of 12% (corresponding to an area of 11.4 cm^2) of the flow at the stall inception point and is approximately 26 cm (3.1 rotor radii) downstream of the rotor. The low speed valve, used primarily for surge control and throttle disturbance generation, has a magnitude saturation of 30% of the flow of the system at the stall inception point and is estimated to have a small signal ($\pm 5°$ angle modulation) bandwidth of 50 Hz and a large signal ($\pm 90°$ angle modulation) bandwidth of 15 Hz. It is located approximately 75 cm downstream of the rotor.

The air injectors are on–off type injectors driven by solenoid valves. For applications on the Caltech compressor rig, the injectors are fed with a pressure source supplying air at a maximum pressure of 80 psig. The injectors are located at approximately 10.4 cm (1.2 rotor radii) upstream of the rotor. Due to significant losses across the solenoid valves and between the valves and the pressure source, the injector back pressure reading does not represent an accurate indication of the actual velocity of the injected air on the rotor face. Using a hotwire anemometer, the maximum velocity of the velocity profile produced by the injected air measured at a distance equivalent to the rotor–injector distance for 50 and 60 psig injector back pressure are measured to be approximately 30.2 and 33.8 m/sec respectively. At the stall inception point, each injector can add approximately 1.7% mass flux, 2.4% momentum flux, and 1.3% energy flux to the system when turned on continuously at 60 psig injector back pressure. The bandwidth associated with the injectors is approximately 200 Hz at 50% duty cycle. The angle of injection, injector back pressure, the axial location of the injectors, and the radial location of the injectors can all be varied.

All experiments are run in real time using the Sparrow real–time operating system [66] with a sampling frequency of 2000 Hz on a Pentium 100 MHz PC.
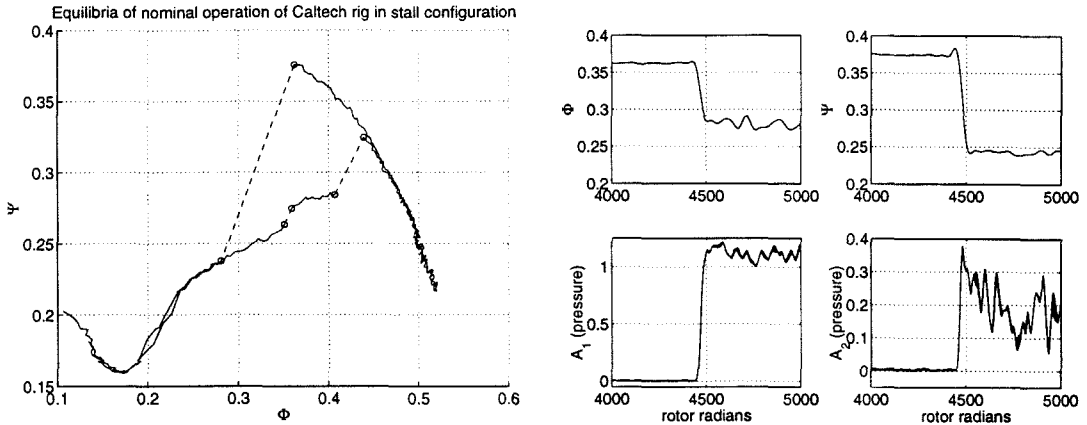
Figure 3.3 Equilibria for nominal operation and time traces during stall transition event on Caltech rig.

3.2 Nominal Operation

In this section, the behavior of the Caltech compressor facility in nominal operation is described.

3.2.1 Low B

With the plenum detached, the compliance in the system alone is not enough for the machine to exhibit surge. The Greitzer B parameter is in the range of 0.1–0.25, whereas a value of approximately 0.8 can be achieved with the plenum.

Without the plenum, only rotating stall is observed. Figure 3.3 shows equilibria of nominal operation in the flow–pressure plane, and time traces of pressure, flow, and first and second stall harmonics in a transition–to–stall event.

3.2.2 High B

With the plenum attached, the system exhibits a mixed stall–surge phenomenon experimentally. The Greitzer B parameter is approximately 0.8.

In this configuration, rotating stall and surge are both observed. Figure 3.4 shows time traces of pressure, flow, and first and second stall harmonics in a surge event. Readers should note that the system exhibits two different sets of surge
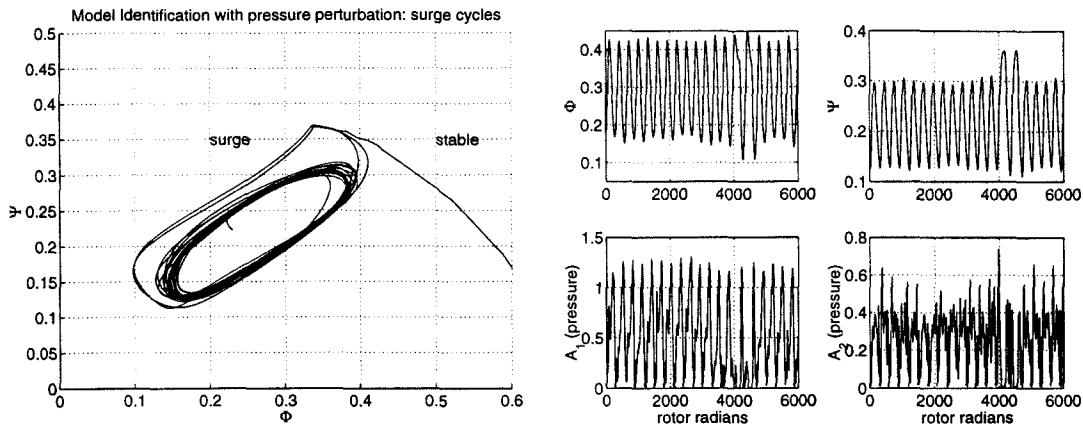
Figure 3.4 Time traces during surge event on Caltech rig.

cycles.

3.3 Identification using Surge Cycles

In this section, an identification algorithm proposed by Behnken [4] is presented and possible improvements discussed. The results of the original algorithm are presented first, followed by those obtained with the proposed improvements.

3.3.1 Original Algorithm [4]

Due to the unstable nature of the portion of the compressor characteristic to the left of its peak, achievable stall–free performance of a given compressor has always been uncertain. Identification of the compressor characteristic and the parameters in the Moore–Greitzer model has been an on–going research topic. The complexity of the identification process has evolved from an assumption based on experience, namely a simplified Moore–Greitzer type cubic [37, 65] of the form

$$\Psi_c(\Phi) = \Psi_{c_0} + H \left[1 + \frac{3}{2} \left(\frac{\Phi}{W} - 1 \right) - \frac{1}{2} \left(\frac{\Phi}{W} - 1 \right)^3 \right],$$

where Ψ_{c_0}, H, and W are fitting coefficients, to an iterative simulation–experiment matching procedure which results in piecewise continuous polynomials [59]. While

the iterative approach gives quantitatively reliable stall inception results when used in simulations, a systematic method that reduces the uncertainty and effort, and increases the accuracy and precision of the identified parameters is extremely desirable. One such identification algorithm via a linear least squares fit of a modified version of the Moore–Greitzer equations using surge cycle data is proposed by Behnken [4].

Using modal decomposition and Galerkin projection, the Moore–Greitzer PDE (equation (2.1)) can be projected onto the modes of interest. As an example, the one–mode Moore–Greitzer model (equation (2.2)) is repeated here in a slightly different form.

$$
\begin{aligned}
\dot{\Psi} &= \frac{1}{4l_c B^2}(\Phi - \gamma\sqrt{\Psi}), \\
\dot{\Phi} &= \frac{1}{l_c}(\Psi_c(\Phi) - \Psi + \frac{A_1^2}{4}\frac{\partial^2\Psi_c(\Phi)}{\partial\Phi^2}), \\
\dot{A}_1 &= \frac{1}{m+\mu}A_1(\frac{\partial\Psi_c(\Phi)}{\partial\Phi} + \frac{A_1^2}{8}\frac{\partial^3\Psi_c(\Phi)}{\partial\Phi^3}).
\end{aligned}
\tag{3.1}
$$

The basic surge model is equation (3.1) with A_1 set to 0. The expanded surge model takes into account the amplitude of the rotating stall in the surge cycle without considering the corresponding time rate of change. Furthermore, for applications on data associated with *pressure* perturbation, a Taylor expansion can be used to express the stall amplitudes associated with pressure perturbation to those with flow perturbation. For instance (from [4]), the first mode associated with pressure perturbation $\hat{A}_1$ is given by

$$
\hat{A}_1 = A_1\sqrt{\left[\Phi + \frac{1}{m+\mu}\left(\Psi_c'(\Phi) + \frac{A_1^2}{8}\Psi_c'''(\Phi)\right)\right]^2 + \dot{r}_1{}^2}.
$$

To pose the problem in a linear least squares form, consider a polynomial description of $\Psi_c(\Phi)$ given by $\Psi_c(\Phi) = \sum_{i=0}^{N} a_i\Phi^i$ where N is an integer. The functional dependence of $\dot{\Phi}$ on $\hat{A}_i$ is neglected and terms higher than 2nd order in $\hat{A}_i$ truncated. For consideration of the first and second modes only, the equations can be written
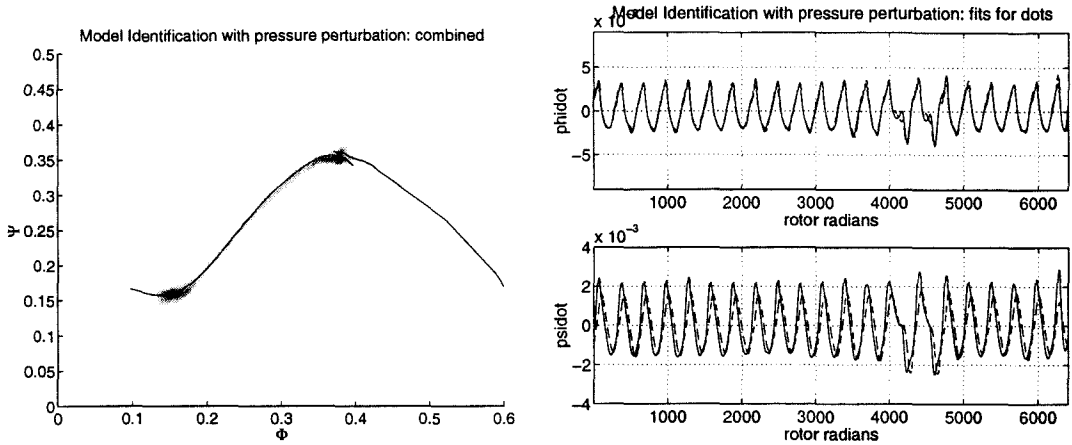
Figure 3.5 Identified compressor characteristic and estimated $\dot{\Phi}$ and $\dot{\Psi}$ using pressure perturbation; on the right plot, solid lines represent measured data and dashed estimated from fit.

as the following:

$$\dot{\Phi} = \sum_{i=0}^{N} \hat{a}_i \Phi^i + c_0 \Psi + d_1 \hat{A}_1 + d_2 \hat{A}_1 \Phi + d_3 \hat{A}_1{}^2 + d_4 \hat{A}_1 \hat{A}_2 + d_5 \hat{A}_2 + d_6 \hat{A}_2 \Phi + d_7 \hat{A}_2^2,$$

$$\dot{\Psi} = \frac{1}{4 l_c B^2} (\Phi - \gamma \sqrt{\Psi}), \tag{3.2}$$

where $\hat{a}_i = a_i / l_c$, $b_1 = 1/4 l_c B^2$, $b_2 = -\gamma/4 l_c B^2$, and $c_0 = -1/l_c$. The algorithm uses surge cycle data from experiment and searches for coefficients that give the best fit to the expanded surge equations. A successful identification of the compressor characteristic is classified as one that gives a close fit to the time rate of change of the flow and pressure signals, and has a tight bound on the range of possible characteristics as a result of the linear least squares fit.

To illustrate the method, surge cycle data is taken on the Caltech rig. Applying the algorithm on the data shown in Figure 3.4 with the model described in equation (3.2), the resulting identified compressor characteristic and the estimated $\dot{\Phi}$ and $\dot{\Psi}$ are shown in Figure 3.5. The solid lines in the right plots represent the actual $\dot{\Phi}$ and $\dot{\Psi}$ time traces while the dashed lines the fitted counterparts. The shaded region in the left plot is a band formed by computing the compressor characteristic from

the surge cycle data using the fitted values of the parameters. The tightness of this band and the close fit to the time traces indicate that the fit is good with respect to the underlying model.

3.3.2 Proposed Improvements

One of the main disadvantages of the method proposed by Behnken [4] is that the lack of flow perturbation prohibits an identification of the rest of the model, namely, the stall dynamics. This problem can be resolved by using the unsteady Bernoulli equation. Writing the flow perturbation $\delta\phi$ as a Fourier series, i.e.

$$\frac{\partial \delta\Theta}{\partial \eta} = \delta\phi = \sum_{n=1}^{\infty} e^{n\eta}(a_n \sin(n\theta + r_n) + b_n \cos(n\theta + r_n)),$$

where a_n and b_n are the amplitudes and r_n the rotation rate of the nth Fourier harmonic, and $\delta\Theta$ the disturbance velocity potential, which can then be written as the following:

$$\delta\Theta = \sum_{n=1}^{\infty} \frac{e^{n\eta}}{n}(a_n \sin(n\theta + r_n) + b_n \cos(n\theta + r_n)).$$

The relation between the pressure and flow perturbation is then expressed as the following:

$$\delta\psi = -\Phi\delta\phi - \frac{1}{2}\delta\phi^2 - \frac{\dot{\delta\phi}}{n},$$

where $\delta\psi$ is the pressure perturbation and $\delta\phi$ the flow perturbation. A local minimization scheme can then be used to compute the $\delta\phi$ that minimizes the error between the actual and computed $\delta\psi$. The stall modes associated with the flow perturbation, namely A_1 or J, can thus be found. The 3–state Moore–Greitzer model [37, 65] (equation (2.2)) can then be used to identify parameters beyond those contained in the expanded surge equations.

To identify the parameters associated with the stall dynamics, the stall modes associated with the flow perturbation is obtained through **the unsteady Bernoulli**

Measured vs. estimated pressure perturbation via relaxation algorithm
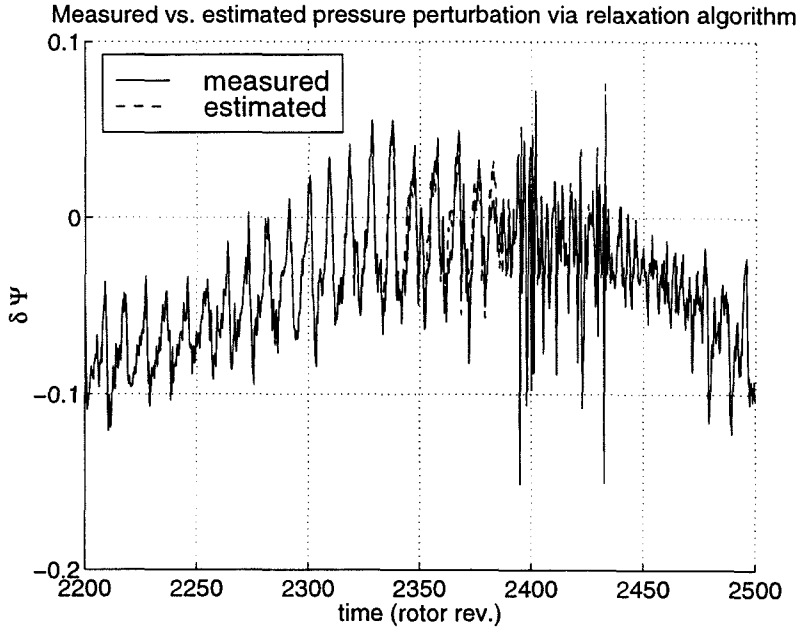
Figure 3.6 Computed vs. measured pressure perturbation; the solid line represents the measured $\delta\psi$ and the dashed the estimated.

equation which relates the pressure perturbation $\delta\Psi$ to the flow perturbation $\delta\phi$:

$$\delta\psi = -\Phi\delta\phi - \frac{1}{2}\delta\phi^2 - \frac{\dot{\delta\phi}}{n}.$$

A simple relaxation type algorithm is used to estimate $\delta\phi$ from each of the six $\delta\psi$ signals obtained from the static pressure transducers. In the fitting routine, the time derivative $\dot{\delta\phi}$ is approximated using a discretized version $\frac{\Delta\delta\phi}{\Delta t}$. For the Caltech rig, Figure 3.6 shows one of the six computed pressure perturbation from the flow perturbation versus the measured values, with the solid line representing the measured $\delta\psi$ and the dashed the estimated. It should be noted that the time derivative on the obtained $\delta\phi$ instead of the discretized approximation is used in computing the estimated $\delta\psi$. Figure 3.7 shows the estimated stall content associated with flow perturbation in the surge cycles shown in Figure 3.4.

With the estimated stall modes for the flow perturbation, identification of the model parameters in the original Moore–Greitzer 3–state model [37, 65] coordinates
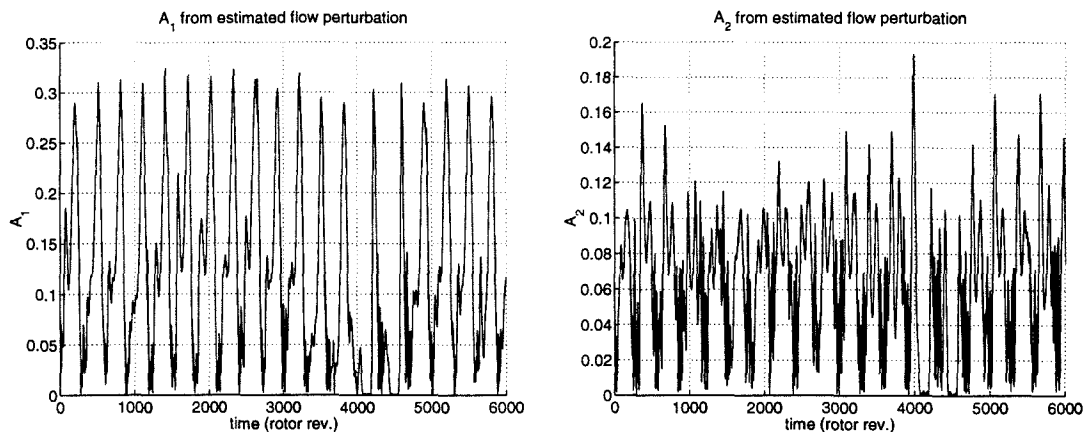
Figure 3.7 Estimated stall content associated with flow perturbation in surge cycle data.

can be achieved. Identification of the compressor characteristic using the $\dot{\Phi}$ and $\dot{\Psi}$ equations is first carried out to compare with that obtained from the identification algorithm using pressure perturbation. Theoretically speaking, inclusion of J_1 and J_2 should take into account (to some extent) the stall content in the surge cycles. In the case of using pressure perturbation, two pressure modes seems to be sufficient to give a reasonable compressor characteristic. In the flow perturbation case, however, that is not sufficient. Figure 3.8 shows the identified compressor characteristic for this case.

A comparison between Figure 3.5 and 3.8 seems to suggest that there are terms that contribute to the expansion but have not been taken into account. As a first cut, the effects of including J_1, J_2, A_1, A_2, $A_1\Phi$, $A_2\Phi$, and A_1A_2 are studied. The "closeness" of the result is characterized by the error between the estimated and measured values of $\dot{\Phi}$, $\dot{\Psi}$, and $\dot{J}$. We define the normalized time derivatives error to be

$$\text{err}_x = \frac{\sum_{i=1}^{N}(\dot{x}_{i,\text{measured}} - \dot{x}_{i,\text{measured}})^2}{\max(\dot{x}_{i,\text{measured}} - \dot{x}_{i,\text{measured}})^2},$$

where $x \in \{\Phi, \Psi, J\}$ and N is the number of data points. Figure 3.9 shows the normalized error in $\dot{\Phi}$, $\dot{\Psi}$, and $\dot{J}$ for combinations of J_1, J_2, A_1, A_2, $A_1\Phi$, $A_2\Phi$, and
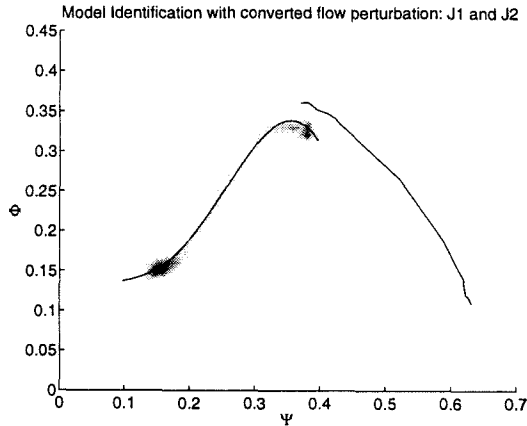
Figure 3.8 Identified compressor characteristic with inclusion of J_1 and J_2 as in Moore–Greitzer model.

$A_1 A_2$ according to Table 3.1.

With inclusion of all of the terms, the resulting identified compressor characteristic is slightly more reasonable (Figure 3.10).

The $\dot{J}$ equation can be used for the identification of the rotor inertia parameter μ. To do so, the compressor characteristic which minimizes the error between the estimated and measured $\dot{\Phi}$ and $\dot{\Psi}$ is first obtained. The coefficients are then substituted into the $\dot{J}$ equation to identify μ. A better scheme for this is to collect the elements in the $\dot{J}$ equation according to the compressor characteristic coefficients, and identify the composite coefficient for each of the groups of terms. For example, for a 6th order compressor characteristic with coefficients denoted by a_i, $i = 0, \cdots, 6$, there are six groups of terms associated with the coefficients $\{a_1, \cdots, a_6\}$ in the $\dot{J}$ equation. The composite terms are then given by $\frac{2a_i}{m+\mu}$, $i = 1, \cdots, 6$. Six estimates of μ can then be obtained and an average and the uncertainty can be computed. For the openloop Caltech rig, the value of μ is identified to be 4.8 ± 1.2. However, the fitted $\dot{J}$ is not close to the actual signal. Figure 3.11 shows the estimated $\dot{\Phi}$, $\dot{\Psi}$, and $\dot{J}$ (magnified) using the fitted flow perturbation.

A peak detection scheme is performed on the $\dot{J}$ signal in order to obtain a better fit and possibly a better estimate of μ. The resulting value of μ for the case with peak detection is 1.6 ± 0.7 and Figure 3.12 shows the fits for the time derivatives.

Terms included	Run number
J_1	1
J_2	2
A_1	3
A_2	4
$A_1\Phi$	5
$A_2\Phi$	6
$A_1 A_2$	7
J_1, J_2	8
A_1, A_2	9
$A_1\Phi, A_2\Phi$	10
J_1, J_2, A_1, A_2	11
$J_1, J_2, A_1\Phi, A_2\Phi$	12
$J_1, J_2, A_1 A_2$	13
$A_1, A_2, A_1 A_2$	14
$A_1\Phi, A_2\Phi, A_1 A_2$	15
$J_1, J_2, A_1, A_2, A_1\Phi, A_2\Phi$	16
$J_1, J_2, A_1, A_2, A_1\Phi, A_2\Phi \ A_1 A_2$	17

Table 3.1 Run number vs. terms included for study of effects of additional terms on identification.
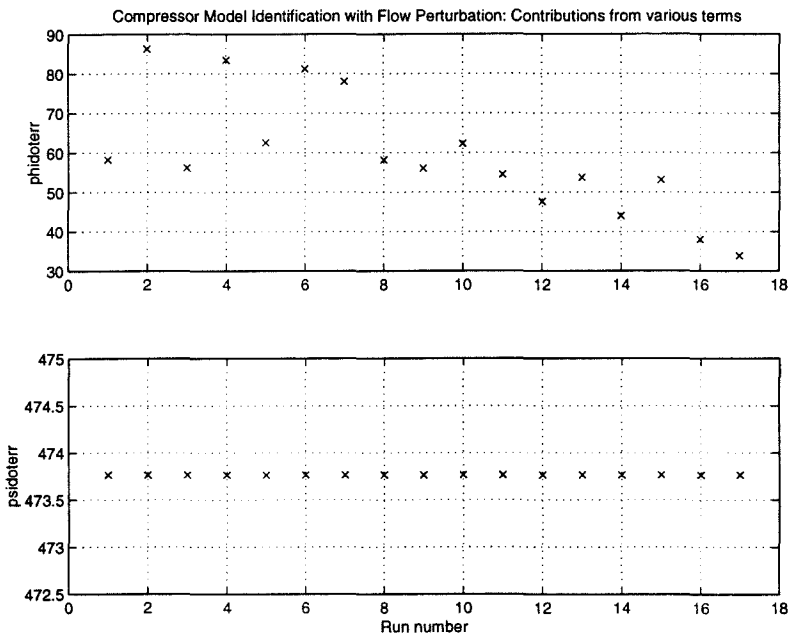
Figure 3.9 Effects of inclusion of various combinations of additional terms for identification.
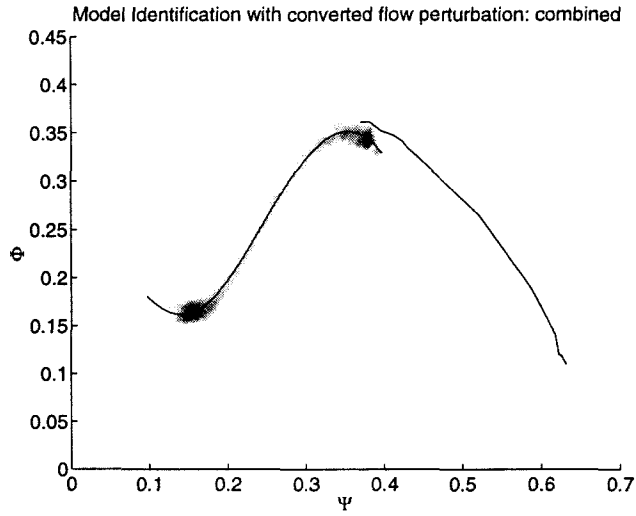
Figure 3.10 Identified compressor characteristic with inclusion of all A_1 and A_2 terms (Run 17).
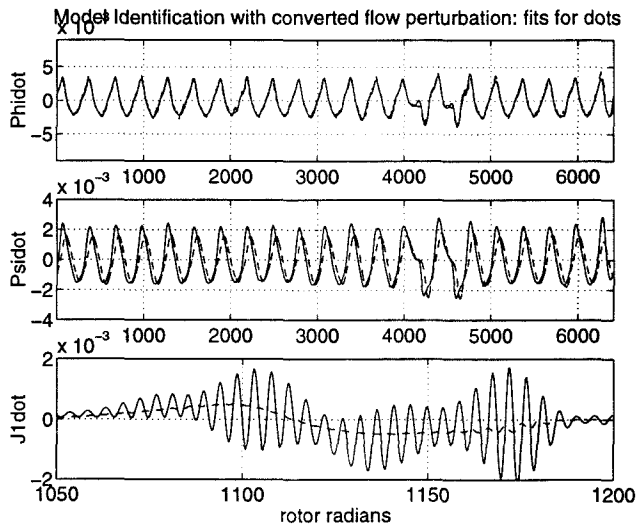
Figure 3.11 Estimated $\dot{\Phi}$ and $\dot{\Psi}$ using flow perturbation: filtered Φ, Ψ.
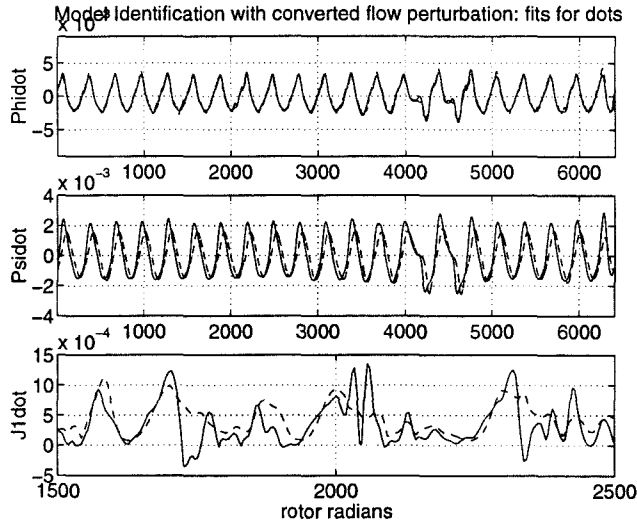
Figure 3.12 Estimated $\dot{\Phi}$ and $\dot{\Psi}$ using flow perturbation: peak detection for $\dot{J}$.

To verify the value of μ, a data set capturing transition to stall is taken. Using the relaxation scheme, the flow perturbation is estimated from the pressure perturbation, and the stall modes are computed. The high fidelity simulation (described in Section 2.3) with 34 states for the compressor block is used to simulate a transition to stall event. Using the compressor characteristic and the parameters given by the identification algorithm using the estimated flow perturbation, the resulting simulated stall transition event is compared to the experiment. Figure 3.13 shows the time evolution of the flow, pressure, and the first mode of stall obtained from simulation and experiment. As the figure shows, the identified parameters, including μ, give a close match between the simulation and the experiment.

Another possible use of the $\dot{J}$ equation is for the identification of the compressor characteristic. However, the validity of this approach must be investigated. To do so, the compressor characteristic is first identified through the surge equations. With an assumed value of μ (from previous paragraph), a new estimate of some of the compressor characteristic coefficients are obtained from fitting the $\dot{J}$ equation. The coefficients are combined with the 0th order coefficient from the compressor characteristic identified with the surge equations to form a new compressor characteristic
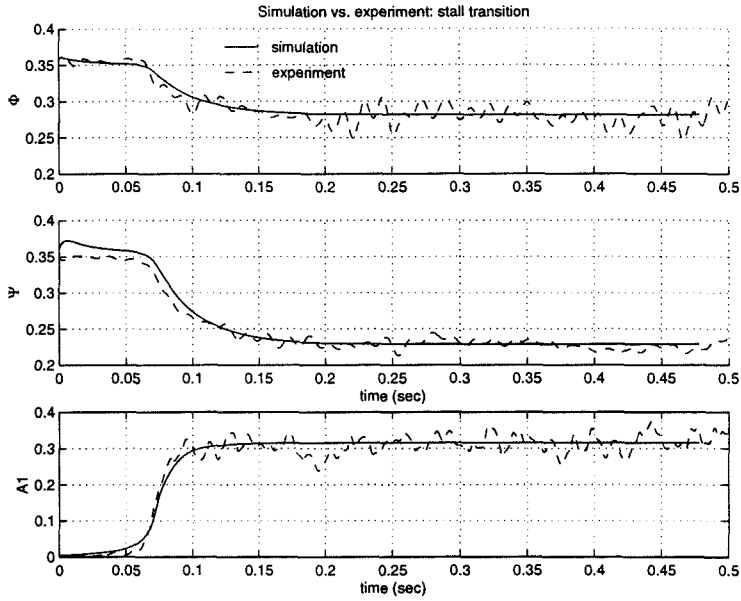
Figure 3.13 Simulated vs. experimental transition to stall event.

description. Results show that the compressor characteristic is not of an expected shape in both the cases with and without peak detection for $\dot{J}$ (Figure 3.14), implying that identification of the compressor characteristic using the $\dot{J}$ equation is not suitable.

Although there are many variations of the original identification algorithm using surge cycles, all of them offer only incremental improvements, if any, at the expense of a much larger computational burden. In particular, although the estimated flow perturbation can be used in the Moore–Greitzer 3–state model to identify parameters such as μ, the fact that the compressor characteristic cannot be reliably identified from the $\dot{J}$ equation is unsatisfying. One can obtain a value for μ easily from simple calculations using the information of the cascade, and improve them via iterative simulations.

3.4 Air Injection Model

To illustrate and verify the proposed method of modeling air injection in axial compressors, experiments are performed to evaluate the validity of the approach.
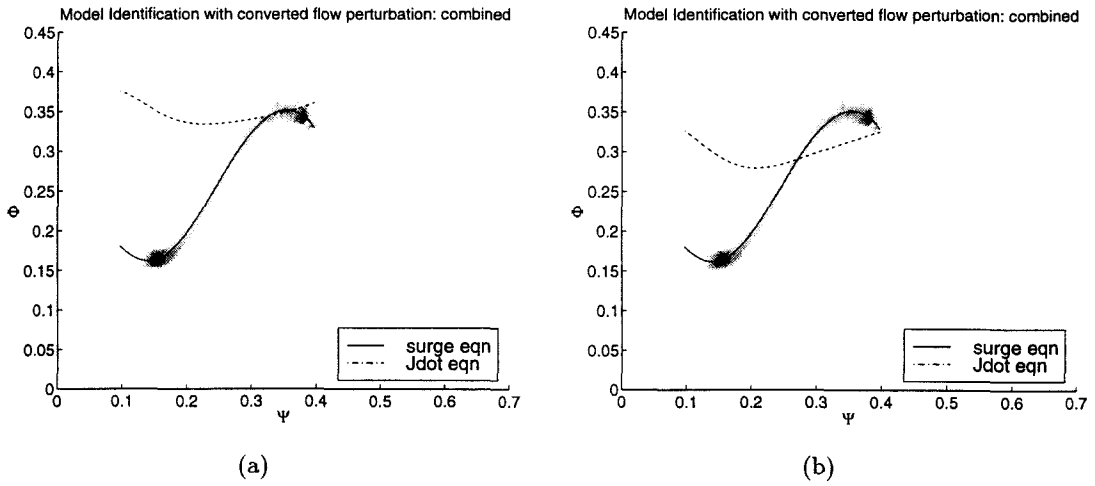
Figure 3.14 Comparison of compressor characteristics from surge equations and $\dot{J}$ equation: (a) with and (b) without $\dot{J}$ peak detection.

Air injection at 13 injector angles are chosen for this study. The use of the oblique jet equation (2.12) to estimate the velocity profile of and area of coverage by an air jet in a background flow is described first in Section 3.4.1. The information is then used as the input to obtain the shifted compressor characteristics for each injector angle, with the details described in Section 3.4.2. Stable sides and surge cycle data are obtained for each setting, from which the compressor characteristic for each of the 13 injector angles identified. The identified and predicted characteristics are then compared in Section 3.4.3.

3.4.1 Oblique Jets

Three air injectors are used to inject air continuously on the Caltech rig. Referring to Figure 2.6, each injector has a radius d of 0.3 cm and an initial centerline velocity U_0 of 87.9 m/sec. The velocity profile of the jet in the presence of a 16.7 m/sec background flow U_1 at an injector angle θ_0 from $-30°$ to $30°$ at $5°$ increments are measured at the rotor face. Figure 3.15 shows all of the velocity profiles as well as a sample at an injector angle of $-30°$.

The mass flux $\dot{m}$ over the mean flow of each profile is computed. The mean axial
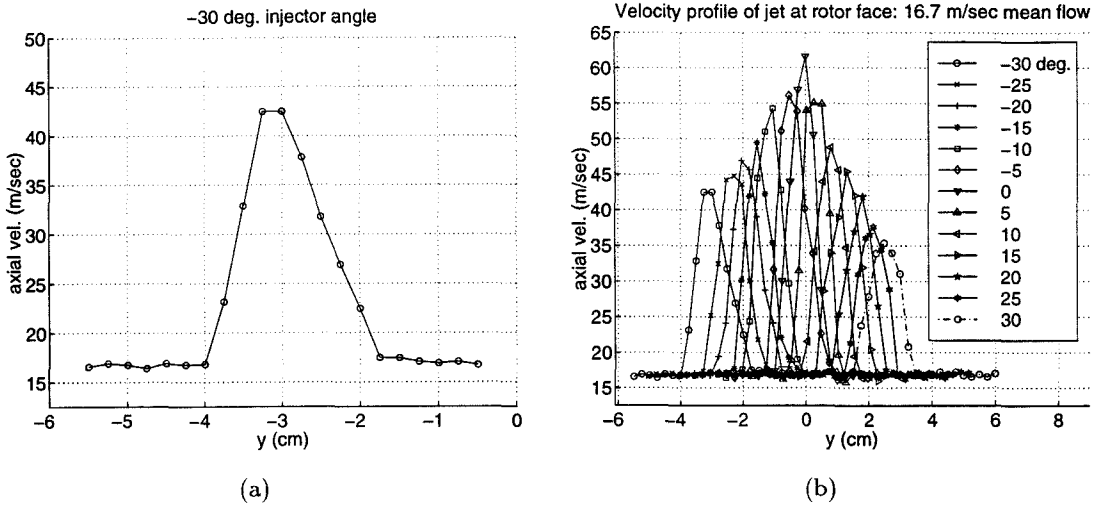
Figure 3.15 Velocity profile of injected air on rotor face in 16.7 m/sec background flow: (a) at $-30°$ and (b) from $-30°$ to $30°$ injector angle.

velocity u_x is chosen to be a fraction f of the maximum axial velocity, and the mean radius b_x can then be obtained as a function of f. From the values of u_x and b_x, the mass flux associated with the assumed mean quantities can be computed. By minimizing the squared difference between actual mass fluxes and those associated with the assumed mean quantities, a value of f is obtained for each injector angle tested. The resulting $(\dot{m}, b_x, u_x, \theta_1)$ in units of (kg/sec, cm, cm, m/sec, deg.) are displayed in Table 3.2.

The mean values of $(\dot{m}, b_x, u_x, \theta_1)$ are used to obtain values for entrainment coefficients a_i for $i = 1, 2, 3$ in equation (2.12), which is repeated here:

$$\frac{d}{d\zeta}(b^2 u) = 2b\tilde{v}_e,$$

$$\frac{d}{d\zeta}(b^2 u^2 \sin \theta_1) = 0,$$

$$\frac{d}{d\zeta}(b^2 u^2 \cos \theta_1) = 2bU_1 \left(a_1(u - U_1 \cos \theta_1) + a_2 U_1(\cos \theta_1 - \cos \theta_0)\right),$$

$$\tilde{v}_e = a_1(u - U_1 \cos \theta_1) + a_2 U_1(\cos \theta_1 - \cos \theta_0) +$$

$$a_3 U_1 \sin \theta_1.$$

θ_0	$\dot{m}$	b_x	u_x	θ_1
$-30°$	0.0033	0.53	31.4	-27.6
$-25°$	0.0032	0.52	30.9	-21.9
$-20°$	0.0034	0.54	30.5	-18.9
$-15°$	0.0037	0.59	28.2	-14.5
$-10°$	0.0038	0.56	31.5	-9.9
$-5°$	0.0039	0.53	37.0	-5.0
$0°$	0.0039	0.53	35.7	0.0
$5°$	0.0041	0.67	24.2	2.6
$10°$	0.0041	0.62	27.8	7.5
$15°$	0.0039	0.58	30.9	12.3
$20°$	0.0034	0.65	25.1	16.7
$25°$	0.0038	0.66	23.4	19.8
$30°$	0.0038	0.63	25.8	22.6

Table 3.2 Mean quantities of air jet at $-30°$ to $30°$ at $5°$ increments.

An exhaustive search is employed to choose the values of (a_1, a_2, a_3) that minimize the quantity

$$(1 - \dot{m}^{\text{est}}/\dot{m}^{\text{act}})^2 + (1 - b_x^{\text{est}}/b_x^{\text{act}})^2 + (1 - u_x^{\text{est}}/u_x^{\text{act}})^2$$

if $\theta_0 = 0°$, or the quantity

$$(1 - \dot{m}^{\text{est}}/\dot{m}^{\text{act}})^2 + (1 - b_x^{\text{est}}/b_x^{\text{act}})^2 + (1 - u_x^{\text{est}}/u_x^{\text{act}})^2 + (1 - \theta_1^{\text{est}}/\theta_1^{\text{act}})^2$$

otherwise, in which the superscript "act" denotes actual and "est" estimated. The distinction between the $0°$ and other cases is made since $\theta_1^{\text{act}} = 0$ for the $0°$ case. The resulting values of (a_1, a_2, a_3) are shown in Table 3.3.

For each mean flow Φ (or U_1 equivalently) at each injector angle, the values of (a_1, a_2, a_3) are substituted into equation (2.12), which is then numerically integrated until the injector–rotor distance is reached and the resulting values of (y, b_x, u_x, θ_1) obtained. The air jet is then assumed to cover an area of πb_x^2 cm^2 with a velocity of u_x m/sec.

θ_0	a_1	a_2	a_3
$-30°$	0.031	0.010	0.060
$-25°$	0.030	0	0.013
$-20°$	0.040	0.010	0.042
$-15°$	0.040	0.136	0
$-10°$	0.050	0.136	0.085
$-5°$	0.047	0.200	0.075
$0°$	0.046	0	0
$5°$	0.043	0.210	0.210
$10°$	0.046	0.125	0.045
$15°$	0.040	0.085	0.053
$20°$	0.030	0	0.044
$25°$	0.032	0.110	0
$30°$	0.010	0	0.092

Table 3.3 Values of (a_1, a_2, a_3) used in predicting compressor characteristics with steady air injection.

Radius (m)	β set	t/c	f/c
0.06	51.6°	0.11	0.094
0.065	45.6°	0.11	0.080
0.07	40.2°	0.11	0.071
0.075	36.1°	0.11	0.066
0.08	32.6°	0.11	0.062
0.085	30.0°	0.11	0.057

Table 3.4 Geometrical information of Caltech compressor rotor cascade.

3.4.2 Computing Shifted Compressor Characteristics

To estimate the actuated compressor characteristic for the Caltech compressor, the isentropic characteristic as well as a description of the pressure loss through the cascade must be obtained first. The Caltech compressor rotor cascade is divided into six sections from hub to tip and the geometrical information on the Caltech compressor rotor blade cascade can be found in Table 3.4, where β set is the angle between the chord and plane of the rotor disk, t/c the maximum thickness divided by the chord, and f/c the camber ratio which is the maximum camber height divided

by the chord. Assuming that $\delta p_{\text{loss}} = 0$ in

$$\frac{P_{\text{qs}}}{\frac{1}{2}\rho C_x^2} = \frac{P_{\text{isen}} - \delta p_{\text{loss}}}{\frac{1}{2}\rho C_x^2} = \left(1 - \frac{\cos^2\alpha}{\cos^2\alpha_o}\right) - \frac{\delta p_{\text{loss}}}{\frac{1}{2}\rho C_x^2},$$

(i.e. equation (2.9)), an estimate to the isentropic compressor performance can be obtained. An application of equation (2.9) to the Caltech compressor rig requires the knowledge of the inlet air flow angle α and outlet air flow angle α_o. For a range of flow coefficient $\Phi = C_x/U$ where U is the rotor velocity at mid–span (0.0725 m), the fluid velocity C_x can be obtained. For each section, the rotor velocity is computed and fluid inlet angle is calculated via a velocity triangle construction. The air outlet angle is the blade outlet angle plus the flow turning angle and deviation. Due to the lack of available data on the amount of flow turning and deviation on the Caltech compressor cascade, the outlet air flow angle is assumed to be equal to the blade outlet angle. The isentropic compressor characteristic Ψ_c^{isen} is approximated as

$$\Psi_c^{\text{isen}} = 1 - \frac{\cos^2\alpha}{\cos^2\alpha_o}.$$

Readers should note that more accurate methods such as one described in Haynes et al. [39] can also be used to compute Ψ_c^{isen}. The unactuated compressor characteristic obtained from the systematic identification using surge cycle data [4] is used as the quasi–static characteristic in the loss computation. The identified compressor characteristic is first dimensionalized by the appropriate functions of U. The pressure loss through the Caltech compressor cascade is then found by subtracting the identified compressor characteristic from the ideal one and nondimensionalized by ρU^2. The pressure loss is then fitted to the inlet flow angle. This fit is used as the description of the pressure loss.

A parallel compressor model consisting of 6x14=84 compressor elements is used to assess the effects of injection at three spots. Using the mean radius b_x, angle θ_1, and velocity u_x obtained via the oblique jet equation (2.12), the amount and magnitude of coverage by each injector at each mean flow is computed. The local

ideal compressor characteristics and losses for the regions where air injection is present are then calculated. The resulting net pressure gain/loss and the momentum addition as described in equation (2.6):

$$\frac{\delta p_{t_2} - \delta p_{t_1}}{\rho U^2} = \frac{\delta l_j}{l_a}(\Phi_{xj}^2 - (\Phi + \delta \phi_1)\Phi_j) - \frac{1}{2}\left(\frac{\delta l_j}{l_a}\Phi_j\right)^2,$$

are added to the unactuated characteristic for the parts of the compressor without air injection. The result is then averaged over the 84 compressors to give an estimate to the actuated quasi–static characteristic. All computations involving coverage of the oblique jet are rounded off to the nearest parallel compressor.

3.4.3   Comparison to Identified Characteristics

The injector angle is set at values from $-30°$ to $30°$ inclusively at $5°$ increment, producing 13 sets of data, with a negative value for the injector angle denoting that the injectors are positioned in the direction opposite to that of the compressor rotor rotation. The stable side as well as surge cycle data are obtained for each case, and the surge cycles identification algorithm is applied to obtain a compressor characteristic. Figure 3.16 shows the resulting 13 characteristics.

These characteristics are used to validate the proposed modeling method. Figure 3.17 shows that results of the estimated characteristic using the mean values of (a_1, a_2, a_3). The upper–left plot displays a typical comparison between the identified characteristic to the estimated one, along with the underlying nominal characteristic, at an injector angle of $-30°$ in this particular case. The upper–right and lower–left plots show a comparison of the flow Φ^* and pressure Ψ^* respectively, where the asterisk represents the underlying quantity at the peak, of the identified and predicted characteristics at each injector angle. The lower–right plot shows the 2–norm square of the error between the identified and predicted characteristics over a range of mean flow coefficient values between 0.2 and 0.5.

As the plots show, there is some discrepancy between the predicted and the measured characteristics in all of the cases. The error of the predicted to the measured
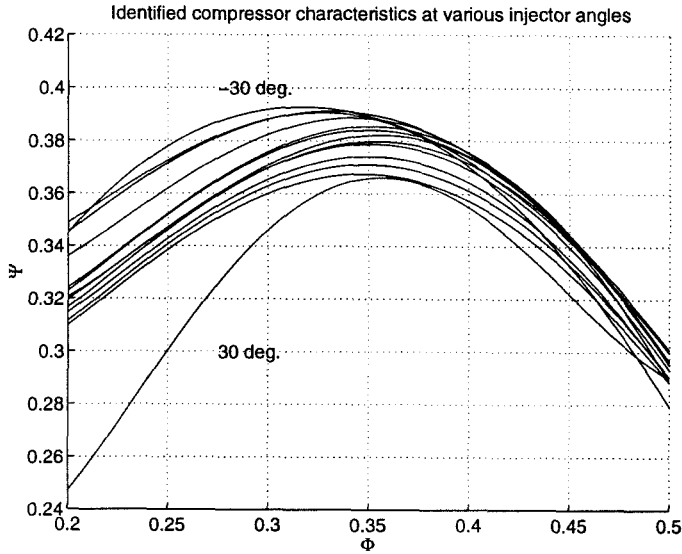
Figure 3.16 Identified compressor characteristics at various injector angles.

peak pressure rise Ψ^* ranges from 0.2% to 13% with an average of 7.1%, that for Φ^* from 0.3% to 22% with an average of 5.2%, and that for the 2–norm square between the predicted and measured characteristics from 0.04 to 0.81 with an average of 0.26. For the case of $-30°$ shown in Figure 3.17, the error for Ψ^* is 3.9%, that for Φ^* 3.4%, and that for the 2–norm square 0.05.

Although the technique shows good qualitative and reasonable quantitative agreement with the identified characteristics, the estimations seem to start failing in matching quantitatively as the air injection angle deviates from $0°$. A few of the factors affecting the accuracy of the estimation in general are:

- lack of the outlet air flow angle information,

- assumption of irrotational flow upstream of the rotor,

- simplified geometry of the injected velocity profile,

- uncertainty associated with the identification results, and

- assumption that unsteady loss dynamics is not changed by air injection.
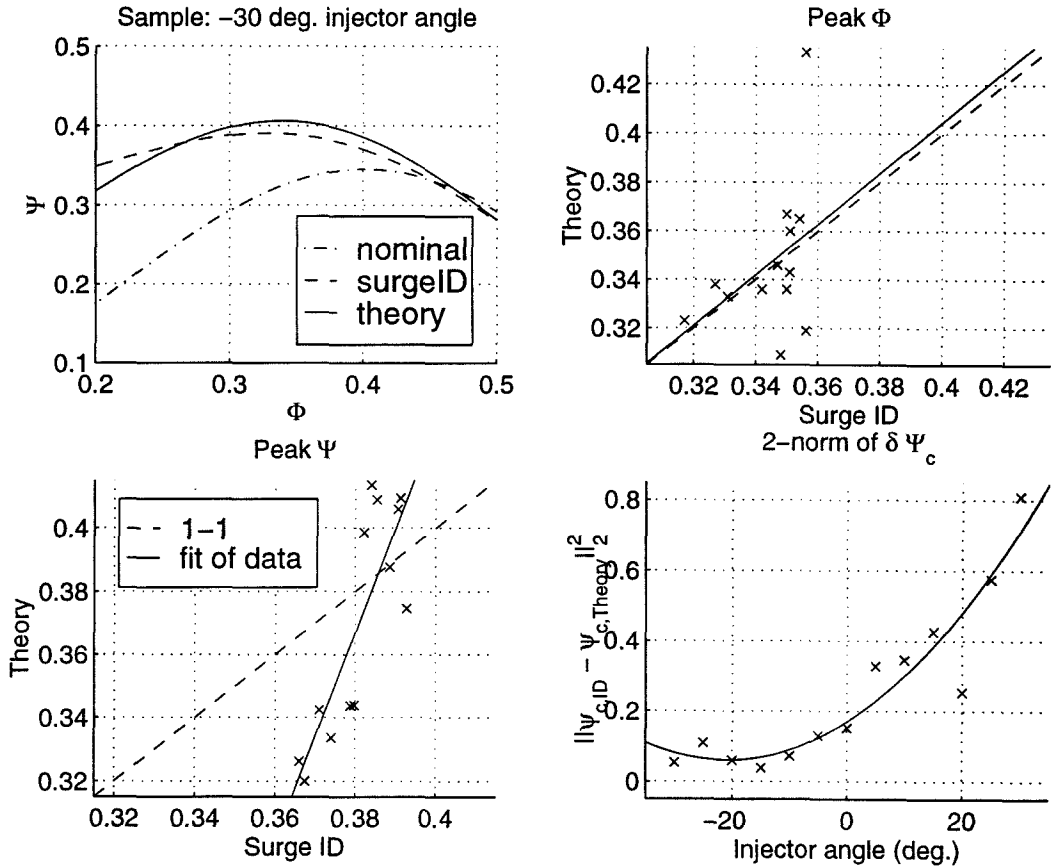
Figure 3.17 Validation of theory against identified compressor characteristics using surge cycles.

For applications on high speed/transonic machines in actual gas turbines, factors such as compressibility, inter-blade shock waves, changing geometry and flow paths are of concern. In this case, a more sophisticated method of losses prediction will be needed.

Chapter 4

Bleed Valve Control

Based on the Moore–Greitzer model [37, 65] described in Section 2.2, Liaw and Abed [54] derived a control law using a bleed valve for rotating stall. Eveker et al. [24] was the first group to report successful experimental implementation of a bleed valve controller. In particular, the bleed valve actuation method tested by Eveker et al. [24] employed a 25 Hz (full open/full close) bleed valve and reports results on a compressor with a rotor frequency between 22.5 and 26.7 Hz. For industrial applications where the compressors may be significantly more powerful (higher flow and pressure rise, higher rotor frequency, etc.) than research compressors, obstacles such as control actuator magnitude and rate saturation can become crucial in these active control methods. Tools that predict and reduce the rate requirements of actuators for purposes of control of rotating stall in compressors can be valuable in designing actuators and circumventing possible actuator magnitude and rate limitations that may prevent successful active control implementations.

Attempts to control rotating stall on a single–stage, low–speed axial compressor at Caltech were carried out initially with a high speed bleed actuator and results were unsuccessful due to the fast growth rate of the stall cell relative to the rate limit of the valve [100]. It has been shown by D'Andrea et al. [12] that air injection can be modeled as a shift of the compressor characteristic. By adding continuous air injection, the compressor characteristic is shifted favorably for bleed valve control of rotating stall and demonstration of control is achieved only with the compressor

characteristic actuation [100, 101]. On the Caltech rig, the amount of compressor characteristic shifting can be varied by modifying the geometric features of the injection actuator's setup [5], providing a family of compressor characteristics. In this chapter, investigation of the trade–off between actuation of the compressor characteristic and the bleed valve rate requirement is carried out, with the following goals:

1. Identify possible functional dependence of the rate limit of a bleed valve in control of rotating stall on the shape of the compressor characteristic.

2. Provide a possible route to circumvent bleed valve rate limitation given the capability of actuation or modification of the compressor characteristic.

3. Provide insights for designing a compressor–bleed pair for purposes of stabilization of rotating stall.

This chapter is organized as follows. Section 4.1 describes the modeling of bleed actuation and continuous air injection is introduced as a modulation of the throttle [54] and compressor characteristic [12] respectively. The relevant control law will be given for the bleed valve. Analytical formulas are presented as theoretical tools used for predicting the minimum gain in the control law and rate limit of the bleed valve required for stabilization. Section 4.2 presents the results of control of rotating stall using bleed valve with continuous air injection. A comparison study correlating the theory, simulation, and experiment in terms of the values of the gain and rate and the various features of the compressor characteristic is included to validate the theoretical and simulation tools. Finally, we summarize the findings of the investigation in Section 4.3.
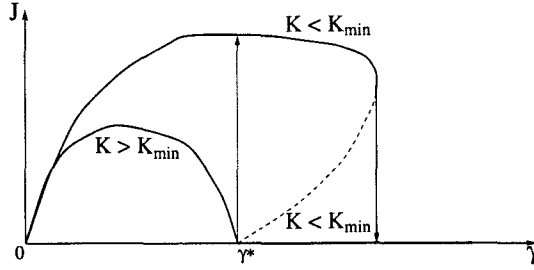
Figure 4.1 Relation of controller gain and behavior of bifurcation.

4.1 Theory

In this section, modeling of bleed actuation in the Moore–Greitzer model:

$$\dot{\Phi} = \frac{1}{l_c}(\Psi_c(\Phi) - \Psi + \frac{J}{4}\frac{\partial^2\Psi_c(\Phi)}{\partial\Phi^2}),$$

$$\dot{\Psi} = \frac{1}{4l_cB^2}(\Phi - \gamma\sqrt{\Psi}),$$

$$\dot{J} = \frac{2}{m+\mu}J(\frac{\partial\Psi_c(\Phi)}{\partial\Phi} + \frac{J}{8}\frac{\partial^3\Psi_c(\Phi)}{\partial\Phi^3}),$$

is introduced and a review of a control law proposed by Liaw and Abed [54] is given. Expressions for the minimum gain and rate required for peak stabilization of rotating stall are presented.

For stall control, Liaw and Abed [54] proposed a control law that modifies the throttle characteristic:

$$\Phi_T(\Psi) = (\gamma + u)\sqrt{\Psi},$$

$$u = K_{\mathrm{RS}}J.$$

This control law can be realized experimentally through the use of a bleed valve. For a large enough value of K_{RS}, the nominally unstable branch of equilibrium solution created at $\gamma = \gamma^*$ "bends over" and eliminates the hysteresis loop, i.e. the subcritical nature of the transcritical bifurcation is changed to supercritical (Figure 4.1).

By substituting the stall control law and computing the quantity $\frac{dJ}{d\gamma}$ at the stall inception throttle coefficient γ^*, the minimum gain needed for this phenomenon to

occur can be found by asserting the condition that $\frac{dJ}{d\gamma}|_{\gamma=\gamma^*} < 0$ (see Figure 4.1). The expression for the minimum gain required for peak stabilization is given by

$$K_{\text{theory}} = K_{\text{RS,min}} = -\frac{\Phi^*\Psi_c'''(\Phi^*)}{8\gamma^*\Psi^*\Psi_c''(\Phi^*)} - \frac{\gamma^*\Psi_c''(\Phi^*)}{8\Psi^*}, \qquad (4.1)$$

which depends on the shape of the compressor characteristic. Since the second term is always non–negative around the peak, the larger the value of $\Psi_c'''(\Phi^*)$, the smaller $K_{\text{RS,min}}$. Roughly speaking, this amounts to a compressor characteristic which is more "filled out" to the left of the peak. This expression serves as one of the theoretical tools for predicting the bleed valve requirement needed for peak stabilization.

In addition to the minimum gain, the requirement on the characteristics of the bleed actuator for control of stall can also be analyzed. The detailed theoretical analysis for the effects of actuator limits can be found in Wang and Murray [93]. In the following the ideas are sketched qualitatively and the main results that are used for comparisons in later sections are presented.

A study of the effects of actuator magnitude and rate saturations can be motivated using Figure 4.2. Figure 4.2(a) shows the effects of the Liaw–Abed controller with finite magnitude saturation and infinite bandwidth. The bleed valve controller fails to stabilize stall when the magnitude saturation is reached, and thus cannot eliminate the hysteresis loop beyond γ_K. Furthermore, any arbitrarily small noise of J will grow to fully developed rotating stall no matter how big the controller gain is if the throttle is operated at $\gamma < \gamma_0^*$. It can also be seen that the region that benefits from the controller is much smaller than the unsaturated case (Figure 4.1) if the magnitude saturation is severe.

Suppose now that the rate limit is finite in addition to the magnitude saturation. Then the region that benefits from the bleed valve control is even smaller (shaded region in Figure 4.2(b)). Roughly speaking, the region of attraction of the operable equilibria is decreased as the rate limit of the actuator decreases. As a result the extended operable region is further restrained.

(a) Saturation with infinite bandwidth

(b) Saturation with finite bandwidth
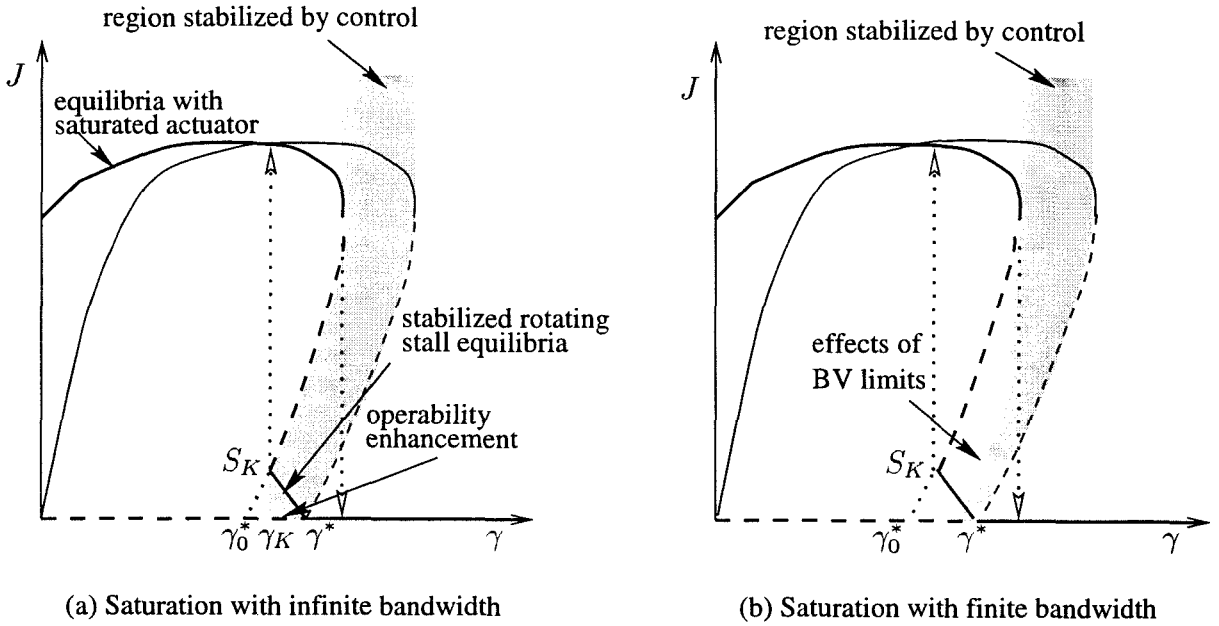
Figure 4.2 Effects of Liaw–Abed control law with actuator limits. Solid line: stable equilibria, dashed line: unstable equilibria. (Figure courtesy of Y. Wang)

The noise level for a real compression system is not arbitrarily small. When the noise level is of finite amplitude, the open loop system will go to rotating stall at a throttle coefficient which is larger than γ^*. In this case, region benefited from active control becomes even smaller. In the following we give an approximate analysis to evaluate the shaded region in Figure 4.2.

Consider the Moore–Greitzer model given in equation (2.2), which is repeated here:

$$\dot{\Phi} = \frac{1}{l_c}(\Psi_c(\Phi) - \Psi + \frac{J}{4}\frac{\partial^2\Psi_c(\Phi)}{\partial\Phi^2}),$$

$$\dot{\Psi} = \frac{1}{4l_cB^2}(\Phi - \gamma\sqrt{\Psi}),$$

$$\dot{J} = \frac{2}{m+\mu}J(\frac{\partial\Psi_c(\Phi)}{\partial\Phi} + \frac{J}{8}\frac{\partial^3\Psi_c(\Phi)}{\partial\Phi^3}).$$

Suppose the Greitzer B parameter is sufficiently small, such that the surge dynamics is exponentially stable, and the compressor characteristic is smooth. The transcrit-
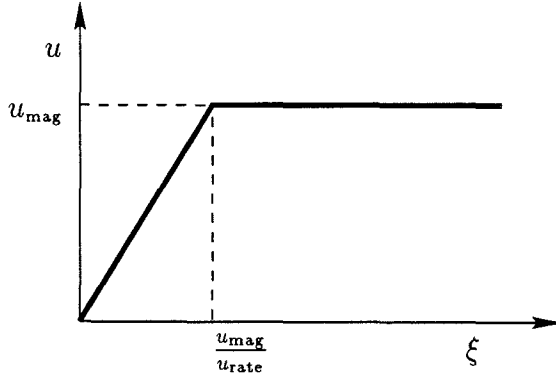
Figure 4.3 Controllers constrained by magnitude and rate limits.

ical bifurcation for the uncontrolled system at γ^* implies the existence of a center manifold near the transcritical bifurcation point. By viewing the control input u as a parameter, system (2.2) can be reduced to the center manifold when the throttle is operated near the stall inception point γ^*. The dynamics on the center manifold is given by the following one–dimensional system:

$$\dot{J} = \alpha_1(\delta + u)J + \alpha_2 J^2, \tag{4.2}$$

where

$$
\begin{aligned}
\delta &= \gamma - \gamma^*, \\
\alpha_1 &= \frac{2\sqrt{\Psi^*}\Psi_c''}{m + \mu}, \\
\alpha_2 &= \frac{1}{4(m + \mu)}\left(\Psi_c''' + \frac{\gamma^*\Psi_c''^2}{\sqrt{\Psi^*}}\right),
\end{aligned}
$$

and all the derivatives are evaluated at the peak of the compressor characteristic. To account for the magnitude and rate limits of the control input u, we assume that the actuator opens according to the rate limit and saturates (see Figure 4.3). The

system then has the following boundary conditions:

$$J(0) = \epsilon, \qquad\qquad u(0) = 0,$$
$$J(\tfrac{u_{\text{mag}}}{u_{\text{rate}}}) = J_c = -\frac{\alpha_1}{\alpha_2}(u_{\text{mag}} + \delta), \quad u(\tfrac{u_{\text{mag}}}{u_{\text{rate}}}) = u_{\text{mag}},$$

$$(4.3)$$

where ϵ is the noise level of the system.

The analytical solution to equation (4.2) can be difficult to obtain. However, an approximation to the solution of this two–point boundary value system can be obtained. The rate limit requirement for stall stabilization in a system of a given noise level can then be found [93]. Let

$$\Delta = 1 + \frac{\alpha_1\delta}{\alpha_2\epsilon}, \quad \eta = \alpha_2\epsilon\xi, \qquad f = \frac{J}{\epsilon}, \quad J_c = \epsilon(\sigma + 1 - \Delta),$$
$$\sigma = \frac{-\alpha_1 u_{\text{mag}}}{\alpha_2\epsilon}, \quad \bar\eta = \alpha_2\epsilon\frac{u_{\text{mag}}}{u_{\text{rate}}}, \quad f' = \frac{df}{d\eta}, \quad \lambda = \frac{\sigma}{\bar\eta},$$

then equation (4.2) with initial and final conditions (4.3) can be written as follows:

$$f' = (\Delta - 1 - \lambda\eta)f + f^2,$$
$$f(0) = 1,$$
$$f(\bar\eta) = 1 + \sigma - \Delta.$$

The approximation to the solution of $f(\bar\eta)$ can be obtained as follows. Additional boundary conditions characterizing derivatives at the boundaries can be obtained from f'. A form for the function f is then assumed while satisfying the desired boundary conditions. For instance, by letting $f(\eta)$ satisfy the following boundary conditions,

$$f(0) = 1, \quad f(\bar\eta) = 1 + \sigma - \Delta, \quad f'(0) = \Delta, \quad f'(\bar\eta) = 0,$$

we obtain

$$\frac{-\alpha_2\epsilon\Delta^*}{\alpha_1} = \frac{-\alpha_2\epsilon\Delta_1^*}{\alpha_1} = \frac{u_{\text{mag}}}{1 + \frac{\pi}{8}\sigma\bar\eta^2\arctan\left(\frac{\pi}{4}\sigma\bar\eta\right)} \qquad (4.4)$$
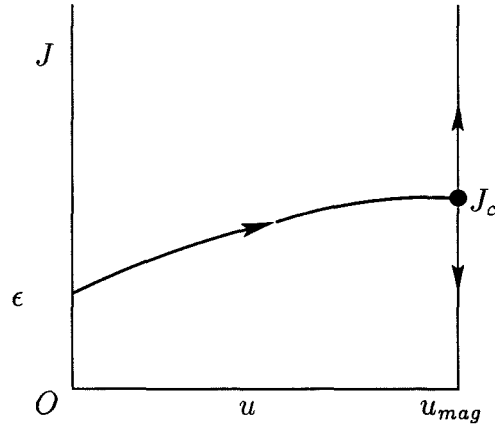
Figure 4.4 The phase portrait of the system (equation (4.2)).

after algebraic manipulations, where Δ^* denotes the extension of operable region as a percentage of γ^*. By specifying Δ_1^*, the value of u_{rate} required can be obtained. This value of u_{rate} is referred to as $R1_{\text{theory}}$. Alternatively,

$$\frac{-\alpha_2 \epsilon \Delta_2^*}{\alpha_1} = u_{\text{mag}} \frac{1 - \frac{2}{\pi} \arctan\left(\frac{\pi}{4}\sigma\bar{\eta}\right)}{1 - \frac{\sigma}{1+\sigma}\frac{2}{\pi} \arctan\left(\frac{\pi}{4}\sigma\bar{\eta}\right)} \tag{4.5}$$

is obtained if a slightly different set of boundary conditions is chosen (see Wang and Murray [93] for details). A value for $R2_{\text{theory}}$ can be obtained similar to the earlier case. These different boundary conditions essentially translate to different values of the growth/decay as the trajectory of J starts and ends (see Figure 4.4).

Formulas (4.4) and (4.5) are used to compare with results from simulations of a high fidelity model and experiments.

4.2 Results

In this section, the results for axisymmetric bleed with continuous air injection are presented. Control of rotating stall is demonstrated first. A description of the procedure leading to the comparison study is then given, followed by the results.

Model Identification for new configuration: compressor characteristic fit
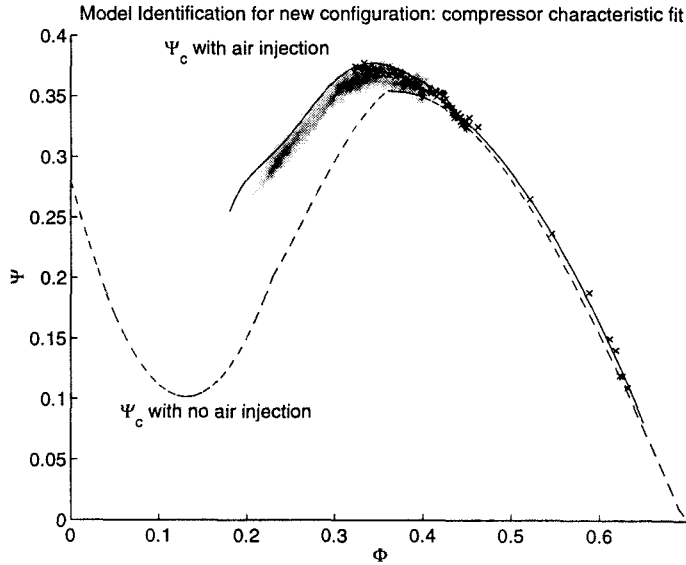
Figure 4.5 Identification of compressor characteristic with continuous air injection at 27° and 60 psig injector back pressure. The crosses represent data points taken from experiments, the solid the identified compressor characteristic, the dashed the compressor characteristic without air injection, and the shaded region the experimental surge cycle data for $\Psi_c(\Phi)$ with air injection.

4.2.1 Demonstration of Control

At certain injector angles and locations, different injector back pressure can reduce the size of the open–loop hysteresis loop by different amounts on the Caltech rig. Addition of continuous air injection is conjectured to reduce rate and magnitude requirements for bleed valve controls of rotating stall by changing the compressor characteristic.

To validate the conjecture, the air injector angle is set at 27° (with positive angles implying counter–compressor–rotation) and 60 psig injector back pressure. With the plenum attached, surge cycle data is taken and the algorithm for identifying the unstable part of the compressor characteristic as described by Behnken [4]. Figure 4.5 shows the results.

The identified compressor characteristic is more "filled out" on the left of the peak. The crosses in Figure 4.5 are experimental data points of the stable side of

the compressor characteristic with continuous air injection, the right solid curve the polynomial fit of the experimental data points, the left solid curve the identified unstable part of the characteristic in the presence of continuous air injection, the dashed the compressor characteristic with no air injection, and the shaded region the experimental surge cycle data for $\Psi_c(\Phi)$ in the presence of air injection. As shown in the figure, the shape of the compressor characteristic is shifted in the presence of continuous air injection.

The shifting of the compressor characteristic serves to reduce the bandwidth and rate requirement of the bleed valve for control of rotating stall. To observe this phenomenon, equation (4.1) can serve as an initial tool. Equation (4.1) gives a formula to the minimum gain required for stabilization of rotating stall at the peak of the compressor characteristic. A 4th order polynomial fit to the unactuated compressor characteristic in Figure 4.5 gives

$$\Psi_c(\Phi) = 0.71 - 10.59\Phi + 60.80\Phi^2 - 126.39\Phi^3 + 87.48\Phi^4,$$

with the peak at $(\Phi, \Psi) = (0.38, 0.35)$, and the second and third derivative values of -14.99 and 39.45 respectively. A similar fit to the actuated characteristic gives

$$\Psi_c(\Phi) = 0.78 - 8.82\Phi + 49.49\Phi^2 - 104.77\Phi^3 + 74.1331\Phi^4,$$

with the peak at $(\Phi, \Psi) = (0.35, 0.38)$, and the second and third derivative values of -12.07 and -5.92 respectively. Equation (4.1) applied to the unactuated characteristic gives $K_{RS,min,unact} = 4.00$ and to the actuated case gives $K_{RS,min,act} = 2.16 < K_{RS,min,unact}$.

With this evidence, a detailed experiment is carried out with the injector back pressure set at 55 psig. Figure 4.6 shows the open- and closed-loop behavior of the system in the Φ-Ψ plane and the γ-J plane respectively.

The closed-loop behavior shows no hysteresis loop on Figure 4.6, as expected from the theory. As Figure 4.6 shows, after the bleed valve saturates, the system returns to the original stalled equilibria. The γ-J plot in Figure 4.6 is expected to
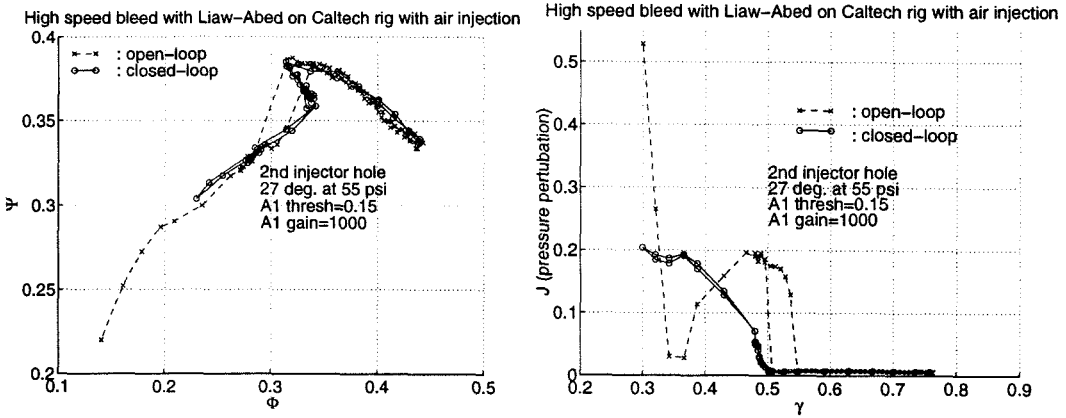
Figure 4.6 Open– and closed–loop behavior of system on Φ–Ψ plane for control with bleed valve and continuous air injection at 55 psig injector back pressure.

show the same observation. The mismatch at low values of γ is due to the formation of the second mode of stall in the open–loop case. For the open–loop system with continuous air injection, the second mode of rotating stall forms at a value of γ smaller than that for the formation of the first mode. At $\gamma = 0.45$ on Figure 4.6, the second mode forms and becomes dominant, and the amplitude of the first mode is decreased. Further decrease in γ leads to a further reduction in the amplitude of the first mode. At around $\gamma = 0.33$, the throttle is almost fully closed and the first mode becomes dominant again. In the closed–loop case, this phenomenon is not observed since the high speed bleed valve saturates and remains open. As a result, the main flow level is not low enough for the second mode of rotating stall to form.

A combined surge and stall control algorithm is implemented by using the high speed bleed valve with continuous air injection for stall and the slow bleed valve (disturbance bleed) for surge. The surge controller is implemented with a proportional feedback on $\dot{\Phi}$. This control law is proposed by Badmus et al. [2]. The combined control law for rotating stall and surge takes the form

$$\Phi_T(\Psi) = (\gamma + K_{\text{RS}}J + K_{\text{S}}\dot{\Phi})\sqrt{\Psi},$$

where K_{RS} is the gain for rotating stall control and K_{S} that for surge control.
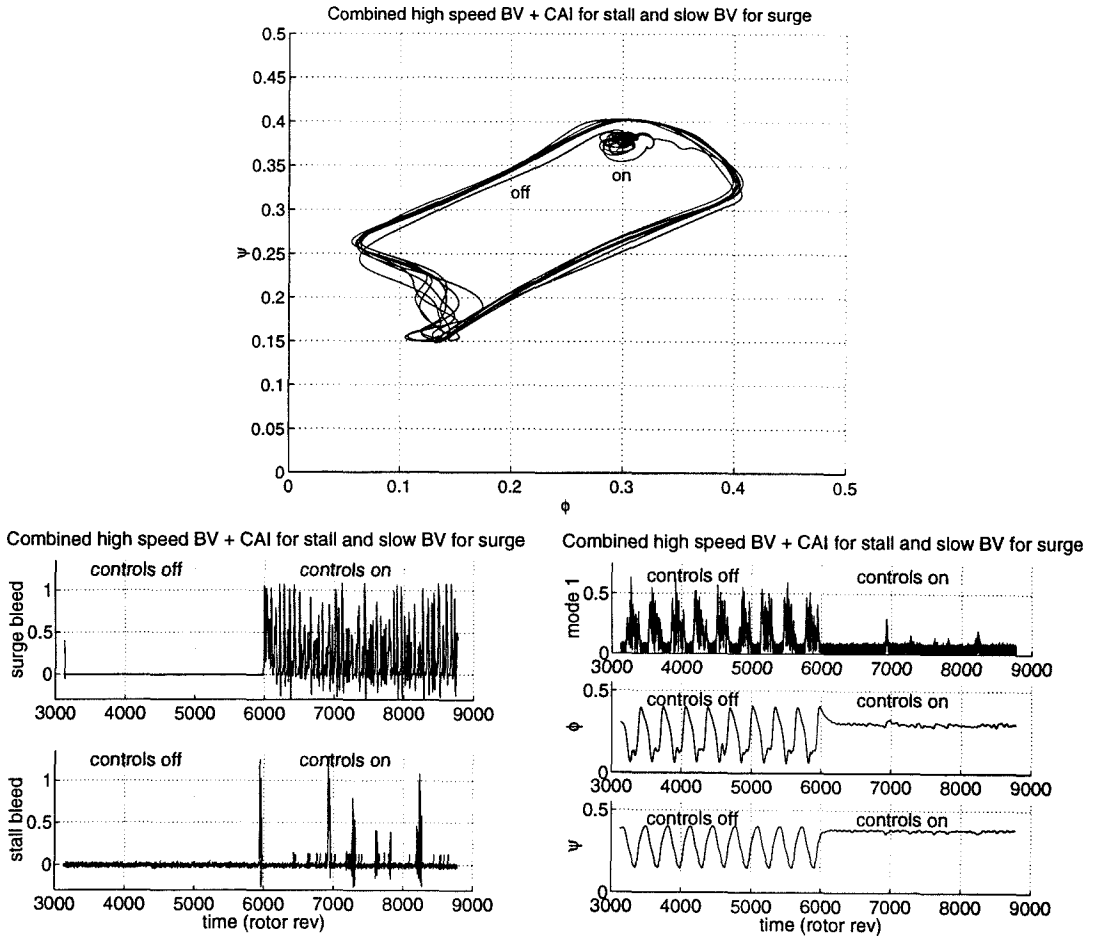
Figure 4.7 Combined stall control with high speed bleed and continuous air injection and surge control with slow bleed: control initially off and turned on at approximately 6000 rotor revolutions.

Figure 4.7 shows plots of the dynamic response of the system. Control is initially turned off and the system is surging. Control is then activated at approximately 6000 rotor revolutions and the system is stable.

4.2.2 Procedure for Comparison Study

We now compare the rate predictions derived in Section 4.2 with the experimental results. The air injectors back pressure and angle are varied to produce a set of scenarios. Data is taken and analyzed to obtain the theoretical and simulation predictions, as well as the experimental values for the rate limit requirement for

stabilization of stall.

The magnitude of the effects of air injection on the system can be varied by modifying various geometrical characteristics of the injector location and configuration [5]. For this study, the injector angle relative to the axial flow direction is varied between 27° and 40° in the opposite direction of the rotor rotation, and the back pressure of the injectors is varied between 40 to 60 psig, producing a total of 16 different scenarios and the nominal open–loop system without air injection. At the various injection settings, experiments are carried out to obtain the gain and rate values required for peak stabilization. For this study, peak stabilization is achieved if the following conditions are met during the experiment:

$$\Phi \geq 0.9\Phi^*,$$

$$A \leq 0.5A_{\text{nom}},$$

where Φ is the axial velocity and A is the amplitude of the first Fourier mode, Φ^* is the flow at stall inception, and A_{nom} is the amplitude of fully developed stall without bleed valve control. It should be noted that Φ^* is taken experimentally at the stall inception point for each of the case of the injection setting under consideration.

The rate limits are determined on the experiment as follows. A function is written to increment the gain until the conditions of peak stabilization are met. An analogous function is written for the rate. The gain/rate required for peak stabilization is then obtained by first setting the system operating point to stable but near stall inception. With the rate/gain fixed, injection and the controller is then activated with the gain/rate set to zero. The load of the compressor is then increased by changing the throttle setting until a nominally unstable operating point is reached. The gain/rate incrementing function then increments the variable of interest until peak stabilization is achieved. The gain and rate obtained from the experiments are referred to as K_{expt} and R_{expt} respectively.

Among the 17 injection settings, peak stabilization is achieved in 11 cases and the nominally stable side of the compressor characteristic is experimentally recorded
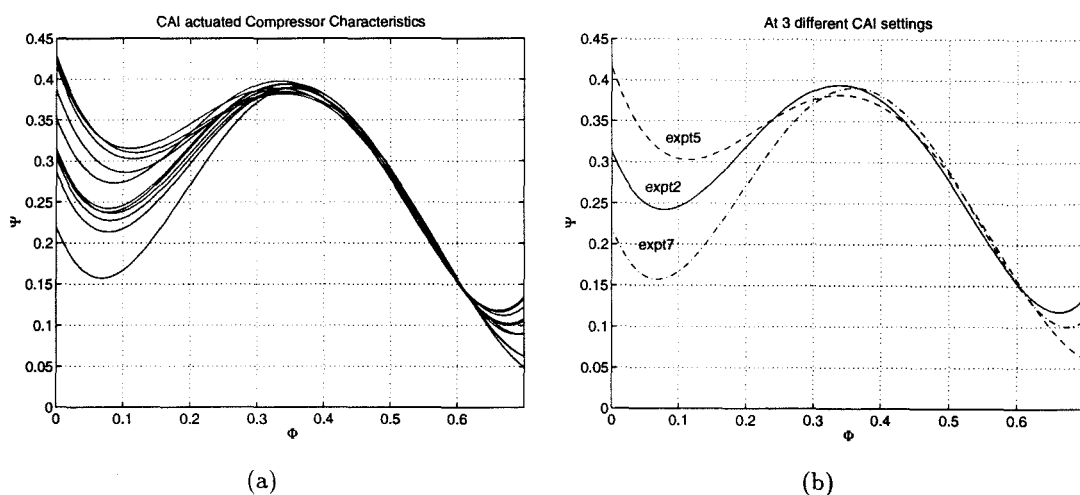
Figure 4.8 Compressor characteristics with continuous air injection:
(a). Fitted compressor characteristics for the 11 cases; (b). Identified
compressor characteristics at three different continuous air injection
settings.

at each of the 11 settings. The unstable sides for each of these cases are identified by
using surge cycle data with an algorithm proposed by Behnken [4]. For this study, a
fourth order polynomial is used to approximate the piecewise continuous curve for
each case. Figure 4.8a shows the fitted compressor characteristics. These polynomial
compressor characteristics are then used with realistic values of various parameters
(e.g. noise level in system) in analytical relations K_{theory}, $R1_{theory}$, and $R2_{theory}$,
and in simulations that estimate the gain K_{simu} and rate R_{simu} requirements on the
bleed valve for stall stabilization. All high fidelity simulations are carried out using
a collocated model described in Section 2.3 with unsteady loss dynamics [39] and a
3-state model for the bleed actuator dynamics.

There is uncertainty associated with the computation of the theoretical predic-
tions and the experimental data. Due mainly to the unsteadiness of the fluid in
the system, there is uncertainty in each of the identified compressor characteristics
from the 17 settings. Results computed using these characteristics thus inherit the
uncertainty which needs to be accounted for. The experiment gain and rate data
also has uncertainty associated with it again due primarily to unsteadiness of the

system.

To determine the level of uncertainty associated with the theoretical predictions and the experiments, an investigation is carried out on 3 of the 11 points, namely, experiment number 2 (expt2), 5 (expt5), and 7 (expt7) (see Figure 4.8b). For each of these settings, ten different segments of the surge cycle data are used to identify the unstable side of the compressor characteristic. The resulting characteristics are then used to compute the theoretical predictions, and 95% confidence error bars (adjusted with T–statistics) are obtained for K_{theory}, $R1_{\text{theory}}$, and $R2_{\text{theory}}$. Similarly, for the uncertainty associated with the experimental gain and rate data, ten experiments are carried out for expt2, expt5, and expt7, to give 95% confidence error bars on K_{expt} and R_{expt}.

4.2.3 Comparison Study

Based on the functional dependence of the analytical relations for the minimum gain and rate requirement on $\Psi_c''(\Phi^*)$ and $\Psi_c'''(\Phi^*)$, an examination of Figure 4.8b would indicate that experiment 5 should require the least gain/rate while experiment 7 should require the most. The theory and simulations are expected to show at least a qualitative trend with respect to the experiment.

The values of the gain predicted by the theory are plotted against the gains obtained on the experiments in Figure 4.9. In all of the plots presented in this section, the dashed line represents the one–to–one line between the theoretically and experimentally obtained values. As shown in the figure, the K_{theory} estimates are not quantitatively reliable but do present the qualitative monotonic trend as expected. The main factor contributing to the quantitative disagreement between K_{theory} and the experiment is the lack of actuator dynamics in the derivation of the analytical expression. The bleed valve is assumed to be ideal with infinite bandwidth and magnitude saturation in the analysis while actuator limits are present in the experiments. Nevertheless, experiment 5 is predicted and verified to require the least gain, and experiment 7 the most.

The values of the rate predicted by the two analytical relations, $R1_{\text{theory}}$ and
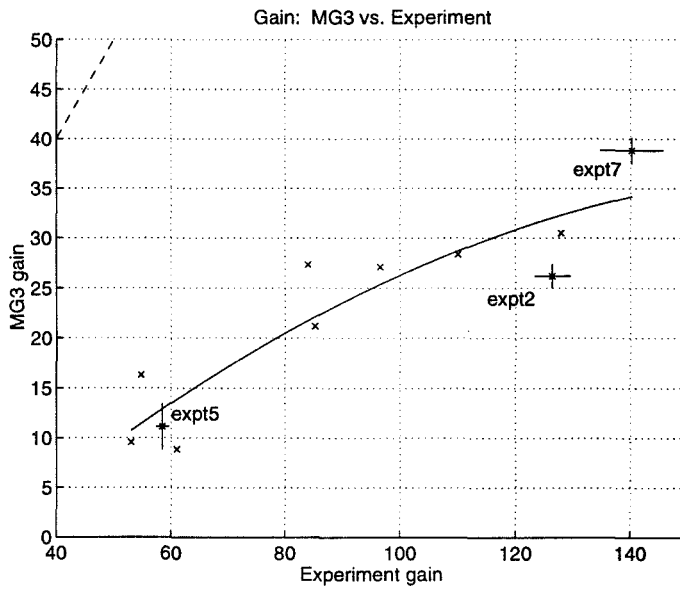
Figure 4.9 Comparison of gain predicted by MG3 and experimental
gain required for stabilization of stall. The dashed line represents the
one–to–one line; the bars in the x direction are error bars associated
with the uncertainty in computing the theoretical gain values (through
identifying the unstable of $\Psi_c(\Phi)$ using surge cycle data); the bars
in the y direction are error bars associated with the experimentally
obtained values.
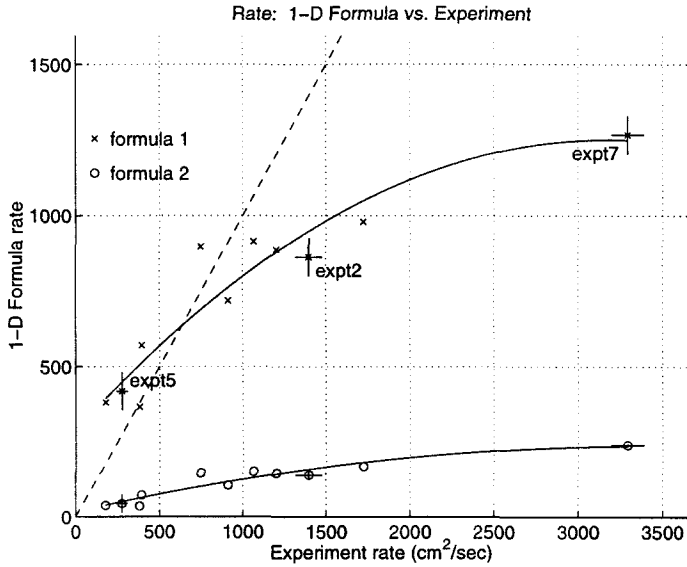
Figure 4.10 Comparison of rate predicted by theory and experimental rate required for stabilization of stall. The dashed line represents the one–to–one line; the bars in the x direction are error bars associated with the uncertainty in computing the theoretical rate values (through identifying the unstable of $\Psi_c(\Phi)$ using surge cycle data), and the bars in the y direction the error bars associated with the experimentally obtained values.

$R2_{\text{theory}}$, are plotted against the rates obtained on the experiments in Figure 4.10. First of all, it should be pointed out that the experiments show that the rate requirement for peak stabilization is reduced from approximately 3300 cm^2/sec to below 230 cm^2/sec (with a magnitude saturation at 11.4 cm^2) by varying the amount of compressor characteristic actuation. Regarding the theoretical tools used for prediction, one can see from the figure that $R1_{\text{theory}}$ predicts the rate requirement more accurately than $R2_{\text{theory}}$. Furthermore, $R1_{\text{theory}}$ seems to be more accurate at more severe rate limit values. The main difference between the two expressions originates from the different ways an approximation to the solution to the one–dimensional center manifold (equation (4.2)) of the Moore–Greitzer equations is made. Despite their quantitative differences, a monotonic trend similar to that observed in the theoretical gain comparison is again displayed.

The values of gain and rate predicted by high fidelity simulations are plotted
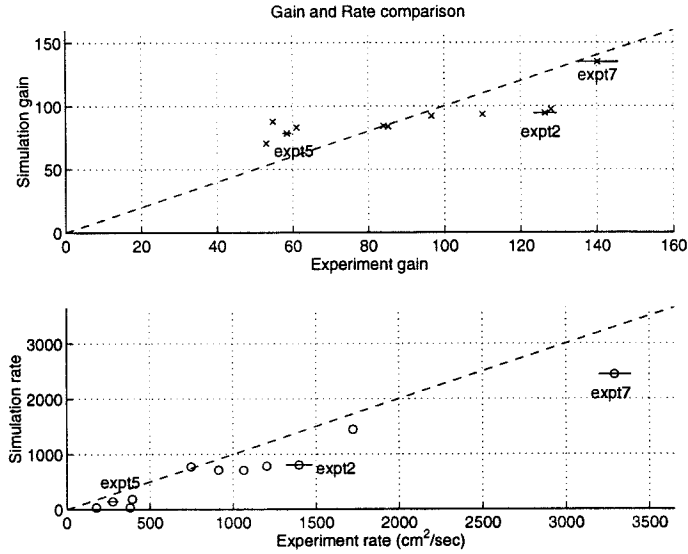
Figure 4.11 Comparison of gain and rate predicted by simulations and
experimental values required for stabilization of stall. The dashed line
represents the one–to–one line; the bars in the y direction are error
bars associated with the experimentally obtained values.

against the experimental values in Figure 4.11. The gain and rate estimates of
the simulations match with the experimentally obtained counterpart more closely
than the theoretical predictions. However, there are a number of factors affecting
the remaining difference. A possible explanation for this phenomenon is that the
only difference in the 11 simulations are the compressor characteristics and the
effective length parameter in the model l_c. The effects of continuous air injection
on the system in certain cases may require modifying more parameters in order to
accurately capture the reality. A more careful identification of the system at each
point should present a more reliable simulation.

From the K_{theory} expression,

$$K_{\text{theory}} = -\frac{\Phi^* \Psi_c'''(\Phi^*)}{8\gamma^* \Psi^* \Psi_c''(\Phi^*)} - \frac{\gamma^* \Psi_c''(\Phi^*)}{8\Psi^*},$$

it can be seen that K_{theory} depends linearly on $\Psi_c'''(\Phi)$ and nonlinearly on $\Psi_c''(\Phi)$.
A similar conclusion can be drawn for $R1_{\text{theory}}$ and $R2_{\text{theory}}$ with a closer exami-
nation of the expressions. The values of the gains from the theory, simulations, and
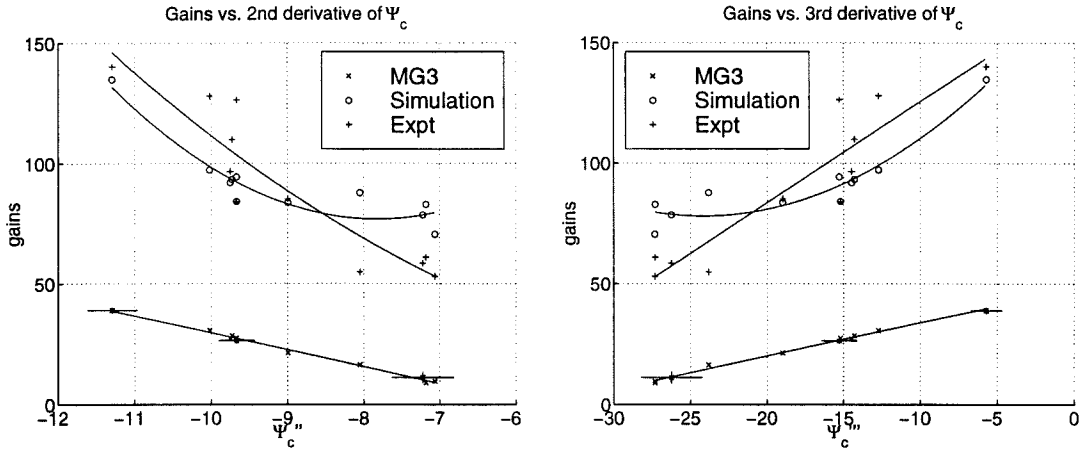
Figure 4.12 Dependence of K_{theory} on $\Psi_c''(\Phi)$ and $\Psi_c'''(\Phi)$: experiment (Expt), gain from theory (MG3), and simulation. The error bars in the x direction indicate the error in computing the derivatives (through identifying the unstable of $\Psi_c(\Phi)$ using surge cycle data); the error bars in the y direction indicate the error in computing/obtaining the predictions/experimental values.

experiments are plotted against $\Psi_c''(\Phi)$ and $\Psi_c'''(\Phi)$ in Figure 4.12.

The analogous plots for the rate expressions are shown in Figure 4.13. It can be seen from both plots that the gain and rate values obtained from theory, simulations, and experiments share the same trend on their dependence on $\Psi_c''(\Phi)$ and $\Psi_c'''(\Phi)$. Since the values of the derivatives cannot be obtained without identifying the unstable part of $\Psi_c(\Phi)$, it is thus a natural conclusion that the shape of the unstable part of Ψ_c contains information for the gain and rate requirements of bleed valve control of stall.

A final remark is that the reduction of the bleed actuator requirement via air injection is demonstrated on the Caltech rig for convenience only. Other realizations of compressor characteristic actuation that result in favorable shifting of the characteristic can in principle serve to reduce the actuator requirement as well. Some possible mechanisms include air injection at the tip of the rotor, casing treatments [34], complete or partial guide vanes that redirect the air flow, hub distortion on tip–loaded compressors [58], and mistuning [97]. More information on possible implementations is described in [99].
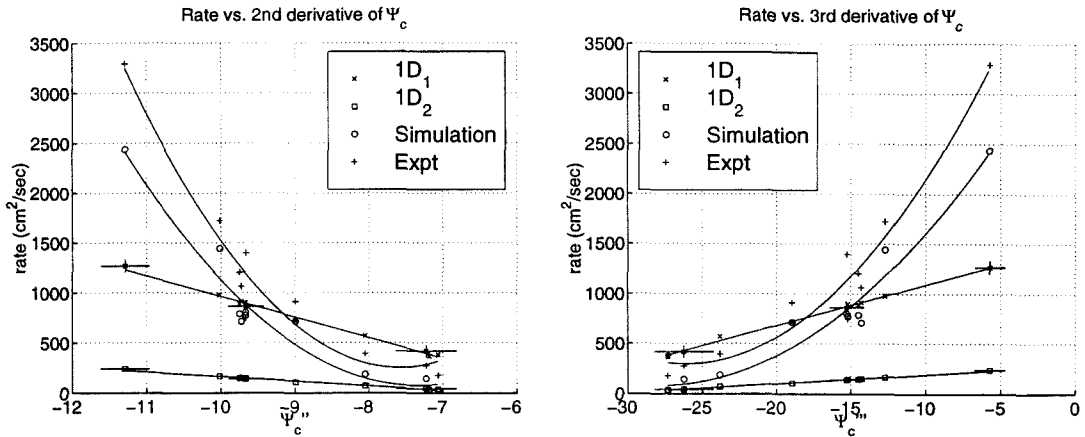
Figure 4.13 Dependence of R_{theory} expressions on $\Psi_c''(\Phi)$ and $\Psi_c'''(\Phi)$: experiment (Expt) and rate expression n from theory (1D_n). The error bars in the x direction indicate the error in computing the derivatives (through identifying the unstable of $\Psi_c(\Phi)$ using surge cycle data); the error bars in the y direction indicate the error in computing/obtaining the predictions/experimental values.

4.3 Conclusions

Control of stall and surge with a bleed valve is studied. It is found that the stall cell growth rate is fast compared to the actuator rate limit and thus forms a bottleneck for successful control implementation if only the bleed actuator is employed. Demonstration of control of stall is achieved only when the compressor characteristic is actuated, in this case, via steady air injection. Simultaneous control of stall and surge is also achieved.

Theoretical and simulation tools have been developed to analyze bleed valve requirements for control of rotating stall and validated against experiments. Compressor characteristic actuation via air injection is found to reduce the bleed valve rate requirement for stall control. *Both* the stable and unstable side of the compressor characteristic are changed by the addition of air injection and found to be crucial in analyzing the closed–loop system.

For the Caltech compression system, the compressor characteristic is more "filled out" on the left of the peak in the presence of air injection, and the peak location, second, and third derivative at the peak are different than those of the unactuated

characteristic. This change of system characteristics reduces the bandwidth and magnitude requirements of a bleed actuator in performing bleed valve controls of rotating stall. With a compressor rotor frequency of 100 Hz, active control of stall with a high speed bleed valve is achieved *only when the compressor characteristic is actuated.* Furthermore, the experiments show that the bleed valve rate requirement is reduced from approximately 3300 cm^2/sec to below 230 cm^2/sec when the amount of compressor characteristic actuation is increased. This actuation is captured by a change of the shape and a shift in the peak of the compressor characteristic. Theoretical tools based on a low order model (2–3 states) and simulations based on a reduced order distributed model (37 states) have been developed to estimate the gain and rate requirements of the bleed controller. All of the proposed analytical formulas and simulations share the same qualitative trends with respect to Ψ_c'', Ψ_c''', and the experiment. The agreement implies that bleed valve control of rotating stall depends crucially on the rate limit of the bleed valve which in turn depends on *both* the stable and the *unstable* part of the compressor characteristic.

The effects of air injection are accounted for via a shift of the compressor characteristic in this paper, whereas the actual effects are much more sophisticated. A more detailed fluid dynamic model of the effects of air injection on compressors will provide a more accurate basis for theoretical analysis as well as simulations.

Aside from rate limit, bandwidth and delay are also parts of actuator dynamics. A comparison study between the theory, simulation, and experiments on various features of actuator limitations will not only validate the model and the analysis, but also allow a more complete picture of how control implementation is affected. The resulting sensitivity analysis can be used as a design guideline for compressor–bleed pair construction with intent of active control of stall implementations.

Chapter 5

Axisymmetric Air Injection

Aside from bleed valves, state–of–the–art actuation mechanisms used for control of rotating stall and surge on axial flow compressors also include inlet guide vanes [39, 71] and air injection. In particular, air injection has received much attention in recent years. Researchers including but not limited to Behnken [4], Behnken et al. [6], D'Andrea et al. [12], Day [15], Freeman et al. [30], Gysling and Greitzer [38], Vo [92], Weigl [95], and Weigl et al. [96] have implemented air injection in various forms and obtained success for extending stability and/or operability of the under-lying compression systems beyond their respective nominal stall inception points.

Air injection control of stall can be realized in an axisymmetric as well as non–axisymmetric implementation. For instance, researchers including Behnken [4], Freeman et al. [30], and Weigl [95] have demonstrated control of stall using ax-isymmetric air injection, while Behnken [4], D'Andrea et al. [12], Gysling and Gre-itzer [38], Vo [92], Weigl [95], and Weigl et al. [96] have reported success using non–axisymmetric implementations.

Control of surge with a 2–D pulsed air injection was reported to fail in Behnken [4]. In Weigl [95], some preliminary work on simultaneous control of stall and surge with axisymmetric air injection is reported, though without success. The purpose of this part of the work is to provide a more thorough investigation into simultaneous con-trol of stall and surge with axisymmetric air injection. This chapter is organized as follows. A description of the theoretical justification of simultaneous stabilization

of stall and surge using axisymmetric air injection in Section 5.1. The results of control of stall only, surge only, and simultaneous stall and surge are presented in Section 5.2. Some conclusions given in Section 5.3 ends the chapter.

5.1   Theory

In this section, the theoretical foundation of control of stall (low B) and stall and surge (high B) is presented.

5.1.1   Low B

Linear stability is investigated first for control of stall. Axisymmetric air injection can be modeled as a shift of the compressor characteristic. The control law using axisymmetric air injection is modeled as a shift in the compressor characteristic with a feedback on J given by the following:

$$\Psi_c(\Phi) = \Psi_{c,\mathrm{nom}}(\Phi) + KJ\Psi_{c,\mathrm{air}}(\Phi), \tag{5.1}$$

where K is the gain. The model takes the following form after substitution:

$$
\begin{aligned}
\dot{\Phi} &= \frac{1}{l_c}\Big(\Psi_{c,\mathrm{nom}}(\Phi) + KJ\Psi_{c,\mathrm{air}}(\Phi) - \Psi + \frac{J}{4}\frac{\partial^2\Psi_{c,\mathrm{nom}}(\Phi)}{\partial\Phi^2} + \frac{KJ^2}{4}\frac{\partial^2\Psi_{c,\mathrm{air}}(\Phi)}{\partial\Phi^2}\Big), \\
\dot{\Psi} &= \frac{1}{4l_cB^2}(\Phi - \Phi_T(\Psi)), \\
\dot{J} &= \frac{2}{m+\mu}J\Big(\frac{\partial\Psi_{c,\mathrm{nom}}(\Phi)}{\partial\Phi} + \frac{KJ\partial\Psi_{c,\mathrm{air}}(\Phi)}{\partial\Phi} + \frac{J}{8}\frac{\partial^3\Psi_{c,\mathrm{nom}}(\Phi)}{\partial\Phi^3} + \\
&\quad \frac{KJ^2}{8}\frac{\partial^3\Psi_{c,\mathrm{air}}(\Phi)}{\partial\Phi^3}\Big).
\end{aligned}
\tag{5.2}
$$

Linearization of the closed–loop $\dot{J}$ equation at and to the left of the peak of $\Psi_{c,\mathrm{nom}}$ about $J = 0$ gives $\frac{d}{dt}(\delta J) = 0$ at and > 0 to the left of the peak, implying that the stall–free solution of the closed–loop system is asymptotically stable at the peak and unstable to the left of the peak.

Next we show through a bifurcation diagram that a shift in the compressor characteristic leads to elimination of the hysteresis loop. The details can be found

in D'Andrea et al. [12]. To illustrate, 3rd order polynomials are used to model a nominal compressor characteristic $\Psi_{c,\text{nom}}$ and the addition $\Psi_{c,\text{air}}$ due to the air injection.

$$\Psi_{c,\text{nom}}(\Phi) = a_0 + a_1\Phi + a_2\Phi^2 + a_3\Phi^3,$$
$$\Psi_{c,\text{air}}(\Phi) = b_0 + b_1\Phi + b_2\Phi^2 + b_3\Phi^3.$$

The new equilibria can be found by solving for the steady state solution (Φ, Ψ, J) to the governing equations. The minimum gain K required to eliminate the hysteresis loop can be found by computing the slope $\frac{dJ}{d\gamma}|_{\gamma=\gamma^*}$ and requiring $\frac{dJ}{d\gamma}|_{\gamma=\gamma^*} < 0$. The resulting expression for K_{min} is presented here without the algebra:

$$K_{\text{min}} = -\frac{\frac{\gamma^{*2}}{4}\Psi_{c,\text{nom}}''^2(\Phi^*) + \frac{\Phi^*}{4}\Psi_{c,\text{nom}}'''(\Phi^*)}{2\Phi^*\Psi_{c,\text{air}}'(\Phi^*) + \gamma^{*2}\Psi_{c,\text{air}}\Psi_{c,\text{nom}}''(\Phi^*)}. \tag{5.3}$$

Figure 5.1 shows sample nominal and shifted compressor characteristics and the location of the new equilibria with $B = 0.1$ and $K = 18$, both in the (Φ, Ψ) plane and the (γ, J) plane.

In addition to the gain computation, analysis on rate limits can also be performed. Wang and Murray [93, 94] presented a method of accounting for system and actuation limits on bleed valve control of stall via dynamical systems tools. Some preliminary work has been done to apply the technique to axisymmetric air injection control of stall.

An approach similar to the one proposed by Wang and Murray [93, 94] is applied to equation (5.2). Loosely speaking, magnitude limits on the actuation prohibits the operable region[1] to be extended to $\gamma = 0$, and the rate limitation cuts the extension further down. Figure 4.2 illustrates the basic ideas.

Assuming B is small so the surge dynamics can be ignored, an approximation

---

[1]Operable region can be thought of as stall-free to "small–stall" operating points associated with supercritical bifurcation for stall.
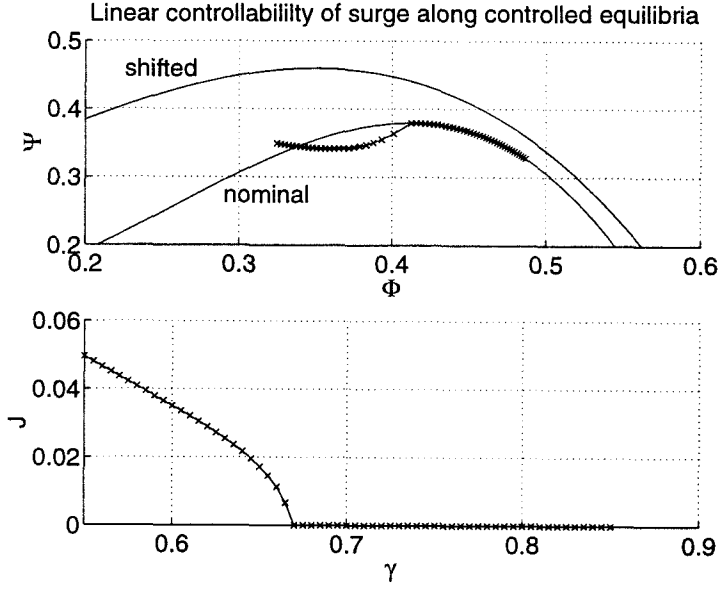
Figure 5.1 Nominal, shifted compressor characteristics, and the new equilibria with axisymmetric air injection controller for stall.

to the center manifold of equation (5.2) is obtained as:

$$\dot{J} = \alpha_1 \delta J + (u + u_1)J + \alpha_2 J^2,$$

where

$$\delta \;=\; \gamma - \gamma^*, \qquad \alpha_1 = \frac{2\sqrt{\Psi^*}\Psi''_{c,\text{nom}}(\Phi^*)}{m + \mu},$$

$$\alpha_2 \;=\; \frac{\Psi'''_{c,\text{nom}}(\Phi^*)}{4(m + \mu)} + \frac{\gamma^*\Psi''_{c,\text{nom}}{}^2(\Phi^*)}{4(m + \mu)\sqrt{\Psi^*}},$$

$$u \;=\; KJ\Psi_{c,\text{air}}\frac{\gamma^*\Psi''_{c,\text{nom}}(\Phi^*)}{(m + \mu)\sqrt{\Psi^*}}, \qquad u_1 = KJ\Psi'_{c,\text{air}}\frac{2}{m + \mu},$$

with x^* denoting x, for $x \in \{\Phi, \Psi, \gamma\}$, evaluated at the peak of $\Psi_{c,\text{nom}}$. In particular, the terms u and u_1 are associated with the pressure rise and compressor characteristic slope contribution from air injection respectively. Let $\tilde{u} = \frac{u+u_1}{\alpha_1}$ and ϵ to be the scaled control effort and the noise level of the system respectively. Define further magnitude limits u_{mag} and $u_{1,\text{mag}}$, and rate limits u_{rate} and $u_{1,\text{rate}}$ for u

and u_1 respectively such that

$$
x = \begin{cases} x_{\text{rate}}\xi & \text{if } 0 \le \xi < \xi_2, \\ x_{\text{mag}} & \text{if } \xi \ge \xi_2, \end{cases}
$$

where $x \in \{u, u_1\}$, ξ the nondimensional time and $\xi_2 = x_{\text{mag}}/x_{\text{rate}}$ the relevant time for the rate limit. This is used as the simplified compressor characteristic actuation dynamics (see Figure 4.3).

The reduced system and the corresponding boundary conditions then become

$$
\begin{aligned}
\dot{J} &= \alpha_1(\delta + \tilde{u})J + \alpha_2 J^2, \\
J(0) &= \epsilon, \\
\tilde{u}(0) &= 0, \\
J(\xi_2) &= -\frac{\alpha_1}{\alpha_2}(\tilde{u}_{\text{mag}} + \delta), \\
\tilde{u}(\xi_2) &= \tilde{u}_{\text{mag}},
\end{aligned}
\tag{5.4}
$$

where ϵ is the level of noise in units of J. The form of equation (5.4) is identical to the pure rate limit case for bleed valves presented in Wang and Murray [93, 94] and equations (4.2) and (4.3) in Section 4.1. Recall in Section 4.1 and [93, 94] that the one–dimensional system is approximated and a formula for the extension of operable region can be found. The formula is repeated here, with a reminder that the actuation $\tilde{u}$ in this case referring to compressor characteristic actuation:

$$
\tilde{\Delta}^* = \frac{\tilde{u}_{\text{mag}}}{1 + \dfrac{\pi\epsilon\tilde{u}_{\text{mag}}^3(-\Psi_c'')\left(\sqrt{\Psi^*}\Psi_c''' + \gamma^*\Psi_c''^2\right)}{16(m+\mu)^2\tilde{u}_{\text{rate}}^2}\arctan\left(\dfrac{\pi\sqrt{\Psi^*}\tilde{u}_{\text{mag}}(-\Psi_c'')}{2(m+\mu)\tilde{u}_{\text{rate}}}\right)},
\tag{5.5}
$$

where $\tilde{\Delta}^* = \frac{-\alpha_2\epsilon\Delta^*}{\alpha_1}$ and Δ^* is the extension of operable region as a percentage of γ^*.

5.1.2 High B

For the surge part, a linearization along the controlled equilibria shows that the surge equations ($\dot{\Phi}$ and $\dot{\Psi}$) are controllable. The linearization of equation (5.2) with (5.1) takes the form:

$$\frac{d}{dt}(\delta x) = \hat{A}x + \hat{B}u,$$

where $x = (\Phi, \Psi, J)$,

$$\hat{A} = \begin{bmatrix} A_1 & A_2 & A_3 \end{bmatrix}^{\mathrm{T}}_{\text{equilibrium}}$$

$$\hat{B} = \begin{bmatrix} 1 & 0 & 1 \end{bmatrix}^{\mathrm{T}}$$

and

$$A_1 = \begin{bmatrix} \dfrac{\Psi'_{c,\text{nom}} + KJ\Psi'_{c,\text{air}} + \frac{J}{4}(\Psi'''_{c,\text{nom}} + KJ\Psi'''_{c,\text{air}})}{l_c} \\[2mm] \dfrac{-1}{l_c} \\[2mm] \dfrac{K\Psi_{c,\text{air}} + \frac{\Psi''_{c,\text{nom}}}{4} + \frac{KJ\Psi''_{c,\text{air}}}{2}}{l_c} \end{bmatrix}^{\mathrm{T}},$$

$$A_2 = \begin{bmatrix} \dfrac{1}{4l_c B^2} & \dfrac{-\gamma}{8\sqrt{\Psi}l_c B^2} & 0 \end{bmatrix},$$

$$A_3 = \begin{bmatrix} A_{31} & 0 & A_{33} \end{bmatrix},$$

$$A_{31} = \frac{2J(\Psi''_{c,\text{nom}} + KJ\Psi''_{c,\text{air}})}{m + \mu},$$

$$A_{33} = \frac{2(\Psi'_{c,\text{nom}} + KJ\Psi'_{c,\text{air}})}{m + \mu} + \frac{J(\Psi'''_{c,\text{nom}} + KJ\Psi'''_{c,\text{air}})}{4(m + \mu)}$$

$$+ \frac{2J(K\Psi'_{c,\text{air}} + \frac{\Psi'''_{c,\text{nom}}}{8} + \frac{KJ\Psi'''_{c,\text{air}}}{4})}{m + \mu}.$$

A numerical evaluation of the rank of the matrix $[\hat{B}, \hat{A}\hat{B}, \hat{A}^2\hat{B}]$, for the values of γ that the controlled stall equilibria exist, shows that the matrix has rank 3 for the range of flow of interest, implying controllability (Figure 5.2).
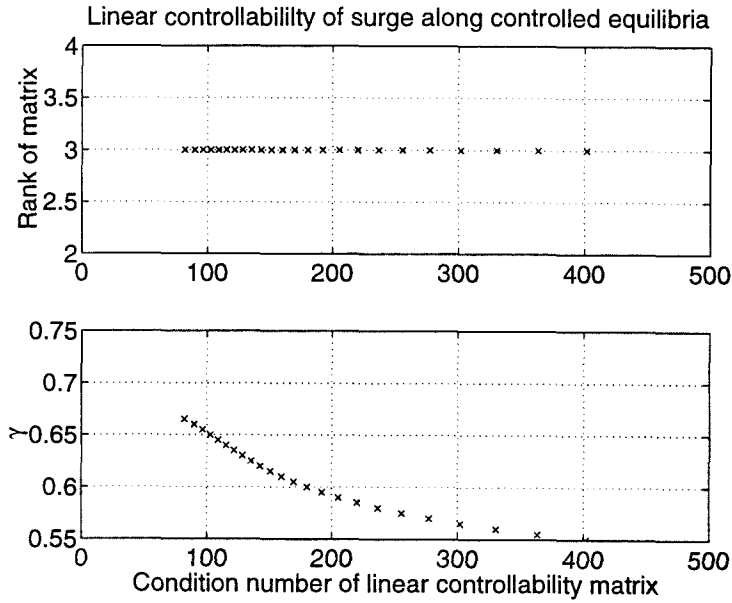
Figure 5.2 Numerical evaluation of the rank of controllability matrix along equilibria of the system with axisymmetric air injection control for stall.

5.2 Results

In this section, the results for the low and high B cases are presented. For the high B case, the results obtained via on–off and a simulated proportional axisymmetric air injection, as well as binary axisymmetric air injection for stall and a bleed valve for surge are compared.

5.2.1 Low B

A preliminary study of control of stall with axisymmetric air injection is performed by Behnken [4]. In [4], the experimental implementation of the algorithm contains a 100 Hz carrier wave and an upper and lower limit on the first mode amplitude such that, if the stall cell size is between the limits, proportional air injection in terms of the injection duty cycle is commanded. Results shows that elimination of hysteresis loop is achieved for the case where there is no overlap between the hysteresis loop of the unactuated open–loop case and the case with continuous air
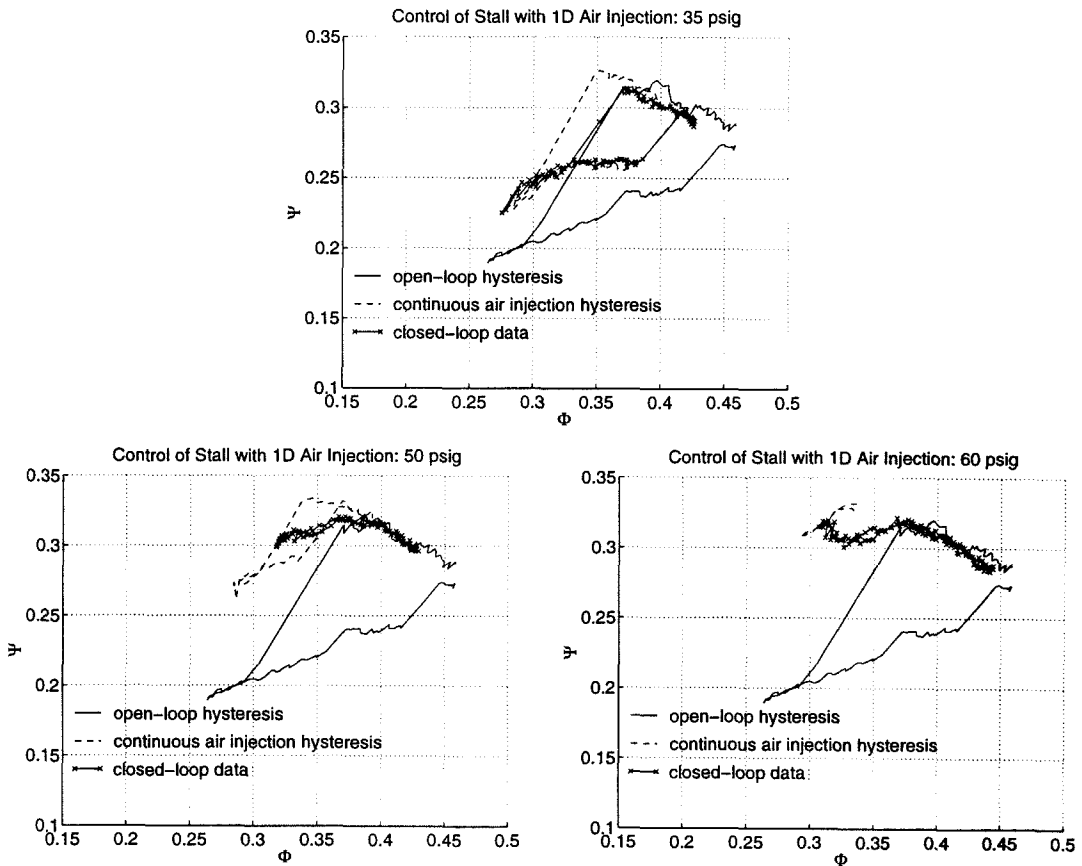
Figure 5.3 Control of stall on Caltech rig: 35 psig, 50 psig, 60 psig injector back pressure.

injection. If there is an overlap, then the system stalls, at the stall inception point of the unactuated open–loop case, to the lower branch of the hysteresis loop of the continuous air injection case, and unstalls at the point of unstall of the continuous air injection case to the stable branch of the unactuated open–loop case.

The first attempt in replicating the results in [4] uses an algorithm where only binary air injection is allowed. Three cases with different injector back pressure at 35 psig, 50 psig, and 60 psig are studied. A threshold for the stall amplitude, below which no control effort is commanded, is used. The closed–loop behavior of the system for the three cases are shown in Figure 5.3 with the hysteresis loops for the unactuated open–loop and with continuous air injection cases shown for comparison. Readers should note that the hysteresis loop for the continuous injection

cases is eliminated in the 60 psig case, while the hysteresis loops overlap between the unactuated open–loop case and the case with 35 psig continuous air injection. Similar to the results reported in [4], active control of stall is not achieved for the case where there is an overlapping region between the hysteresis loop for the unactuated open–loop case and the case with 35 psig continuous air injection. Control of stall is achieved for the 50 psig and 60 psig cases where there is no overlap.

Despite the observed evidence on the importance of overlapping of hystereses on control via axisymmetric air injection, the same conclusion is not at all clear from the model. When the control gain K in equation (5.1) is larger than K_{min} in equation (5.3), the criticality of the bifurcation is changed and the hysteresis loop is eliminated. Since K can be chosen arbitrarily large, the nominal hysteresis loop can always be eliminated regardless of whether there is overlapping.

However, there is no account for actuation limits such as magnitude and rate saturations in the model. Due to noise on the experiment, a threshold on J below which control is not activated is implemented. This threshold, along with magnitude saturation, clearly limits the largest K that can be chosen since the largest gain becomes $1/J_{thresh}$. Also, bandwidth and rate limits on the actuation are essential in determining whether the control can "catch" the system, and are further constraints when coupled with magnitude saturations.

For the results reported in this thesis, the rate limit is conjectured to be the limiting factor in the overlapping hystereses case. When the system is operating at the stall inception point, the results of the actuation must be fast enough to trap the states of the system in the region of attraction of the controlled equilibrium. Otherwise the system stalls and the control is commanded to be fully on. And since the hystereses overlap, the system would remain stalled on the stalled branch of the actuated characteristic, and unstalls at the point of unstall of the actuated characteristic.

In the non–overlapping hystereses case, however, rate limit is *not* of importance. Since the hystereses do not overlap, the characteristic can be shifted *after* the system is stalled and the system will return to stall–free operation on the actuated
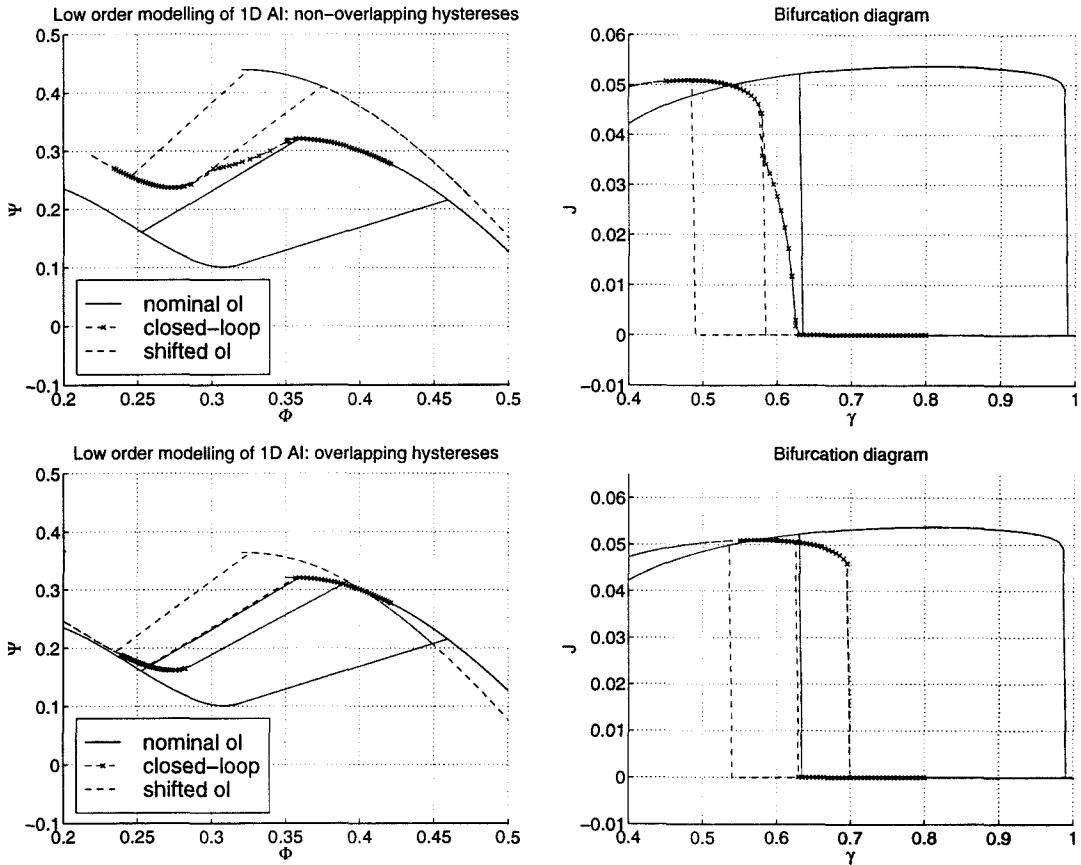
Figure 5.4 Bifurcation diagrams of axisymmetric air injection in the
Φ-Ψ and J-γ planes from simulations with magnitude and rate limit
for the non-overlapping and overlapping hystereses case on the left
and right respectively: the solid and dashed lines represent the un-
controlled unactuated and uncontrolled actuated cases respectively,
and the crosses the equilibria with control.

characteristic. This is analogous to the case for bleed valve control in which the
bleed valve magnitude limit is enough to clear the hysteresis loop.

The simulation tool is then augmented with bandwidth and rate limit capabilities
for the compressor characteristic actuation. The bifurcation diagrams in the Φ-Ψ
and J-γ planes for the non-overlapping and overlapping hystereses are shown, on the
left and right respectively, in Figure 5.4, with the solid and dashed lines representing
the uncontrolled unactuated and uncontrolled actuated cases respectively, and the
crosses the equilibria with control.
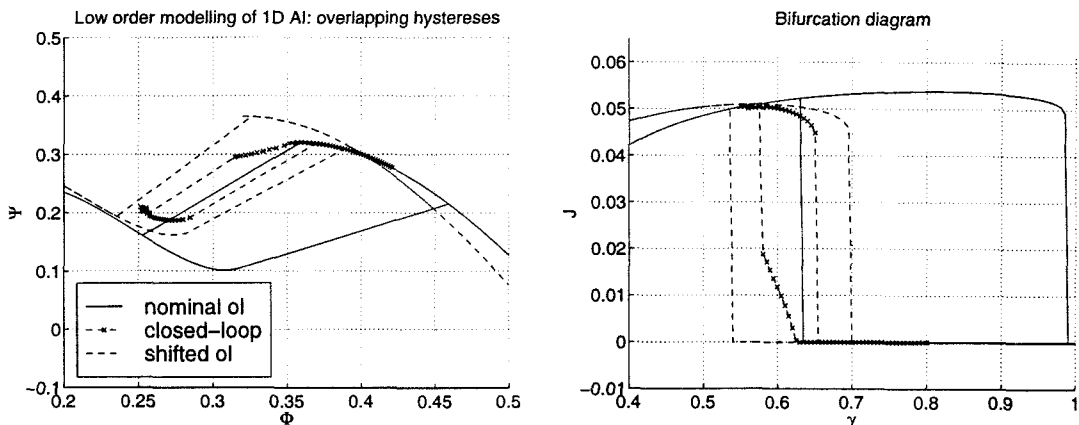
Figure 5.5 Bifurcation diagrams of axisymmetric air injection in the
Φ–Ψ and J–γ planes for the overlapping hystereses case with less rate
limit: the solid and dashed lines represent the uncontrolled unactu-
ated and uncontrolled actuated cases respectively, and the crosses the
equilibria with control.

For the case where the hysteresis loops in the actuated and unactuated cases
have an overlapping region, the actuation is rate limited with the same rate limit
imposed on the non–overlapping hystereses case[2]. These results are consistent with
their experimental counterparts reported in Behnken [4]. For comparison to the
theory, less rate limit is imposed on the overlapping hystereses case until partial
elimination of the hysteresis is achieved (Figure 5.5).

For the compressor characteristics used in the simulations, the rate requirement
(i.e. $\tilde{u}_{mag}/\tilde{u}_{rate}$ in Section 5.1.1) obtained from MG3 simulations for an 8.7% ex-
tension of operable region is approximately 111 units in nondimensional time while
that computed from equation (5.5) for the same amount of extension with a 2%
noise in J is approximately 123 units.

5.2.2 High B

In this subsection, the results for surge control only is presented first, followed by
those for simultaneous stall and surge stabilization.

---

[2]For applications on the Caltech rig, this is consistent with the experimental setting since the
non–overlapping case requires air injection at a higher velocity, which intuitively results in at least
the same rate limit as in the overlapping case.
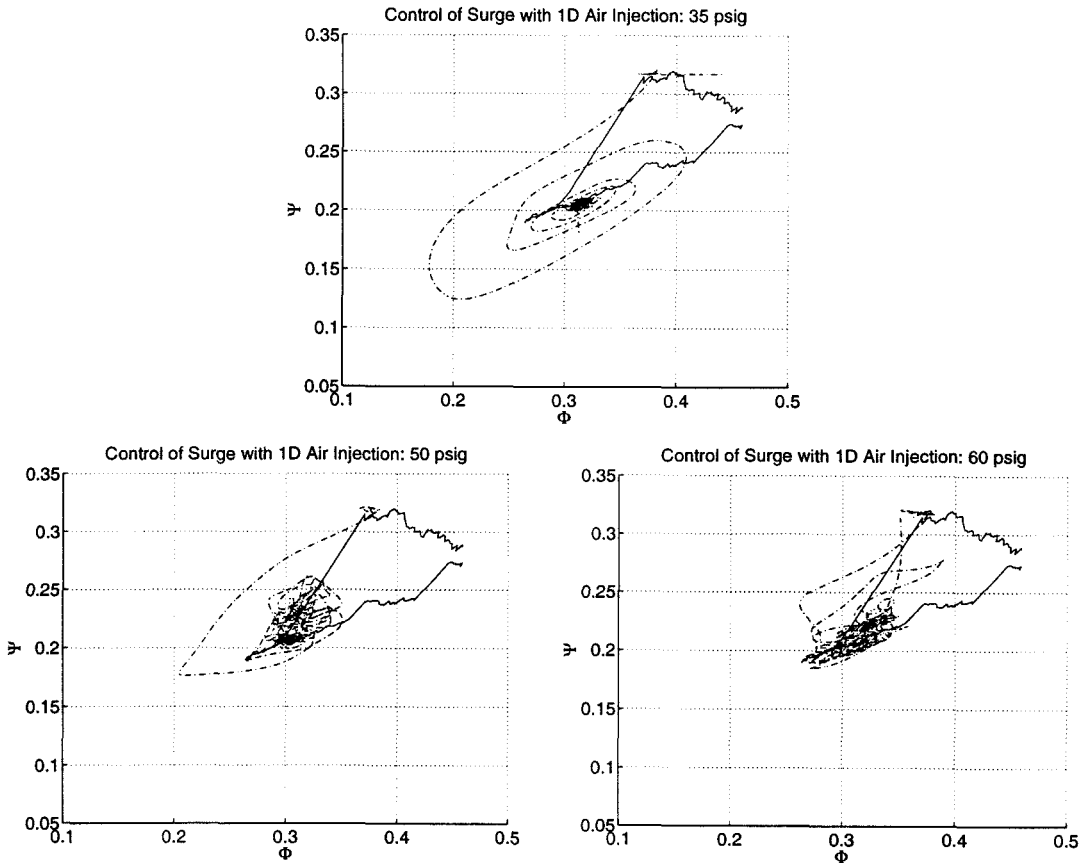
Figure 5.6 Control of surge on Caltech rig: 35 psig, 50 psig, 60 psig injector back pressure.

A surge control algorithm using a feedback on $\dot{\Phi}$ is implemented for surge control only. The algorithm consists of a threshold for $\dot{\Phi}$, set to be negative, above which no control effort is commanded. The first attempt of the algorithm allows binary air injection only. In all of the three cases studied, surge is eliminated and the system stalled as expected, since a control algorithm for stall is not implemented. Figure 5.6 shows the results of the controlled surge inception events with the injector back pressure at 35, 50, and 60 psig.

A combined algorithm of stall and surge control is implemented. The algorithm commands the injectors to inject air axisymmetrically when stall and/or surge is detected. For the cases of 50 psig and 60 psig injector back pressure, the system is stable without stall or surge. For the 35 psig case, the system stalls due to the
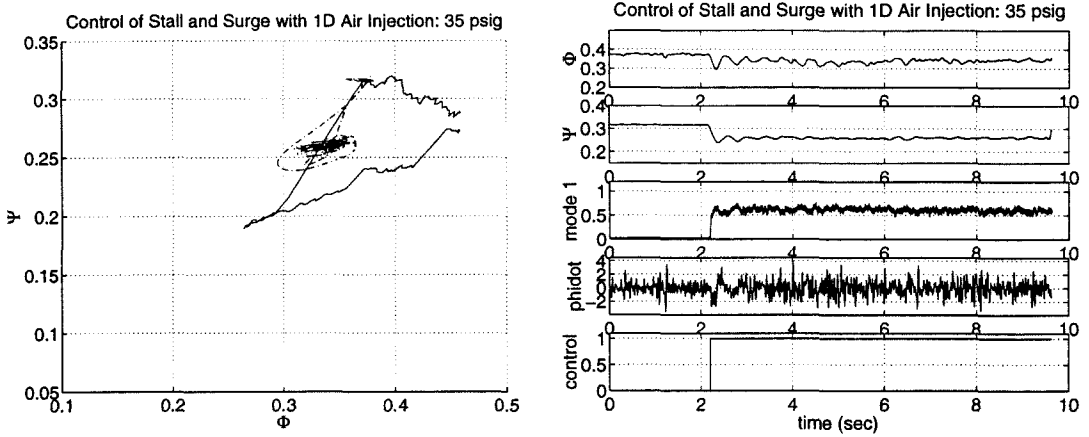
Figure 5.7 Control of stall and surge on Caltech rig: 35 psig injector
back pressure.

inability of stall control. Figure 5.7, 5.8, and 5.9 show the dynamic response of
the system in the flow–pressure plane and the time series of the Φ, Ψ, A_1, $\dot{\Phi}$, and
commanded jets data for 35 psig, 50 psig, and 60 psig injector back pressure settings
respectively.

A modification to the code is made to simulate proportional injection. Similar
to the implementation found in Behnken [4], an upper and a lower limit on the first
mode amplitude associated with pressure perturbation as well as $\dot{\Phi}$ are introduced.
The duty cycle of the injection mechanism is modified online according to the size
of the detected stall and $\dot{\Phi}$ amplitudes according to the following, with A_u and A_l
representing the upper and lower limit of A, and $\dot{\Phi}_u$ and $\dot{\Phi}_l$ representing the upper
and lower limit of $\dot{\Phi}$ respectively.

$$\text{duty cycle} = \begin{cases} 1 & (A > A_u) \text{ or } (\dot{\Phi} < \dot{\Phi}_u), \\[2mm] \frac{A-A_l}{A_u-A_l} + \frac{\dot{\Phi}-\dot{\Phi}_u}{\dot{\Phi}_l-\dot{\Phi}_u} & (A_u > A > A_l) \text{ and } (\dot{\Phi}_l > \dot{\Phi} > \dot{\Phi}_u), \\[2mm] \frac{A-A_l}{A_u-A_l} & (A_u > A > A_l) \text{ and } (\dot{\Phi}_l < \dot{\Phi}), \\[2mm] \frac{\dot{\Phi}-\dot{\Phi}_u}{\dot{\Phi}_l-\dot{\Phi}_u} & (A < A_l) \text{ and } (\dot{\Phi}_l > \dot{\Phi} > \dot{\Phi}_u), \\[2mm] 0 & (A < A_l) \text{ and } (\dot{\Phi}_l < \dot{\Phi}). \end{cases}$$
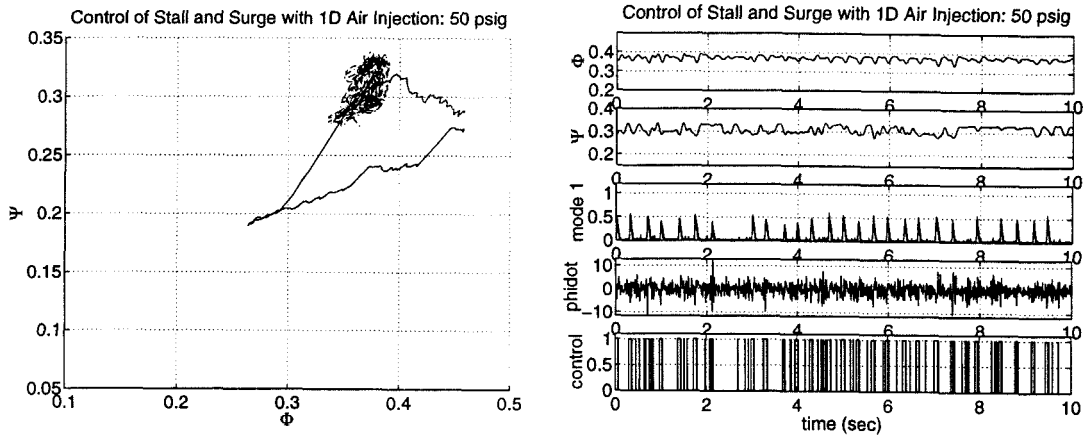
Figure 5.8 Control of stall and surge on Caltech rig: 50 psig injector back pressure.
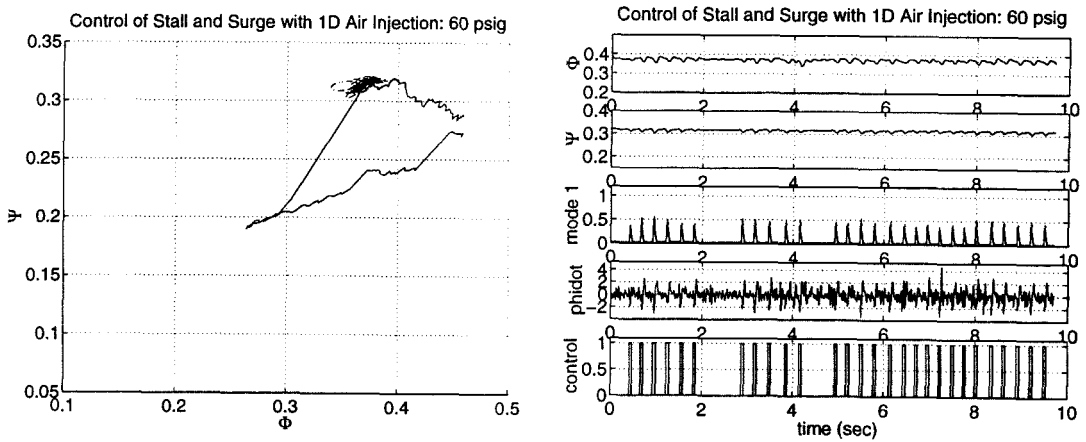
Figure 5.9 Control of stall and surge on Caltech rig: 60 psig injector back pressure.

This implementation allows a simulated proportional injection. In this case, the *effective* bandwidth of the actuation becomes important. The bandwidth of the binary injectors is approximately 200 Hz. The bandwidth of the *actuation*, however, is considerably less than that because of the various delays (electronic, software, air supply response, etc.) in the system and the fact that there is a delay in the response of the compression system to the actuation, that is, the shifting of the compressor characteristic takes time. Initial attempts in implementing the simulated proportional injection algorithm failed due to inappropriately chosen upper and lower limits for A and $\dot{\Phi}$. The choice of A_l and $\dot{\Phi}_l$ are the same as thresholds for A and $\dot{\Phi}$ respectively. The initial choices of A_u and $\dot{\Phi}_u$ are the maximum of A and minimum of $\dot{\Phi}$ respectively observed in the unactuated open–loop case. This proves to give too wide of a range over which the duty cycle has to be proportionally computed against, and the resulting duty cycle is often too small for the air injection to have a significant enough effect for the purposes of control of stall and surge. After modifying the limits to significantly reduce the range of proportional control in A and $\dot{\Phi}$ (essentially changing the gain), results similar to that shown in Figures 5.7, 5.8, and 5.9 for 35 psig, 50 psig, and 60 psig injector back pressure settings respectively are obtained, except for the stall control case. Figure 5.10 shows the closed–loop surge only and stall only control, and Figure 5.11 the dynamic data during closed–loop operation at surge inception point for 50 psig injector back pressure. A comparison of Figure 5.8 and Figure 5.10 shows that, in the stall only case, the hysteresis loop in the proportional case is eliminated but the equilibrium locations are different than the binary case.

Control of stall using axisymmetric air injection and surge using a slow bleed valve (with a feedback on $\dot{\Phi}$) is also implemented (Figure 5.12). A comparison of Figure 5.8 and 5.12 shows that the fluctuation in flow is greater while that in pressure is less in the latter case.
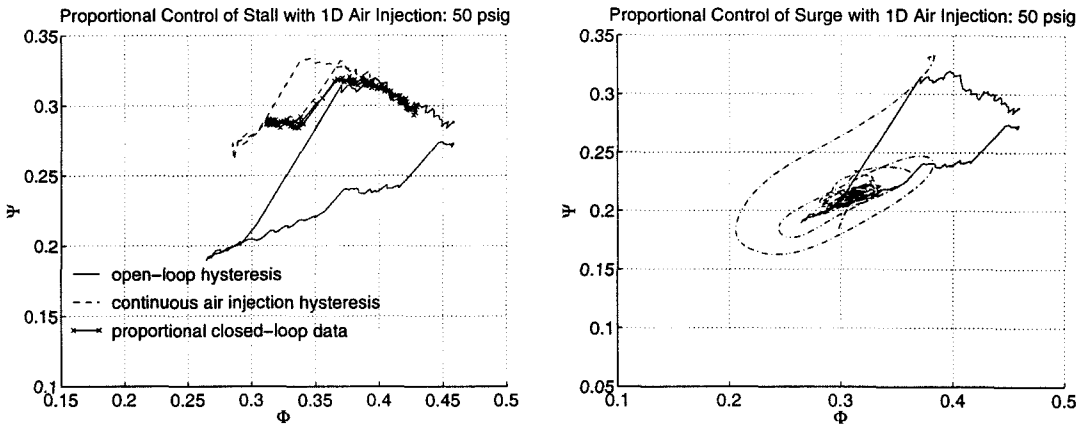
Figure 5.10 Proportional control of stall only and surge only on Caltech rig: 50 psig injector back pressure.
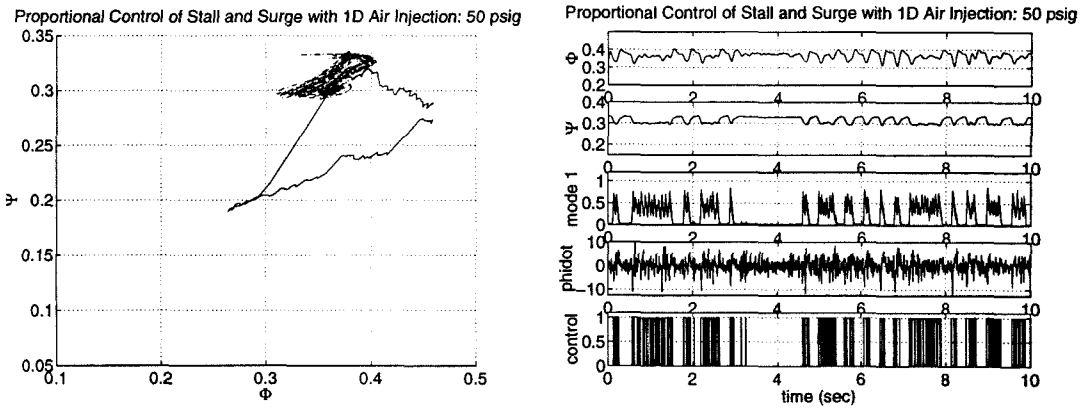
Figure 5.11 Proportional control of stall and surge on Caltech rig: surge inception point operation at 50 psig injector back pressure.
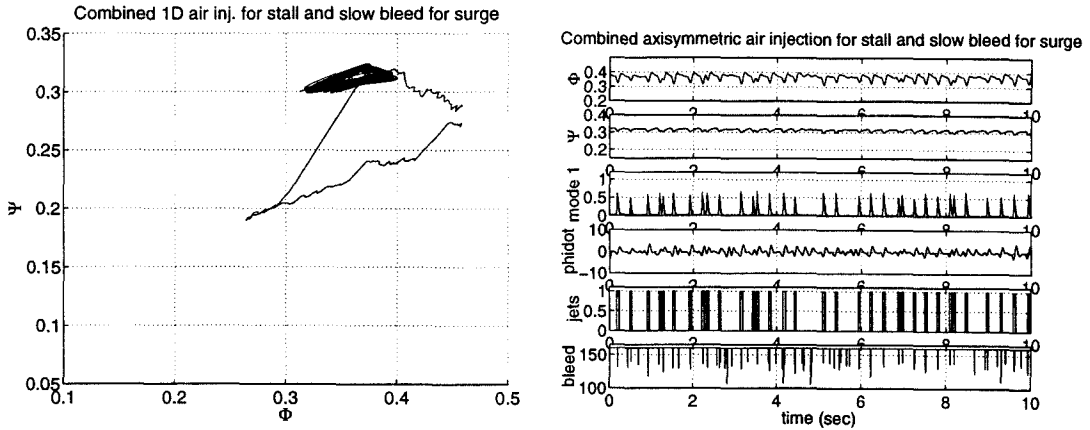
Figure 5.12 Combined axisymmetric air injection for stall and slow bleed for surge on Caltech rig: 50 psig injector back pressure.

5.3 Conclusion

Control of stall and surge is achieved on the Caltech rig with axisymmetric air injection. The injector back pressure are set at 35 psig, 50 psig, and 60 psig as the three cases studied. Stall only control with A feedback and binary air injection is achieved for 50 psig and 60 psig but not 35 psig where the hysteresis loop of the unactuated open–loop case overlaps with that in the case with 35 psig continuous air injection. Surge control with $\dot{\Phi}$ feedback and binary air injection is achieved in all three cases. Proportional air injection is simulated and results are similar to those of the binary case.

A number of things are of future research interest. The experiments reported in this thesis are carried out at fixed physical location at three different pressure settings. A full parametric study in terms of the axial, radial, and circumferential position of the injectors, and injector back pressure can identify the "optimal" axisymmetric air injection stall–surge controller. Also, while some preliminary theoretical work has been carried out to investigate the effects of the rate limit of the actuation, the qualitative as well as quantitative reliability of the formulas needs to be addressed, via a validation against experiments for instance.

Given the possibility of stall and surge control with both bleed valves and air

injection, various combinations of the actuation mechanisms can be studied. Examples of such combinations include

- control of stall with 2–D pulsed air injection and surge with 1–D axisymmetric air injection, and

- control of stall with 1–D bleed valve with continuous air injection and surge with 1–D axisymmetric air injection.

The more general and interesting issue is the trade–off between the various actuation mechanisms and hence, the issue of actuator allocation. The difference between the results from the two realizations of axisymmetric air injection control of stall and surge, as well as that between control of surge using air injection and a bleed valve confirms the need for further investigations. In a multi–stage compressor with redundant sets of actuators, this issue becomes particularly important.

Chapter 6

Non–axisymmetric Air Injection

Aside from an axisymmetric usage, air injection can also be implemented in a non–axisymmetric fashion. For control of rotating stall, various implementations of non–axisymmetric air injection have been used, with very different results qualitatively and quantitatively. The two main types reported in literature are the extension of stall–free operation (e.g. Vo [92] and Weigl [95]), and the elimination of hysteresis loop (e.g. Behnken [4] and D'Andrea et al. [12]).

Since the physical actuation is the same in all of the implementations, namely, air injection, it is logical to expect a common starting model to exist. Furthermore, the qualitative differences are expected to originate from the form of the control law, and the quantitative from the particular applications. Due to the qualitative differences, one implementation may be more favorable than another in certain circumstances and vice versa.

The goal of this chapter is to provide a unified view of non–axisymmetric air injection control of rotating stall and surge. Control–theoretic models in terms of "implementation–oriented" variables such as number of injectors is used for analysis as well as synthesis. Control–oriented modeling of air injection in axial flow compressors, in the context of the Moore–Greitzer model [37, 65], is given in Section 6.1. The derivation of low order models for three existing algorithms found in literature, namely, a uni–directional pulsed algorithm [4, 12], and bi– and uni–directional proportional harmonic control [92, 95, 96], are described in Section 6.2, 6.3, and
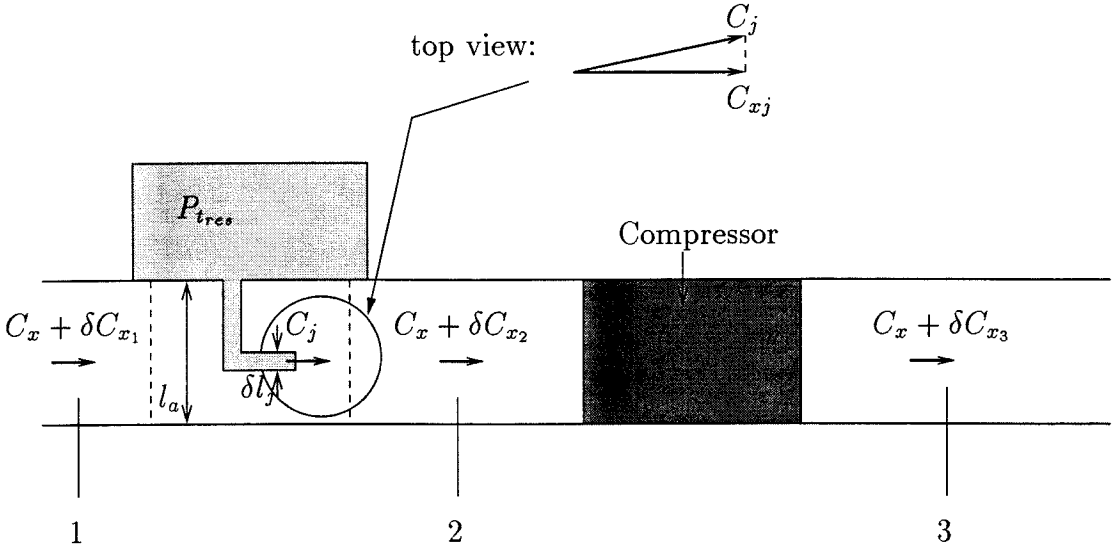
Figure 6.1 Mass and momentum addition by air injection.

6.4 respectively. Using the low order models, a theoretical comparison between the various non–axisymmetric implementation is made in Section 6.5 to explore the pros and cons associated with the techniques in the context of operability. Some conclusions and remarks in Section 6.6 will end the chapter.

6.1 Modeling

To incorporate non–axisymmetric air injection in a compression system model, the mass, momentum, as well as compressor performance effects must be taken into account properly. Readers are referred to Section 2.4 for details.

The relevant picture is displayed in Figure 2.3 which is repeated in this section. The mass balance between stations 1 and 2 is given by

$$\rho l_a(C_x + \delta C_{x_1}) + \rho \delta l_j C_j = \rho l_a(C_x + \delta C_{x_2}),$$

where ρ denotes the density of air, l_a the annular radius, C_x the mean axial velocity, δC_{x_i} the axial velocity perturbation at station i, δl_j the distance of opening of the injector in the plane normal to the axial direction, C_j the injected velocity, and l_a

the radial distance of annulus. The momentum balance is given by

$$l_a(P + \delta p_1) + \rho l_a(C_x + \delta C_{x_1})^2 + \rho \delta l_j C_{xj}^2 = l_a(P + \delta p_2) + \rho l_a(C_x + \delta C_{x_2})^2,$$

where P denotes the static pressure, δp_i the static pressure perturbation at station i, and C_{xj} the magnitude of axial component of injected velocity. The total–to–static pressure between stations 1 and 3 can be non–dimensionalized and expressed as

$$\frac{p_3 - p_{t_1}}{\rho U^2} = \Psi_c(\phi_2, \Phi_j) - \lambda \frac{\partial \phi_2}{\partial \theta} - \mu \frac{\partial \phi_2}{\partial \xi} + \frac{\delta l_j}{l_a}(\Phi_{xj}^2 - (\Phi + \delta \phi_1)\Phi_j) - \frac{1}{2}(\frac{\delta l_j}{l_a}\Phi_j)^2,$$

where p_i denotes the static pressure at station i, p_{t_i} the total pressure at station i, $\phi_i = \Phi + \delta \phi_i$ the nondimensional axial velocity at station i, U the mean rotor speed, Ψ_c the compressor characteristic, $\Phi_j = C_j/U$ the nondimensional injected velocity, $\delta \phi_i = \delta C_{x_i}/U$ the nondimensional flow perturbation at station i, λ the rotor inertia parameter, θ the circumferential angle, μ the fluid inertia parameter, $\xi = tU/R$ the nondimensional time where t is the time and R the mean rotor radius, and $\Phi_{xj} = C_{xj}/U$ the nondimensional injected velocity in the axial direction.

It should be noted that the term $\Psi_c(\phi_2, \Phi_j)$ is *not* the nominal open–loop compressor characteristic evaluated at ϕ_2, but a shifted one (see Section 2.4 for details). With the usual nondimensionalization, the following PDE is obtained:

$$\begin{aligned} \Psi &= \Psi_c(\phi_2, \Phi_j) - l_c\frac{d\Phi}{d\xi} - \lambda\frac{\partial \delta\phi_2}{\partial \theta} - \mu\frac{\partial \delta\phi_2}{\partial \xi} - m\frac{\partial \delta\phi_2}{\partial \xi} + \frac{\delta l_j}{l_a}(\Phi_{xj}^2 - (\Phi + \delta\phi_1)\Phi_j) \\ &\quad - \frac{1}{2}(\frac{\delta l_j}{l_a}\Phi_j)^2, \end{aligned} \tag{6.1}$$

where $\delta\phi_2 = \delta\phi_1 + \frac{\delta l_j}{l_a}\phi_j$, l_c the nondimensional effective length of the compressor, and m the throttle exit parameter. Taking $\delta l_j/l_a = 1$, approximating Φ_{xj} with Φ_j, and defining actuation $u_j = \frac{\delta l_j}{l_a}\Phi_j$, we have

$$\begin{aligned} \Psi &= \hat{\Psi}_c(\Phi + \delta\phi_2, \Phi_j) - l_c\frac{d\Phi}{d\xi} - \lambda\frac{\partial \delta\phi_2}{\partial \theta} - \mu\frac{\partial \delta\phi_2}{\partial \xi} - m\frac{\partial \delta\phi_2}{\partial \xi} + \\ &\quad u_j(\Phi_j - (\Phi + \delta\phi_1)) - \frac{1}{2}u_j^2, \end{aligned} \tag{6.2}$$

where $\hat{\Psi}_c = \Psi_{c,\text{nom}} + \Psi_{c,\text{shifted}}$, and $\Psi_{c,\text{shifted}}$ is the contribution due to a change of the losses in the compressor cascade as a result of air injection. For simplicity, $\Psi_{c,\text{shifted}}$ is approximated as $\frac{l_a u_j}{\delta l_j \Phi_j} \Psi_{c,\text{air}}$ for $\Phi_j > 0$, where $\Psi_{c,\text{air}}$ is the contribution from air injection if commanded to give full and steady actuation, since no air injection implies no contribution. The notation is also simplified by using $\Psi_c = \Psi_{c,\text{nom}}$ and $\Psi_{ai} = \Psi_{c,\text{air}}$. In summary, $\hat{\Psi}_c \approx \Psi_c + \frac{l_a u_j}{\delta l_j \Phi_j} \Psi_{ai}$.

To arrive to a set of ODEs from equation (6.2), the perturbation $\delta\phi_1$ is assumed to take the form:

$$\delta\phi_1 = A(\xi)\sin(\theta - r(\xi)),$$

where $A(\xi)$ denotes the amplitude and $r(\xi)$ the phase angle of the flow perturbation. The annulus average

$$l_c \frac{d\Phi}{d\xi} + \Psi = \int_0^{2\pi} \left[\hat{\Psi}_c(\Phi + \delta\phi_2, \Phi_j) - \lambda \frac{\partial \delta\phi_2}{\partial\theta} - \mu\frac{\partial\delta\phi_2}{\partial\xi} - m\frac{\partial\delta\phi_2}{\partial\xi} + \right.$$
$$\left. u_j\big(\Phi_j - (\Phi + \delta\phi_1)\big) - \frac{1}{2}u_j^2 \right] d\theta,$$

and sine moment

$$0 = \int_0^{2\pi} \left[\hat{\Psi}_c(\Phi + \delta\phi_2, \Phi_j) - l_c\frac{d\Phi}{d\xi} - \lambda\frac{\partial\delta\phi_2}{\partial\theta} - \mu\frac{\partial\delta\phi_2}{\partial\xi} - m\frac{\partial\delta\phi_2}{\partial\xi} + \right.$$
$$\left. u_j\big(\Phi_j - (\Phi + \delta\phi_1)\big) - \frac{1}{2}u_j^2 \right] \sin(\theta - r)d\theta$$

of (6.2) can be computed and the equations for $\dot{\Phi}$ and $\dot{A}$ or $\dot{J}$ obtained respectively. To realize various control laws with discrete injectors, we note that the control u_j is fixed in θ. Integration over θ is then separated into the regions with and without injectors. For simplicity, a flat injection profile is assumed throughout the rest of the chapter.
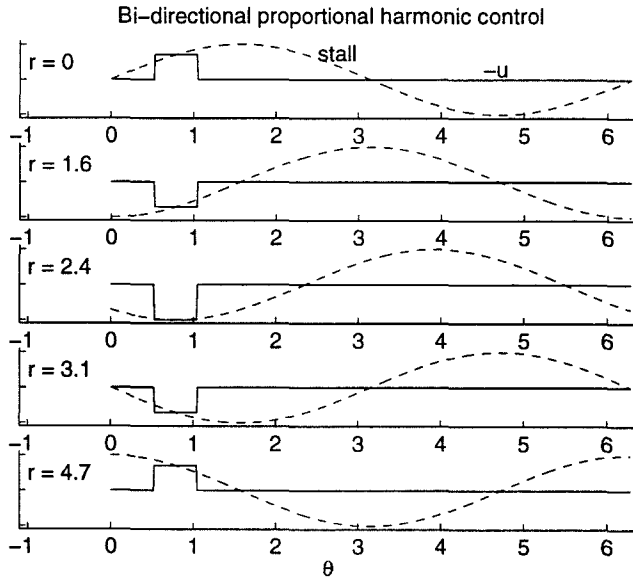
Figure 6.2 Control action of bi–directional proportional harmonic control relative to stall cell; dashed line represents the stall cell and solid the control.

6.2 Bi–directional Harmonic Control

In this section, a bi–directional proportional harmonic control algorithm proposed by Vo [92] and Weigl [95] is described. The derivation of a low order model is given first, followed by a comparison of the model to a high fidelity simulation.

6.2.1 Low Order Model

For the case of bi–directional harmonic control with one harmonic feedback, the control law takes the form

$$u_j(A, \theta, r) = -A(\xi) \sin(\theta_i - r), \tag{6.3}$$

where θ_i is the center of an injector with width w. Figure 6.2 illustrates the control action relative to the stall cell.

The annulus average is written as the following:

$$l_c\dot{\Phi} + \Psi = \int_{\text{w/ injectors}} \left(\hat{\Psi}_c(\Phi + \delta\phi_2, \Phi_j) - l_c\frac{d\Phi}{d\xi} - \lambda\frac{\partial\delta\phi_2}{\partial\theta} - \mu\frac{\partial\delta\phi_2}{\partial\xi} - m\frac{\partial\delta\phi_2}{\partial\xi} + \right.$$

$$\left. u_j\left(\Phi_j - (\Phi + \delta\phi_1)\right) - \frac{1}{2}u_j^2 \right) d\theta +$$

$$\int_{\text{w/ no injectors}} \left(\Psi_c(\Phi + \delta\phi_1) - l_c\frac{d\Phi}{d\xi} - \lambda\frac{\partial\delta\phi_1}{\partial\theta} - \mu\frac{\partial\delta\phi_1}{\partial\xi} - m\frac{\partial\delta\phi_1}{\partial\xi} \right) d\theta,$$

and the sine moment analogously.

Proposition 6.2.1 Consider a compressor with k injectors with width w each, such that $kw \leq 2\pi$, and the injectors evenly distributed along the annulus of the compressor. Given the PDE model in equation (6.2) and control law (6.3), the Galerkin projection onto the first harmonic results in the closed–loop $\dot{\Phi}$ and $\dot{J}$ equations with the following form:

$$l_c\dot{\Phi} = \Psi_c - \Psi + a_1 J\Psi_c'' + a_2 J + a_3\frac{J}{\Phi_j}\Psi_{ai}' + a_4\frac{J^2}{\Phi_j}\Psi_{ai}''',$$

$$\frac{m+\mu}{2J}\dot{J} = b_1\Psi_c' + b_2 J\Psi_c''' + b_3(\Phi - \Phi_j) + b_4\frac{\Psi_{ai}}{\Phi_j} + b_5\frac{J}{\Phi_j}\Psi_{ai}'', \qquad (6.4)$$

where

$$a_1 = \frac{1}{4} + \frac{kw}{8\pi} - \frac{k}{2\pi}\sin\left(\frac{w}{2}\right),$$

$$a_2 = -\frac{kw}{8\pi} + \frac{k}{2\pi}\sin\left(\frac{w}{2}\right),$$

$$a_3 = \frac{kw}{4\pi} - \frac{k}{2\pi}\sin\left(\frac{w}{2}\right),$$

$$a_4 = \frac{3kw}{32\pi} + \frac{k}{32\pi}\sin w - \frac{k}{4\pi}\sin\left(\frac{w}{2}\right),$$

$$b_1 = 1 - \frac{k}{\pi}\sin\left(\frac{w}{2}\right),$$

$$b_2 = \frac{1}{8} + \frac{kw}{8\pi} - \frac{k}{2\pi}\sin\left(\frac{w}{2}\right) + \frac{k}{16\pi}\sin(w),$$

$$b_3 = \frac{k}{\pi}\sin\left(\frac{w}{2}\right),$$

$$b_4 = -\frac{k}{\pi}\sin\left(\frac{w}{2}\right),$$

$$b_5 = \frac{k}{8\pi}\sin w + \frac{kw}{4\pi} - \frac{3k}{4\pi}\sin\left(\frac{w}{2}\right).$$

The derivation is as follows. Assume that there are k injectors with width w each such that $kw \leq 2\pi$, and that the injectors are evenly distributed along the annulus. Furthermore, assume that the control law is given by equation (6.3). Let θ_i denote the center of the ith injector, and a control law given by $u_j = -A(\xi) \sin(\theta_i - r)$. By accounting for the regions with and without injectors, the annulus average of equation (6.2) can be found from the following.

$$
\begin{aligned}
l_c \dot{\Phi} + \Psi &= \frac{1}{2\pi} \left[\int_0^{\theta_1 - \frac{w}{2}} \left(\Psi_c(\Phi + \delta\phi_1) - \lambda \frac{\partial \delta\phi_1}{\partial \theta} - \mu \frac{\partial \delta\phi_1}{\partial \xi} - m \frac{\partial \delta\phi_1}{\partial \xi} \right) d\theta + \right. \\
&\quad \sum_{i=1}^{k} \int_{\theta_i - \frac{w}{2}}^{\theta_i + \frac{w}{2}} \left(\hat{\Psi}_c(\Phi + \delta\phi_2, \Phi_j) - \lambda \frac{\partial \delta\phi_2}{\partial \theta} - \mu \frac{\partial \delta\phi_2}{\partial \xi} - m \frac{\partial \delta\phi_2}{\partial \xi} + \right. \\
&\quad \left. u_j \left(\Phi_j - (\Phi + A \sin(\theta - r)) \right) - \frac{1}{2} u_j^2 \right) d\theta + \\
&\quad \sum_{i=1}^{k-1} \int_{\theta_i + \frac{w}{2}}^{\theta_{i+1} - \frac{w}{2}} \left(\Psi_c(\Phi + \delta\phi_1) - \lambda \frac{\partial \delta\phi_1}{\partial \theta} - \mu \frac{\partial \delta\phi_1}{\partial \xi} - m \frac{\partial \delta\phi_1}{\partial \xi} \right) d\theta + \\
&\quad \left. \int_{\theta_k + \frac{w}{2}}^{2\pi} \left(\Psi_c(\Phi + \delta\phi_1) - \lambda \frac{\partial \delta\phi_1}{\partial \theta} - \mu \frac{\partial \delta\phi_1}{\partial \xi} - m \frac{\partial \delta\phi_1}{\partial \xi} \right) d\theta \right],
\end{aligned}
$$

where $\delta\phi_2 = \delta\phi_1 + u_j$ and $\delta\phi_1 = A \sin(\theta - r)$.

The contributions from the regions with and without injectors evaluate to the following using Maple [90]:

$$
\begin{aligned}
&\int_0^{\theta_1 - \frac{w}{2}} \left(\Psi_c(\Phi + \delta\phi_1) - \lambda \frac{\partial \delta\phi_1}{\partial \theta} - \mu \frac{\partial \delta\phi_1}{\partial \xi} - m \frac{\partial \delta\phi_1}{\partial \xi} \right) d\theta + \\
&\sum_{i=1}^{k-1} \int_{\theta_i + \frac{w}{2}}^{\theta_{i+1} - \frac{w}{2}} \left(\Psi_c(\Phi + \delta\phi_1) - \lambda \frac{\partial \delta\phi_1}{\partial \theta} - \mu \frac{\partial \delta\phi_1}{\partial \xi} - m \frac{\partial \delta\phi_1}{\partial \xi} \right) d\theta + \\
&\int_{\theta_k + \frac{w}{2}}^{2\pi} \left(\Psi_c(\Phi + \delta\phi_1) - \lambda \frac{\partial \delta\phi_1}{\partial \theta} - \mu \frac{\partial \delta\phi_1}{\partial \xi} - m \frac{\partial \delta\phi_1}{\partial \xi} \right) d\theta \\
&= \left(\Psi_c + \frac{J}{4} \Psi_c'' \right) (2\pi - kw), \\
&\sum_{i=1}^{k} \int_{\theta_i - \frac{w}{2}}^{\theta_i + \frac{w}{2}} \left(\hat{\Psi}_c(\Phi + \delta\phi_2, \Phi_j) - \lambda \frac{\partial \delta\phi_2}{\partial \theta} - \mu \frac{\partial \delta\phi_2}{\partial \xi} - m \frac{\partial \delta\phi_2}{\partial \xi} + \right. \\
&\quad \left. u_j \left(\Phi_j - (\Phi + A \sin(\theta - r)) \right) - \frac{1}{2} u_j^2 \right) d\theta
\end{aligned}
$$

$$= k \left(w\Psi_c + w\frac{J}{2}\Psi_c'' - w\Psi - w\frac{J}{4} + J \sin(\frac{w}{2}) - J\Psi_c'' \sin(\frac{w}{2}) + \frac{J}{2\Phi_j}\Psi_{ai}'w - \right.$$
$$\left. \frac{J}{\Phi_j}\Psi_{ai}' \sin(\frac{w}{2}) - \frac{J^2}{2\Phi_j}\Psi_{ai}''' \sin(\frac{w}{2}) + \frac{3J^2}{16\Phi_j}\Psi_{ai}'''w + \frac{J^2}{16\Phi_j}\Psi_{ai}''' \sin w \right),$$

which, after the summation and reorganization, give

$$l_c\dot{\Phi} = \Psi_c - \Psi + \left(\frac{1}{4} + \frac{kw}{8\pi} - \frac{k}{2\pi} \sin(\frac{w}{2})\right) J\Psi_c'' + \left(\frac{k}{2\pi} \sin(\frac{w}{2}) - \frac{kw}{8\pi}\right) J +$$
$$\left(\frac{kw}{4\pi} - \frac{k}{2\pi} \sin(\frac{w}{2})\right) \frac{J}{\Phi_j}\Psi_{ai}' + \left(\frac{3kw}{32\pi} + \frac{k}{32\pi} \sin w - \frac{k}{4\pi} \sin(\frac{w}{2})\right) \frac{J^2}{\Phi_j}\Psi_{ai}'''.$$

Similarly, the sine moment of equation (6.2) can be computed and $\dot{J}$ equation in (6.4) verified.

Given equation (6.4), the linear stability condition is given by

$$\frac{k}{\pi} \sin(\frac{w}{2}) > \frac{\Phi_j\Psi_c'}{\Phi_j\Psi_c' + \Phi_j^2 - \Phi_j\Phi + \Psi_{ai}} \qquad \text{for } \gamma < \gamma^*, \text{ and } \Phi_j > 0, \tag{6.5}$$

and the supercritical stall bifurcation condition is

$$0 > \frac{2\gamma\Psi\Phi_j\omega}{-2(\Phi\Phi_j^2 b_2\Psi_c''' + \Phi\Phi_j b_5\Psi_{ai}'') - \gamma^2\omega(a_1\Phi_j\Psi_c'' + a_2\Phi_j + a_3\Psi_{ai}')}\Big|_{x=x^*},$$
$$\omega = b_1\Phi_j\Psi_c'' + b_3\Phi_j + b_4\Psi_{ai}',$$

for $\Phi_j > 0$, where $x = \gamma, \Phi, \Psi, J$ and $J^* = 0$.

For a fixed value of k or w, the left–hand–side of the linear stability condition (6.5) is a monotonically increasing function for increasing w or k. As a result, a full coverage, i.e. $kw = 2\pi$, offers the most desired condition. Going further, the left–hand–side of (6.5) for a fixed value of $kw = 2\pi$ is also a monotonically increasing function for increasing values of k. Therefore, the most favorable configuration for linear stability extension is a high number of injectors k with a small width w.

6.2.2 High Fidelity Simulation

Using the collocated model proposed by Mansoux et al. [59] with realistic effects such as unsteady loss dynamics [39] and actuator dynamics, a high fidelity simulation
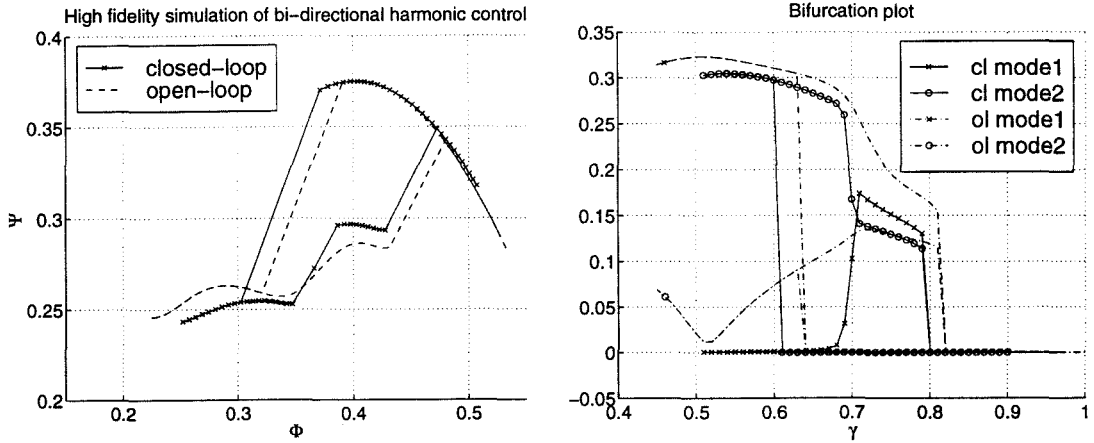
Figure 6.3 High fidelity simulation of a bi–directional proportional harmonic control.

is developed. Figure 6.3 shows a typical simulation with the Caltech compressor parameters. As shown in the figure, the controller is able to stabilize the nominally unstable equilibria past the peak of the compressor characteristic. However, at a value of approximately $\Phi = 0.37$, the second harmonic loses stability, and the system stalls and suffers a hysteresis. This is consistent with experimental observations reported in Vo [92] and Weigl [95].

Multiple simulations are performed to validate the linear stability condition in equation (6.5). By varying k, w, and Φ_j in both equation (6.5) and the simulation, a percentage of stability extension in Φ is obtained from each tool. Figure 6.4 shows a plot of the percentage of stability extension predicted by the formula obtained from the low order model and that from the high fidelity simulation. As shown in the figure, the formula obtained from the low order model shares the same qualitative trend to the simulation. The formula fails to match the simulation results quantitatively due to the absence of actuator dynamics and other realistic effects in the derivation of the low order models.
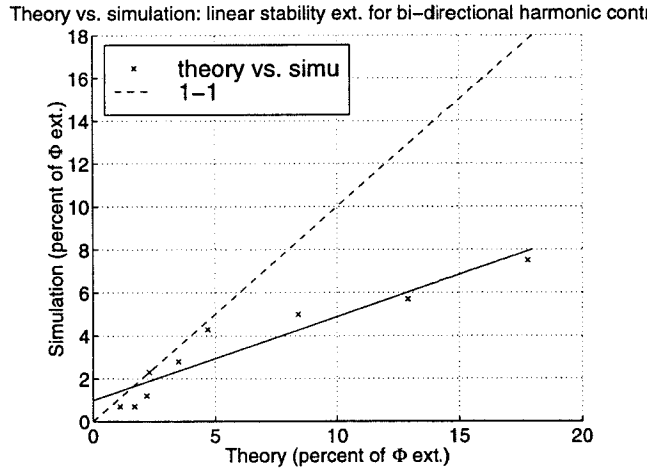
Figure 6.4 Comparison of low order model to high fidelity simulation: percentage of linear stability extension predicted by low order model vs. simulation.

6.3   Uni–directional Harmonic Control

In this section, a uni–directional proportional harmonic control algorithm is described. Similar to the bi–directional case, a low order model is described first, followed by a high fidelity simulation tool.

6.3.1   Low Order Model

For the case of uni–directional harmonic control with one harmonic feedback, the control law takes the form

$$u_j(A, \theta, r) = -A(\xi) \sin(\theta_i - r) \geq 0, \tag{6.6}$$

where θ_i is the center of an injector with width w. Figure 6.5 illustrates the control action relative to the stall cell.

In this case, the integration over θ is treated in a similar way as in the bi–directional case, with the distinction that the regions with injectors may not be actuated if a negative control effort is commanded. The annulus average is written

Figure 6.5 Control action of uni–directional proportional harmonic control relative to stall cell; dashed line represents the stall cell and solid the negative of the control.

as the following:

$$
l_c \dot{\Phi} = -\Psi + \frac{1}{2\pi} \left[\int_{\text{no injectors}} \left(\Psi_c(\Phi + \delta\phi_1) - \lambda \frac{\partial \delta\phi_1}{\partial \theta} - \mu \frac{\partial \delta\phi_1}{\partial \xi} - m \frac{\partial \delta\phi_1}{\partial \xi} \right) d\theta + \right.
$$

$$
\int_{\text{w/ injectors, control off}} \left(\Psi_c(\Phi + \delta\phi_1) - \lambda \frac{\partial \delta\phi_1}{\partial \theta} - \mu \frac{\partial \delta\phi_1}{\partial \xi} - m \frac{\partial \delta\phi_1}{\partial \xi} \right) d\theta +
$$

$$
\int_{\text{w/ injectors, control on}} \left(\hat{\Psi}_c(\Phi + \delta\phi_2, \Phi_j) - \lambda \frac{\partial \delta\phi_2}{\partial \theta} - \mu \frac{\partial \delta\phi_2}{\partial \xi} - m \frac{\partial \delta\phi_2}{\partial \xi} + \right.
$$

$$
\left. \left. u_j \left(\Phi_j - (\Phi + A \sin(\theta - r)) \right) - \frac{1}{2} u_j^2 \right) d\theta \right],
$$

and the sine moment analogously.

Proposition 6.3.1 Consider a compressor with k injectors with width w each, such that $kw \leq 2\pi$, and the injectors evenly distributed along the annulus of the compressor. Given the PDE model in equation (6.2) and **control law (6.6)**, the Galerkin projection onto the first harmonic results in the closed–loop $\dot{\Phi}$ and $\dot{J}$

equations with the following form:

$$l_c \dot{\Phi} = \Psi_c - \Psi + a_1 J \Psi_c'' + a_2 J + a_3 \sqrt{J} (\Psi_c' + \Phi_j - \Phi) + a_4 J \sqrt{J} \Psi_c''' +$$

$$\tilde{a}_0 \frac{\sqrt{J}}{\Phi_j} \Psi_{ai} + \tilde{a}_1 \frac{J}{\Phi_j} \Psi_{ai}' + \tilde{a}_2 \frac{J \sqrt{J}}{\Phi_j} \Psi_{ai}'' + \tilde{a}_3 \frac{J^2}{\Phi_j} \Psi_{ai}''',$$

$$\frac{m+\mu}{2J} \dot{j} = b_1 \Psi_c' + b_2 J \Psi_c''' + b_3 (\Phi - \Phi_j) + b_4 \sqrt{J} (1 - \Psi_c'') + \frac{\tilde{b}_0}{\Phi_j} \Psi_{ai} + \tilde{b}_1 \frac{\sqrt{J}}{\Phi_j} \Psi_{ai}' +$$

$$\tilde{b}_2 \frac{J}{\Phi_j} \Psi_{ai}'' + \tilde{b}_3 \frac{J \sqrt{J}}{\Phi_j} \Psi_{ai}''', \tag{6.7}$$

where

$$\tilde{a}_0 = \frac{kw}{2\pi^2},$$

$$\tilde{a}_1 = \frac{kw}{8\pi} - \frac{k}{4\pi} \sin(\frac{w}{2}),$$

$$\tilde{a}_2 = \frac{7kw}{24\pi^2} + \frac{k}{24\pi^2} \sin(w) - \frac{2k}{3\pi^2} \sin(\frac{w}{2}),$$

$$\tilde{a}_3 = \frac{3kw}{64\pi} + \frac{k}{64\pi} \sin(w) - \frac{k}{8\pi} \sin(\frac{w}{2}),$$

$$a_1 = \frac{1}{4} + \frac{kw}{16\pi} - \frac{k}{4\pi} \sin(\frac{w}{2}),$$

$$a_2 = -\frac{kw}{16\pi} + \frac{k}{4\pi} \sin(\frac{w}{2}),$$

$$a_3 = \frac{kw}{2\pi^2},$$

$$a_4 = \frac{\frac{k}{12} \sin(w) + \frac{13kw}{36} - \frac{2k}{3} \sin(\frac{w}{2})}{2\pi^2},$$

$$\tilde{b}_0 = \frac{-k}{2\pi} \sin(\frac{w}{2}),$$

$$\tilde{b}_1 = \frac{kw}{2\pi^2} + \frac{k}{6\pi^2} \sin(w) - \frac{4k}{3\pi^2} \sin(\frac{w}{2}),$$

$$\tilde{b}_2 = \frac{k}{16\pi} \sin(w) - \frac{3k}{8\pi} \sin(\frac{w}{2}) + \frac{kw}{8\pi},$$

$$\tilde{b}_3 = \frac{11kw}{48\pi^2} - \frac{k}{720\pi^2} \sin(w) \cos(w) + \frac{23k}{180\pi^2} \sin(w) - \frac{61k}{90\pi^2} \sin(\frac{w}{2}) - \frac{k}{90\pi^2} \sin(\frac{3w}{2}),$$

$$b_1 = 1 - \frac{k}{2\pi} \sin(\frac{w}{2}),$$

$$b_2 = \frac{1}{8} + \frac{kw}{16\pi} - \frac{k}{4\pi} \sin(\frac{w}{2}) + \frac{k}{32\pi} \sin(w),$$

$$b_3 = \frac{k}{2\pi} \sin\left(\frac{w}{2}\right),$$

$$b_4 = \frac{-kw + \frac{4k}{3} \sin\left(\frac{w}{2}\right) - \frac{k}{3} \sin w}{2\pi^2}.$$

The derivation is similar to the bi–directional case. Maple is also used to obtain the coefficients as shown above.

Given equation (6.7), the linear stability condition is given by

$$\frac{k}{\pi} \sin\left(\frac{w}{2}\right) > \frac{2\Phi_j \Psi_c'}{\Phi_j \Psi_c' + \Phi_j^2 - \Phi_j \Phi + \Psi_{ai}} \qquad \text{for } \gamma < \gamma^*, \text{ and } \Phi_j > 0. \qquad (6.8)$$

Some remarks are in order. First of all, the form of equation (6.4) differs from that of (6.7). In particular, there are terms with $\sqrt{J}$ and $J\sqrt{J}$ in $\dot{\Phi}$ and $\sqrt{J}$ in $\dot{J}$ for the uni–directional case. These extra terms come from the breaking of the flip symmetry of the control law (equation (6.6)). The following exercise is performed to illustrate this. To simplify the computations, assume that there are infinite injectors each with infinitesimal width such that the control action is continuous in the $\alpha := \theta - r$ coordinate. Assume that we have a control law $u_j(A, \alpha)$ such that $u_j(A, \alpha) \neq -u_j(A, \alpha+\pi)$ and $\Psi_{ai} \approx 0$. Consider the annulus average equation given by

$$l_c \dot{\Phi} = \frac{1}{2\pi} \int_0^{2\pi} \left[\Psi_c(\Phi + A \sin\alpha + u_j(A, \alpha)) - \Psi + u_j(A, \alpha)(\Phi_j - \Phi - A \sin\alpha) \right.$$
$$\left. - \frac{u_j^2(A, \alpha)}{2} \right] d\alpha.$$

Using a Taylor series expansion,

$$\Psi_c(\Phi + A \sin\alpha + u_j(A, \alpha)) = \Psi_c(\Phi + A \sin\alpha) + u_j(A, \alpha)\Psi_c'(\Phi + A \sin\alpha) + \text{H.O.T},$$

and the integral becomes

$$l_c\dot{\Phi} = \frac{1}{2\pi}\int_0^{2\pi}\left[\Psi_c(\Phi + A\sin\alpha) + u_j(A,\alpha)\Psi_c'(\Phi + A\sin\alpha) - \Psi + \right.$$
$$\left. u_j(A,\alpha)(\Phi_j - \Phi - A\sin\alpha) - \frac{u_j^2(A,\alpha)}{2} + \text{H.O.T}\right]d\alpha,$$

$$= \frac{1}{2\pi}\int_0^{2\pi}\left[\Psi_c(\Phi + A\sin\alpha) + u_j(A,\alpha)\Psi_c'(\Phi) + u_j(A,\alpha)A\sin\alpha\Psi_c''(\Phi) - \Psi \right.$$
$$\left. + u_j(A,\alpha)(\Phi_j - \Phi - A\sin\alpha) - \frac{u_j^2(A,\alpha)}{2} + \text{H.O.T}\right]d\alpha.$$

If $u_j(A,\alpha)$ is affine in A so that $u_j(A,\alpha) = A\hat{u}_j(\alpha)$, the integral can then be written as

$$l_c\dot{\Phi} = \Psi_c(\Phi) + \frac{J}{4}\Psi_c''(\Phi) + \sqrt{J}(\Psi_c' + \Phi_j - \Phi)\frac{1}{2\pi}\int_0^{2\pi}\hat{u}_j(\alpha)d\alpha - \Psi$$
$$-J\frac{1}{2\pi}\int_0^{2\pi}\left[\hat{u}_j(\alpha)\sin\alpha(1 - \Psi_c''(\Phi)) + \frac{\hat{u}_j^2(\alpha)}{2}\right]d\alpha + \text{H.O.T.}$$

Since $u_j(A,\alpha)$ is not flip symmetric, $\hat{u}_j(\alpha)$ is also not flip symmetric, i.e.

$$\frac{1}{2\pi}\int_0^{2\pi}\hat{u}_j(\alpha)d\alpha \neq 0,$$

which gives rise to the $\sqrt{J}$ terms in $\dot{\Phi}$. The $J\sqrt{J}$ terms in $\dot{\Phi}$ and $\sqrt{J}$ terms in $\dot{J}$ can be obtained similarly.

Secondly, the right–hand–side of the linear stability condition for the uni–directional case is exactly twice that for the bi–directional case. This implies that exactly half of the stability extension from the bi–directional case is expected for the uni–directional case for fixed values of Ψ_{ai}, Φ_j, k, and w. Clearly, this is due to the uni–directionality of the actuation. Also, the left–hand–side of (6.8) is identical to that of (6.5), implying that the most favorable configuration for linear stability extension is a high number of injectors k with a small width w.

If stall is expressed in A rather than J, the equations become

$$l_c\dot{\Phi} = \Psi_c - \Psi + a_1 A^2 \Psi_c'' + a_2 A^2 + a_3 A(\Psi_c' + \Phi_j - \Phi) + a_4 A^3 \Psi_c''' +$$
$$\tilde{a}_0 \frac{A}{\Phi_j}\Psi_{ai} + \tilde{a}_1 \frac{A^2}{\Phi_j}\Psi_{ai}' + \tilde{a}_2 \frac{A^3}{\Phi_j}\Psi_{ai}'' + \tilde{a}_3 \frac{A^4}{\Phi_j}\Psi_{ai}''',$$

$$(m+\mu)\dot{A} = b_1 A\Psi_c' + b_2 A^3 \Psi_c''' + b_3 A(\Phi - \Phi_j) + b_4 A^2(1 - \Psi_c'') + \frac{\tilde{b}_0}{\Phi_j}A\Psi_{ai} +$$
$$\tilde{b}_1 \frac{A^2}{\Phi_j}\Psi_{ai}' + \tilde{b}_2 \frac{A^3}{\Phi_j}\Psi_{ai}'' + \tilde{b}_3 \frac{A^4}{\Phi_j}\Psi_{ai}'''.$$

While the open–loop equations (in A) exhibit a pitchfork bifurcation, the closed–loop ones exhibit a transcritical one. A computation of $dA/d\gamma$ yields

$$\frac{dA}{d\gamma}\Big|_{x=x^*} = \frac{2\Phi_j\gamma\Psi\beta}{2\Phi\Phi_j(b_4\Phi_j(\Psi_c''-1) - \tilde{b}_1\Psi_{ai}') - \gamma^2(a_3\Phi_j(\Psi_c' + \Phi_j - \Phi) + \tilde{a}_0\Psi_{ai})\beta}\Big|_{x=x^*},$$

where $\beta = b_1\Phi_j\Psi_c'' + b_3\Phi_j + \tilde{b}_0\Psi_{ai}'$, $x = \gamma, \Phi, \Psi, A$ and $A^* = 0$, and supercriticality is obtained if $(dA/d\gamma)|_{x=x^*} < 0$.

6.3.2   High Fidelity Simulation

Similar to the bi–directional case, a high fidelity simulation is developed. Figure 6.6 shows a typical simulation with the Caltech compressor parameters. As shown in the figure, the controller is able to stabilize the nominally unstable equilibria past the peak of the compressor characteristic to approximately $\Phi = 0.38$, but the system suffers a hysteresis when stall occurs, though the size of the hysteresis is significantly smaller than that in the bi–directional case (Figure 6.3).

Multiple simulations are performed to validate the linear stability condition in equation (6.8). Similar to the bi–directional case, various combinations of k, w, and Φ_j are used in both equation (6.8) and the simulation. A percentage of stability extension in Φ is obtained from each tool. Figure 6.7 shows a plot of the percentage of stability extension predicted by the formula obtained from the low order model and that from the high fidelity simulation. As shown in the figure, the formula
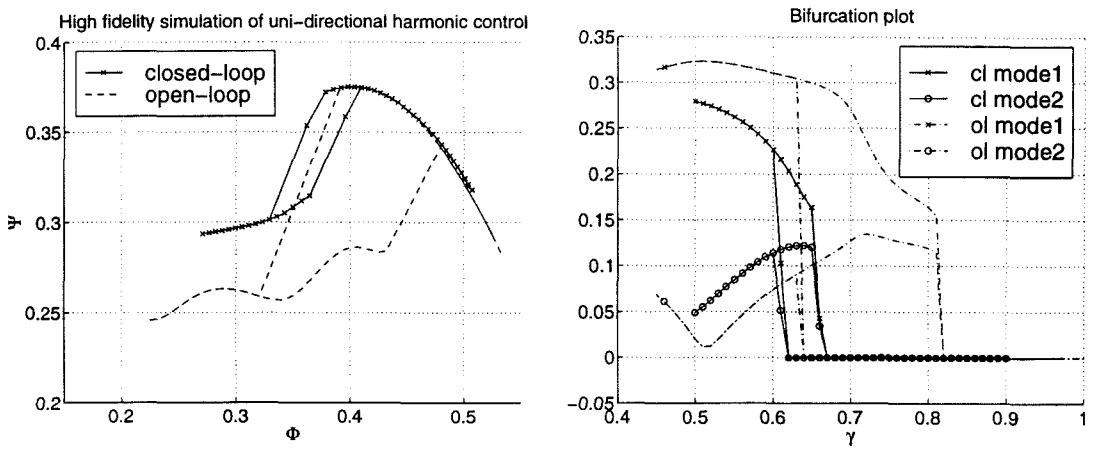
Figure 6.6 High fidelity simulation of a uni–directional proportional harmonic control.
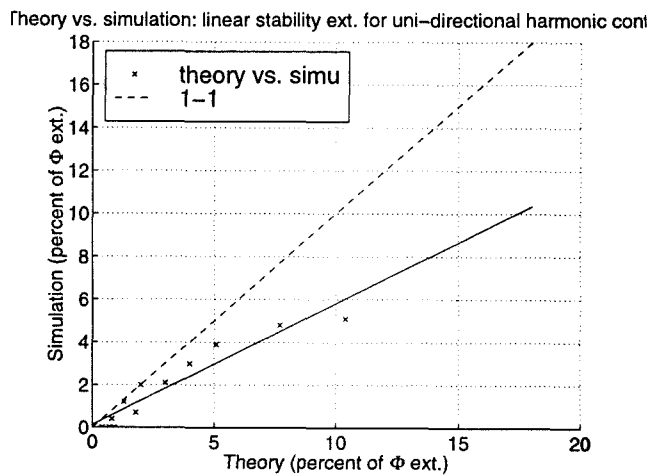
Figure 6.7 Comparison of low order model to high fidelity simulation: percentage of linear stability extension predicted by low order model vs. simulation.

obtained from the low order model shares the same qualitative trend to the simulation. Similar to the bi–directional case, quantitative accuracy is relatively poor due to the absence of actuator and unsteady loss dynamics in the low order model.

6.4 Pulsed Control

In this section, the background and modeling of pulsed controller reported in Behnken [4] and D'Andrea et al. [12] are given. Taking the implementation–oriented variables such as the number of injectors into account, a projection of the PDE model is made and an ODE model is obtained and discussed.

6.4.1 Background

The "pulsed controller" as in Behnken [4] and D'Andrea et al. [12] makes use of uni–directional binary injection, targeted at the tip region of the rotor face, with a low number (3, evenly distributed along the annulus) of injectors for control of rotating stall. The basic idea of the algorithm is as follows. The magnitude and phase of the first mode component of the stall cell are sensed. For each injector, if the magnitude is above a certain threshold, and the stalled region is within a certain window of the injector of interest, then the injector valve is commanded to be fully open (Figure 6.8a). It should be noted that, if the window width is wider than the span of the injector, the control can be activated even if the minimum of the stall cell is *not* within the span of the injector. Figure 6.8b illustrates the control action relative to the stall cell pictorially. Due to the rotation of the stall cell, the algorithm results in the air injection "chasing" the stall cell around the annulus, injecting at the low flow region. Readers are referred to [4] and [12] for details.

By varying the back pressure and/or angle of the injector, the velocity of the injected air can be changed. Figure 6.9 displays the experimental results of the closed–loop behavior of the non–axisymmetric pulsed air injection controller with higher and lower injected velocity on the left and right respectively.

(a)

(b)
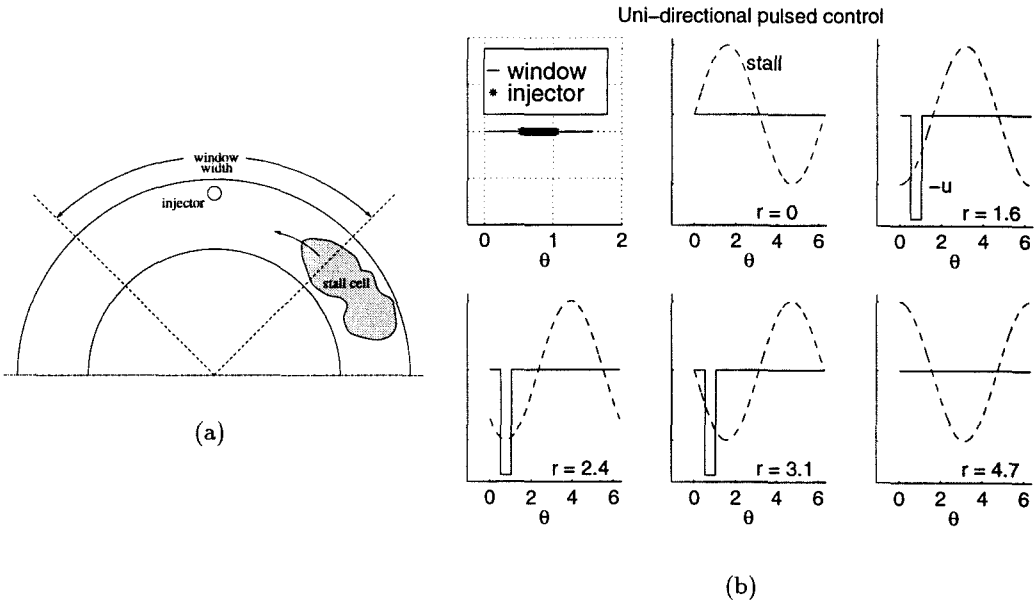
Figure 6.8 Uni–direction pulsed controller: (a). Experimental implementation of pulsed controller; (b). Control action relative to stall cell; dashed line represents the stall cell and solid the control.
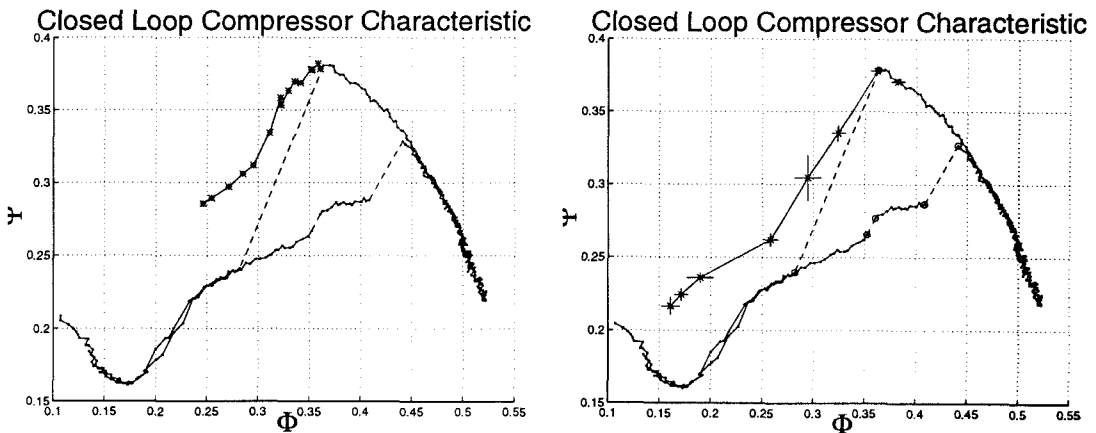
Figure 6.9 Experimental results of control of stall on Caltech rig via non–axisymmetric pulsed air injection: higher and lower injected velocity on the left and right respectively.

Approximation to binary control law
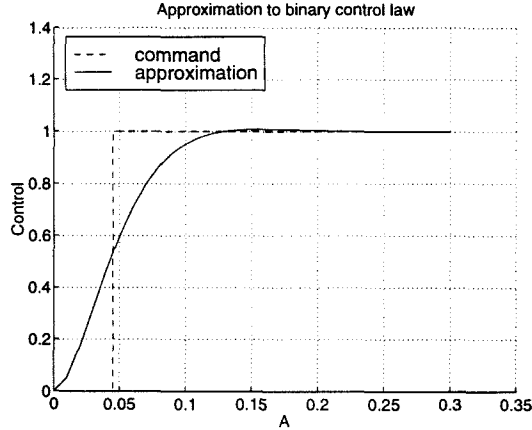
Figure 6.10 Approximation of uni–directional pulsed control for derivation of low order model.

6.4.2 Low Order Model

The pulsed control law takes the form:

$$
u_j(A, \theta, r(\xi)) = \begin{cases} \frac{\delta l_j}{l_a} \Phi_j & \text{if } \theta_l \leq \theta - r(\xi) \leq \theta_u \text{ and } A \geq A_{\text{th}} \\ 0 & \text{otherwise,} \end{cases}
$$

where θ_l and θ_u denote the lower and upper limit of the **window respectively, and** A_{th} the threshold on A below which the control is not activated. The resulting control law resembles a delayed step command in A. The following expression is used to simulate the step command in the derivation of the low order model.

$$
u_j(A, \theta, r(\xi)) = \begin{cases} \frac{\delta l_j \Phi_j}{l_a} \left[1 - e^{u_1 A} \left(\cos(u_2 A) - \frac{u_1}{u_2} \sin(u_2 A) \right) \right] & \text{if } \theta_l \leq \theta - r(\xi) \leq \theta_u, \\ 0 & \text{otherwise.} \end{cases}
$$

(6.9)

This expression is simply the step response of a second order transfer function, using A as the "time", with the natural frequency and damping ratio as functions of u_1 and u_2 (see Figure 6.10).

Proposition 6.4.1 Consider a compressor with k injectors with width w each, such
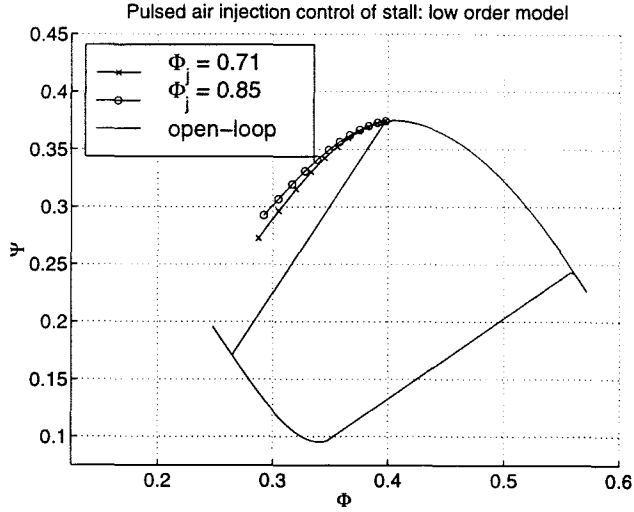
Figure 6.11 Simulation results of low order model for non–axisymmetric
   pulsed air injection control of stall; higher and lower values of Φ_j are
   represented by circles and crosses respectively.

that $kw \leq 2\pi$, and the injectors evenly distributed along the annulus of the com-
pressor. Given the PDE model in equation (6.2) and control law (6.9), the Galerkin
projection onto the first harmonic results in the closed-loop $\dot{\Phi}$ and $\dot{A}$ equations with
the following form:

$$
\begin{aligned}
l_c\dot{\Phi} &= \Psi_c - \Psi + a_1\Psi_c' + a_2\Psi_c'' + a_3\Psi_c''' + \tilde{a}_0\Psi_{ai} + \tilde{a}_1\Psi_{ai}' + \tilde{a}_2\Psi_{ai}'' + \\
&\quad \tilde{a}_3\Psi_{ai}''' + a_4, \\
(m+\mu)\dot{A} &= b_1\Psi_c' + b_2\Psi_c'' + b_3\Psi_c''' + \tilde{b}_0\Psi_{ai} + \tilde{b}_1\Psi_c' + \tilde{b}_2\Psi_c'' + \tilde{b}_3\Psi_c''' + b_4, (6.10)
\end{aligned}
$$

where the coefficients are described in detail in Appendix A.

The derivation is similar to the treatment in the uni–directional proportional
harmonic control case.

A few remarks are in order. First of all, the qualitative behavior of the low order
model agrees with the experimental results. To illustrate, the closed–loop equilibria
are obtained for $\Phi_j = 0.71$ and 0.85. The results are presented in Figure 6.11. The
performance in terms of pressure is better with a higher value of Φ_j, which agrees

with Figure 6.9. Quantitatively, however, the low order model fails to capture the features as observed on the experiments. By matching the experimental conditions in more detail, and using a high fidelity model with realistic effects in a parallel compressor framework, quantitatively reliable results can be obtained. The details can be found in the Section 6.4.3.

Secondly, the control law does *not* affect nominal linear stability. The linearization of the $\dot{A}$ equation in (6.10) around $A = 0$ results in the following equation.

$$(m + \mu)\dot{\delta A} = \delta A \left[\frac{db_1}{dA}\big|_{A=0}\Psi_c' + \frac{db_2}{dA}\big|_{A=0}\Psi_c'' + \frac{db_3}{dA}\big|_{A=0}\Psi_c''' + \frac{d\tilde{b}_0}{dA}\big|_{A=0}\Psi_{ai} + \right.$$

$$\left. \frac{d\tilde{b}_1}{dA}\big|_{A=0}\Psi_c' + \frac{d\tilde{b}_2}{dA}\big|_{A=0}\Psi_c'' + \frac{d\tilde{b}_3}{dA}\big|_{A=0}\Psi_c''' + \frac{db_4}{dA}\big|_{A=0} \right] .$$

The coefficient $x \in \{b_1, b_2, b_3, \tilde{b}_0, \tilde{b}_1, \tilde{b}_2, \tilde{b}_3, b_4\}$ has the following property:

$$\frac{dx}{dA}\big|_{A=0} = \begin{cases} 1 & \text{if } x = b_1, \\ 0 & \text{otherwise.} \end{cases}$$

As a result, $(m + \mu)\dot{\delta A} = \Psi_c'$ which is identical to the open-loop linearization around $A = 0$. In other words, the control law does not alter linear stability. This is consistent with results reported in [4] and [12].

6.4.3 High Fidelity Simulation

To validate the proposed model for non–axisymmetric pulsed air injection and match the experiments, simulations with four Fourier modes with unsteady loss dynamics are carried out to validate the modeling approach to experiments. Most of the compressor parameter values are obtained using an identification algorithm proposed by Behnken [4]. A number of realistic features of the pulsed controller, found in the experimental implementation as in Behnken [4] and D'Andrea et al. [12] are incorporated into the simulation model. The values for the parameters associated

with the actuation are obtained from the actual experimental setting.

Unlike the approximation used in the derivation of the low order model (i.e. control as a function of A), a binary command is implemented as the control law to match the experimental condition exactly. A threshold below which control is not activated is also implemented on A in the simulation. For actuator/actuation dynamics, a third order system is used for each injection point to simulate the response of the velocity of the injected air measured on the rotor face to a step command on the injector valve (see Appendix C of Behnken [4]). The window (θ_l, θ_u) as reported in Behnken [4] and D'Andrea et al. [12] covers approximately $2\pi/3$ for each injector. This feature is also incorporated into the simulation model.

Regarding the tip injection feature, in order to take the appropriate amount of the compressor characteristic shifts as well as the momentum contribution into account, a parallel compressor model in the radial direction is used for the simulation. For the Caltech compressor, each blade is divided into six sections radially. Using information of the blade metal angles of the Caltech compressor (see Section 3.4), the shifted characteristic $\Psi_{c,air}$ is obtained as a function of Φ. The sections that are affected by air injection are then augmented with the characteristic shift as well as the momentum terms, while those that are not are left unchanged. The resulting contributions from the radial sections are summed and averaged to give the dynamics of the collocation point of interest. The nominal and shifted compressor characteristics used in all simulations are fourth order polynomials. A typical simulation and experiment are shown in Figure 6.12. As the plots show, there is oscillation in all of the signals. This is a result of using discrete uni–directional injectors, and is consistent with experiments. For the purpose of obtaining closed–loop equilibria as a function of γ, the signals are temporally averaged on the experiment. The simulation tool is hence augmented with a temporal averaging routine for each fluctuating signal. In the plots that follow, all closed–loop equilibria shown are temporally averaged (and spatially, where appropriate) values over the latter half of each individual simulation.

For the purpose of validation, simulations are carried out with a higher and lower
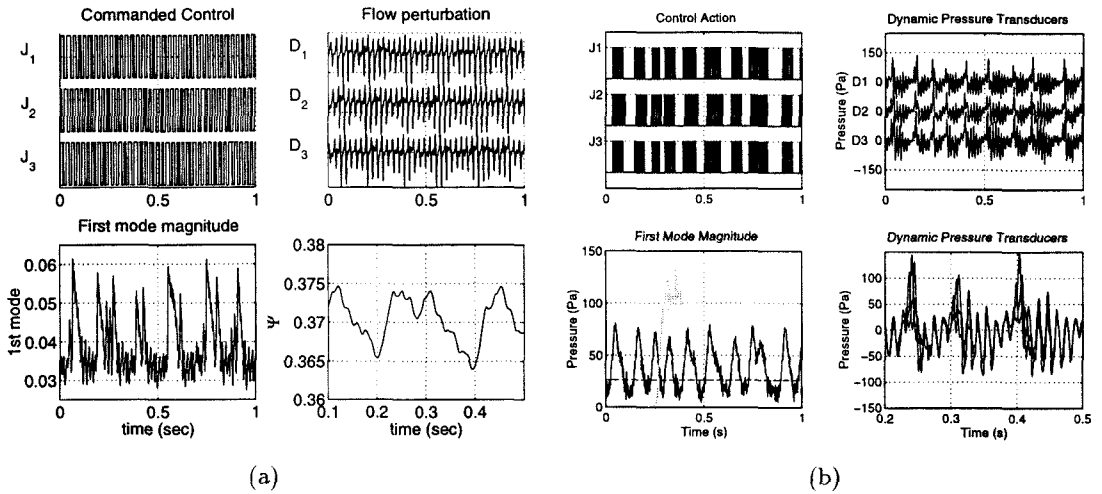
Figure 6.12 Typical simulation of uni–directional pulsed control of rotating stall compared to experiment: (a). High fidelity simulation; (b). Experiment.

Φ_j corresponding to the experiments. The results, along with the experiments, are shown in Figure 6.13. A comparison of Figure 6.13 and 6.9 shows that there is good qualitative as well as quantitative agreement.

Multiple simulations are also carried out while perturbing one of the various parameters in the model. In particular, the following parameters are perturbed.

- μ: inertia parameter for compressor,

- λ: inertia parameter for compressor rotor(s),

- $\tilde{R}$: reaction ratio,

- τ: unsteady loss dynamics time constant,

- ω_n: natural frequency of 2nd order system for actuation dynamics,

- ζ: damping ratio of 2nd order system for actuation dynamics,

- k: number of injectors, and

- Φ_j: nondimensional injection velocity.
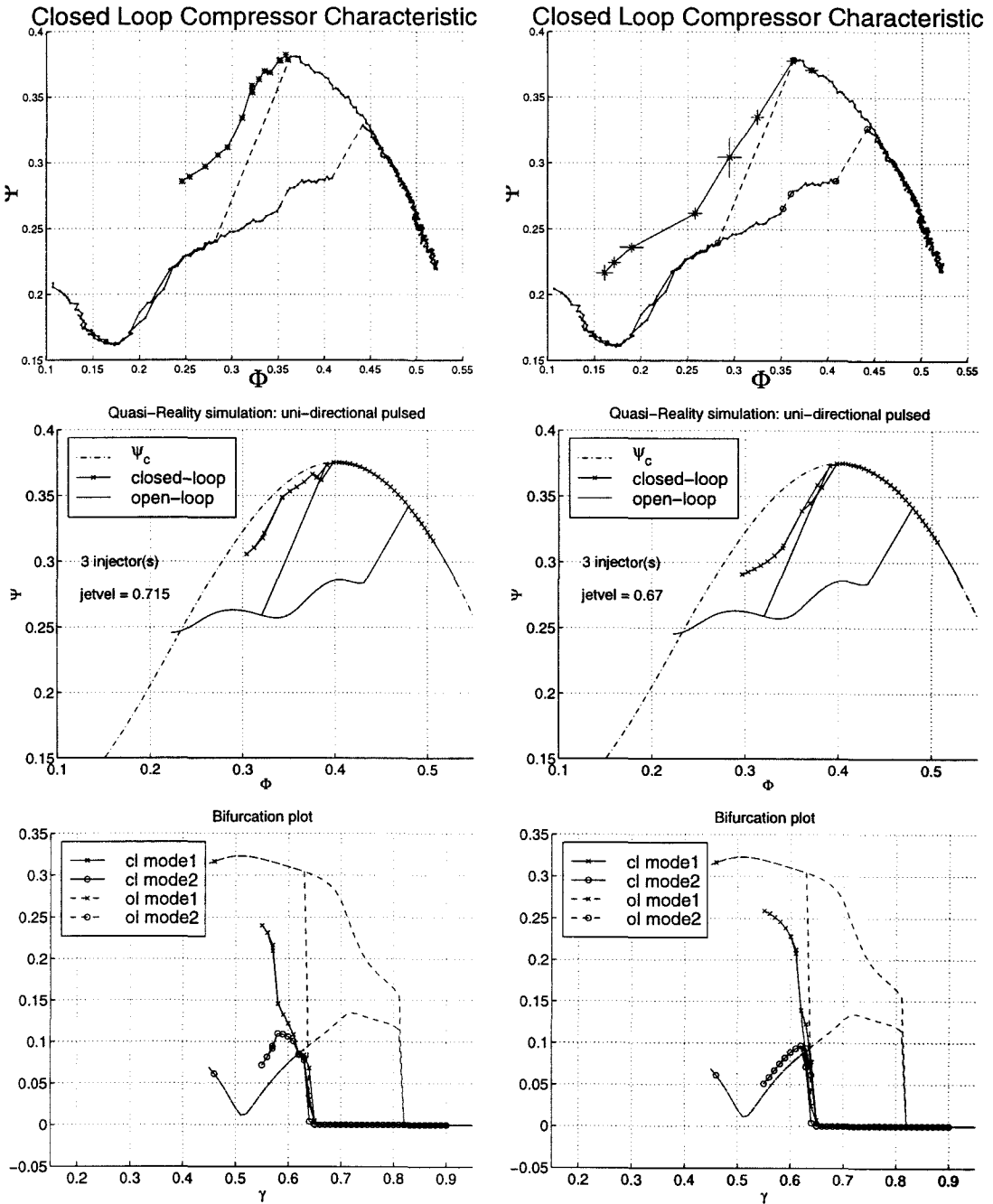
Figure 6.13 Simulation results of control of stall on Caltech rig via nonaxisymmetric pulsed air injection: higher and lower injected velocity on the left and right respectively; from top down: experiment, simulation (Φ–Ψ, γ–stall).

x / –	nominal	test range	slope for low x $\frac{d\Psi}{d\Phi}$ | $\frac{dA_1}{d\gamma}$ | $\frac{dA_2}{d\gamma}$			slope for high x $\frac{d\Psi}{d\Phi}$ | $\frac{dA_1}{d\gamma}$ | $\frac{dA_2}{d\gamma}$		
μ	1.55	$1.24 - 1.86$	0.93	-6.22	-2.96	0.72	-4.52	-2.92
λ	0.575	$0.46 - 0.69$	0.86	-4.59	-2.89	1.16	-6.09	-2.92
$\tilde{R}$	0.98	$0.794 - 0.99999$	1.09	-5.83	-1.93	1.14	-5.87	-2.92
τ	0.4	$0.32 - 0.48$	1.01	-4.75	-1.13	0.39	-2.36	-2.09
ω_n	0.95	$0.76 - 1.14$	1.11	-5.92	-2.78	0.65	-2.73	-2.73
ζ	0.9	$0.72 - 1.08$	0.53	-2.21	-3.00	1.09	-6.09	-2.66
k	3	3, 6	1.13	-5.75	-2.64	0.15	-0.97	-1.73
Φ_j	0.67	$0.536 - 0.804$	0.61	-7.61	-2.01	-0.72	-1.6	-3.09

Table 6.1 Sensitivity analysis of pulsed air injection control of rotating stall: slope values.

The boundaries of a $\pm 20\%$ on each parameter is taken as the test range when allowed. For each case, the equilibria from the nominal stall inception to a γ value representing an additional 10% load beyond stall inception are obtained. For the stable case, this 10% load represents a 16.9% extension in Φ. Performance measures in terms of the sum of the difference, over the range of throttle coefficient tested, between the stable and tested systems are computed in the pressure, first, second, and third harmonics. The slopes at which the equilibria of the closed–loop system emerge from stall inception on the Φ–Ψ as well as γ–A_n plane, for $n = 1, 2$, are also computed. In the case of the slopes computation, each slope is computed via finite difference followed by averaging over three throttle coefficients beyond nominal stall inception. This is performed to capture near stall–inception behavior. For the stable case, the slopes $\frac{d\Psi}{d\Phi} = 0$ and $\frac{dA_n}{d\gamma} = 0$ for $n = 1, 2, 3$. Qualitatively speaking, a more positive $\frac{d\Psi}{d\Phi}$ and/or higher value of the summed difference in Ψ implies steeper drop–off in pressure, while a more negative $\frac{dA_n}{d\gamma} = 0$ and/or higher value of the summed difference in A_n implies more stall. In some cases, hysteresis loops are observed and comments made. The results are compiled into Table 6.1 and 6.2.

For comparison in terms of computational expense, the time required to generate 70 closed–loop equilibria for the low order (3 states) model is approximately a factor of 7 faster than the reduced order (58 states) one, with 87 seconds being the actual time required for the former case. All simulation packages are written in C and

x / $-$	nominal	test range	$\sum$ for low x			$\sum$ for high x			comments
			Ψ	A_1	A_2	Ψ	A_1	A_2	
μ	1.55	$1.24-1.86$	-0.45	1.67	0.62	-0.35	1.49	0.56	hys. at low μ
λ	0.575	$0.46-0.69$	-0.34	1.46	0.54	-0.47	1.72	0.66	hys. at high λ
$\bar{R}$	0.98	$0.794-0.99999$	-0.50	1.89	0.61	-0.40	1.59	0.61	
τ	0.4	$0.32-0.48$	-0.47	1.82	0.73	-0.31	1.30	0.46	
ω_n	0.95	$0.76-1.14$	-0.48	1.80	0.72	-0.35	1.46	0.58	
ζ	0.9	$0.72-1.08$	-0.27	1.25	0.69	-0.47	1.78	0.67	
k	3	3, 6	-0.42	1.65	0.64	-0.02	0.61	0.52	
Φ_j	0.67	$0.536-0.804$	-0.74	2.23	0.52	0.083	0.73	0.83	hys. at low Φ_j

Table 6.2 Sensitivity analysis of pulsed air injection control of rotating stall: $\sum$ difference values.

carried out on a Sun Ultra 2170.

6.5   Theoretical Comparison of Existing Methods

In this section, a theoretical comparison of the three air injection techniques is presented using the models derived in this report. The objective is to weigh the advantages and disadvantages of each technique in the context of operability. Elements such as number and width of injectors, injection authority, and type of extension are considered.

6.5.1   Procedure of Comparison

The theoretical comparison effort is carried out via low order simulations. For each control algorithm, namely, the bi–directional and uni–directional harmonic, and uni–directional pulsed air injection, simulations are performed to seek the minimum requirement on the injected velocity Φ_j for each combination of the number k and width w of injectors (subject to the constraint $kw \le 2\pi$) such that the system is "operable" within a set of pre–selected criteria. A system is deemed "operable" if the system achieves an extension of x percent in the axial velocity Φ relative to the nominal stall inception axial velocity Φ_{stall}, while keeping the stall amplitude A below y percent of the nominal, fully grown first mode stall amplitude A_{full}.
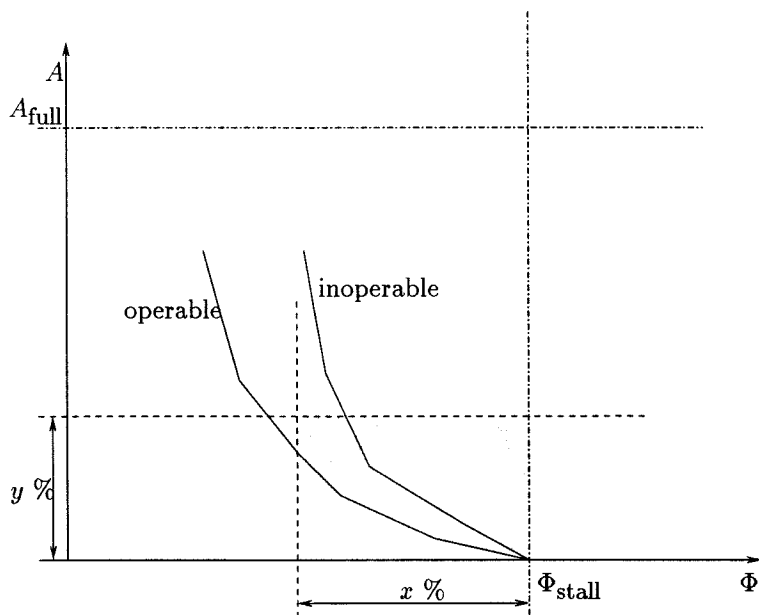
Figure 6.14 Pictorial representation of criterion in theoretical comparison study for non–axisymmetric air injection.

Figure 6.14 shows the idea pictorially.

Four values for x, namely, $x = 5, 10, 15, 20$ and six for y, namely $y = 1$, 2, 5, 10, 20, 30, resulting in 24 scenarios, are chosen for the results presented in this report. For each control algorithm in each scenario, values of w ranging from $3°$ to $120°$ in $3°$ increments, and k from 1 to $w/360$ in 1 injector increments are chosen and the value of Φ_j is varied from 200 to 1 percent of Φ_{stall} in -1 percent of Φ_{stall} increments until the criterion of the scenario is violated. The values of k, w, and Φ_j of the last successful run are then recorded as the minimum requirement. All simulations are carried out using the compressor parameters for a low speed, single stage, axial compressor at Caltech.

6.5.2   Results of Comparison and Discussion

Figure 6.15 shows the minimum Φ_j required for various combinations of **k and w**, at six different values of w, for $x = 5$ and $y = 1$, i.e. a criterion of 5 percent extension in Φ within 1 percent of A_{full}. A few remarks are in order. Firstly,
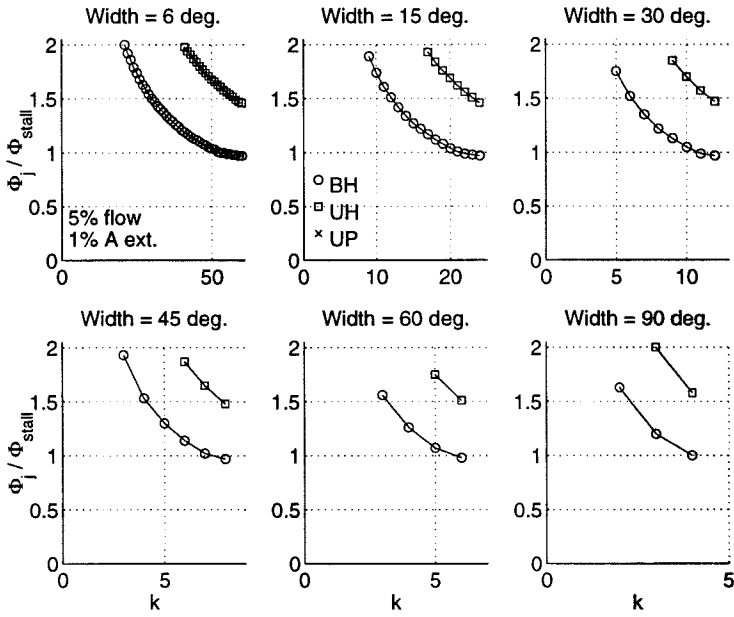
Figure 6.15 Minimum Φ_j requirement for various combinations of k and w for five percent extension in Φ within one percent of A_{full}; BH denotes bi–directional proportional harmonic control, UH uni–directional proportional harmonic control, and UP uni–directional pulsed control.
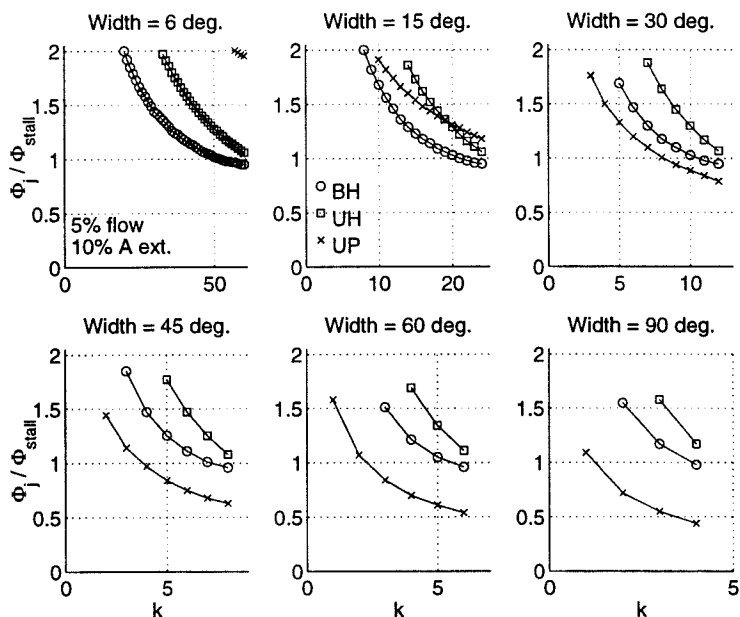
Figure 6.16 Minimum Φ_j requirement for various combinations of k and w for five percent extension in Φ within ten percent of A_{full}.

the uni–directional pulsed algorithm is not effective due to the narrow range of allowable stall amplitude. Due to the inability of stability extension of the uni–directional pulsed algorithm, the criterion of 5 percent extension in Φ within 1 percent of A_{full} proves to be too stringent to satisfy. Secondly, it is also clear from the figure that the bi–directional harmonic algorithm requires smaller values of Φ_j than the uni–directional harmonic algorithm. An inspection of the stability criteria described by equations (6.5) and (6.8) reveals that this is expected. Finally, the loci do not seem to change shape or location dramatically as a function of w for either algorithm, though a closer inspection reveals that the minimum Φ_j requirement decreases slightly as w decreases.

Figure 6.16 shows the minimum Φ_j required for various combinations of k and w, at again six different values of w, for $x = 5$ and $y = 10$, i.e. a criterion of 5 percent extension in Φ within 10 percent of A_{full}. In this case, the uni–directional pulsed algorithm not only succeeds in satisfying the criterion, but also requires the smallest Φ_j for some values of w. A more interesting observation is that, although the shape

Uni–directional pulsed control: effects of injector width
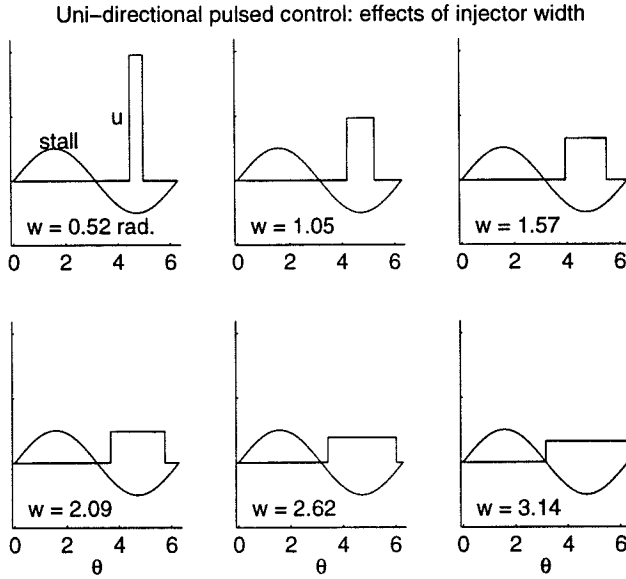
Figure 6.17 Effects of injector width w on minimum Φ_j requirement.

of the loci of the uni–directional pulsed algorithm does not change dramatically as w increases, the location does. In fact, the minimum Φ_j requirement decreases as w *increases*, which is the opposite of the behavior observed for the bi– and uni–directional harmonic algorithms.

While closed–form solutions from equation (6.10) explaining the effects of w on the minimum Φ_j requirement for the uni–directional pulsed controller are difficult to obtain due to complexity, an intuitive argument can be provided. Consider a flow perturbation $\delta\phi = \sin\theta$. Since the main purpose of the pulsed control algorithm is to inject air in the region of flow deficit, it is logical to assume that the required injection is proportional to the negative of the flow deficit. Thus, the region of $\pi \leq \theta \leq 2\pi$ is the target with an area of $\int_{\pi}^{2\pi} \sin\theta d\theta = 2$. Define the injected air to be $w\Phi_j$. For a fixed value of $w\Phi_j$, Φ_j is clearly inversely proportional to w, which is consistent with the observation on Figure 6.16. Figure 6.17 shows the level of Φ_j as w increases for a fixed $w\Phi_j = 2$.

Figure 6.18 shows the minimum Φ_j required for various combinations of k and w, at again six different values of w, for $x = 5$ and $y = 30$, i.e. a criterion of 5
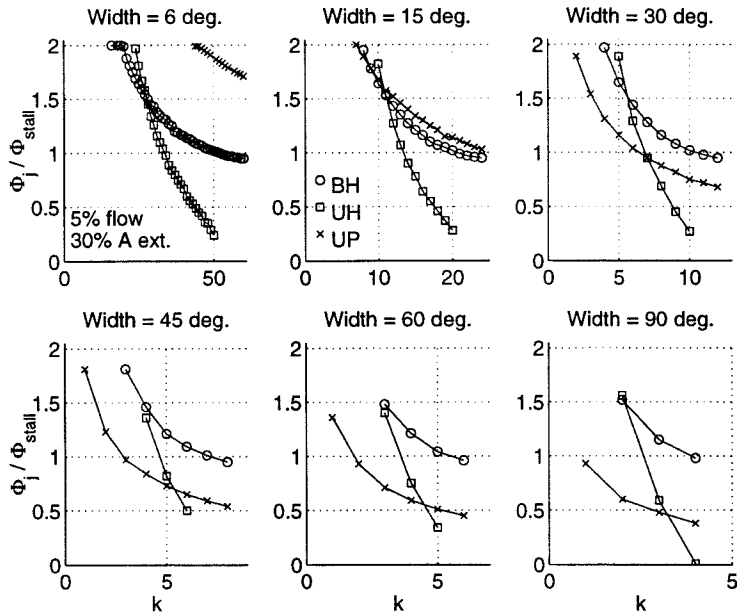
Figure 6.18 Minimum Φ_j requirement for various combinations of k and w for five percent extension in Φ within 30 percent of A_{full}.

percent extension in Φ within 30 percent of A_{full}. In this case the uni–directional harmonic algorithm requires the least Φ_j for all six values of w. At lower number of injectors, however, the uni–directional pulsed algorithm becomes more favorable as w increases, which is consistent with one of the observations made on Figure 6.16.

With the quantity $kw/360$ defined as the coverage, the minimum coverage for each Φ_j is obtained for each A percentage criterion for each control law. The results for each A requirement are grouped. Figure 6.19 shows the results. A few notes of clarification are in order. The numbers on the (1,1) plot denote the percentage of extension requirement in Φ for the bi–directional harmonic controller. Since the direction with respect to increasing Φ requirement is found to be the same for all cases, only the five percent case is labeled for each control law in subsequent plots.

For the case of the uni–directional pulsed algorithm, the loci of points consist of combinations of kw with *different* values of w, while those for the bi–directional harmonic cases are the kw combinations for the smallest w possible. This is due to the fact that the trend of minimum Φ_j requirement with respect to w is reversed
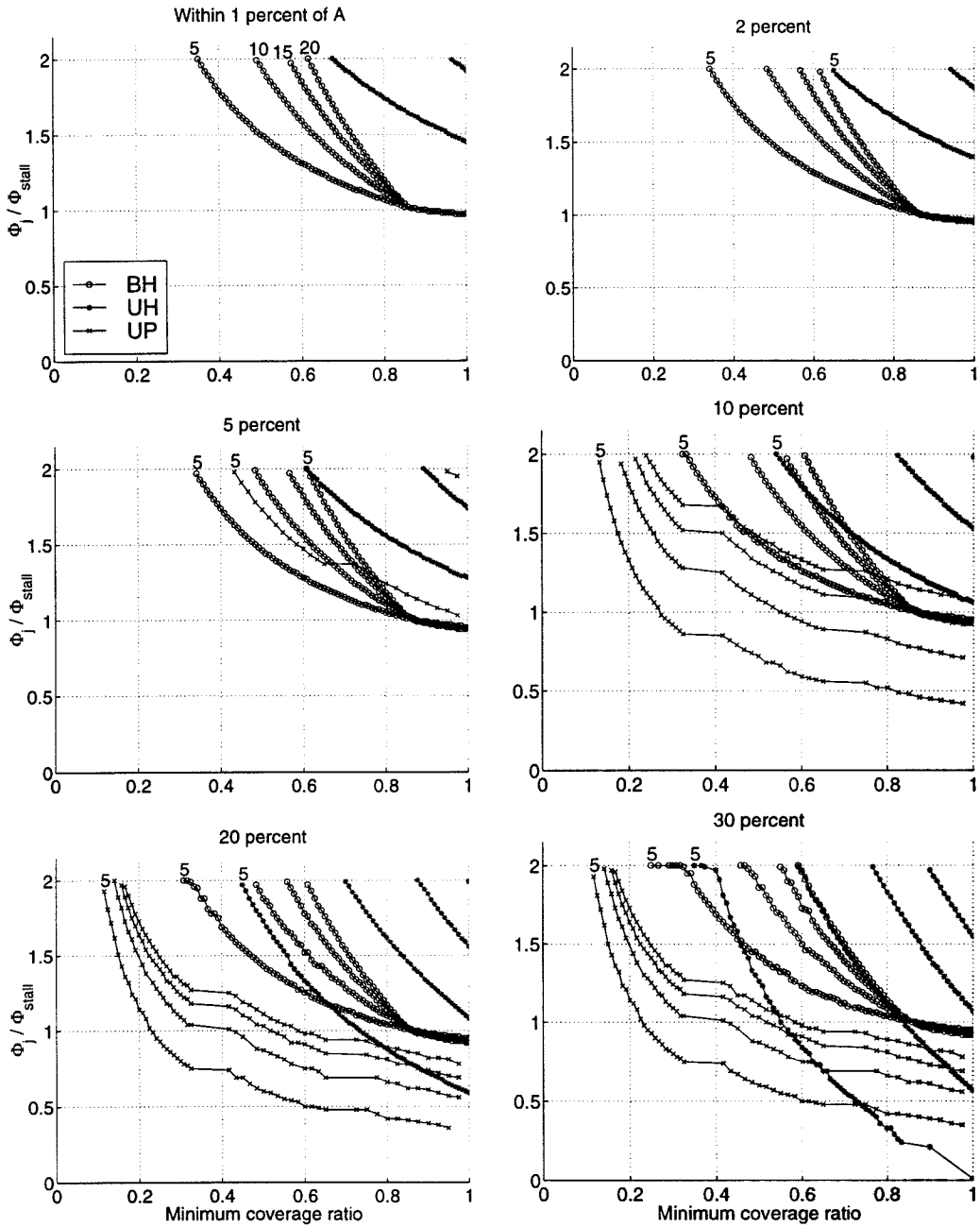
Figure 6.19 Minimum coverage for 1, 2, 5, 10, 20, and 30 percent *A* requirement cases: BH — Bi-directional Harmonic, UH — Uni-directional Harmonic, UP — Uni-directional Pulsed.

between the harmonic and pulsed cases. For the uni–directional harmonic case, the vast majority of the loci of points consist of combinations of kw for the smallest w possible, with the exception of a few points at very low Φ_j requirement.

A few observations can be made from the figure. Firstly, the Φ_j requirement for the uni–directional pulsed case changes initially and then levels out as the A requirement is relaxed. Also, the pulsed algorithm does not perform well for stringent A requirement, while the harmonic cases do. Secondly, as the requirement on A is relaxed, the minimum Φ_j requirement for the bi–directional harmonic algorithm does not change dramatically. This is expected since the purpose of the control law is to "annihilate" the harmonic and extend stability. The Φ_j requirement for the uni–directional harmonic case, however, changes dramatically as the A requirement is relaxed.

A few observations can also be made as the Φ requirement becomes more demanding. Firstly, the loci of points for all of the algorithm shift toward the upper right corner. This is expected since the requirement is becoming harder to satisfy. Secondly, at an A requirement of 30 percent, although the uni–directional harmonic case achieves the lowest overall Φ_j requirement, the uni–directional pulsed algorithm starts to perform better as the Φ requirement increases.

6.6 Conclusions and Remarks

ODE models are derived, from a common PDE model, for bi– and uni–directional proportional harmonic, and pulsed control of stall with air injection. Conditions for linear stability as well as bifurcation criticality are derived for the first two cases, in terms of implementation–oriented variables such as number of injectors. The functional form of the $\dot{\Phi}$ and $\dot{J}$ equations for the uni–directional proportional case differ from those for the bi–directional proportional case. The extra terms in the uni–directional case are found to be a result of the breaking of the flip symmetry of the control law.

For the pulsed controller, although the model is low in order (3 states), the sys-

tem is described by transcendental equations. As a result, closed–form solutions for the closed–loop equilibria as well as conditions for bifurcation criticality are difficult to obtain. Linearized analysis, however, shows that the control implementation does not affect linear stability. A high fidelity simulation tool is developed and validation thereof performed by matching experimental results found in Behnken [4] and D'Andrea et al. [12]. Results show that the model gives good qualitative as well as quantitative agreement. To further explore the behavior of the system, a sensitivity analysis is also performed by perturbing the model parameters in the simulations.

A theoretical comparison is made between two harmonic and pulsed controls via low order simulations. Results show that, for a given Φ extension, the bi–directional harmonic controller is more favorable for more stringent demands on A, while the uni–directional harmonic and pulsed are more favorable as the requirement on A is relaxed. For a given A requirement, the uni–directional pulsed controller is more favorable as the Φ extension requirement increases if the A requirement is sufficient (at least five percent for the model of the Caltech compressor). The bi–directional harmonic control is more favorable otherwise. Also, the harmonic controls are most effective with a high number of injectors with a small width, while the pulsed control seem to favor a low number of injectors with a large width.

Since the models are derived from a common PDE on which the form of the control law is not specified, different approaches can clearly be applied and tested with different objectives. For instance, the control laws for both bi– and uni–directional cases described in this thesis are idealized since a perfect knowledge of the stall cell, as well as the ability to match the actuation to the amount of stalled region, are assumed implicitly. Various implementations from one with sensing and actuation imperfections to one with a different form of the control law can be used to obtain the respective projected ODE models. Conditions, such as optimal gain given a control law for instance, can then be derived.

Chapter 7

Static Distortion

Inlet disturbance is an important performance barrier that prevents compressors to operate close to the nominal stall/surge line. There are three main sources of inlet disturbances: planar waves, static distortions, and rotating distortions. Since a significant portion of the surge margin is devoted to avoiding stall and surge of engines due to distortions, the subject of the effects of inlet disturbances and characterization thereof has naturally received a lot of attention over the years.

Various aspects of the effects of static and rotating total pressure distortions on axial compressors have been studied by research groups in the past, including but not limited to Lucas et al. [58], the SAE S–16 committee [81, 82], Chue et al. [9], Hynes et al. [45], Longley and Greitzer [56], Longley et al. [57], Greitzer et al. [36], Stenning [88], and Mazzawy [61]. Some results for control in the presence of static distortion have been achieved by Schalkwyk et al. [91] and Spakovszky et al. [87].

The goals of this chapter are to explore the modeling and control in the presence of static distortion. Section 7.1 presents the notion of a parallel compressor model, proposed by Hynes and Greitzer [45] and Mazzawy [61], to account for static distortion. Section 7.2 presents that results of an experimental characterization of the effects of five patterns of static distortion on the Caltech facility. The non-axisymmetric pulsed air injection algorithm [4, 12] is used to control rotating stall in the presence of each pattern, and the results are reported. Conclusions are drawn and presented in Section 7.3 which ends the chapter.

7.1 Theory

The principle of parallel compressors, proposed by Hynes et al. [45] and Maz-zawy [61], is used to treat static circumferential flow distortions. Static distortion is modeled as a circumferential total pressure profile specified at the inlet of the compression system. This pattern is then assumed to be convected downstream to the compressor face along streamlines of the undistorted flow, i.e.

$$\Psi_{\text{inlet}}(\theta) = \Psi_{\text{compressor face}}(\theta),$$

where θ is the circumferential angle. A collocation method that accounts for inlet distortion patterns is also proposed in [45].

There are two classes of static distortions that are of interest:

- constant steady distortion

- local flow–dependent distortion

Making use of the distributed model as proposed by Mansoux et al. [59] and the assumption of convection of the distortion pattern, the distorted compressor characteristic is

$$(\Psi_c)_{\text{distorted}}(\theta, \Phi) = (\Psi_c)_{\text{undistorted}}(\theta, \Phi) + \frac{S(\theta, \Phi)}{2}, \qquad (7.1)$$

where $S(\theta, \Phi)$ is the distortion screen parameter. For each of the two cases mentioned above, $S(\theta, \Phi)$ is given by:

$$S(\theta, \Phi) = \begin{cases} \tilde{S}(\theta), & \text{constant steady distortion} \\ \tilde{S}(\theta)\Phi^2, & \text{local flow–dependent distortion,} \end{cases}$$

where $\tilde{S}(\theta)$ is a vector of constants as a function of θ. The distorted compressor characteristic $(\Psi_c)_{\text{distorted}}(\theta, \Phi)$ replaces the nominal undistorted version $(\Psi_c)_{\text{undistorted}}$

in the governing PDE:

$$\Psi = \Psi_c(\Phi + \delta\phi) - l_c\frac{d\Phi}{d\xi} - \lambda\frac{\partial\delta\phi}{\partial\theta} - \mu\frac{\partial\delta\phi}{\partial\xi} - m\frac{\partial\delta\phi}{\partial\xi},$$

i.e. equation (2.1).

7.2 Results

7.2.1 Model Validation

In this section, the effects of static distortion on the Caltech compressor setup are characterized experimentally. A high fidelity simulation is developed and validated against the experiments.

Static distortions are generated by a stationary screen placed approximately 2 rotor radii upstream of the compressor rotor face. The patterns tested are:

1. 120° one/rev,

2. tip radial,

3. hub radial,

4. 60° two/rev (90° apart between the two closest axes), and

5. aircraft pattern (tip radial and 120° one/rev at mid–span).

The area of the blockage is kept constant (33% of annulus area) in these five cases and the material used for blockage is also identical. See Figure 7.1. In four evenly circumferentially distributed ports around the annulus, a set of five pressure rakes are spaced at radial distances such that probe positions are area–normalized and placed into the flow in the annulus area. Static pressure transducers are used in conjunction with the rakes and the pressure profile across the screen is recorded for each distortion pattern by averaging the data over 100 rotor revolutions. The pressure profile data is then averaged across the four rake ports and presented here. In cases 2, 3, and 5, 95% confidence error bars (calculated by averaging the
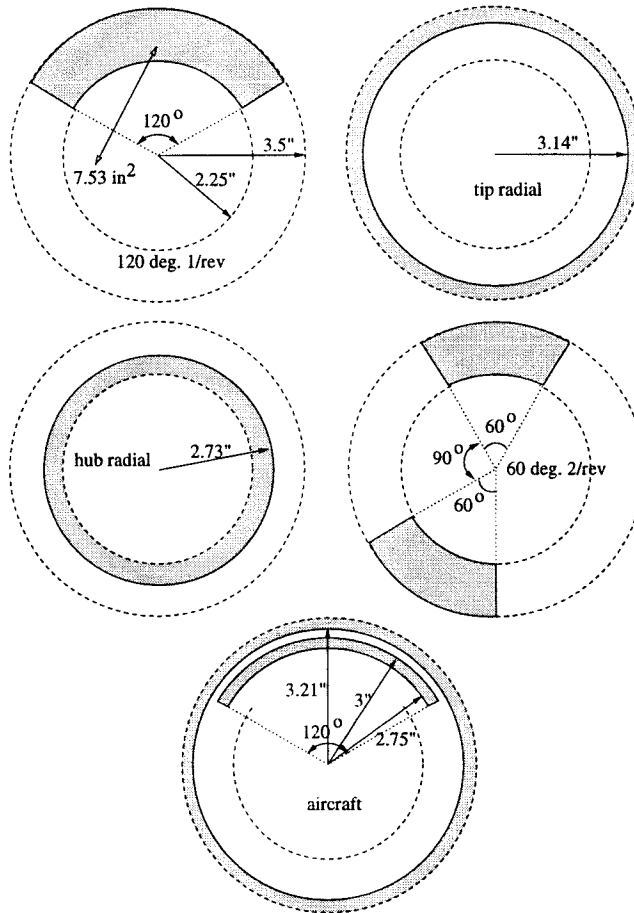
Figure 7.1 Screen configurations used for static distortions tests.

standard deviations of the pressure profile data of each rake port and adjusted with T–statistics) are given at each data point.

120° one/rev

The pressure profile is obtained by rotating the screen 15° for 24 times and recording the pressure loss characteristics. The compressor characteristic and the pressure profile downstream of the screen are shown in Figure 7.2. The compressor performance suffers a pressure loss at the new stall inception point at a flow coefficient slightly to the left of that of the undistorted case.
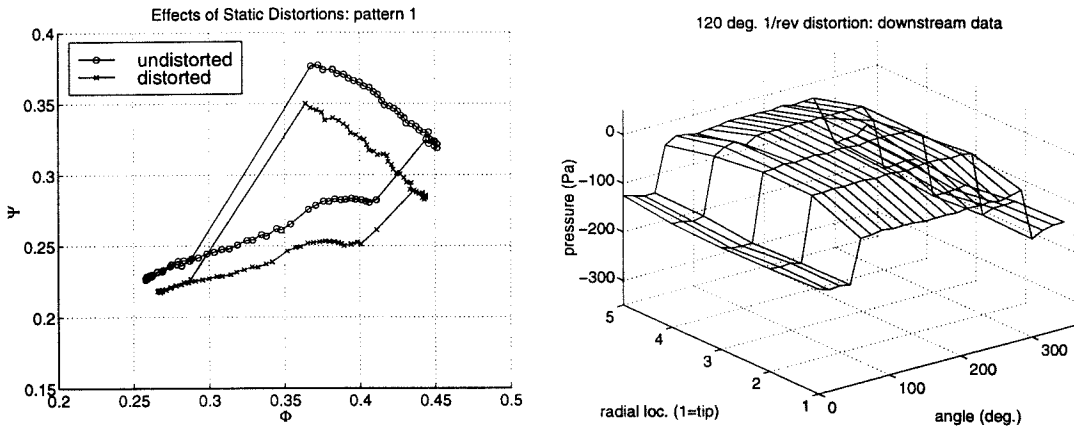
Figure 7.2 Compressor characteristic data: 120° one/rev.
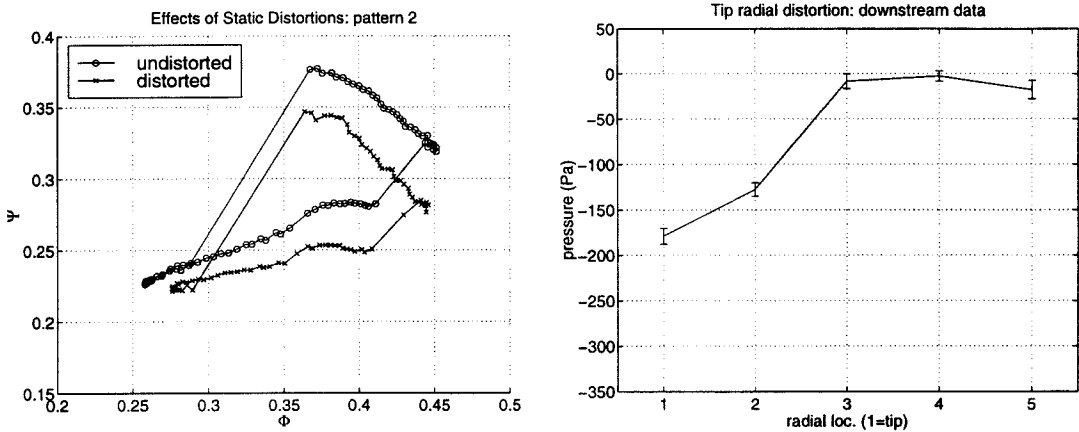
Figure 7.3 Compressor characteristic data: tip radial.

Tip Radial

Due to the presence of circumferential symmetry, the pressure profile is obtained by simply taking the pressure data at the four rake ports. The compressor characteristic and the pressure profile downstream of the screen are shown in **Figure 7.3**. In this case, a close inspection reveals that the stall inception flow coefficient is slightly larger than that for the 120° one/rev case, implying that the **pattern causes more** performance degradation to the compressor.
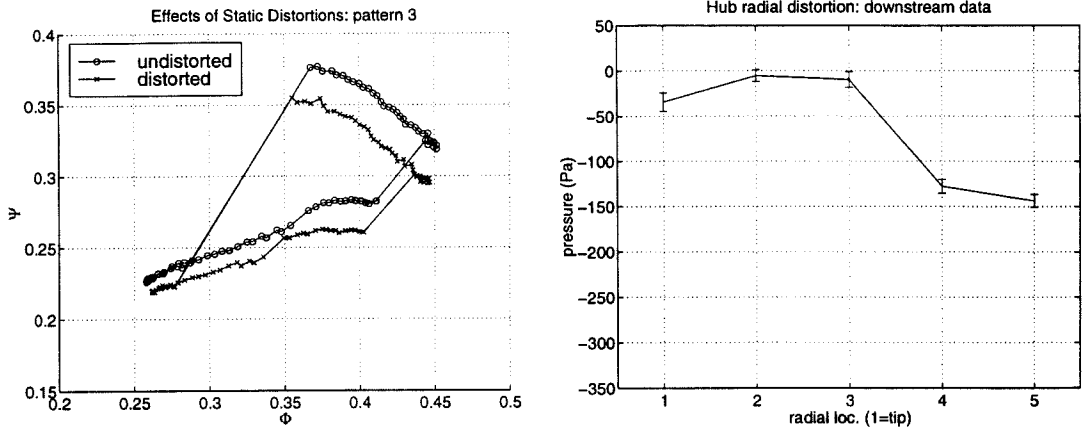
Figure 7.4 Compressor characteristic data: hub radial.

Hub Radial

Again, due to the presence of symmetry, only the pressure data from the four rake ports are taken. The compressor characteristic and the pressure profile downstream of the screen are shown in Figure 7.4.

In tip–loaded compressors, hub distortion tend to delay the onset of rotating stall [44, 58]. Although Figure 7.4 indicates that there is not a delay of the stall inception point in terms of the throttle coefficient, a comparison of the distorted cases in Figure 7.2 and 7.3 shows that the hub radially distorted case does delay the onset of stall relative to the tip radial and 120° one/rev cases. This is consistent with observations found in literature [58].

60° two/rev

Similar to the 120° one/rev case, the pressure profile for the 60° two/rev case is obtained by rotating the screen 15° for 24 times and recording the pressure loss characteristics for each configuration. The compressor characteristic and the pressure profile downstream of the screen are shown in Figures 7.5.

A comparison of Figure 7.5 with 7.2 indicates that, although the angle of the spoiled sector is kept constant across both cases, the 120° one/rev case appears to stall earlier than the 60° two/rev case. This is consistent with experimental obser-
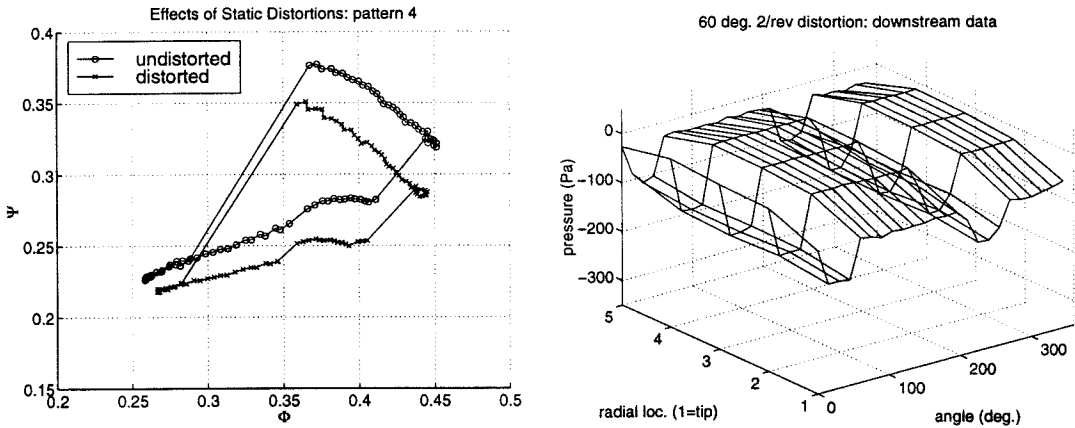
Figure 7.5 Compressor characteristic data: 60° two/rev.

vations [45, 79] as well as direct fluid dynamic stability calculations [45] reported in literature that, under constant angle of spoiled sector, an increase in the number of spoiled sectors gives smaller effects. Furthermore, a comparison between Figure 7.5, 7.3, and 7.4 indicates that the level of flow degradation at stall inception by the 60° two/rev distortion lies between that of the tip and the hub radial patterns.

Aircraft Pattern: tip radial and 120° one/rev at mid–span

The pressure profile data is taken only at the four rake ports. The compressor characteristic and the pressure profile downstream of the screen are shown in Figures 7.6. By comparing the expected pressure profile from the aircraft pattern shown in Figure 7.1 and the experimental data from Figure 7.6, it is concluded that a set of five pressure rakes does not provide a fine enough resolution to distinguish the important parts of the pattern, thus the probes are not rotated to give the 24 sets of circumferential pressure profile data.

A close inspection of Figure 7.6 and 7.5 shows that the flow coefficient of the stall inception point for the aircraft pattern is slightly smaller than that of the 60° two/rev pattern.
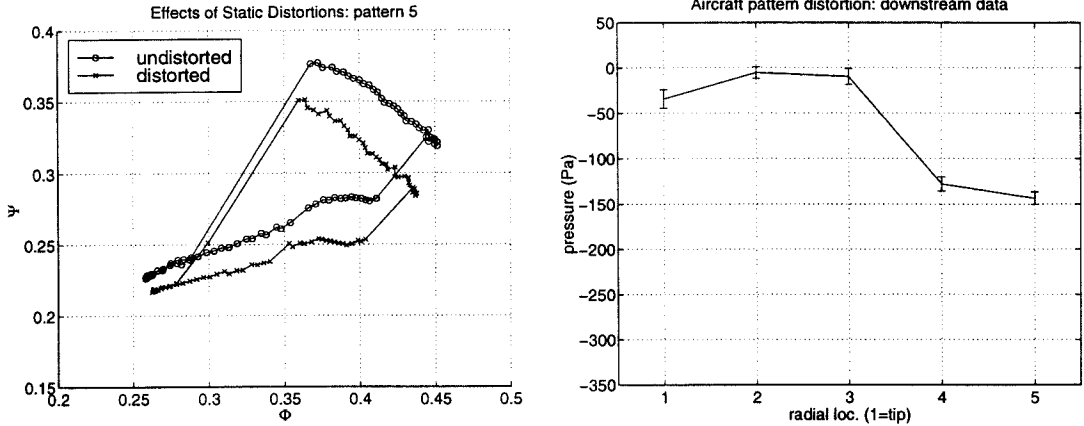
Figure 7.6 Compressor characteristic data: aircraft pattern.

Simulations

Simulations of the open–loop quasi–static compressor characteristic of the 120° one/rev (pattern 1) and 60° two/rev (pattern 4) cases are carried out. The collocated model as described in Section 2.3 with the static distortion model as described in equation (7.1) are used to generate the results. Figure 7.7(a) shows the equilibria for the 120° one/rev case with $\tilde{S}(\theta) = -1.15$ for $\theta = [0, \frac{2\pi}{3}]$ and $\tilde{S}(\theta) = 0$ for $\theta = (\frac{2\pi}{3}, 2\pi)$, and (b) the 60° two/rev case with $\tilde{S}(\theta) = -1.15$ for $\theta = \{[0, \frac{\pi}{3}], [\frac{5\pi}{6}, \frac{7\pi}{6}]\}$ and $\tilde{S}(\theta) = 0$ otherwise. As the plots show, the model agrees both qualitatively and quantitatively with the experiments.

7.2.2 Control

The results of an investigation on the robustness of the non–axisymmetric pulsed air injection controller to static distortion are described in this subsection. The distortion configurations are the same as in the nominal, open–loop cases reported in Section 3.5. Due to the static nature of the distortion patterns, the controller is expected to be successful.
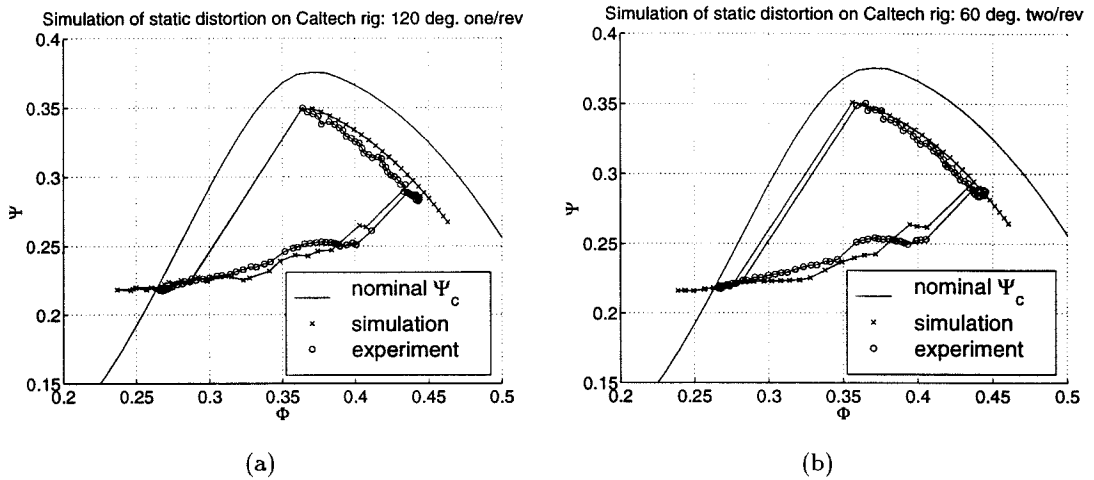
Figure 7.7 Simulation of static distortion: (a) 120° one/rev, (b) 60° two/rev.

120° one/rev

The open– and closed–loop results of the undistorted and distorted cases for 120°, one/rev static distortion are shown in Figure 7.8.

Tip Radial

The open– and closed–loop results of the undistorted and distorted cases for tip radial static distortion are shown in Figure 7.9.

Hub Radial

The open– and closed–loop results of the undistorted and distorted cases for hub radial static distortion are shown in Figure 7.10.

60° two/rev

The open– and closed–loop results of the undistorted and distorted cases for 60°, two/rev static distortion are shown in Figure 7.11.
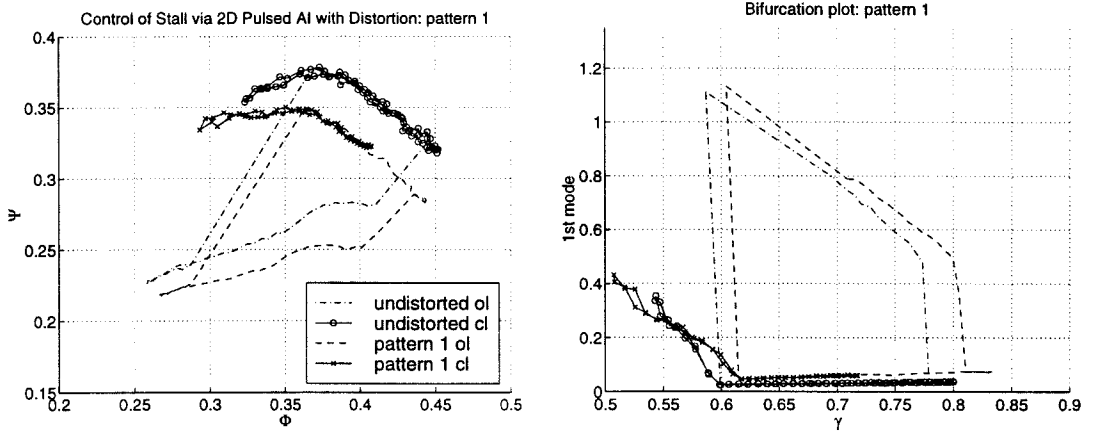
Figure 7.8 Open– and closed–loop compressor characteristic data: 120°
one/rev.
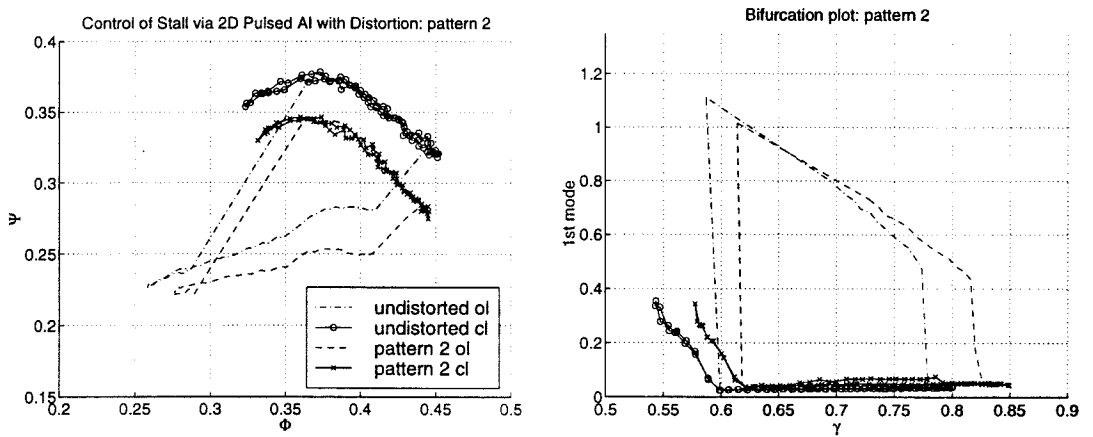
Figure 7.9 Open– and closed–loop compressor characteristic data: tip
radial.
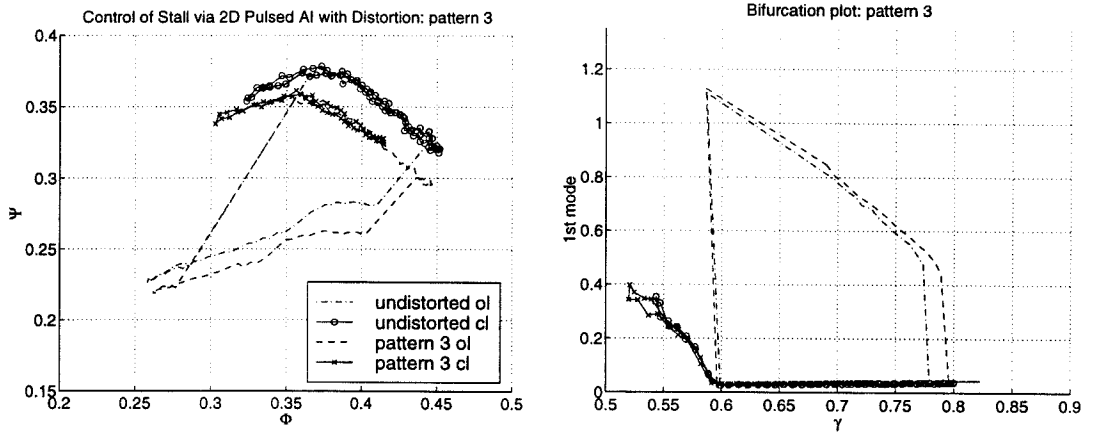
Figure 7.10 Open– and closed–loop compressor characteristic data: hub radial.
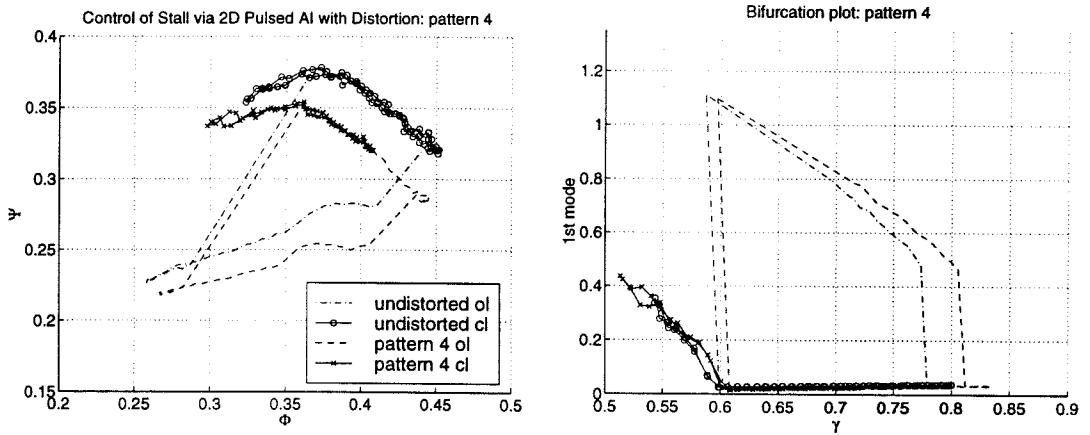
Figure 7.11 Open– and closed–loop compressor characteristic data: 60° two/rev.
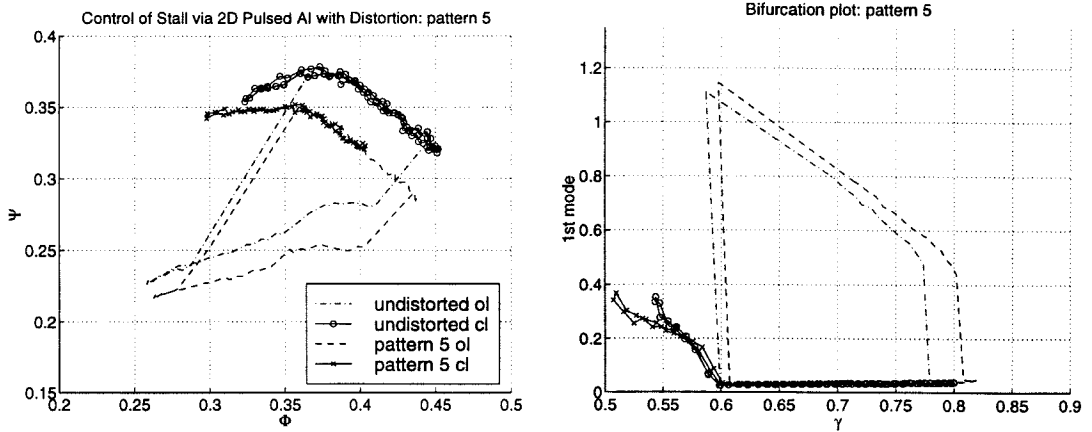
Figure 7.12 Open– and closed–loop compressor characteristic data: aircraft pattern.

Aircraft Pattern: tip radial and 120° one/rev at mid–span

The open– and closed–loop results of the undistorted and distorted cases for an aircraft pattern static distortion are shown in Figure 7.12.

From the plots shown in this section, it is clear that the non–axisymmetric pulsed controller is robust to the tested static distortion patterns, as expected. Performance in terms of pressure rise, however, varies slightly. In particular, the branches of equilibria appear to be flatter in the cases of the 120° one/rev and the aircraft pattern cases than the others.

7.3 Conclusion

The study of static distortions gives conclusions that are consistent with those reported in the literature. In particular, the effects of the tip radial pattern is most severe, in terms of stall onset as a function of load, among the pattern tested, while the hub radial pattern has the least effects. This is consistent with observations found in literature [58]. The 120° one/rev circumferential distortion pattern is found to have more severe effects compared to the 60° two/rev, which is also consistent with literature [45, 79]. Numerical simulation of the 120° one/rev pattern via a high fidelity model (34 states) agrees well both qualitatively and quantitatively to

the experiments.

The robustness of the pulsed controller to static distortion is also investigated experimentally. Results show that the control algorithm is robust to the disturbance, as expected, due to the static nature of the distortion.

Chapter 8

Conclusions and Future Work

Conclusions from the work presented in this thesis are summarized in this chapter. Suggestions for future work are also made.

8.1   Conclusions

The main focus of this thesis is to study the use of bleed valves and air injection for control of rotating stall and surge, the compressor behavior in the presence of various types of inlet disturbances, and the effectiveness of an air injection control algorithm, developed for the undistorted case, on the distorted cases.

For bleed valve control of stall and surge, demonstration of control on the Caltech facility is found to be successful only when the compressor characteristic is actuated, in this particular case, via steady air injection. This is due to the fast stall cell growth rate compared to the bandwidth and rate limits of the bleed valve.

Theoretical and high fidelity simulation tools are developed and used to predict the rate requirement of the bleed valve for control of stall. By varying the amount of air injection, a family of compressor characteristics are obtained experimentally and used to perform a comparison study between theory, simulation, and experiments. The tools are found to agree qualitatively with the experiments. The rate limit requirement is found to be reduced by a factor of 14 experimentally.

For axisymmetric air injection control, a theoretical justification is provided for control of stall and surge. In particular, axisymmetric air injection is found to alter

the criticality of the bifurcation without affecting the nominal linear stability. Surge is then shown to be linearly controllable along the controlled branch.

Demonstration of control is also carried out for axisymmetric air injection. Three cases with varying authority are tested and simultaneous control of stall and surge is achieved for two cases, but not the lowest authority case. The difference between the overlapping and non–overlapping hystereses cases is conjectured to be rate limit based. Theoretically, the axisymmetric air injection scenario is found to be analogous to the bleed valve case and previous efforts by Wang and Murray [93, 94] can be applied to study the effects of actuator limits on control. Some preliminary calculations are carried out and found to be consistent with predictions from low order models.

For non–axisymmetric air injection, efforts are made to model the effects in axial compressors in the context of the Moore–Greitzer model [37, 65]. The effects of steady air injection is modeled as a combination of the mass, momentum, and compressor characteristic shifting effects. The mass and momentum effects are taken into account via the appropriate macroscopic balances similar to Behnken [4] and Hendricks and Gysling [40]. The compressor characteristic shifting effect is modeled as a change of losses and incidence angles due to air injection. In this case a model of an oblique jet with a mean background flow similar to those found in Rajaratnam [77] is used to estimate the velocity profile of the deflected jet on the rotor face. The losses are parameterized by the incidence angle and used to estimate the new losses in the presence of air injection. Using parameter values from the experiments, a comparison of the compressor characteristics with air injection predicted by the theory to their identified counterparts is made for 13 injection configurations. Results show that the prediction agrees well qualitatively and reasonably well quantitatively with the experiments.

For active control, low order models are derived for non–axisymmetric air injection in terms of implementation–oriented variables such as number and width of injectors, and injected velocity. A theoretical comparison is performed between three existing control algorithms found in literature, namely, a bi– and uni–directional pro-

portional harmonic [92, 95], and a uni–directional binary pulsed control law [4, 12], in terms of operability versus control authority. Results show that the bi–directional harmonic control is favorable when only a small amplitude of stall is acceptable, while the uni–directional pulsed becomes attractive when a large amplitude of stall can be tolerated. It is also observed that, given a constant coverage by actuators, a large number of injectors with a small width, i.e. fine resolution, favors the harmonic control laws, while a small number of injectors with a large width favors the pulsed control law.

In addition to the theoretical comparison, simulations of the uni–directional binary pulsed control law [4, 12] using a high fidelity model proposed by Mansoux et al. [59], realistic dynamics proposed by Haynes et al. [39], and air injection effects described in this thesis are also carried out. Results show that the model agrees qualitatively as well as quantitatively with experiments.

The effects of static distortion on the Caltech compressor facility is studied. Five patterns, namely, 120° one/rev, 60° two/rev, tip and hub radial, and an aircraft pattern (tip radial and 120° one/rev at mid–span) are studied, with the total area of spoiled flow kept constant. Results show that 120° one/rev gives an earlier stall inception point compared to 60° two/rev which is consistent with literature [45, 79]. Tip and hub radial induce the earliest and latest stall inception respectively among the five cases, which is also consistent with the expected behavior of tip–loaded compressors [44, 58]. Furthermore, simulations of the 120° one/rev and 60° two/rev patterns using a high fidelity model show good qualitative and quantitative agreement to the corresponding experiments.

The effectiveness of the uni–directional pulsed control algorithm [4, 12], which is designed for undistorted flow, is evaluated in the presence of the static distortions. Results show that the pulsed algorithm is robust to circumferential, radial, as well as aircraft distortion patterns.

8.2 Future Work

Despite the models and results reported in literature and this thesis, there are many open issues in control of rotating stall and surge. A few of these issues are discussed in this section.

8.2.1 Modeling and Control

In the study of static distortion, the model is applicable for circumferential but not radial patterns. Preliminary investigations of rotating distortion and planar turbulence also show that existing models capture some but not all of the essential features observed from experiments. Accurate models for inlet disturbances are highly desirable in the interests of understanding the effects and controlling in the presence of them.

The existing control–oriented models are primarily two–dimensional — the dynamics in the radial direction is largely ignored. However, since the stall inception process is intimately related to flow separation (particularly in the tip region) and secondary flows, the variation in the radial direction is important. Some flavor of three–dimensional modeling has been used and discussed by researchers such as Chue et al. [9], Hynes et al. [45] and this thesis for distortion and air injection. A full three–dimensional model capturing stall inception process is highly beneficial in terms of not only providing an understanding of the physical process of stall but also control opportunities. Exploitation of the finer scales may lead to a reduction of the actuator requirements.

One stage of a compressor contains a rotor and a stator. Most of the existing control–oriented models approximate the entire stage as one semi–actuator disc without considering the inter–blade–row dynamics. On actual gas turbine engines, multi–stage as opposed to single–stage axial flow compressors are commonly found. The multiple stages are arranged in blocks, where each block contains a few stages, with a small gap between adjacent blocks. Existing control–oriented models again ignore the inter–block dynamics. A multi–block model can be formulated where

inter–blade–row and/or inter–block dynamics is taken into account. If actuation capabilities are present for each block, an actuator allocation problem can be formulated and addressed.

One of the themes of the work in the field of modeling and control of compressor instabilities is the use of low order, control–oriented models for control analysis and synthesis. To obtain quantitative accuracy, tools and methodologies that allow analysis and synthesis on higher order models are highly desirable. Also, the bifurcation–theoretic approach found in the literature and this thesis focus mainly on static bifurcations. Other approaches such as control of limit cycles are also important for both the flow control and nonlinear control communities.

8.2.2 Sensing and Actuation

On most of the current research facilities, sensing of stall and surge is performed using hotwire anemometry and strain gauges. There are survival and maintainability issues associated with the use of these types of sensors on actual engines. Research and investigation in sensing technologies that provide inexpensive, durable, and high resolution sensors, and algorithms that detect stall and surge events will complement controls to a great extent. Some examples of the latter include Breuer [7], Bright et al. [8], Krener and Krstić [48], and Palomba [72].

The results for bleed valve presented in this thesis employ the actuator in a one–dimensional fashion, for which the nominal linear stability is not affected. Two–dimensional use of closed–coupled downstream bleed actuators can potentially be used to achieve stability extension. Some models [53] as well as preliminary experimental results by Fahim [27] have been reported in this direction.

One aspect of the effects of actuator limits, namely, the rate limit, on bleed valve control of stall has been studied. Other aspects such as bandwidth and delay are also parts of actuator dynamics. A comparison study between the theory, simulation, and experiments on various features of actuator limitations will not only validate the model and the analysis, but also allow a more complete picture of how control implementation is affected. The resulting sensitivity analysis can be used as a design

guideline for compressor–bleed pair construction with intent of active control of stall implementations. Analogous studies can be performed for other types of actuation mechanisms. An extension of this idea leads to the study of actuator dynamics in control.

Demonstration of harmonic control, via non–axisymmetric air injection, has been reported on experimental facilities of various scales [92, 95]. On the other hand, the uni–directional pulsed algorithm has only been demonstrated on a low speed, single stage, axial compressor with a low pressure ratio ($\approx$ 1.01). Validation of the approach as well as evaluation of feasibility in terms of blade stress and noise issues are of definite interests.

While stability and/or operability can be achieved via control of stall and surge, industry has not been too enthusiastic about actual implementations. In the set of reports [21, 22, 46] prepared for the National Technical Information Service of the U.S. Department of Commerce on an evaluation of control concepts applied to gas turbine engine operations for both civilian and military aircraft, active controls of stall and surge is termed "high risk, high reward" relative to the level of technology at the time. The main concern is that the weight, life, and maintainability of the required actuators might offset the potential gains brought about by active controls. It is also concluded in Przybylko [76] that the bottleneck of active control technology in aircraft engines seems to reside in the actuator level. To increase incentive to implement existing ideas of control of stall and surge, development and validation of actuators low in cost, weight, bandwidth, energy and maintenance requirements is a clearly logical step in that direction. Promising techniques may include synthetic jets by Wiltse and Glezer [98], Jacobson and Reynolds [47], and Rathnasingham and Breuer [78], glow discharge actuators by Corke [10], and microelectromechanical systems (MEMS) technology.

8.2.3 Beyond

While some success for control of compressors has been achieved, it is not clear what effects the control strategies implemented upstream will have on downstream

components. For instance, non–uniformity in the flow field created via air injection for control of stall in the compressor may trigger combustion instabilities and/or hot–spots formation in the combustion chamber. To guarantee stability and performance of an engine, an integrated systems approach should be taken to consider interactions between components.

On a larger horizon, the study of compressor instabilities has induced exploration of new ideas and use of various tools for controls. Extension of these ideas and tools from compressors onto other control problems found in other fluid systems may be made.

Appendix A

Low Order Model for Pulsed Controller

Using Maple [90], the coefficients in equation (6.10)

$$l_c \dot{\Phi} = \Psi_c - \Psi + a_1 \Psi_c' + a_2 \Psi_c'' + a_3 \Psi_c''' + \tilde{a}_0 \Psi_{ai} + \tilde{a}_1 \Psi_{ai}' + \tilde{a}_2 \Psi_{ai}'' +$$
$$\tilde{a}_3 \Psi_{ai}''' + a_4,$$
$$(m + \mu) \dot{A} = b_1 \Psi_c' + b_2 \Psi_c'' + b_3 \Psi_c''' + \tilde{b}_0 \Psi_{ai} + \tilde{b}_1 \Psi_c' + \tilde{b}_2 \Psi_c'' + \tilde{b}_3 \Psi_c''' + b_4$$

are computed to be the following:

$$a_1 = -\frac{k\Phi_j w^2 \left(-u_2 + e^{u_1 A} \cos(u_2 A)u_2 - e^{u_1 A}u_1 \sin(u_2 A)\right)}{8 u_2 \pi^3},$$

$$a_2 = \frac{1}{16 u_2{}^2 \pi^3} \left[4 k\Phi_j u_2{}^2 A + k\Phi_j{}^2 w^2 u_2{}^2 + 4 k\Phi_j \cos(w)Ae^{u_1 A} \cos(u_2 A)u_2{}^2 - \right.$$
$$4 k\Phi_j u_2{}^2 Ae^{u_1 A} \cos(u_2 A) - 2 k\Phi_j{}^2 e^{2 u_1 A} \cos(u_2 A)u_1 \sin(u_2 A)w^2 u_2 -$$
$$2 k\Phi_j{}^2 e^{u_1 A} \cos(u_2 A)w^2 u_2{}^2 - k\Phi_j{}^2 e^{2 u_1 A}u_1{}^2 w^2 \left(\cos(u_2 A)\right)^2 -$$
$$4 k\Phi_j \cos(w)Au_2{}^2 - 4 k\Phi_j \cos(w)Ae^{u_1 A}u_1 \sin(u_2 A)u_2 +$$
$$2 k\Phi_j{}^2 e^{u_1 A}u_1 \sin(u_2 A)w^2 u_2 + 4 k\Phi_j u_2 Ae^{u_1 A}u_1 \sin(u_2 A) +$$
$$\left. k\Phi_j{}^2 e^{2 u_1 A}u_1{}^2 w^2 + k\Phi_j{}^2 e^{2 u_1 A} \cos(u_2 A))^2 w^2 u_2{}^2 + 4 A^2 u_2{}^2 \pi^3 \right],$$

$$a_3 = -\frac{k\Phi_j}{96 u_2{}^3 \pi^3} \left[-24 \Phi_j u_2{}^2 Ae^{u_1 A}u_1 \sin(u_2 A) - 12 \Phi_j u_2{}^3 A + \right.$$
$$24 \Phi_j u_2{}^3 Ae^{u_1 A} \cos(u_2 A) - 6 \Phi_j{}^2 e^{u_1 A}u_1 \sin(u_2 A)w^2 u_2{}^2 - 2 \Phi_j{}^2 w^2 u_2{}^3 -$$
$$3 A^2 u_2{}^3 + 24 \cos(w)A\Phi_j e^{u_1 A}u_1 \sin(u_2 A)u_2{}^2 -$$
$$24 \cos(w)A\Phi_j e^{u_1 A} \cos(u_2 A)u_2{}^3 +$$

$$3\,A^2\mathrm{e}^{u_1\,A}\cos(u_2\,A)w^2{u_2}^3 + 12\,\cos(w)A\Phi_j\,{u_2}^3 +$$

$$24\,A\Phi_j\,\mathrm{e}^{2\,u_1\,A}\cos(u_2\,A)u_1\,\sin(u_2\,A){u_2}^2 -$$

$$24\,\cos(w)A\Phi_j\,\mathrm{e}^{2\,u_1\,A}\cos(u_2\,A)u_1\,\sin(u_2\,A){u_2}^2 -$$

$$6\,{\Phi_j}^2\mathrm{e}^{2\,u_1\,A}\,(\cos(u_2\,A))^2\,w^2{u_2}^3 +$$

$$2\,{\Phi_j}^2\mathrm{e}^{3\,u_1\,A}\,(\cos(u_2\,A))^3\,w^2{u_2}^3 + 6\,{\Phi_j}^2\mathrm{e}^{3\,u_1\,A}\cos(u_2\,A){u_1}^2w^2u_2 +$$

$$6\,{\Phi_j}^2\mathrm{e}^{2\,u_1\,A}{u_1}^2w^2\,(\cos(u_2\,A))^2\,u_2 + 12\,\cos(w)A\Phi_j\,\mathrm{e}^{2\,u_1\,A}\,(\cos(u_2\,A))^2\,{u_2}^3 -$$

$$12\,A\Phi_j\,\mathrm{e}^{2\,u_1\,A}\,(\cos(u_2\,A))^2\,{u_2}^3 - 3\,A^2\mathrm{e}^{u_1\,A}u_1\,\sin(u_2\,A)w^2{u_2}^2 +$$

$$3\,A^2\mathrm{e}^{u_1\,A}\cos(u_2\,A){u_2}^3 + 3\,A^2\,(\cos(w))^2\,{u_2}^3 - 3\,A^2w^2{u_2}^3 +$$

$$6\,{\Phi_j}^2\mathrm{e}^{u_1\,A}\cos(u_2\,A)w^2{u_2}^3 +$$

$$3\,A^2\mathrm{e}^{u_1\,A}u_1\,\sin(u_2\,A)\,(\cos(w))^2\,{u_2}^2 - 3\,A^2\mathrm{e}^{u_1\,A}u_1\,\sin(u_2\,A){u_2}^2 -$$

$$3\,A^2\mathrm{e}^{u_1\,A}\cos(u_2\,A)\,(\cos(w))^2\,{u_2}^3 - 6\,{\Phi_j}^2\mathrm{e}^{2\,u_1\,A}{u_1}^2w^2u_2 +$$

$$12\,\cos(w)A\Phi_j\,\mathrm{e}^{2\,u_1\,A}{u_1}^2u_2 -$$

$$6\,{\Phi_j}^2\mathrm{e}^{3\,u_1\,A}\,(\cos(u_2\,A))^2\,u_1\,\sin(u_2\,A)w^2{u_2}^2 -$$

$$6\,{\Phi_j}^2\mathrm{e}^{3\,u_1\,A}\,(\cos(u_2\,A))^3\,{u_1}^2w^2u_2 +$$

$$12\,{\Phi_j}^2\mathrm{e}^{2\,u_1\,A}\cos(u_2\,A)u_1\,\sin(u_2\,A)w^2{u_2}^2 - 2\,{\Phi_j}^2\mathrm{e}^{3\,u_1\,A}{u_1}^3w^2\sin(u_2\,A) +$$

$$2\,{\Phi_j}^2\mathrm{e}^{3\,u_1\,A}{u_1}^3w^2\sin(u_2\,A)\,(\cos(u_2\,A))^2 + 12\,A\Phi_j\,\mathrm{e}^{2\,u_1\,A}{u_1}^2\,(\cos(u_2\,A))^2\,u_2 -$$

$$12\,\cos(w)A\Phi_j\,\mathrm{e}^{2\,u_1\,A}{u_1}^2\,(\cos(u_2\,A))^2\,u_2 - 12\,A\Phi_j\,\mathrm{e}^{2\,u_1\,A}{u_1}^2u_2\Big]\,,$$

$$\tilde{a}_0 = \frac{kw^2\left(u_2 - \mathrm{e}^{u_1\,A}\cos(u_2\,A)u_2 + \mathrm{e}^{u_1\,A}u_1\,\sin(u_2\,A)\right)}{8\,u_2\,\pi^3}\,,$$

$$\tilde{a}_1 = \frac{-1}{8\,{u_2}^2\pi^3}\Big[k\left(-\Phi_j\,w^2{u_2}^2 - 2\,A{u_2}^2 + 2\,\Phi_j\,\mathrm{e}^{2\,u_1\,A}\cos(u_2\,A)u_1\,\sin(u_2\,A)w^2u_2 +\right.$$

$$2\,A\mathrm{e}^{u_1\,A}\cos(u_2\,A){u_2}^2 + 2\,\Phi_j\,\mathrm{e}^{u_1\,A}\cos(u_2\,A)w^2{u_2}^2 +$$

$$2\,\cos(w)A\mathrm{e}^{u_1\,A}u_1\,\sin(u_2\,A)u_2$$

$$-\Phi_j\,\mathrm{e}^{2\,u_1\,A}\,(\cos(u_2\,A))^2\,w^2{u_2}^2 + 2\,\cos(w)A{u_2}^2 - \Phi_j\,\mathrm{e}^{2\,u_1\,A}{u_1}^2w^2 -$$

$$2\,A\mathrm{e}^{u_1\,A}u_1\,\sin(u_2\,A)u_2 - 2\,\cos(w)A\mathrm{e}^{u_1\,A}\cos(u_2\,A){u_2}^2 +$$

$$\Phi_j\,\mathrm{e}^{2\,u_1\,A}{u_1}^2w^2\,(\cos(u_2\,A))^2 -$$

$$\left.2\,\Phi_j\,\mathrm{e}^{u_1\,A}u_1\,\sin(u_2\,A)w^2u_2\right)\Big]\,,$$

$$\tilde{a}_2 = \frac{1}{32\,{u_2}^3\pi^3}\Big[k\left(8\,A\Phi_j\,{u_2}^3 + 8\,A\Phi_j\,\mathrm{e}^{2\,u_1\,A}\,(\cos(u_2\,A))^2\,{u_2}^3 +\right.$$

$$6\,{\Phi_j}^2\mathrm{e}^{3\,u_1\,A}\,(\cos(u_2\,A))^3\,{u_1}^2w^2u_2 - 8\,A\Phi_j\,\mathrm{e}^{2\,u_1\,A}{u_1}^2\,(\cos(u_2\,A))^2\,u_2 +$$

$$6\,\Phi_j{}^2\mathrm{e}^{2\,u_1\,A}u_1{}^2w^2u_2 + 16\,\cos(w)A\Phi_j\,\mathrm{e}^{2\,u_1\,A}\cos(u_2\,A)u_1\sin(u_2\,A)u_2{}^2 -$$

$$(\cos(w))^2\,A^2u_2{}^3 -$$

$$6\,\Phi_j{}^2\mathrm{e}^{2\,u_1\,A}u_1{}^2w^2\,(\cos(u_2\,A))^2\,u_2 - 6\,\Phi_j{}^2\mathrm{e}^{3\,u_1\,A}\cos(u_2\,A)u_1{}^2w^2u_2 -$$

$$8\,\cos(w)A\Phi_j\,u_2{}^3 + 2\,\Phi_j{}^2\mathrm{e}^{3\,u_1\,A}u_1{}^3w^2\sin(u_2\,A) - 16\,A\Phi_j\,\mathrm{e}^{u_1\,A}\cos(u_2\,A)u_2{}^3 +$$

$$6\,\Phi_j{}^2\mathrm{e}^{2\,u_1\,A}\,(\cos(u_2\,A))^2\,w^2u_2{}^3 + A^2u_2{}^3 + 2\,\Phi_j{}^2w^2u_2{}^3 + A^2w^2u_2{}^3 -$$

$$2\,\Phi_j{}^2\mathrm{e}^{3\,u_1\,A}u_1{}^3w^2\sin(u_2\,A)\,(\cos(u_2\,A))^2 - (\cos(w))^2\,A^2\mathrm{e}^{u_1\,A}u_1\sin(u_2\,A)u_2{}^2 +$$

$$A^2\mathrm{e}^{u_1\,A}u_1\sin(u_2\,A)u_2{}^2 - A^2\mathrm{e}^{u_1\,A}\cos(u_2\,A)w^2u_2{}^3 +$$

$$A^2\mathrm{e}^{u_1\,A}u_1\sin(u_2\,A)w^2u_2{}^2 -$$

$$16\,\cos(w)A\Phi_j\,\mathrm{e}^{u_1\,A}u_1\sin(u_2\,A)u_2{}^2 + (\cos(w))^2\,A^2\mathrm{e}^{u_1\,A}\cos(u_2\,A)u_2{}^3 +$$

$$16\,A\Phi_j\,\mathrm{e}^{u_1\,A}u_1\sin(u_2\,A)u_2{}^2 - 2\,\Phi_j{}^2\mathrm{e}^{3\,u_1\,A}\,(\cos(u_2\,A))^3\,w^2u_2{}^3 -$$

$$8\,\cos(w)A\Phi_j\,\mathrm{e}^{2\,u_1\,A}\,(\cos(u_2\,A))^2\,u_2{}^3 - 6\,\Phi_j{}^2\mathrm{e}^{u_1\,A}\cos(u_2\,A)w^2u_2{}^3 +$$

$$8\,\cos(w)A\Phi_j\,\mathrm{e}^{2\,u_1\,A}u_1{}^2\,(\cos(u_2\,A))^2\,u_2 + 16\,\cos(w)A\Phi_j\,\mathrm{e}^{u_1\,A}\cos(u_2\,A)u_2{}^3 +$$

$$6\,\Phi_j{}^2\mathrm{e}^{u_1\,A}u_1\sin(u_2\,A)w^2u_2{}^2 - 12\,\Phi_j{}^2\mathrm{e}^{2\,u_1\,A}\cos(u_2\,A)u_1\sin(u_2\,A)w^2u_2{}^2 -$$

$$A^2\mathrm{e}^{u_1\,A}\cos(u_2\,A)u_2{}^3 +$$

$$6\,\Phi_j{}^2\mathrm{e}^{3\,u_1\,A}\,(\cos(u_2\,A))^2\,u_1\sin(u_2\,A)w^2u_2{}^2 - 8\,\cos(w)A\Phi_j\,\mathrm{e}^{2\,u_1\,A}u_1{}^2u_2 +$$

$$8\,A\Phi_j\,\mathrm{e}^{2\,u_1\,A}u_1{}^2u_2 - 16\,A\Phi_j\,\mathrm{e}^{2\,u_1\,A}\cos(u_2\,A)u_1\sin(u_2\,A)u_2{}^2)\Big]\,,$$

$$\tilde{a}_3 = \frac{1}{864\,u_2{}^4\pi^3}\Big[k\,\Big(72\,\Phi_j{}^3\mathrm{e}^{4\,u_1\,A}u_1{}^3\,(\cos(u_2\,A))^3\,w^2\sin(u_2\,A)u_2 -$$

$$324\,\cos(w)A\Phi_j{}^2\mathrm{e}^{3\,u_1\,A}u_1{}^2\,(\cos(u_2\,A))^3\,u_2{}^2 -$$

$$324\,A\Phi_j{}^2\mathrm{e}^{3\,u_1\,A}u_1{}^2\cos(u_2\,A)u_2{}^2 +$$

$$108\,\Phi_j{}^3\mathrm{e}^{4\,u_1\,A}\,(\cos(u_2\,A))^2\,u_1{}^2w^2u_2{}^2 + 72\,\Phi_j{}^3\mathrm{e}^{3\,u_1\,A}u_1{}^3w^2\sin(u_2\,A)u_2 +$$

$$324\,\cos(w)A\Phi_j{}^2\mathrm{e}^{2\,u_1\,A}u_1{}^2\,(\cos(u_2\,A))^2\,u_2{}^2 +$$

$$324\,A\Phi_j{}^2\mathrm{e}^{3\,u_1\,A}\,(\cos(u_2\,A))^2\,u_1\sin(u_2\,A)u_2{}^3 +$$

$$324\,A\Phi_j{}^2\mathrm{e}^{2\,u_1\,A}\,(\cos(u_2\,A))^2\,u_2{}^4 +$$

$$324\,\cos(w)A\Phi_j{}^2\mathrm{e}^{3\,u_1\,A}u_1{}^2\cos(u_2\,A)u_2{}^2 - 324\,A\Phi_j{}^2\mathrm{e}^{2\,u_1\,A}u_1{}^2\,(\cos(u_2\,A))^2\,u_2{}^2 -$$

$$324\,A\Phi_j{}^2\mathrm{e}^{u_1\,A}\cos(u_2\,A)u_2{}^4 - 72\,\Phi_j{}^3\mathrm{e}^{u_1\,A}\cos(u_2\,A)w^2u_2{}^4 -$$

$$324\,\cos(w)A\Phi_j{}^2\mathrm{e}^{2\,u_1\,A}u_1{}^2u_2{}^2 - 324\,\cos(w)A\Phi_j{}^2\mathrm{e}^{u_1\,A}u_1\sin(u_2\,A)u_2{}^3 -$$

$$648\,A\Phi_j{}^2\mathrm{e}^{2\,u_1\,A}\cos(u_2\,A)u_1\sin(u_2\,A)u_2{}^3 -$$

$$324 \cos(w) A \Phi_j{}^2 \mathrm{e}^{2\,u_1\,A} \left(\cos(u_2\,A)\right)^2 u_2{}^4 +$$

$$18\,\Phi_j{}^3 \mathrm{e}^{4\,u_1\,A} \left(\cos(u_2\,A)\right)^4 w^2 u_2{}^4 - 27 \left(\cos(w)\right)^2 A^2 \Phi_j\,\mathrm{e}^{2\,u_1\,A} \left(\cos(u_2\,A)\right)^2 u_2{}^4 -$$

$$27\,A^2 \Phi_j\,\mathrm{e}^{2\,u_1\,A} u_1{}^2 w^2 \left(\cos(u_2\,A)\right)^2 u_2{}^2 -$$

$$216\,\Phi_j{}^3 \mathrm{e}^{3\,u_1\,A} \cos(u_2\,A) u_1{}^2 w^2 u_2{}^2 - 4 \left(\cos(w)\right)^3 A^3 u_2{}^4 +$$

$$108\,\Phi_j{}^3 \mathrm{e}^{2\,u_1\,A} \left(\cos(u_2\,A)\right)^2 w^2 u_2{}^4 +$$

$$27\,A^2 \Phi_j\,\mathrm{e}^{2\,u_1\,A} u_1{}^2 \left(\cos(w)\right)^2 \left(\cos(u_2\,A)\right)^2 u_2{}^2 +$$

$$216\,\Phi_j{}^3 \mathrm{e}^{3\,u_1\,A} \left(\cos(u_2\,A)\right)^3 u_1{}^2 w^2 u_2{}^2 - 27\,A^2 \Phi_j\,\mathrm{e}^{2\,u_1\,A} u_1{}^2 \left(\cos(u_2\,A)\right)^2 u_2{}^2 -$$

$$72\,\Phi_j{}^3 \mathrm{e}^{3\,u_1\,A} \left(\cos(u_2\,A)\right)^3 w^2 u_2{}^4 + 27\,A^2 \Phi_j\,\mathrm{e}^{2\,u_1\,A} u_1{}^2 u_2{}^2 -$$

$$108 \cos(w) A \Phi_j{}^2 \mathrm{e}^{3\,u_1\,A} u_1{}^3 \sin(u_2\,A) u_2 -$$

$$54\,A^2 \Phi_j\,\mathrm{e}^{2\,u_1\,A} \cos(u_2\,A) u_1 \sin(u_2\,A) w^2 u_2{}^3 +$$

$$108\,A \Phi_j{}^2 \mathrm{e}^{3\,u_1\,A} u_1{}^3 \sin(u_2\,A) u_2 - 108\,\Phi_j{}^3 \mathrm{e}^{2\,u_1\,A} u_1{}^2 w^2 \left(\cos(u_2\,A)\right)^2 u_2{}^2 -$$

$$24 \cos(w) A^3 u_2{}^4 - 72\,\Phi_j{}^3 \mathrm{e}^{4\,u_1\,A} u_1{}^3 \cos(u_2\,A) w^2 \sin(u_2\,A) u_2 +$$

$$54 \left(\cos(w)\right)^2 A^2 \Phi_j\,\mathrm{e}^{2\,u_1\,A} \cos(u_2\,A) u_1 \sin(u_2\,A) u_2{}^3 +$$

$$27\,A^2 \Phi_j\,\mathrm{e}^{2\,u_1\,A} \left(\cos(u_2\,A)\right)^2 w^2 u_2{}^4 - 108\,\Phi_j{}^3 \mathrm{e}^{4\,u_1\,A} \left(\cos(u_2\,A)\right)^4 u_1{}^2 w^2 u_2{}^2 +$$

$$324\,A \Phi_j{}^2 \mathrm{e}^{2\,u_1\,A} u_1{}^2 u_2{}^2 -$$

$$108\,A \Phi_j{}^2 \mathrm{e}^{3\,u_1\,A} u_1{}^3 \sin(u_2\,A) \left(\cos(u_2\,A)\right)^2 u_2 -$$

$$324 \cos(w) A \Phi_j{}^2 \mathrm{e}^{3\,u_1\,A} \left(\cos(u_2\,A)\right)^2 u_1 \sin(u_2\,A) u_2{}^3 +$$

$$648 \cos(w) A \Phi_j{}^2 \mathrm{e}^{2\,u_1\,A} \cos(u_2\,A) u_1 \sin(u_2\,A) u_2{}^3 - 108 \cos(w) A \Phi_j{}^2 u_2{}^4 +$$

$$27\,A^2 \Phi_j\,w^2 u_2{}^4 + 28\,A^3 u_2{}^4 + 27\,A^2 \Phi_j\,u_2{}^4 + 18\,\Phi_j{}^3 w^2 u_2{}^4 +$$

$$108\,A \Phi_j{}^2 u_2{}^4 + 108 \cos(w) A \Phi_j{}^2 \mathrm{e}^{3\,u_1\,A} u_1{}^3 \sin(u_2\,A) \left(\cos(u_2\,A)\right)^2 u_2 +$$

$$216\,\Phi_j{}^3 \mathrm{e}^{3\,u_1\,A} \left(\cos(u_2\,A)\right)^2 u_1 \sin(u_2\,A) w^2 u_2{}^3 -$$

$$27\,A^2 \Phi_j\,\mathrm{e}^{2\,u_1\,A} u_1{}^2 \left(\cos(w)\right)^2 u_2{}^2 +$$

$$324\,A \Phi_j{}^2 \mathrm{e}^{3\,u_1\,A} u_1{}^2 \left(\cos(u_2\,A)\right)^3 u_2{}^2 -$$

$$216\,\Phi_j{}^3 \mathrm{e}^{2\,u_1\,A} u_1 \sin(u_2\,A) \cos(u_2\,A) w^2 u_2{}^3 +$$

$$324 \cos(w) A \Phi_j{}^2 \mathrm{e}^{u_1\,A} \cos(u_2\,A) u_2{}^4 + 18\,\Phi_j{}^3 \mathrm{e}^{4\,u_1\,A} u_1{}^4 w^2 \left(\cos(u_2\,A)\right)^4 +$$

$$18\,\Phi_j{}^3 \mathrm{e}^{4\,u_1\,A} u_1{}^4 w^2 - 54\,A^2 \Phi_j\,\mathrm{e}^{u_1\,A} \cos(u_2\,A) w^2 u_2{}^4 -$$

$$28\,A^3 \mathrm{e}^{u_1\,A} \cos(u_2\,A) u_2{}^4 - 27 \left(\cos(w)\right)^2 A^2 \Phi_j\,u_2{}^4 +$$

$$54\,A^2\Phi_j\,e^{u_1\,A}u_1\,\sin(u_2\,A)w^2{u_2}^3 - 4\,(\cos(w))^3\,A^3\mathrm{e}^{u_1\,A}u_1\,\sin(u_2\,A){u_2}^3 +$$

$$27\,A^2\Phi_j\,e^{2\,u_1\,A}{u_1}^2w^2{u_2}^2 - 54\,A^2\Phi_j\,e^{u_1\,A}\cos(u_2\,A){u_2}^4 +$$

$$28\,A^3\mathrm{e}^{u_1\,A}u_1\,\sin(u_2\,A){u_2}^3 + 324\,A{\Phi_j}^2\mathrm{e}^{u_1\,A}u_1\,\sin(u_2\,A){u_2}^3 -$$

$$54\,(\cos(w))^2\,A^2\Phi_j\,e^{u_1\,A}u_1\,\sin(u_2\,A){u_2}^3 - 24\,\cos(w)A^3\mathrm{e}^{u_1\,A}u_1\,\sin(u_2\,A){u_2}^3 +$$

$$24\,\cos(w)A^3\mathrm{e}^{u_1\,A}\cos(u_2\,A){u_2}^4 + 54\,A^2\Phi_j\,e^{u_1\,A}u_1\,\sin(u_2\,A){u_2}^3 -$$

$$72\,{\Phi_j}^3\mathrm{e}^{4\,u_1\,A}(\cos(u_2\,A))^3\,u_1\,\sin(u_2\,A)w^2{u_2}^3 -$$

$$36\,{\Phi_j}^3\mathrm{e}^{4\,u_1\,A}{u_1}^4w^2\,(\cos(u_2\,A))^2 +$$

$$4\,(\cos(w))^3\,A^3\mathrm{e}^{u_1\,A}\cos(u_2\,A){u_2}^4 + 54\,(\cos(w))^2\,A^2\Phi_j\,e^{u_1\,A}\cos(u_2\,A){u_2}^4 +$$

$$72\,{\Phi_j}^3\mathrm{e}^{u_1\,A}u_1\,\sin(u_2\,A)w^2{u_2}^3 - 54\,A^2\Phi_j\,e^{2\,u_1\,A}\cos(u_2\,A)u_1\,\sin(u_2\,A){u_2}^3 +$$

$$108\,{\Phi_j}^3\mathrm{e}^{2\,u_1\,A}{u_1}^2w^2{u_2}^2 + 108\,\cos(w)A{\Phi_j}^2\mathrm{e}^{3\,u_1\,A}(\cos(u_2\,A))^3\,{u_2}^4 +$$

$$27\,A^2\Phi_j\,e^{2\,u_1\,A}(\cos(u_2\,A))^2\,{u_2}^4 -$$

$$72\,{\Phi_j}^3\mathrm{e}^{3\,u_1\,A}{u_1}^3w^2\,\sin(u_2\,A)\,(\cos(u_2\,A))^2\,u_2 -$$

$$108\,A{\Phi_j}^2\mathrm{e}^{3\,u_1\,A}(\cos(u_2\,A))^3\,{u_2}^4\Big)\Big]\,,$$

$$a_4 = \frac{k\Phi_j}{16\,{u_2}^2\pi^3}\Big[\Phi_j\,w^2{u_2}^2 - 2\,\Phi\,w^2{u_2}^2 - 4\,{u_2}^2A + \Phi_j\,\mathrm{e}^{2\,u_1\,A}{u_1}^2w^2\,(\cos(u_2\,A))^2 -$$

$$4\,u_2\,A\mathrm{e}^{u_1\,A}u_1\,\sin(u_2\,A) + 4\,\cos(w)A\mathrm{e}^{u_1\,A}u_1\,\sin(u_2\,A)u_2 -$$

$$4\,\cos(w)A\mathrm{e}^{u_1\,A}\cos(u_2\,A){u_2}^2 + 4\,\cos(w)A{u_2}^2 + 2\,\Phi\,\mathrm{e}^{u_1\,A}\cos(u_2\,A)w^2{u_2}^2 -$$

$$\Phi_j\,\mathrm{e}^{2\,u_1\,A}(\cos(u_2\,A))^2\,w^2{u_2}^2 + 2\,\Phi_j\,\mathrm{e}^{2\,u_1\,A}\cos(u_2\,A)u_1\,\sin(u_2\,A)w^2u_2 -$$

$$\Phi_j\,\mathrm{e}^{2\,u_1\,A}{u_1}^2w^2 - 2\,\Phi\,\mathrm{e}^{u_1\,A}u_1\,\sin(u_2\,A)w^2u_2 + 4\,{u_2}^2A\mathrm{e}^{u_1\,A}\cos(u_2\,A)\Big]\,,$$

$$b_1 = \frac{1}{2\,u_2\,\pi^3}\Big[k\Phi_j\,u_2 + k\Phi_j\,\mathrm{e}^{u_1\,A}u_1\,\sin(u_2\,A) + 2\,Au_2\,\pi^3 - k\Phi_j\,u_2\,\cos(w) +$$

$$k\Phi_j\,u_2\,\cos(w)\mathrm{e}^{u_1\,A}\cos(u_2\,A) - k\Phi_j\,u_2\,\mathrm{e}^{u_1\,A}\cos(u_2\,A) -$$

$$k\Phi_j\,\cos(w)\mathrm{e}^{u_1\,A}u_1\,\sin(u_2\,A)\Big]\,,$$

$$b_2 = \frac{-1}{8\,{u_2}^2\pi^3}\Big[k\Phi_j\,\Big(-A\mathrm{e}^{u_1\,A}\cos(u_2\,A)\,(\cos(w))^2\,{u_2}^2 +$$

$$4\,\cos(w)\Phi_j\,\mathrm{e}^{u_1\,A}u_1\,\sin(u_2\,A)u_2 +$$

$$4\,\Phi_j\,\mathrm{e}^{u_1\,A}\cos(u_2\,A){u_2}^2 + 2\,\cos(w)\Phi_j\,\mathrm{e}^{2\,u_1\,A}(\cos(u_2\,A))^2\,{u_2}^2 +$$

$$2\,\cos(w)\Phi_j\,{u_2}^2 - 4\,\cos(w)\Phi_j\,\mathrm{e}^{u_1\,A}\cos(u_2\,A){u_2}^2 +$$

$$4\,\Phi_j\,\mathrm{e}^{2\,u_1\,A}\cos(u_2\,A)u_1\,\sin(u_2\,A)u_2 - 2\,\Phi_j\,{u_2}^2 +$$

$$A\mathrm{e}^{u_1\,A}\cos(u_2\,A)w^2{u_2}^2 + A\mathrm{e}^{u_1\,A}u_1\,\sin(u_2\,A)\,(\cos(w))^2\,u_2 -$$

$$2\,\Phi_j\,\mathrm{e}^{2\,u_1\,A}\,(\cos(u_2\,A))^2\,{u_2}^2\,+$$

$$A\,(\cos(w))^2\,{u_2}^2 - A\mathrm{e}^{u_1\,A}u_1\,\sin(u_2\,A)w^2u_2 - 4\,\Phi_j\,\mathrm{e}^{u_1\,A}u_1\,\sin(u_2\,A)u_2\,+$$

$$2\,\cos(w)\Phi_j\,\mathrm{e}^{2\,u_1\,A}{u_1}^2\,-$$

$$2\,\cos(w)\Phi_j\,\mathrm{e}^{2\,u_1\,A}{u_1}^2\,(\cos(u_2\,A))^2 - 2\,\Phi_j\,\mathrm{e}^{2\,u_1\,A}{u_1}^2\,+$$

$$2\,\Phi_j\,\mathrm{e}^{2\,u_1\,A}{u_1}^2\,(\cos(u_2\,A))^2\,-$$

$$4\,\cos(w)\Phi_j\,\mathrm{e}^{2\,u_1\,A}\cos(u_2\,A)u_1\,\sin(u_2\,A)u_2 - A w^2{u_2}^2\,-$$

$$u_2\,A\mathrm{e}^{u_1\,A}u_1\,\sin(u_2\,A)\,+$$

$${u_2}^2 A\mathrm{e}^{u_1\,A}\cos(u_2\,A) - {u_2}^2 A)\big]\,,$$

$$b_3 \;=\; \frac{1}{144\,{u_2}^3\pi^3}\big[12\,k{\Phi_j}^3{u_2}^3 + 9\,k{\Phi_j}^2 A{u_2}^3 + 24\,k\Phi_j\,\cos(w)A^2\mathrm{e}^{u_1\,A}\cos(u_2\,A){u_2}^3\,-$$

$$18\,k{\Phi_j}^2 A\mathrm{e}^{u_1\,A}\cos(u_2\,A)w^2{u_2}^3 + 18\,k{\Phi_j}^2 A\mathrm{e}^{u_1\,A}\cos(u_2\,A)\,(\cos(w))^2\,{u_2}^3\,-$$

$$9\,k{\Phi_j}^2 A\,(\cos(w))^2\,{u_2}^3 - 36\,k{\Phi_j}^3\mathrm{e}^{2\,u_1\,A}{u_1}^2\,(\cos(u_2\,A))^2\,u_2\,+$$

$$12\,k{\Phi_j}^3\cos(w)\mathrm{e}^{3\,u_1\,A}\,(\cos(u_2\,A))^3\,{u_2}^3\,+$$

$$18\,k{\Phi_j}^2 A\mathrm{e}^{2\,u_1\,A}\cos(u_2\,A)u_1\,\sin(u_2\,A)\,(\cos(w))^2\,{u_2}^2\,+$$

$$9\,k{\Phi_j}^2 A\mathrm{e}^{2\,u_1\,A}{u_1}^2\,(\cos(w))^2\,(\cos(u_2\,A))^2\,u_2\,-$$

$$9\,k{\Phi_j}^2 A\mathrm{e}^{2\,u_1\,A}{u_1}^2 w^2\,(\cos(u_2\,A))^2\,u_2 + 9\,k{\Phi_j}^2 A\mathrm{e}^{2\,u_1\,A}\,(\cos(u_2\,A))^2\,w^2{u_2}^3\,-$$

$$36\,k{\Phi_j}^3\mathrm{e}^{3\,u_1\,A}\cos(u_2\,A){u_1}^2 u_2 + 36\,k{\Phi_j}^3\cos(w)\mathrm{e}^{3\,u_1\,A}\cos(u_2\,A){u_1}^2 u_2\,-$$

$$12\,k{\Phi_j}^3\mathrm{e}^{3\,u_1\,A}\,(\cos(u_2\,A))^3\,{u_2}^3\,+$$

$$36\,k{\Phi_j}^3\mathrm{e}^{3\,u_1\,A}\,(\cos(u_2\,A))^2\,u_1\,\sin(u_2\,A){u_2}^2 + 9\,k{\Phi_j}^2 A\mathrm{e}^{2\,u_1\,A}{u_1}^2 w^2 u_2\,+$$

$$18\,A^3{u_2}^3\pi^3\,-$$

$$36\,k{\Phi_j}^3\cos(w)\mathrm{e}^{2\,u_1\,A}{u_1}^2 u_2 + 18\,k{\Phi_j}^2 A\mathrm{e}^{u_1\,A}u_1\,\sin(u_2\,A)w^2{u_2}^2\,-$$

$$72\,k{\Phi_j}^3\mathrm{e}^{2\,u_1\,A}\cos(u_2\,A)u_1\,\sin(u_2\,A){u_2}^2\,-$$

$$18\,k{\Phi_j}^2 A\mathrm{e}^{2\,u_1\,A}\cos(u_2\,A)u_1\,\sin(u_2\,A)w^2{u_2}^2\,+$$

$$36\,k{\Phi_j}^3\cos(w)\mathrm{e}^{2\,u_1\,A}{u_1}^2\,(\cos(u_2\,A))^2\,u_2\,+$$

$$36\,k{\Phi_j}^3\cos(w)\mathrm{e}^{u_1\,A}\cos(u_2\,A){u_2}^3\,+$$

$$12\,k{\Phi_j}^3\cos(w)\mathrm{e}^{3\,u_1\,A}{u_1}^3\sin(u_2\,A)\,(\cos(u_2\,A))^2\,-$$

$$36\,k{\Phi_j}^3\cos(w)\mathrm{e}^{2\,u_1\,A}\,(\cos(u_2\,A))^2\,{u_2}^3 + 36\,k{\Phi_j}^3\mathrm{e}^{2\,u_1\,A}\,(\cos(u_2\,A))^2\,{u_2}^3\,+$$

$$72\,k{\Phi_j}^3\cos(w)\mathrm{e}^{2\,u_1\,A}\cos(u_2\,A)u_1\,\sin(u_2\,A){u_2}^2\,-$$

$$12\,k\Phi_j{}^3\cos(w)\mathrm{e}^{3\,u_1\,A}u_1{}^3\sin(u_2\,A)+$$

$$12\,k\Phi_j{}^3\mathrm{e}^{3\,u_1\,A}u_1{}^3\sin(u_2\,A)-36\,k\Phi_j{}^3\cos(w)\mathrm{e}^{u_1\,A}u_1\sin(u_2\,A)u_2{}^2-$$

$$9\,k\Phi_j{}^2A\mathrm{e}^{2\,u_1\,A}u_1{}^2\left(\cos(w)\right)^2u_2-$$

$$36\,k\Phi_j{}^3\cos(w)\mathrm{e}^{3\,u_1\,A}\left(\cos(u_2\,A)\right)^2u_1\sin(u_2\,A)u_2{}^2-$$

$$18\,k\Phi_j{}^2A\mathrm{e}^{2\,u_1\,A}\cos(u_2\,A)u_1\sin(u_2\,A)u_2{}^2+$$

$$9\,k\Phi_j{}^2A\mathrm{e}^{2\,u_1\,A}\left(\cos(u_2\,A)\right)^2u_2{}^3-9\,k\Phi_j{}^2A\mathrm{e}^{2\,u_1\,A}u_1{}^2\left(\cos(u_2\,A)\right)^2u_2+$$

$$9\,k\Phi_j{}^2A\mathrm{e}^{2\,u_1\,A}u_1{}^2u_2-$$

$$12\,k\Phi_j{}^3\cos(w)u_2{}^3-28\,k\Phi_j\,A^2\mathrm{e}^{u_1\,A}\cos(u_2\,A)u_2{}^3-$$

$$18\,k\Phi_j{}^2A\mathrm{e}^{u_1\,A}\cos(u_2\,A)u_2{}^3+$$

$$28\,k\Phi_j\,A^2\mathrm{e}^{u_1\,A}u_1\sin(u_2\,A)u_2{}^2+18\,k\Phi_j{}^2A\mathrm{e}^{u_1\,A}u_1\sin(u_2\,A)u_2{}^2+$$

$$28\,k\Phi_j\,A^2u_2{}^3+$$

$$36\,k\Phi_j{}^3\mathrm{e}^{2\,u_1\,A}u_1{}^2u_2+9\,k\Phi_j{}^2Aw^2u_2{}^3-24\,k\Phi_j\cos(w)A^2u_2{}^3+$$

$$36\,k\Phi_j{}^3\mathrm{e}^{u_1\,A}u_1\sin(u_2\,A)u_2{}^2-$$

$$12\,k\Phi_j{}^3\mathrm{e}^{3\,u_1\,A}u_1{}^3\sin(u_2\,A)\left(\cos(u_2\,A)\right)^2-$$

$$36\,k\Phi_j{}^3\cos(w)\mathrm{e}^{3\,u_1\,A}\left(\cos(u_2\,A)\right)^3u_1{}^2u_2+$$

$$36\,k\Phi_j{}^3\mathrm{e}^{3\,u_1\,A}\left(\cos(u_2\,A)\right)^3u_1{}^2u_2+4\,k\Phi_j\left(\cos(w)\right)^3A^2\mathrm{e}^{u_1\,A}\cos(u_2\,A)u_2{}^3-$$

$$18\,k\Phi_j{}^2A\mathrm{e}^{u_1\,A}u_1\sin(u_2\,A)\left(\cos(w)\right)^2u_2{}^2-$$

$$9\,k\Phi_j{}^2A\mathrm{e}^{2\,u_1\,A}\left(\cos(u_2\,A)\right)^2\left(\cos(w)\right)^2u_2{}^3-$$

$$36\,k\Phi_j{}^3\mathrm{e}^{u_1\,A}\cos(u_2\,A)u_2{}^3-4\,k\Phi_j\left(\cos(w)\right)^3A^2u_2{}^3-$$

$$4\,k\Phi_j\left(\cos(w)\right)^3A^2\mathrm{e}^{u_1\,A}u_1\sin(u_2\,A)u_2{}^2-$$

$$24\,k\Phi_j\cos(w)A^2\mathrm{e}^{u_1\,A}u_1\sin(u_2\,A)u_2{}^2\Big]\,,$$

$$\tilde{b}_0\;=\;\frac{-1}{2\,u_2\,\pi^3}\left[k\left(-u_2+\cos(w)u_2-\mathrm{e}^{u_1\,A}u_1\sin(u_2\,A)-\cos(w)\mathrm{e}^{u_1\,A}\cos(u_2\,A)u_2+\right.\right.$$
$$\left.\left.\mathrm{e}^{u_1\,A}\cos(u_2\,A)u_2+\cos(w)\mathrm{e}^{u_1\,A}u_1\sin(u_2\,A)\right)\right]\,,$$

$$\tilde{b}_1\;=\;\frac{1}{8\,u_2{}^2\pi^3}\left[k\left(A\mathrm{e}^{u_1\,A}u_1\sin(u_2\,A)u_2+Au_2{}^2-A\mathrm{e}^{u_1\,A}\cos(u_2\,A)u_2{}^2+\right.\right.$$

$$8\cos(w)\Phi_j\,\mathrm{e}^{u_1\,A}\cos(u_2\,A)u_2{}^2+8\cos(w)\Phi_j\,\mathrm{e}^{2\,u_1\,A}\cos(u_2\,A)u_1\sin(u_2\,A)u_2-$$

$$8\cos(w)\Phi_j\,\mathrm{e}^{u_1\,A}u_1\sin(u_2\,A)u_2+A\mathrm{e}^{u_1\,A}u_1\sin(u_2\,A)w^2u_2+$$

$$4\cos(w)\Phi_j\,\mathrm{e}^{2\,u_1\,A}u_1{}^2\left(\cos(u_2\,A)\right)^2-$$

$$4\cos(w)\Phi_j\,\mathrm{e}^{2\,u_1\,A}{u_1}^2 - A\mathrm{e}^{u_1\,A}\cos(u_2\,A)w^2{u_2}^2 + 4\,\Phi_j\,\mathrm{e}^{2\,u_1\,A}{u_1}^2 -$$

$$4\,\Phi_j\,\mathrm{e}^{2\,u_1\,A}{u_1}^2\left(\cos(u_2\,A)\right)^2 + Aw^2{u_2}^2 - \left(\cos(w)\right)^2 A{u_2}^2 -$$

$$8\,\Phi_j\,\mathrm{e}^{2\,u_1\,A}\cos(u_2\,A)u_1\,\sin(u_2\,A)u_2 + 4\,\Phi_j\,\mathrm{e}^{2\,u_1\,A}\left(\cos(u_2\,A)\right)^2{u_2}^2 +$$

$$\left(\cos(w)\right)^2 A\mathrm{e}^{u_1\,A}\cos(u_2\,A){u_2}^2 - \left(\cos(w)\right)^2 A\mathrm{e}^{u_1\,A}u_1\,\sin(u_2\,A)u_2 +$$

$$8\,\Phi_j\,\mathrm{e}^{u_1\,A}u_1\,\sin(u_2\,A)u_2 - 8\,\Phi_j\,\mathrm{e}^{u_1\,A}\cos(u_2\,A){u_2}^2 + 4\,\Phi_j\,{u_2}^2 -$$

$$4\cos(w)\Phi_j\,{u_2}^2 - 4\cos(w)\Phi_j\,\mathrm{e}^{2\,u_1\,A}\left(\cos(u_2\,A)\right)^2{u_2}^2\Big)\Big]\,,$$

$$\tilde{b}_2 \;=\; \frac{1}{72\,{u_2}^3\pi^3}\Big[k\,\Big(9\,\Phi_j\,Aw^2{u_2}^3 + 18\,{\Phi_j}^2{u_2}^3 -$$

$$18\cos(w)\mathrm{e}^{3\,u_1\,A}{u_1}^3{\Phi_j}^2\sin(u_2\,A) - 18\,\mathrm{e}^{3\,u_1\,A}{u_1}^3{\Phi_j}^2\sin(u_2\,A)\left(\cos(u_2\,A)\right)^2 -$$

$$2\left(\cos(w)\right)^3\mathrm{e}^{u_1\,A}u_1\,\sin(u_2\,A)A^2{u_2}^2 - 54\cos(w){\Phi_j}^2\mathrm{e}^{u_1\,A}u_1\,\sin(u_2\,A){u_2}^2 +$$

$$2\left(\cos(w)\right)^3\mathrm{e}^{u_1\,A}\cos(u_2\,A)A^2{u_2}^3 +$$

$$18\cos(w)\mathrm{e}^{3\,u_1\,A}{u_1}^3{\Phi_j}^2\sin(u_2\,A)\left(\cos(u_2\,A)\right)^2 -$$

$$9\,A\Phi_j\,\mathrm{e}^{2\,u_1\,A}{u_1}^2w^2\left(\cos(u_2\,A)\right)^2 u_2 - 9\left(\cos(w)\right)^2 A\Phi_j\,\mathrm{e}^{2\,u_1\,A}\left(\cos(u_2\,A)\right)^2{u_2}^3 -$$

$$9\,A\Phi_j\,\mathrm{e}^{2\,u_1\,A}{u_1}^2\left(\cos(w)\right)^2 u_2 + 54\,{\Phi_j}^2\mathrm{e}^{u_1\,A}u_1\,\sin(u_2\,A){u_2}^2 +$$

$$18\,\mathrm{e}^{3\,u_1\,A}{u_1}^3{\Phi_j}^2\sin(u_2\,A) - 9\left(\cos(w)\right)^2\Phi_j\,A{u_2}^3 -$$

$$18\left(\cos(w)\right)^2\Phi_j\,A\mathrm{e}^{u_1\,A}u_1\,\sin(u_2\,A){u_2}^2 + 54\cos(w){\Phi_j}^2\mathrm{e}^{u_1\,A}\cos(u_2\,A){u_2}^3 -$$

$$54\cos(w){\Phi_j}^2\mathrm{e}^{2\,u_1\,A}\left(\cos(u_2\,A)\right)^2{u_2}^3 +$$

$$18\,\Phi_j\,A\mathrm{e}^{u_1\,A}u_1\,\sin(u_2\,A)w^2{u_2}^2 - 12\cos(w)\mathrm{e}^{u_1\,A}u_1\,\sin(u_2\,A)A^2{u_2}^2 -$$

$$18\,\Phi_j\,A\mathrm{e}^{u_1\,A}\cos(u_2\,A)w^2{u_2}^3 + 18\left(\cos(w)\right)^2\Phi_j\,A\mathrm{e}^{u_1\,A}\cos(u_2\,A){u_2}^3 +$$

$$12\cos(w)\mathrm{e}^{u_1\,A}\cos(u_2\,A)A^2{u_2}^3 + 9\,A\Phi_j\,\mathrm{e}^{2\,u_1\,A}{u_1}^2w^2u_2 +$$

$$54\cos(w){\Phi_j}^2\mathrm{e}^{2\,u_1\,A}{u_1}^2\left(\cos(u_2\,A)\right)^2 u_2 - 54\cos(w){\Phi_j}^2\mathrm{e}^{2\,u_1\,A}{u_1}^2u_2 -$$

$$108\,{\Phi_j}^2\mathrm{e}^{2\,u_1\,A}\cos(u_2\,A)u_1\,\sin(u_2\,A){u_2}^2 +$$

$$108\cos(w){\Phi_j}^2\mathrm{e}^{2\,u_1\,A}\cos(u_2\,A)u_1\,\sin(u_2\,A){u_2}^2 -$$

$$54\cos(w)\mathrm{e}^{3\,u_1\,A}\left(\cos(u_2\,A)\right)^3{\Phi_j}^2{u_1}^2u_2 -$$

$$54\cos(w)\mathrm{e}^{3\,u_1\,A}\left(\cos(u_2\,A)\right)^2{\Phi_j}^2u_1\,\sin(u_2\,A){u_2}^2 -$$

$$54\,{\Phi_j}^2\mathrm{e}^{2\,u_1\,A}{u_1}^2\left(\cos(u_2\,A)\right)^2 u_2 - 12\cos(w)A^2{u_2}^3 +$$

$$18\cos(w)\mathrm{e}^{3\,u_1\,A}\left(\cos(u_2\,A)\right)^3{\Phi_j}^2{u_2}^3 +$$

$$54\,\mathrm{e}^{3\,u_1\,A}\left(\cos(u_2\,A)\right)^2{\Phi_j}^2u_1\,\sin(u_2\,A){u_2}^2 + 54\,{\Phi_j}^2\mathrm{e}^{2\,u_1\,A}\left(\cos(u_2\,A)\right)^2{u_2}^3 +$$

$$54\,\Phi_j{}^2\mathrm{e}^{2\,u_1\,A}u_1{}^2u_2 + 54\,\cos(w)\mathrm{e}^{3\,u_1\,A}\cos(u_2\,A)\Phi_j{}^2u_1{}^2u_2 +$$

$$54\,\mathrm{e}^{3\,u_1\,A}\left(\cos(u_2\,A)\right)^3\Phi_j{}^2u_1{}^2u_2 -$$

$$54\,\mathrm{e}^{3\,u_1\,A}\cos(u_2\,A)\Phi_j{}^2u_1{}^2u_2 - 18\,A\Phi_j\,\mathrm{e}^{2\,u_1\,A}u_1\,\sin(u_2\,A)\cos(u_2\,A)w^2u_2{}^2 +$$

$$18\,\left(\cos(w)\right)^2 A\Phi_j\,\mathrm{e}^{2\,u_1\,A}u_1\,\sin(u_2\,A)\cos(u_2\,A)u_2{}^2 +$$

$$9\,A\Phi_j\,\mathrm{e}^{2\,u_1\,A}\left(\cos(u_2\,A)\right)^2 w^2u_2{}^3 - 2\,\left(\cos(w)\right)^3 A^2u_2{}^3 +$$

$$9\,A\Phi_j\,\mathrm{e}^{2\,u_1\,A}u_1{}^2\left(\cos(w)\right)^2\left(\cos(u_2\,A)\right)^2 u_2 -$$

$$18\,\mathrm{e}^{3\,u_1\,A}\left(\cos(u_2\,A)\right)^3\Phi_j{}^2u_2{}^3 - 54\,\Phi_j{}^2\mathrm{e}^{u_1\,A}\cos(u_2\,A)u_2{}^3 -$$

$$18\,\cos(w)\Phi_j{}^2u_2{}^3 + 9\,A\Phi_j\,u_2{}^3 + 9\,A\Phi_j\,\mathrm{e}^{2\,u_1\,A}\left(\cos(u_2\,A)\right)^2 u_2{}^3 -$$

$$9\,A\Phi_j\,\mathrm{e}^{2\,u_1\,A}u_1{}^2\left(\cos(u_2\,A)\right)^2 u_2 - 18\,A\Phi_j\,\mathrm{e}^{u_1\,A}\cos(u_2\,A)u_2{}^3 +$$

$$14\,A^2u_2{}^3 + 14\,A^2\mathrm{e}^{u_1\,A}u_1\,\sin(u_2\,A)u_2{}^2 + 18\,A\Phi_j\,\mathrm{e}^{u_1\,A}u_1\,\sin(u_2\,A)u_2{}^2 -$$

$$14\,A^2\mathrm{e}^{u_1\,A}\cos(u_2\,A)u_2{}^3 + 9\,A\Phi_j\,\mathrm{e}^{2\,u_1\,A}u_1{}^2u_2 -$$

$$\left.18\,A\Phi_j\,\mathrm{e}^{2\,u_1\,A}\cos(u_2\,A)u_1\,\sin(u_2\,A)u_2{}^2\right)\Big],$$

$$\tilde{b}_3 \;=\; \frac{1}{576\,u_2{}^4\pi^3}\left[k\left(108\,A\Phi_j{}^2\mathrm{e}^{3\,u_1\,A}u_1{}^2\cos(u_2\,A)u_2{}^2 -\right.\right.$$

$$108\,A\Phi_j{}^2\mathrm{e}^{3\,u_1\,A}\left(\cos(u_2\,A)\right)^2 u_1\,\sin(u_2\,A)u_2{}^3 -$$

$$108\,A\Phi_j{}^2\mathrm{e}^{2\,u_1\,A}\left(\cos(u_2\,A)\right)^2 u_2{}^4 +$$

$$108\,A\Phi_j{}^2\mathrm{e}^{2\,u_1\,A}u_1{}^2\left(\cos(u_2\,A)\right)^2 u_2{}^2 +$$

$$108\,A\Phi_j{}^2\mathrm{e}^{u_1\,A}\cos(u_2\,A)u_2{}^4 + 216\,A\Phi_j{}^2\mathrm{e}^{2\,u_1\,A}\cos(u_2\,A)u_1\,\sin(u_2\,A)u_2{}^3 +$$

$$112\,A^2\Phi_j\,\mathrm{e}^{2\,u_1\,A}u_1{}^2\left(\cos(u_2\,A)\right)^2 u_2{}^2 -$$

$$112\,A^2\Phi_j\,\mathrm{e}^{2\,u_1\,A}u_1{}^2u_2{}^2 - 36\,A\Phi_j{}^2\mathrm{e}^{3\,u_1\,A}u_1{}^3\sin(u_2\,A)u_2 -$$

$$108\,A\Phi_j{}^2\mathrm{e}^{2\,u_1\,A}u_1{}^2u_2{}^2 + 36\,A\Phi_j{}^2\mathrm{e}^{3\,u_1\,A}u_1{}^3\sin(u_2\,A)\left(\cos(u_2\,A)\right)^2 u_2 -$$

$$12\,A^3u_2{}^4 - 112\,A^2\Phi_j\,u_2{}^4 - 36\,A\Phi_j{}^2u_2{}^4 - 108\,A\Phi_j{}^2\mathrm{e}^{3\,u_1\,A}u_1{}^2\left(\cos(u_2\,A)\right)^3 u_2{}^2 +$$

$$12\,A^3\mathrm{e}^{u_1\,A}\cos(u_2\,A)u_2{}^4 + 224\,A^2\Phi_j\,\mathrm{e}^{u_1\,A}\cos(u_2\,A)u_2{}^4 -$$

$$12\,A^3\mathrm{e}^{u_1\,A}u_1\,\sin(u_2\,A)u_2{}^3 - 108\,A\Phi_j{}^2\mathrm{e}^{u_1\,A}u_1\,\sin(u_2\,A)u_2{}^3 -$$

$$224\,A^2\Phi_j\,\mathrm{e}^{u_1\,A}u_1\,\sin(u_2\,A)u_2{}^3 + 224\,A^2\Phi_j\,\mathrm{e}^{2\,u_1\,A}\cos(u_2\,A)u_1\,\sin(u_2\,A)u_2{}^3 -$$

$$112\,A^2\Phi_j\,\mathrm{e}^{2\,u_1\,A}\left(\cos(u_2\,A)\right)^2 u_2{}^4 + 36\,A\Phi_j{}^2\mathrm{e}^{3\,u_1\,A}\left(\cos(u_2\,A)\right)^3 u_2{}^4 - 48\,\Phi_j{}^3u_2{}^4 -$$

$$9\,A^3w^2u_2{}^4 - 36\,A\Phi_j{}^2w^2u_2{}^4 - 48\,\mathrm{e}^{4\,u_1\,A}u_1{}^4\Phi_j{}^3 + 3\,\left(\cos(w)\right)^4 A^3u_2{}^4 +$$

$$48\,\cos(w)\Phi_j{}^3u_2{}^4 - 192\,\cos(w)\Phi_j{}^3\mathrm{e}^{3\,u_1\,A}u_1{}^3\sin(u_2\,A)\left(\cos(u_2\,A)\right)^2 u_2 -$$

$$108\,A\Phi_j{}^2\mathrm{e}^{2\,u_1\,A}u_1{}^2w^2u_2{}^2 + 108\,A\Phi_j{}^2\mathrm{e}^{2\,u_1\,A}u_1{}^2w^2\left(\cos(u_2\,A)\right)^2u_2{}^2 -$$

$$108\,A\Phi_j{}^2\mathrm{e}^{2\,u_1\,A}\left(\cos(u_2\,A)\right)^2w^2u_2{}^4 + 192\,\Phi_j{}^3\mathrm{e}^{u_1\,A}\cos(u_2\,A)u_2{}^4 -$$

$$9\left(\cos(w)\right)^2A^3\mathrm{e}^{u_1\,A}\cos(u_2\,A)u_2{}^4 + 16\left(\cos(w)\right)^3A^2\Phi_j\,u_2{}^4 +$$

$$192\,\mathrm{e}^{4\,u_1\,A}\left(\cos(u_2\,A)\right)^3\Phi_j{}^3u_1\sin(u_2\,A)u_2{}^3 -$$

$$576\,\Phi_j{}^3\mathrm{e}^{3\,u_1\,A}\left(\cos(u_2\,A)\right)^2u_1\sin(u_2\,A)u_2{}^3 +$$

$$192\,\Phi_j{}^3\mathrm{e}^{3\,u_1\,A}u_1{}^3\sin(u_2\,A)\left(\cos(u_2\,A)\right)^2u_2 -$$

$$192\,\mathrm{e}^{4\,u_1\,A}\left(\cos(u_2\,A)\right)^3\Phi_j{}^3u_1{}^3\sin(u_2\,A)u_2 +$$

$$192\,\mathrm{e}^{4\,u_1\,A}\cos(u_2\,A)\Phi_j{}^3u_1{}^3\sin(u_2\,A)u_2 - 192\,\Phi_j{}^3\mathrm{e}^{3\,u_1\,A}u_1{}^3\sin(u_2\,A)u_2 +$$

$$576\,\cos(w)\Phi_j{}^3\mathrm{e}^{3\,u_1\,A}\left(\cos(u_2\,A)\right)^3u_1{}^2u_2{}^2 -$$

$$36\,A\Phi_j{}^2\mathrm{e}^{3\,u_1\,A}u_1{}^3\left(\cos(w)\right)^2\sin(u_2\,A)\left(\cos(u_2\,A)\right)^2u_2 +$$

$$36\,A\Phi_j{}^2\mathrm{e}^{3\,u_1\,A}u_1{}^3w^2\sin(u_2\,A)\left(\cos(u_2\,A)\right)^2u_2 -$$

$$36\,A\Phi_j{}^2\mathrm{e}^{3\,u_1\,A}u_1{}^3w^2\sin(u_2\,A)u_2 + 108\,A\Phi_j{}^2\mathrm{e}^{3\,u_1\,A}u_1{}^2\cos(u_2\,A)w^2u_2{}^2 +$$

$$16\left(\cos(w)\right)^3\mathrm{e}^{2\,u_1\,A}\left(\cos(u_2\,A)\right)^2A^2\Phi_j\,u_2{}^4 +$$

$$16\left(\cos(w)\right)^3\mathrm{e}^{2\,u_1\,A}u_1{}^2A^2\Phi_j\,u_2{}^2 + 96\,\cos(w)\mathrm{e}^{2\,u_1\,A}u_1{}^2A^2\Phi_j\,u_2{}^2 -$$

$$16\left(\cos(w)\right)^3\mathrm{e}^{2\,u_1\,A}u_1{}^2A^2\Phi_j\left(\cos(u_2\,A)\right)^2u_2{}^2 + 36\left(\cos(w)\right)^2A\Phi_j{}^2u_2{}^4 +$$

$$576\,\Phi_j{}^3\mathrm{e}^{3\,u_1\,A}\cos(u_2\,A)u_1{}^2u_2{}^2 -$$

$$576\,\cos(w)\Phi_j{}^3\mathrm{e}^{2\,u_1\,A}\cos(u_2\,A)u_1\sin(u_2\,A)u_2{}^3 +$$

$$192\,\cos(w)\mathrm{e}^{4\,u_1\,A}\left(\cos(u_2\,A)\right)^3\Phi_j{}^3u_1{}^3\sin(u_2\,A)u_2 -$$

$$192\,\cos(w)\mathrm{e}^{4\,u_1\,A}\left(\cos(u_2\,A)\right)^3\Phi_j{}^3u_1\sin(u_2\,A)u_2{}^3 +$$

$$288\,\cos(w)\Phi_j{}^3\mathrm{e}^{2\,u_1\,A}\left(\cos(u_2\,A)\right)^2u_2{}^4 +$$

$$108\,A\Phi_j{}^2\mathrm{e}^{u_1\,A}\cos(u_2\,A)w^2u_2{}^4 - 192\,\cos(w)\Phi_j{}^3\mathrm{e}^{u_1\,A}\cos(u_2\,A)u_2{}^4 +$$

$$96\,\cos(w)A^2\Phi_j\,u_2{}^4 + 108\,A\Phi_j{}^2\mathrm{e}^{3\,u_1\,A}u_1{}^2\left(\cos(u_2\,A)\right)^3\left(\cos(w)\right)^2u_2{}^2 -$$

$$96\,\cos(w)\mathrm{e}^{2\,u_1\,A}u_1{}^2A^2\Phi_j\left(\cos(u_2\,A)\right)^2u_2{}^2 -$$

$$576\,\cos(w)\Phi_j{}^3\mathrm{e}^{3\,u_1\,A}\cos(u_2\,A)u_1{}^2u_2{}^2 +$$

$$576\,\cos(w)\Phi_j{}^3\mathrm{e}^{3\,u_1\,A}\left(\cos(u_2\,A)\right)^2u_1\sin(u_2\,A)u_2{}^3 -$$

$$32\left(\cos(w)\right)^3\mathrm{e}^{2\,u_1\,A}\cos(u_2\,A)A^2\Phi_j\,u_1\sin(u_2\,A)u_2{}^3 +$$

$$108\left(\cos(w)\right)^2A\Phi_j{}^2\mathrm{e}^{3\,u_1\,A}\left(\cos(u_2\,A)\right)^2u_1\sin(u_2\,A)u_2{}^3 -$$

$$216 \, (\cos(w))^2 \, A\Phi_j{}^2 \mathrm{e}^{2\,u_1\,A} \cos(u_2\,A)u_1 \, \sin(u_2\,A)u_2{}^3 -$$

$$108 \, A\Phi_j{}^2 \mathrm{e}^{3\,u_1\,A} u_1{}^2 \cos(u_2\,A) \, (\cos(w))^2 \, u_2{}^2 -$$

$$9 \, A^3 \mathrm{e}^{u_1\,A} u_1 \, \sin(u_2\,A)w^2 u_2{}^3 - 48 \, \mathrm{e}^{4\,u_1\,A} \, (\cos(u_2\,A))^4 \, \Phi_j{}^3 u_2{}^4 -$$

$$576 \, \Phi_j{}^3 \mathrm{e}^{3\,u_1\,A} \, (\cos(u_2\,A))^3 \, u_1{}^2 u_2{}^2 +$$

$$576 \, \Phi_j{}^3 \mathrm{e}^{2\,u_1\,A} \cos(u_2\,A)u_1 \, \sin(u_2\,A)u_2{}^3 + 288 \, \cos(w)\Phi_j{}^3 \mathrm{e}^{2\,u_1\,A} u_1{}^2 u_2{}^2 +$$

$$96 \, \cos(w)\mathrm{e}^{2\,u_1\,A} \, (\cos(u_2\,A))^2 \, A^2\Phi_j \, u_2{}^4 + 48 \, \cos(w)\mathrm{e}^{4\,u_1\,A} \, (\cos(u_2\,A))^4 \, \Phi_j{}^3 u_2{}^4 +$$

$$216 \, A\Phi_j{}^2 \mathrm{e}^{2\,u_1\,A} \cos(u_2\,A)u_1 \, \sin(u_2\,A)w^2 u_2{}^3 +$$

$$108 \, (\cos(w))^2 \, A\Phi_j{}^2 \mathrm{e}^{2\,u_1\,A} \, (\cos(u_2\,A))^2 \, u_2{}^4 -$$

$$192 \, \cos(w)A^2\Phi_j \, \mathrm{e}^{u_1\,A} \cos(u_2\,A)u_2{}^4 - 288 \, \Phi_j{}^3 \mathrm{e}^{2\,u_1\,A} \, (\cos(u_2\,A))^2 \, u_2{}^4 -$$

$$288 \, \Phi_j{}^3 \mathrm{e}^{2\,1\,A} u_1{}^2 u_2{}^2 - 288 \, \cos(w)\Phi_j{}^3 \mathrm{e}^{2\,u_1\,A} u_1{}^2 \, (\cos(u_2\,A))^2 \, u_2{}^2 -$$

$$288 \, \cos(w)\mathrm{e}^{4\,u_1\,A} \, (\cos(u_2\,A))^4 \, \Phi_j{}^3 u_1{}^2 u_2{}^2 -$$

$$288 \, \mathrm{e}^{4\,u_1\,A} \, (\cos(u_2\,A))^2 \, \Phi_j{}^3 u_1{}^2 u_2{}^2 + 9 \, (\cos(w))^2 \, A^3 \mathrm{e}^{u_1\,A} u_1 \, \sin(u_2\,A)u_2{}^3 +$$

$$3 \, (\cos(w))^4 \, A^3 \mathrm{e}^{u_1\,A} u_1 \, \sin(u_2\,A)u_2{}^3 - 192 \, \Phi_j{}^3 \mathrm{e}^{u_1\,A} u_1 \, \sin(u_2\,A)u_2{}^3 -$$

$$108 \, A\Phi_j{}^2 \mathrm{e}^{u_1\,A} u_1 \, \sin(u_2\,A)w^2 u_2{}^3 - 108 \, (\cos(w))^2 \, A\Phi_j{}^2 \mathrm{e}^{u_1\,A} \cos(u_2\,A)u_2{}^4 +$$

$$9 \, A^3 \mathrm{e}^{u_1\,A} \cos(u_2\,A)w^2 u_2{}^4 + 48 \, \cos(w)\mathrm{e}^{4\,u_1\,A} u_1{}^4\Phi_j{}^3 +$$

$$48 \, \cos(w)\mathrm{e}^{4\,u_1\,A} u_1{}^4\Phi_j{}^3 \, (\cos(u_2\,A))^4 +$$

$$96 \, \mathrm{e}^{4\,u_1\,A} u_1{}^4\Phi_j{}^3 \, (\cos(u_2\,A))^2 - 32 \, (\cos(w))^3 \, A^2\Phi_j \, \mathrm{e}^{u_1\,A} \cos(u_2\,A)u_2{}^4 +$$

$$32 \, (\cos(w))^3 \, A^2\Phi_j \, \mathrm{e}^{u_1\,A} u_1 \, \sin(u_2\,A)u_2{}^3 -$$

$$192 \, \cos(w)\mathrm{e}^{4\,u_1\,A} \cos(u_2\,A)\Phi_j{}^3 u_1{}^3 \sin(u_2\,A)u_2 +$$

$$288 \, \Phi_j{}^3 \mathrm{e}^{2\,u_1\,A} u_1{}^2 \, (\cos(u_2\,A))^2 \, u_2{}^2 + 9 \, (\cos(w))^2 \, A^3 u_2{}^4 +$$

$$288 \, \cos(w)\mathrm{e}^{4\,u_1\,A} \, (\cos(u_2\,A))^2 \, \Phi_j{}^3 u_1{}^2 u_2{}^2 +$$

$$192 \, \cos(w)\Phi_j{}^3 \mathrm{e}^{3\,u_1\,A} u_1{}^3 \sin(u_2\,A)u_2 + 192 \, \cos(w)A^2\Phi_j \, \mathrm{e}^{u_1\,A} u_1 \, \sin(u_2\,A)u_2{}^3 -$$

$$3 \, (\cos(w))^4 \, A^3 \mathrm{e}^{u_1\,A} \cos(u_2\,A)u_2{}^4 + 192 \, \cos(w)\Phi_j{}^3 \mathrm{e}^{u_1\,A} u_1 \, \sin(u_2\,A)u_2{}^3 -$$

$$108 \, A\Phi_j{}^2 \mathrm{e}^{3\,u_1\,A} u_1{}^2 \, (\cos(u_2\,A))^3 \, w^2 u_2{}^2 +$$

$$108 \, (\cos(w))^2 \, A\Phi_j{}^2 \mathrm{e}^{u_1\,A} u_1 \, \sin(u_2\,A)u_2{}^3 +$$

$$36 \, A\Phi_j{}^2 \mathrm{e}^{3\,u_1\,A} u_1{}^3 \, (\cos(w))^2 \, \sin(u_2\,A)u_2 + 288 \, \mathrm{e}^{4\,u_1\,A} \, (\cos(u_2\,A))^4 \, \Phi_j{}^3 u_1{}^2 u_2{}^2 -$$

$$108 \, A\Phi_j{}^2 \mathrm{e}^{3\,u_1\,A} \, (\cos(u_2\,A))^2 \, u_1 \, \sin(u_2\,A)w^2 u_2{}^3 +$$

$$36\,A\Phi_j{}^2\mathrm{e}^{3\,u_1\,A}\left(\cos(u_2\,A)\right)^3 w^2 u_2{}^4 + 108\,A\Phi_j{}^2\mathrm{e}^{2\,u_1\,A}u_1{}^2\left(\cos(w)\right)^2 u_2{}^2 -$$

$$108\,A\Phi_j{}^2\mathrm{e}^{2\,u_1\,A}u_1{}^2\left(\cos(w)\right)^2\left(\cos(u_2\,A)\right)^2 u_2{}^2 -$$

$$36\left(\cos(w)\right)^2 A\Phi_j{}^2\mathrm{e}^{3\,u_1\,A}\left(\cos(u_2\,A)\right)^3 u_2{}^4 +$$

$$192\,\Phi_j{}^3\mathrm{e}^{3\,u_1\,A}\left(\cos(u_2\,A)\right)^3 u_2{}^4 -$$

$$192\,\cos(w)\mathrm{e}^{2\,u_1\,A}\cos(u_2\,A)A^2\Phi_j\,u_1\,\sin(u_2\,A)u_2{}^3 -$$

$$192\,\cos(w)\Phi_j{}^3\mathrm{e}^{3\,u_1\,A}\left(\cos(u_2\,A)\right)^3 u_2{}^4 - 48\,\mathrm{e}^{4\,u_1\,A}u_1{}^4\Phi_j{}^3\left(\cos(u_2\,A)\right)^4 -$$

$$96\,\cos(w)\mathrm{e}^{4\,u_1\,A}u_1{}^4\Phi_j{}^3\left(\cos(u_2\,A)\right)^2\Big)\Big],$$

$$b_4 \;=\; \frac{-1}{8\,u_2{}^2\pi^3}\Big[k\Phi_j\left(-4\,\cos(w)\Phi\,u_2{}^2 + 4\,\Phi\,u_2{}^2 -\right.$$

$$2\,\Phi_j\,u_2{}^2 + 2\,\cos(w)\Phi_j\,\mathrm{e}^{2\,u_1\,A}u_1{}^2\left(\cos(u_2\,A)\right)^2 - 2\,\Phi_j\,\mathrm{e}^{2\,u_1\,A}u_1{}^2\left(\cos(u_2\,A)\right)^2 +$$

$$A\mathrm{e}^{u_1\,A}u_1\,\sin(u_2\,A)w^2 u_2 - 4\,\Phi_j\,\mathrm{e}^{2\,u_1\,A}\cos(u_2\,A)u_1\,\sin(u_2\,A)u_2 -$$

$$A\mathrm{e}^{u_1\,A}\cos(u_2\,A)w^2 u_2{}^2 -$$

$$A\mathrm{e}^{u_1\,A}u_1\,\sin(u_2\,A)\left(\cos(w)\right)^2 u_2 + 2\,\Phi_j\,\mathrm{e}^{2\,u_1\,A}\left(\cos(u_2\,A)\right)^2 u_2{}^2 -$$

$$2\,\cos(w)\Phi_j\,\mathrm{e}^{2\,u_1\,A}u_1{}^2 + 4\,\cos(w)\Phi_j\,\mathrm{e}^{2\,u_1\,A}\cos(u_2\,A)u_1\,\sin(u_2\,A)u_2 -$$

$$2\,\cos(w)\Phi_j\,\mathrm{e}^{2\,u_1\,A}\left(\cos(u_2\,A)\right)^2 u_2{}^2 +$$

$$2\,\cos(w)\Phi_j\,u_2{}^2 - A\left(\cos(w)\right)^2 u_2{}^2 + 2\,\Phi_j\,\mathrm{e}^{2\,u_1\,A}u_1{}^2 +$$

$$A\mathrm{e}^{u_1\,A}\cos(u_2\,A)\left(\cos(w)\right)^2 u_2{}^2 +$$

$$Aw^2 u_2{}^2 + 4\,\mathrm{e}^{u_1\,A}u_1\,\sin(u_2\,A)\Phi\,u_2 - 4\,\mathrm{e}^{u_1\,A}\cos(u_2\,A)\Phi\,u_2{}^2 -$$

$$4\,\cos(w)\mathrm{e}^{u_1\,A}u_1\,\sin(u_2\,A)\Phi\,u_2 + 4\,\cos(w)\mathrm{e}^{u_1\,A}\cos(u_2\,A)\Phi\,u_2{}^2 +$$

$$u_2\,A\mathrm{e}^{u_1\,A}u_1\,\sin(u_2\,A) -$$

$$\left.u_2{}^2 A\mathrm{e}^{u_1\,A}\cos(u_2\,A) + u_2{}^2 A\right)\Big].$$

Bibliography

[1] J. J. Adamczyk. Unsteady Fluid Dynamic Response of an Isolated Rotor with Distorted Inflow, 1974. AIAA 74-49.

[2] O. O. Badmus, C. N. Nett, and F. J. Schork. An Integrated Full-Range Surge Control/Rotating Stall Avoidance Compressor Control System. In *Proceedings of American Control Conference*, pages 3173–3180, June 1991.

[3] W. W. Bathie. *Fundamentals of Gas Turbines*. John Wiley & Sons, 1984.

[4] R. L. Behnken. *Nonlinear Control and Modeling of Rotating Stall in an Axial Flow Compressor*. PhD thesis, California Institute of Technology, September 1996.

[5] R. L. Behnken, M. Leung, and R. M. Murray. Characterizing the Effects of Air Injection on Compressor Performance for use in Active Control of Rotating Stall. In *Proceedings of The International Gas Turbine and Aeroengine Congress and Exhibition*, 1997. ASME 97-GT-316.

[6] R. L. Behnken and R. M. Murray. Combined Air Injection Control of Rotating Stall and Bleed Valve Control of Surge. In *Proceedings of American Control Conference*, pages 987–992, 1997.

[7] T. Breuer. Compressor Flow Instabilities, Part II: Analysis Techniques. In *von Karman Institute for Fluid Dynamics, Lecture Series 1996-05*, volume 1, March 1996.

[8] M. M. Bright, H. K. Qammar, H. J. Weigl, and J. D. Paduano. Stall Precursor

Identification in High-Speed Compressor Stages using Chaotic Time Series Analysis Methods. *ASME Journal of Turbomachinery*, 119(3):491–500, 1997.

[9] R. Chue, T. P. Hynes, E. M. Greitzer, C. S. Tan, and J. P. Longley. Calculations of Inlet Distortion Induced Compressor Flow Field Instability. *International Journal of Heat and Fluid Flow*, 10(3):211–223, 1989.

[10] T. C. Corke. Illinois Institute of Technology.

[11] A. J. Crook, E. M. Greitzer, C. S. Tan, and J. J. Adamczyk. Numerical-Simulation of Compressor Endwall and Casing Treatment Flow Phenomena. *ASME Journal of Turbomachinery*, 115(3):501–512, 1993.

[12] R. D'Andrea, R. L. Behnken, and R. M. Murray. Active Control of an Axial Flow Compressor via Pulsed Air Injection. *ASME Journal of Turbomachinery*, 119(4):742–752, 1998.

[13] W. N. Dawes. A Numerical Analysis of the Three-Dimensional Viscous Flow in a Transonic Compressor Rotor and Comparison with Experiment. *ASME Journal of Turbomachinery*, 109(1):83–90, 1987.

[14] W. N. Dawes. The Simulation of 3-Dimensional Viscous-Flow in Turbomachinery Geometries using a Solution-Adaptive Unstructured Mesh Methodology. *ASME Journal of Turbomachinery*, 114(3):528–537, 1992.

[15] I. J. Day. Active Suppression of Rotating Stall and Surge in Axial Compressors. *ASME Journal of Turbomachinery*, 115(1):40–47, 1993.

[16] I. J. Day, E. M. Greitzer, and N. A. Cumpsty. Prediction of Compressor Performance in Rotating Stall. *ASME Journal of Engineering Power*, 100:1–14, 1978.

[17] F. R. S. D.Küchemann. *The Aerodynamic Design of Aircraft*. Pergamon, 1978.

[18] J. Dunham. Non Axisymmetric Flows in Axial Flow Compressors, 1963. Mechanical Engineering Sciences Monograph No. 3, Inst. of Mechanical Engineers.

[19] H. W. Emmons, R. E. Kronauer, and J. A. Rockett. A Survey of Stall Propaga-
tion – Experiment and Theory. *ASME Journal of Basic Engineering*, 81:409–
416, 1959.

[20] H. W. Emmons, C. E. Pearson, and H. P. Grant. Compressor Surge and Stall
Propagation. *ASME Transactions*, 6(6):429–455, 1955.

[21] Allison Engines. Advanced Control for Air Breathing Engines – Volume 3,
Allison Gas Turbine, July 1993. N94-12272, U.S. Department of Commerce,
National Technical Information Service.

[22] General Electric Aircraft Engines. Advanced Control for Air Breathing En-
gines – Volume 2, General Electric Aircraft Engines, July 1993. N94-12271,
U.S. Department of Commerce, National Technical Information Service.

[23] J. F. Escuret and V. Garnier. Numerical Simulations of Aerodynamic Flow In-
stabilities in Axial Compressors. In *von Karman Institute for Fluid Dynamics,
Lecture Series 1996-05*, volume 1, March 1996.

[24] K. M. Eveker, D. L. Gysling, and C. N. Nett. Integrated Control of Rotating
Stall and Surge in Aeroengines. In *Proceedings of The International Society
for Optical Engineering*, pages 21–35, April 1995.

[25] J. Fabri. Rotating Stall in Axial Flow Compressors, 1967. *Internal Aerody-
namics (Turbomachinery)*, Inst. of Mechanical Engineers.

[26] J. Fabri. Growth of a Perturbation in an Axial Flow Compressor. In *Proceed-
ings of International Gas Turbine and Aeroengine Congress and Exhibition*,
1978. ASME 78-GT-30.

[27] A. Fahim. Experimental Evaluation of Asymmetric Bleed Actuation for Ro-
tating Stall and Surge Control. Master's thesis, Massachusetts Institute of
Technology, Feb 1998.

[28] J. A. Fligg. Tests of a Low Speed Three-Stage Axial Flow Compressor at

Aspect Ratios of One, Two and Four. In *Proceedings of Propulsion Joint Specialist Conference*, 1966. AIAA 66-613.

[29] L. G. Fréchette. Implications of Stability Modeling for High-Speed Axial Compressor Design. Master's thesis, Massachusetts Institute of Technology, February 1997.

[30] C. Freeman, A. G. Wilson, I. J. Day, and M. A. Swinbanks. Experiments in Active Control of Stall on an Aeroengine Gas Turbine. In *Proceedings of International Gas Turbine and Aeroengine Congress and Exhibition*, 1997. ASME 97-GT-280.

[31] B. Gal-Or. *Turbo and Jet-Engine Technology*. Israel Gas Turbine Association, 1980.

[32] A. Goto. Suppression of Mixed-flow Pump Instability and Surge by the Active Alteration of Impeller Secondary Flows. *ASME Transactions*, 116(4):621–628, 1994.

[33] E. M. Greitzer. Surge and Rotating Stall in Axial Flow Compressors: Part 1–Theoretical Compression System Model, Part 2–Experimental Results and Comparison with Theory. *ASME Journal for Engineering for Power*, 98(2):190–198, 1976.

[34] E. M. Greitzer. Review – Axial Compressor Stall Phenomena. *ASME Journal of Fluids Engineering*, 102(2):134–151, 1980.

[35] E. M. Greitzer. The Stability of Pumping Systems – the 1980 freeman scholar lecture. *ASME Journal of Fluids Engineering*, 103(2):193–242, 1981.

[36] E. M. Greitzer and H. R. Griswold. Compressor-Diffuser Interaction with Circumferential Flow Distortion. *Journal of Mechanical Engineering Science*, 18(1):25–38, 1976.

[37] E. M. Greitzer and F. K. Moore. A Theory of Post-Stall Transients in Axial

Compression Systems: Part 2–Application. *ASME Journal for Engineering for Power*, 108(2):231–239, 1986.

[38] D. L. Gysling and E. M. Greitzer. Dynamic Control of Rotating Stall in Axial-flow Compressors using Aeromechanical Feedback. *ASME Journal of Turbomachinery*, 117(3):307–319, 1995.

[39] J. M. Haynes, G. J. Hendricks, and A. H. Epstein. Active Stabilization of Rotating Stall in a Three-Stage Axial Compressor. *ASME Journal of Turbomachinery*, 116(2):226–239, 1994.

[40] G. J. Hendricks and D. L. Gysling. Theoretical Study of Sensor-Actuator Schemes for Rotating Stall Control. *AIAA Journal of Propulsion and Power*, 10(1):101–109, 1994.

[41] J. H. Horlock. *Axial Flow Compressors*. Butterworths Scientific Publications, 1958.

[42] J. H. Horlock. *Axial Flow Compressors*. Krieger Publishers, 1973.

[43] D. P. Hoult and J. C. Weil. Turbulent Plume in a Laminar Cross Flow. Technical Report 70-8, Massachusetts Institute of Technology, October 1970.

[44] W. Hurwitz. Personal communication.

[45] T. P. Hynes and E. M. Greitzer. A Method for Assessing Effects of Circumferential Flow Distortion on Compressor Stability. *ASME Journal of Turbomachinery*, 109(3):371–379, 1987.

[46] United Technologies Incorporated. Advanced Control for Air Breathing Engines – Volume 1, Pratt and Whitney, July 1993. N94-12270, U.S. Department of Commerce, National Technical Information Service.

[47] S. A. Jacobson and W. C. Reynolds. Active Control of Streamwise Vortices and Streaks in Boundary-Layers. *Journal of Fluid Mechanics*, 360(2):179–211, 1998.

[48] A. J. Krener and M. Krstić. Detecting Precursors to Stall in Experimental Data. U. S. Patent Disclosure, April, 1997.

[49] M. Krstić, I. Kanellakopoulos, and P. Kokotović. *Nonlinear and Adaptive Control Design*. John Wiley and Sons, 1995.

[50] C. Lakhwani and H. Marsh. Rotating Stall in an Isolated Rotor Row and a Single Stage Compressor, 1973. Conference Publication 3, Institution of Mechanical Engineering.

[51] S. Leiblein. Loss and Stall Analysis of Compressor Cascades. *ASME Journal of Basic Engineering*, 81:387–400, 1959.

[52] S. Leiblein. *Experimental Flow in Two Dimensional Cascades*, chapter VI. NASA SP-36, 1965.

[53] S. Liao. Personal communication.

[54] D. C. Liaw and E. H. Abed. Control of Compressor Stall Inception – A Bifurcation-theoretic Approach. *Automatica*, 32(1):109–115, 1996.

[55] J. P. Longley. A Review of Nonsteady Flow Models for Compressor Stability. *ASME Journal of Turbomachinery*, 116(2):202–214, 1994.

[56] J. P. Longley and E. M. Greitzer. Inlet Distortion Effects in Aircraft Propulsion Systems Integration. Lecture Series LS-183, May 1992.

[57] J. P. Longley, H-W Shin, R. E. Plumley, P. D. Silkowski, I. J. Day, E. M. Greitzer, C. S. Tan, and D. C. Wisler. Effects of Rotating Inlet Distortion on Multistage Compressor Stability. *ASME Journal of Turbomachinery*, 118(2):181–188, 1996.

[58] J. G. Lucas, H. B. Finger, and R. E. Filippi. Effect of Inlet-Annulus Area Blockage on Overall Performance and Stall Characteristics of an Experimental 15-Stage Axial-Flow Compressor. Technical Report R&M E53L28, NACA, 1958.

[59] C. A. Mansoux, D. L. Gysling, J. D. Setiawan, and J. D. Paduano. Distributed Nonlinear Modeling and Stability Analysis of Axial Compressor Stall and Surge. In *Proceedings of American Control Conference*, pages 2305–2316, 1994.

[60] J. D. Mattingly, W. H. Heiser, and D. H. Daley. *Aircraft Engine Design*. AIAA Education Series, 1987.

[61] R. S. Mazzawy. Multiple Segment Parallel Compressor Model for Circumferential Flow Distortion. *ASME Journal of Engineering for Power*, 99(2):288–296, 1977.

[62] R. E. McNair. Tip Clearance Effects on Stalling Pressure Rise in Axial Flow Compressors, 1960. ASME Symposium of Stall, Surge, and System Response.

[63] S. R. Montgomery and J. J. Braun. Investigation of Rotating Stall in a Single Stage Axial Compressor. Technical Report TN3823, NACA, 1955.

[64] F. K. Moore. A Theory of Rotating Stall of Multistage Axial Compressors: Part 1–3. *ASME Journal of Engineering for Gas Turbines and Power*, 106(2):313–336, 1984.

[65] F. K. Moore and E. M. Greitzer. A Theory of Post-Stall Transients in Axial Compression Systems: Part 1–Development of Equations. *ASME Journal for Engineering for Power*, 108(1):68–78, 1986.

[66] R. M. Murray, E. L. Wemhoff, and M. Kantner. *Sparrow Reference Manual*. California Institute of Technology, February 1995.

[67] J. P. Nenni and G. R. Lugwig. A Theory to Predict the Inception of Rotating Stall in Axial Flow Compressors. In *Proceedings of AIAA 7th Fluid and Plasma Dynamics Conference*, 1974. AIAA 74-528.

[68] Gordon C. Oates. The aerodynamics of aircraft gas turbine engines. Technical Report AFAPL-TR-78-52, Air Force Propulsion Laboratory, 1978.

[69] Gordon C. Oates. *Aerothermodynamics of Gas Turbine and Rocket Propulsion*. AIAA Education Series, 1984.

[70] N. Orner. Rotating Stall in Axial Flow Compressors, 1979. von Karman Institute Lecture Series, "Unsteady Flow in Turbomachines".

[71] J. D. Paduano, A. H. Epstein, L. Valavani, J. P. Longley, E. M. Greitzer, and G. R. Guenette. Active Control of Rotating Stall in a Low-Speed Axial Compressor. *ASME Journal of Turbomachinery*, 115(1):48–56, 1993.

[72] C. Palomba. Nonlinear Dynamics and Chaos Theory Applied to Rotating Stall. In *von Karman Institute for Fluid Dynamics, Lecture Series 1996-05*, volume 2, March 1996.

[73] M. Pandolfi and Colasurdo. Numerical Investigations on the Generation and Development of Rotating Stalls, 1978. ASME 78-WA/GT-5.

[74] J. L. Platten and J. F. Keffer. Entrainment in Deflected Axisymmetric Jets at Various Angles to the Stream. Technical Report 6808, University of Toronto, 1968.

[75] J. H. Potter. The Gas Turbine Cycle, November 1972. ASME paper presented at the Gas Turbine Division Forum Dinner.

[76] S. Przybylko. Active-Control Technology for Aircraft Engines. In *Proceedings of Joint Propulsion Conference and Exhibit*, Seattle Washington, 1997. AIAA 97-2769.

[77] N. Rajaratnam. *Turbulent Jets*. Elsevier, 1976.

[78] R. R. Rathnasingham and K. S. Breuer. Coupled Fluid-Structural Characteristics of Actuators for Flow-Control. *AIAA Journal*, 35(5):832–837, May 1997.

[79] C. Reid. The Response of Axial Flow Compressors to Intake Flow Distortion. In *Proceedings of International Gas Turbine and Aeroengine Congress and Exhibition*, 1969. ASME 69-GT-29.

[80] C. Rodgers. A Diffusion Factor Correlation for Centrifugal Compressor Stalling. *ASME Journal of Engineering Power*, 100(4):592–603, 1978.

[81] Aerospace Council Division Technical Committee S-16. Gas Turbine Engine Inlet Flow Distortion Guidelines. Technical Report AIR1420, Society of Automotive Engineers, 1978.

[82] Aerospace Council Division Technical Committee S-16. Inlet Total-Pressure-Distortion Considerations for Gas-Turbine Engines. Technical Report AIR1419, Society of Automotive Engineers, 1983.

[83] R. T. Sawyer. Gas-Turbines Progress Report – Introduction. *Transaction of ASME*, 75:123–126, 1953.

[84] C. Seippel. Gas Turbines in Our Century. *Transaction of ASME*, 75:121–122, 1953.

[85] L. H. Smith. The Effect of Tip Clearance on the Peak Pressure Rise of Axial Fans and Compressors, 1958. ASME Symposium of Stall.

[86] L. H. Smith. Casing Boundary Layers in Multistage Axial Flow Compressors, 1970. *Flow Research on Blading*, edited by L. S. Dzung, Elsevier Publishing Co.

[87] Z. S. Spakovszky, C. M. van Schalkwyk, H. J. Weigl, J. D. Paduano, K. L. Suder, M. M. Bright, and A. J. Strazisar. Rotating Stall Control in a High-Speed Stage with Inlet Distortion, Parts I and II. In *Proceedings of International Gas Turbine and Aeroengine Congress and Exhibition*, 1998.

[88] A. H. Stenning. Inlet Distortion Effects in Axial Compressors. *ASME Journal of Fluids Engineering*, 102(1):7–13, 1980.

[89] H. Takata and S. Nagano. Nonlinear Analysis of Rotating Stall. In *Proceedings of International Gas Turbine and Aeroengine Congress and Exhibition*, 1972. ASME 72-GT-3.

[90] Waterloo Maple V. *Maple V*. Waterloo Maple V, 1991.

[91] C. M. van Schalkwyk, J. D. Paduano, E. M. Greitzer, and A. H. Epstein. Active Stabilization of Axial Compressors with Circumferential Inlet Distortion. In *Proceedings of International Gas Turbine and Aeroengine Congress and Exhibition*, 1997. ASME 97-GT-279.

[92] H. D. Vo. Active Control of Rotating Stall in a Three-Stage Axial Compressor with Jet Actuators. Master's thesis, Massachusetts Institute of Technology, February 1997.

[93] Y. Wang and R. M. Murray. Effects of Noise, Magnitude Saturation and Rate Limits on Rotating Stall Control. In *Proceedings of Conference on Decision and Control*, pages 4682–4689, 1997.

[94] Y. Wang and R. M. Murray. Effects of the Shape of Compressor Characteristics on Actuator Requirements for Rotating Stall Control. In *Proceedings of American Control Conference*, pages 1996–2002, 1998.

[95] H. J. Weigl. Active Stabilization of Rotating Stall and Surge in a Transonic Single Stage Axial Compressor. Technical Report GTL 226, Massachusetts Institute of Technology, July 1997.

[96] H. J. Weigl, J. D. Paduano, L.G. Frechette, A. H. Epstein, and E. M. Greitzer. Active Stabilization of Rotating Stall in a Transonic Single Stage Axial Compressor. In *Proceedings of International Gas Turbine and Aeroengine Congress and Exhibition*, 1997. ASME 97-GT-411.

[97] D. S. Whitehead. Torsional Flutter of Unstalled Cascade Blades at Zero Deflection. *Great Britain A.R.C.*, RM 3429, 1964.

[98] J. M. Wiltse and A. Glezer. Manipulation of Free Shear Flows using Piezoelectric Actuators. *Journal of Fluid Mechanics*, 249(2):261–285, 1993.

[99] S. Yeung and R. M. Murray. Actuator Bandwidth and Rate Limit Reduction for Control of Compressor Rotating Stall. U. S. Patent Application, Serial No. 60/037,774, October, 1997.

[100] S. Yeung and R. M. Murray. Nonlinear Control of Rotating Stall using 1-D Bleed Valve with Continuous Air Injection. In *Proceedings of Joint Propulsion Conference and Exhibit*, Seattle Washington, 1997. AIAA 97-2660.

[101] S. Yeung and R. M. Murray. Reduction of Bleed Valve Rate Requirements for Control of Rotating Stall using Continuous Air Injection. In *Proceedings of Conference on Control Applications*, pages 683–690, 1997.